

REPUBLIQUE DU CAMEROUN

Paix – Travail – Patrie

UNIVERSITE DE YAOUNDE I
FACULTE DES SCIENCES
DEPARTEMENT DE PHYSIQUES

CENTRE DE RECHERCHE ET DE
FORMATION DOCTORALE EN
SCIENCES,
TECHNOLOGIES ET GEOSCIENCES
Laboratoire de Mécanique, Matériaux et
Structures



REPUBLIC OF CAMEROUN

Peace – Work – Fatherland

UNIVERSITY OF YAOUNDE I
FACULTY OF SCIENCE
DEPARTMENT OF PHYSICS

POSTGRADUATE SCHOOL OF
SCIENCES, TECHNOLOGY AND
GEOSCIENCES
Laboratory of Mechanics, Materials
and Structures

**HYBRID AND ELECTROMAGNETIC ENERGY
HARVESTING SYSTEMS EXHIBITING STRUCTURAL
NONLINEARITIES AND FRACTIONAL PROPERTIES:
CONTRIBUTION TO DESIGN AND OPTIMIZATION**

Thesis submitted in partial fulfillment of the requirements for the
award of the degree of Doctor of Philosophy / PhD in Physics

Par : **FOUPOUAPOUGNIGNI Oumarou**
Masters in Physics

Sous la direction de
TCHAWOUA Clément
Professor
University of Yaounde I

Année Académique : 2020





DEPARTEMENT DE PHYSIQUE
DEPARTMENT OF PHYSICS

ATTESTATION DE CORRECTION DE LA
THESE DE DOCTORAT/Ph.D

Nous, Professeur **BODO Bertrand** et Professeur **MKANKAM KAMGA François**, respectivement Examineur et Président du jury de la Thèse de Doctorat/Ph.D de Monsieur **FOUPOUPOUOGNIGNI Oumarou**, Matricule **04R222**, préparée sous la direction du Professeur **TCHAWOUA Clément**, intitulée : « **Hybrid and Electromagnetic Energy Harvesting Systems Exhibiting Structural Nonlinearities And Fractional Properties: Contribution To Design And Optimization** », soutenue le **Lundi 13 Juillet 2020**, en vue de l'obtention du grade de Docteur/Ph.D en Physique, Spécialité **Mécanique, Matériaux et Structures** option **Mécanique Fondamentale et Systèmes Complexes**, attestons que toutes les corrections demandées par le jury de soutenance ont été effectuées.

En foi de quoi, la présente attestation lui est délivrée pour servir et valoir ce que de droit.

Fait à Yaoundé, le **20 JUIL 2020**.....

Examineur

BODO Bertrand
Maître de Conférences

Le Président du jury

MKANKAM KAMGA François
Professeur



Le **Chef de Département de Physique**

J.M.
Jean-Marie
Bienvenu
Professeur

University of Yaoundé I

Faculty of Science

Department of Physics

**HYBRID AND ELECTROMAGNETIC ENERGY
HARVESTING SYSTEMS EXHIBITING STRUCTURAL
NONLINEARITIES AND FRACTIONAL PROPERTIES:
CONTRIBUTION TO DESIGN AND OPTIMIZATION**

Submitted and defended in Fulfillment of the Requirements for the Degree of Doctor of
Philosophy/PhD in Physics

Option: Fundamental Mechanics and Complex Systems

By

FOUPOUAPOUOGNIGNI Oumarou

Registration number: 04R222

Master in Physics

Director

Pr TCHAWOUA Clément

Professor, University of Yaoundé I (Cameroon)

Laboratory of mechanics, Materials and Structures

July 20, 2020

Dedication

This thesis is dedicated to God and in particular to:

✠ My parents, NCHARE Moussa and MFANGAM Pasma for their love, patience and support.

✠ My wife, NAP NJIEMESSA Fahtima, who simplifies my days, realizes my dreams and encourages me. May she find in here my sincere gratitude and love.

Acknowledgements

At the end of this PhD study, I am deeply grateful for the opportunity I have learned from and worked with so many brilliant teachers, collaborators and students. I am happy to express my sincere gratitude to all those from who near or far have helped me during this doctoral years and have directly or indirectly contributed to the completion of this document. Nevertheless, I will do my best to condense my thoughts about this.

✠ Firstly, I would like to express my sincere gratitude to my supervisor **Professor TCHAWOUA Clément** who, despite his multiple academic, administrative and family occupations, accepted to guide this work. This thesis would not have been possible without his pernickety vision in nonlinear physics and the multitude seminars organized in the Laboratory. I want to thank him for the advices he has provided me and the expertise that he has enabled me to acquire.

✠ I would like to deeply thank the honorable members of the Jury, **Professor MKANKAM KAMGA François**, **Professor TCHAWOUA Clément**, **Professor SIEWE SIEWE Martin**, **Professor EFFA Joseph Yves**, **Professor BODO Bertrand**, who agreed to set aside their multitude occupations so as to evaluate this work. I express to them all my greatest respect.

✠ I would like to thank **Professor NJAKA Jean-Marie Bienvenu**, Head of the Department of Physics for his teaching.

✠ I would like to thank **Professor KOFANE Timoléon Crépin**, head of the Laboratory of Mechanics, Materials and Structures, Option: Mechanics and complex systems. I am very grateful for the quality of his teaching and for his constructive comments.

✠ I am grateful to **Professor WOAFO Paul**, Chairman of the Cameroon Physical Society for his teaching and his encouragements.

✠ I also thank **Professor ZEKENG Serge sylvain**, Division of the organization of Scientific Meeting of the Cameroon Physical Society, for his teaching. I greatly appreciate his vision of the evolution of Science and news.

✠ Special thanks go to **Professor SIEWE SIEWE Martin** for his kindness, his availability, his encouragements and for many fruitful discussions. Despite his multiple occupations, he initiated me and gave me a taste for research.

✠ I would like to thank **Doctor NONO DUEYOU Buckjohn Clémence**, for fruitful

discussions about some aspects of the physics and especially the numerical simulations. At the end of this path, I am very grateful to him.

✂ It would be very pleasing to recognize trade and constructive discussions combined with great moments of sharing with my seniors of Mechanics laboratory. I have named:

- Professor NANA NBENDJO;
- Professor DJUIDJE Germaine;
- Professor FEWO Serge Ibraïd;
- Doctor WOULACHE Rosalie.

✂ I would like to express my gratitude to Professor VONDOU Derbetini for the fruitful discussions and his encouragements.

✂ I would like to express my gratitude to Professor SIMO Elie for his encouragement.

✂ I would also like to express my gratitude to my eldest from the Professor TCHAWOUA research team in the laboratory of Mechanics, Materials and Structures who supported me in my research work. I want to thank them for all their help, support, interest and valuable hints. Especially I thank Doctor TATCHIM BEMMO David; Doctor TOGUEU MOTCHEYO Alain; Doctor MANDENG Lucien; Doctor TCHINANG Joel; Doctor MOKEM FOKOU Igor Simplicite and Doctor DJOMO Thierry for multitude exchanges.

My sincere thanks go to the official editors and referees of Chaos, Solitons and Fractals, Physica A, for their detailed review, constructive criticism and excellent advice during the preparation of my different publications.

✂ I would also like to thank several colleagues (former and current) for their help and collaborative contributions: Doctor CHAMGOUE Andre, Doctor PATOUASSA Issoufa, KOUNGAYAP Emmanuel and TCHAGOM Evrad.

✂ I specially express my acknowledgements to the teaching staff of the Department of Physics, Faculty of Science and University of Yaounde I for their teaching during my higher education. My sincere thanks go to the Postgraduate School of Science, Technology and Geosciences.

✂ I would also like to thank the teachers I met during my primary, secondary and university school. They found here my warmest thanks.

✂ I would like to extend a special thank you to my family. They have been a constant source of love and support throughout my life, and my time in graduate school was no different. I would like to thank:

- My brothers MBOUOMBOUO Amadou, NCHOUWAT Ibrahim, YOUMIE Abdou;
- My sister NFOUPUENMO Rachidetou;

- NJIGAM family;
- NJIMONCHOUT family;
- NJIEMESSA family;
- NCHARE family;
- LOUH family;
- NSANGOU family;
- MOUNCHEROU family;
- NGOUYAMSSA family;
- MOUMPOU family.

✂ Thanks to all the unmentioned persons who have contributed even a little to this work. I did not forget you.

List of Abbreviations

AFPE:	Approximate Fokker-Planck Equation
AC:	Alternating Current
CFOAs :	Current Feedback-Operational Amplifiers
CMOS :	Complementary Metal Oxide Semiconductor
CPEs :	Constant Phase-Elements
CSA :	Classical Stochastic Averaging
DC:	Direct Current
EMEH:	Electromagnetic Energy-Harvester
EEG:	Electroencephalogram
ECG:	Electrocardiogram
EM:	Electromagnetic
FC:	Fractional Calculus
FI:	Fractional Inductor
FO:	Fractional Order
FPE :	Fokker-Planck Equation
FPK :	Fokker-Planck -Kolmogorov
G I C:	General Impedance Converter
G P S:	Global Positioning System
HEH:	Hybrid EnergyHarvester
MEMS:	Micro Electromechanical System
NdFeB:	Neodymium Magnets
ODE :	Ordinary Differential Equation
PE :	piezoelectric
PEH :	piezoelectric Energy Harvester
RF :	Radio Frequency
RK4 :	Fourth-order Runge-Kutta
RHS :	Right Hand-Side
S:	Stratonovich
SDE :	Stochastic Differential Equation
Sdof :	single -degree-of freedom
SPV :	Solar Photovoltaic

SNL : Statistical Nonlinearization
SL : Statistical Linearization
SPD : Steady-state Probability Distribution
SR : Stochastic Resonance
WZ : Wong and Zakai

Contents

Dedication	i
Acknowledgements	ii
List of Abbreviations	v
Table of Contents	vii
List of Figures	x
Abstract	xvi
Résumé	xviii
Chapter I LITERATURE REVIEW ON ENERGY HARVESTERS AND PROBLEMS STATEMENTS	6
I.1 Introduction	6
I.2 Motivations	7
I.3 Energy Sources and Energy Harvesting Technologies	8
I.3.1 Solar energy	9
I.3.2 Wind Energy	10
I.3.3 Thermal energy	10
I.3.4 RF-Based Sources	11
I.3.5 Vibration energy	12
I.3.6 The advantages and disadvantages of different types of energy harvesting	35
I.3.7 Power density of various technologies for energy harvesting	35
I.3.8 Summary of Power Scavenging Sources	36
I.3.9 Potential applications	37
I.4 Fractional Property of Energy Harvesting Systems	39
I.4.1 State of the art of fractional calculus	39
I.4.2 Fractional theory	40

I.4.3	Elements with fractional order physical properties	43
I.5	Hybrid systems	50
I.5.1	State of the Art on hybrid Systems	50
I.6	Aims of this thesis	52
I.7	Conclusion	53
Chapter II	METHODOLOGY: MODELING AND NUMERICAL METHODS	54
II.1	Introduction	54
II.2	Nonlinear Electromechanical Energy Harvesters with Fractional Inductance	54
II.2.1	Governing equations	54
II.2.2	Harmonic balance method	61
II.2.3	Amplitude equation	63
II.3	Hybrid Electromagnetic and Piezoelectric Vibration Energy Harvester with Gaussian white Noise Excitation	68
II.3.1	Description and modelling of the hybrid model	68
II.3.2	Stochastic averaging method and stochastic p-bifurcation	74
II.4	Numerical simulation techniques	85
II.4.1	Algorithms of the numerical simulations	85
II.4.2	Stochastic resonance phenomenon	88
II.4.3	Mathematical formula for determining the mean amplitude response in this thesis	89
II.4.4	Bifurcation diagram, Poincaré maps, time history and power spec- tral density	91
II.4.5	Bifurcation diagrams	92
II.4.6	Poincaré maps	94
II.4.7	Power Spectral Density	94
II.4.8	phase space and time series methods	95
II.4.9	The 0-1 test for chaos	96
II.5	Discrete schematic of the different models	97
II.5.1	Investigating Bifurcations and Chaos in Nonlinear electromechan- ical energy harvesters with fractional inductance	97
II.5.2	Discrete schematic of the nonlinear analysis of a Nonlinear elec- tromechanical energy harvesters with fractional	98
II.5.3	Discrete schematic of the probabilistic distribution and stochastic P-bifurcation of a hybrid energy harvester under Gaussian white noise	100
II.6	Conclusion	101

Chapter III RESULTS AND DISCUSSION	102
III.1 Introduction	102
III.2 Nonlinear Electromechanical Energy Harvesters with Fractional Inductance	102
III.2.1 Potential configuration	102
III.2.2 Amplitudes of the harmonic oscillatory states	103
III.2.3 Numerical simulation of bifurcation diagram, 0 – 1 test, Poincaré maps, Times History and Power Spectral Density	109
III.2.4 Numerical simulation of the system Performance under the Gaussian white Noise	114
III.2.5 Discussion	119
III.3 Numerical simulation of the probabilistic distribution and stochastic P-bifurcation of a hybrid energy harvester with Gaussian white noise excitation	120
III.3.1 Potential configuration and bifurcation diagram	120
III.3.2 Numerical simulation of the probability density of the system . . .	124
III.3.3 Mean Square Current and voltage	129
III.3.4 Stochastic Resonance	130
III.3.5 Discussion	139
III.4 Conclusion	140
General Conclusion	142
Bibliography	144
List of Publications	165

List of Figures

Figure 1	Composition of toxic batteries (http://phys.org).	7
Figure 2	Self-discharge of Lithium-ion batteries according to the temperature of use [28].	8
Figure 3	Improvement of the constituents performance of the wearable devices in the logarithmic scale between 1900 - 2003 [29]	8
Figure 4	solar panels [32].	9
Figure 5	wind turbine [33].	10
Figure 6	Example of thermoelectric generators: (a) principles and (b) realization [36].	11
Figure 7	Electrostatic Energy Harvester [37].	13
Figure 8	Three types of electrostatic generators [38]; (a) In-plane overlap, (b) In-plane gap closing, (c) Out-of-plane gap closing	14
Figure 9	(a)The direct piezoelectric effect, (b) The indirect piezoelectric effect [46].	16
Figure 10	Illustration of 33 mode and 31 mode operation of piezoelectric material [47].	17
Figure 11	Definition of forces affecting a piezoelectric element relative to the polarization.	20
Figure 12	(a) Construction of the piezoelectric generator; (b) Mechanical model of the piezoelectric generator [51].	20
Figure 13	(a) A two-layer bender mounted as a cantilever [59], (b) Piezoelectric diaphragm generator developed by Xu et al. [60]	21
Figure 14	Overview of the smart tag. (a) Perspective view of the smart tag, (b) Integration concept of the smart tag: lamination of different layers, (c) Layout of the smart tag [61].	22
Figure 15	(a) Prototype of the piezoelectric film energy harvesting device inserted in a shoe [65], (b) Two approaches to harvest piezoelectric energy in shoes [66].	23
Figure 16	Bar magnet with magnetic field lines	24

Figure 17	Popular models for linearized electromagnetic transducer analysis [67]. (a) rectangular cross section and concentrated windings, (b) circular cross section with spacious windings.	26
Figure 18	Electromagnetic Energy Harvester [68].	27
Figure 19	Relative location and parameters of the magnet and induction coil [69].	28
Figure 20	Schematic of a general energy harvesting device, which is a single-degree-of-freedom damped simple harmonic oscillator, as described by Williams and Yates [5].	30
Figure 21	(a) Schematic design developed by Beeby et al. [78], (b) the electromagnetic generator developed by Zhu et al. [79].	31
Figure 22	Electromagnetic generator developed by Von Büren et al. [83]. . .	33
Figure 23	MEMS electromagnetic generators developed by (a) Wang et al. [84], (b) Water et al. [85], (c) Kulkarni et al. [86].	34
Figure 24	Power density versus lifetime for batteries, solar cells, and vibration generators [40].	36
Figure 25	Power consumption of wireless sensor nodes [94].	38
Figure 26	PEH for pacemaker. Expansion and relaxation of the pacemaker for the generation of voltage [95].	38
Figure 27	The fractional derivative is a global operator [15].	42
Figure 28	Modelling of coils using fractional derivatives (derivation of order β , lossy inductance L_β) [105].	48
Figure 29	(a) Wearable wireless EEG system with hybrid power supply [123], (b) Hybrid generator for feeding an ECG [124].	51
Figure 30	Schematic model with the associated electric circuit [132].	55
Figure 31	Schematic of the hybrid energy harvester	68
Figure 32	The force acting on the oblique spring	69
Figure 33	Potential of the system (84) for $\lambda = 0.1$, the dot line obtained for $\varrho = 1.0$ and solid line for $\varrho = -1.0$	103
Figure 34	Amplitudes response-curves of the driving frequency ω and $E_0 = 0.5$, $\kappa = 0.25$ with the parameters $\lambda = 0.1$, $\mu_1 = 0.1$, $\mu_3 = 0.018$, $\gamma = 0.5$, $\vartheta_m = 0.76$, $\vartheta_e = 0.0056$, $\mu_e = 0.96$ and $\varrho = 1.0$	104
Figure 35	Amplitudes response-curves of the driving frequency ω and $E_0 = 0.5$, $\kappa = 0.25$ with the parameters $\lambda = 0.1$, $\mu_1 = 0.1$, $\mu_3 = 0.018$, $\gamma = 0.5$, $\vartheta_m = 0.76$, $\vartheta_e = 0.0056$, $\mu_e = 0.96$ and $\varrho = 1.0$	106

- Figure 36** Output electric power as function of the driving frequency with the parameters $\lambda = 0.1, \mu_1 = 0.1, \mu_3 = 0.018, \gamma = 0.5, \vartheta_m = 0.76, \vartheta_e = 0.0056, \mu_e = 0.96, \varrho = 1, E_0 = 0.5$ and $\kappa = 0.25$ 107
- Figure 37** Effects on the amplitude of parametric coupling γ on the amplitude response curve B and output power with the parameters $\lambda = 0.1, \mu_1 = 0.1, \mu_3 = 0.018, \vartheta_m = 0.76, \vartheta_e = 0.0056, \mu_e = 0.96, \varrho = 1, E_0 = 0.5$ and $\kappa = 1.0$. (a) amplitude response B , (b) mechanical input, (c) output electric power and (d) efficiency. 108
- Figure 38** Bifurcation diagram (a)-(b) and asymptotic growth rate k_c (c) curves for system (84) for E_0 varying with the parameters $\lambda = 0.1, \mu_1 = 0.1, \mu_3 = 0.018, \gamma = 0.5, \vartheta_m = 0.76, \vartheta_e = 0.0056, \mu_e = 0.96, \omega = 1.0, \varrho = -1.0$ and $\kappa = 1.0$ 110
- Figure 39** Phase portrait and times history of the bistable mechanical system for $\kappa = 1$; (a-b) $E_0 = 0.0911$; (c-d) $E_0 = 0.83$; (e-f) $E_0 = 0.92$. The parameters used are : $\lambda = 0.1, \mu_1 = 0.1, \mu_3 = 0.018, \gamma = 0.5, \vartheta_m = 0.76, \vartheta_e = 0.0056, \mu_e = 0.96, \varrho = -1.0$ and $\omega = 1.0$ 111
- Figure 40** Phase portraits of the mechanical part for crossing well dynamics as function of E_0 for $\kappa = 1$ and the value of Fig.38: (a) $E_0 = 0.09$, (b) $E_0 = 0.8$, (c) $E_0 = 0.9$, (d) $E_0 = 0.96$, with the parameters $\lambda = 0.1, \mu_1 = 0.1, \mu_3 = 0.018, \gamma = 0.5, \vartheta_m = 0.76, \vartheta_e = 0.0056, \mu_e = 0.96, \omega = 1.0, \varrho = -1.0$ and $\kappa = 1.0$ 112
- Figure 41** Poincaré maps, time history and power spectral density from system (84) for $\kappa = 1$ and $E_0 = 0.0911$ with the parameters: $\lambda = 0.1, \mu_1 = 0.1, \mu_3 = 0.018, \gamma = 0.5, \vartheta_m = 0.76, \vartheta_e = 0.0056, \mu_e = 0.96, \varrho = -1.0$ and $\omega = 1.0$ 115
- Figure 42** Poincaré maps, time history and power spectral density from system (84) for $\kappa = 1$ and $E_0 = 0.8284$ with the parameters: $\lambda = 0.1, \mu_1 = 0.1, \mu_3 = 0.018, \gamma = 0.5, \vartheta_m = 0.76, \vartheta_e = 0.0056, \mu_e = 0.96, \varrho = -1.0$ and $\omega = 1.0$ 116
- Figure 43** Poincaré maps, time history and power spectral density from system (84) for $\kappa = 1$ and $E_0 = 0.9318$ with the parameters: $\lambda = 0.1, \mu_1 = 0.1, \mu_3 = 0.018, \gamma = 0.5, \vartheta_m = 0.76, \vartheta_e = 0.0056, \mu_e = 0.96, \varrho = -1.0$ and $\omega = 1.0$ 117
- Figure 44** Means square of the system with the parameters $\lambda = 0.1, \mu_1 = 0.1, \mu_3 = 0.018, \vartheta_m = 0.76, \vartheta_e = 0.0056, \mu_e = 0.96, \varrho = -1.0$ and $\omega = 1.0$ 118

- Figure 45** One-dimensional potential governed by Eq.(129) with parameters $\omega_1 = 1$, $\alpha_2 = 0.72$ and metastable potentials $\alpha_3 = 0.13$, symmetric bistable potentials $\alpha_3 = 0.115$ and asymmetric bistable potentials $\alpha_3 = 0.097$ 120
- Figure 46** Effective potential $U(a)$ versus amplitude a for various values of noise intensity 122
- Figure 47** (a)Bifurcation diagram of Eq.(172) in the parameter plane (μ_3, μ_1) , (b) Stationary probability density of amplitude for three value of ζ_3 . The other parameters used are given as: $\zeta_1 = 0.25$, $\alpha_1 = 0.72$, $\alpha_3 = 0.97$, $\zeta_e = 0.84$, $\lambda = 2.0$, $\zeta_m = 0.057$, $\vartheta_p = 0.38$, $\beta = 2.05$, $\omega_0 = 1.0$, $\vartheta_e = 0.05$ and $D = 0.4$ 122
- Figure 48** (a) Amplitude response of mechanical subsystem versus ζ_1 for $D=0.4$, (b) Amplitude response of mechanical subsystem versus D for $\zeta_3 = -0.064$. The parameters are the same as those in Fig.47. 123
- Figure 49** Amplitude response of mechanical subsystem versus noise intensity D for various (a) electro-magnetic coupling coefficient ϑ_p , (b) impedance λ . The parameters are the same as those in Fig.47. . . . 123
- Figure 50** Stationary probability density of mechanical subsystem for different values of electrical impedance λ . The other parameters used are given as : $\zeta_1 = 0.25$, $\zeta_3 = 0.064$, $\alpha_1 = 0.72$, $\alpha_3 = 0.97$, $\zeta_e = 0.84$, $\zeta_m = 0.057$, $\vartheta_p = 0.38$, $\beta = 2.05$, $\omega_0 = 1.0$, $\vartheta_e = 0.05$. The initial conditions: $(z(0), \frac{dz(0)}{d\tau}, y(0), \rho(0)) = (0, 0, 0, 0)$ 125
- Figure 51** Stationary probability density function of mechanical system: (a) for different values of linear damping with $\zeta_3 = 0.064$, (b) for different values of nonlinear damping with $\zeta_1 = 0.25$. The other parameters used are given as : $\alpha_1 = 0.72$, $\alpha_3 = 0.97$, $\zeta_e = 0.84$, $\lambda = 2.0$, $\zeta_m = 0.057$, $\vartheta_p = 0.38$, $\beta = 2.05$, $\omega_0 = 1.0$, $\vartheta_e = 0.05$ and $D = 0.4$ 126
- Figure 52** Stationary probability density function of mechanical system: (a) for different values of noise intensity D with $\lambda = 2.0$, (b) for different values of impedance λ with $D = 0.4$. The other parameters used are given as : $\zeta_1 = 0.25$, $\zeta_3 = -0.064$, $\alpha_1 = 0.72$, $\alpha_3 = 0.97$, $\zeta_e = 0.84$, $\zeta_m = 0.057$, $\vartheta_p = 0.38$, $\beta = 2.05$, $\omega_0 = 1.0$, $\vartheta_e = 0.05$ 126
- Figure 53** Stationary probability density of the system in 3D representation for: (a) $D = 0.09$; (b) $D= 0.2$; (c) $D= 0.4$; (d) $D=0.6$. The other parameters used are given as : $\zeta_1 = 0.25$, $\zeta_3 = -0.064$, $\alpha_1 = 0.72$, $\alpha_3 = 0.97$, $\zeta_e = 0.84$, $\zeta_m = 0.057$, $\vartheta_p = 0.38$, $\beta = 2.05$, $\omega_0 = 1.0$, $\vartheta_e = 0.05$ and $\lambda = 2.0$ 127

Figure 54 Stationary probability density of the system in 3D representation for: (a) $\vartheta_e = 0.01$; (b) $\vartheta_e = 0.05$; (c) $\vartheta_e = 0.1$; (d) $\vartheta_e = 0.15$. The other parameters used are given as : $\zeta_1 = 0.25, \zeta_3 = -0.064, \alpha_1 = 0.72, \alpha_3 = 0.97, \zeta_e = 0.84, \zeta_m = 0.057, \beta = 2.05, \omega_0 = 1.0, \vartheta_p = 0.38, \lambda = 2.0$ and $D=0.4$ 127

Figure 55 Stationary probability density of the system in 3D representation for: (a) $\vartheta_p = 0.05$; (b) $\vartheta_p = 0.18$; (c) $\vartheta_p = 0.38$; (d) $\vartheta_p = 0.5$. The other parameters used are given as : $\zeta_1 = 0.25, \zeta_3 = -0.064, \alpha_1 = 0.72, \alpha_3 = 0.97, \zeta_e = 0.84, \zeta_m = 0.057, \beta = 2.05, \omega_0 = 1.0, \vartheta_e = 0.05, \lambda = 2.0$ and $D=0.4$ 128

Figure 56 (a) Evolution of mean square current of magnetic circuit versus ϑ_e for $\vartheta_p = 0.38$; (b) Evolution of mean square voltage of piezoelectric circuit versus ϑ_p for $\vartheta_e = 0.05$. The other parameters are given as: $\zeta_1 = 0.25, \zeta_3 = 0.064, \alpha_1 = 0.72, \alpha_3 = 0.115, \zeta_e = 0.84, \zeta_m = 0.057, \beta = 2.05, \omega_0 = 1.0$ and $\lambda = 2.0$ 131

Figure 57 (a) Evolution of mean square current of magnetic circuit versus noise intensity D for $\vartheta_p = 0.38$; (b) Evolution of mean square voltage of piezoelectric circuit versus noise intensity D for $\vartheta_e = 0.05$. The other parameters used are given as: $\zeta_1 = 0.25, \zeta_3 = 0.064, \alpha_1 = 0.72, \alpha_3 = 0.115, \zeta_e = 0.84, \zeta_m = 0.057, \beta = 2.05, \omega_0 = 1.0$ and $\lambda = 2.0$ 131

Figure 58 The mean square value $\langle \rho^2 \rangle$ of the electric current and mean square value $\langle y^2 \rangle$ of the voltage versus noise intensity D for various (a)-(b) nonlinear damping coefficient ζ_3 , (c) resistance and inductance ratio β , (d) impedance of the (PE) system λ 132

Figure 59 Output power harvested by the hybrid system as function of the driving noise intensity with the parameters $\zeta_1 = 0.25, \zeta_3 = 0.064, \alpha_1 = 0.72, \alpha_3 = 0.115, \zeta_e = 0.84, \zeta_m = 0.057, \beta = 2.05, \omega_0 = 1.0$ and $\lambda = 2.0$ 133

Figure 60 (a) Evolution of output power harvested by the hybrid system versus ϑ_e for $\vartheta_p = 0.38$; (b) Evolution of output power harvested by the hybrid system versus ϑ_p for $\vartheta_e = 0.05$. The other parameters are given as: $\zeta_1 = 0.25, \zeta_3 = 0.064, \alpha_1 = 0.72, \alpha_3 = 0.115, \zeta_e = 0.84, \zeta_m = 0.057, \beta = 2.05, \omega_0 = 1.0$ and $\lambda = 2.0$ 133

Figure 61 Increase rate op_{max} versus noise intensity, (a) overall view; (b) detailed view for $\zeta_1 = 0.25, \zeta_3 = 0.064, \alpha_1 = 0.72, \alpha_3 = 0.115, \zeta_e = 0.84, \zeta_m = 0.057, \vartheta_p = 0.38, \beta = 2.05, \vartheta_e = 0.05$ and $\lambda = 2.0$ and $\omega = 0.35$ 134

- Figure 62** Comparison of the output power with $E_0 = 0.05$; with the parameters $\zeta_1 = 0.25$, $\zeta_3 = 0.064$, $\alpha_1 = 0.72$, $\alpha_3 = 0.115$, $\zeta_e = 0.84$, $\zeta_m = 0.057$, $\vartheta_p = 0.38$, $\beta = 2.05$, $\vartheta_e = 0.05$ and $\lambda = 2.0$ and $\omega = 0.35$. 134
- Figure 63** Mean response amplitude versus noise intensity D ; with the parameters $\zeta_1 = 0.25$, $\zeta_3 = 0.064$, $\alpha_1 = 0.72$, $\alpha_3 = 0.115$, $\zeta_e = 0.84$, $\zeta_m = 0.057$, $\vartheta_p = 0.38$, $\beta = 2.05$, $\vartheta_e = 0.05$ and $\lambda = 2.0$ and $\omega = 0.35$. 135
- Figure 64** Mean response amplitude versus noise intensity D for various (a) linear damping ζ_1 , (b) nonlinear damping ζ_3 , (c) quadratic nonlinear coefficient α_2 and (d) electro-magnetic coupling coefficient ζ_e . 136

Abstract

Recent advances in both micro electronics and energy harvesting allows nowadays the conception of truly autonomous devices, energetically speaking. Such a possibility, combined with a growing industrial and biomedical interest in autonomous sensors and autonomous sensor networks, has led to important research and development efforts in the field of smart structures and self-powered smart systems. Nevertheless, microgenerators that harvest energy from their environment have a very limited amount of output power typically a few milliwatts, and new energy scavenging methods that enhance the harvesting process would benefit in embedding more functions in autonomous systems.

This thesis deals with a theoretical study of the conversion of the mechanical energy of ambient vibrations into electrical energy. First of all, a discussion was given on current advances in energy harvesting technologies as well as their economic and social interest. Indeed, two theoretical physical models were retained for the harvesting of ambient vibration energy.

Firstly, we consider a vibration energy harvesting system subjected to a harmonic excitation and exhibiting fractional properties induced by losses due to ohmic resistance, eddy currents and hysteresis phenomenon. The harmonic balance method is used to predict the analytical response of the system. The analytical results and those obtained numerically are in agreement and thus make it possible to justify the effectiveness of the analytical technique used. On the one hand, the impact of the fractional derivative order characterizing the memory effect brought by the inductance and the parametric coupling induced by time variation magnetic field on the performances of the system is analyzed. Subsequently, the effect of nonlinear damping on the output power of the system is presented. Also, the dynamics of the system are examined in detail through the plot, bifurcation diagrams, phase portraits, time series as well as spectral densities of power. These results are corroborated by the 0-1 test. Through these indicators, we identified the system parameters for which the system is chaotic, which characterizes a maximum energy harvesting. From the frequency response of the system, our results show that the resonance amplitude of the electrical vibration as well as the power generated by the system increases with the order of the fractional derivative. We also show that the generated power also increases with the parametric coupling amplitude. More-

over, by replacing the harmonic excitation by a random excitation, it is found that the output power increases with the intensity of the noise characterizing the environment in which the device will function.

In a second part, a hybrid model subjected to a Gaussian white noise was presented. Its dynamic behavior is studied using a probabilistic approach. The stochastic mean method is used to predict analytically the stationary response of the system, which allowed observing the stochastic bifurcation phenomenon. The concordance between the analytical results and those obtained numerically validates the effectiveness of the analytical method used. The average square of the intensity of the current and the voltage are obtained for different intensities of the white noise and other parameters of the system. As in the first model, we saw an increase in the average power output with the noise intensity, showing that the system performance can be improved by appropriate choice of noise intensity and other system parameters. Moreover, by combining a random signal with a harmonic excitation, the stochastic resonance phenomenon is observed. This phenomenon is reinforced with the increase of certain parameters of the system such as; the amplitude of the periodic excitation, the coefficient of quadratic nonlinearity and the coupling terms, this makes it possible to obtain large amplitudes of vibrations and consequently improves the energy harvested.

The results presented in this thesis can provide a theoretical idea for the design and optimization of the systems, and allow making an optimal choice of the environment in which the energy harvesters could function. Moreover, the results obtained show the need to use materials exhibiting fractional properties as well as the combination of several technologies in order to make the energy harvesting systems more efficient.

Keywords: Electromechanical System, Fractional Derivative, Parametric Coupling, Stochastic P-bifurcation, Probability, Stochastic Resonance.

Résumé

Les récents progrès en microélectronique ainsi qu'en récupération d'énergie ambiante permettent désormais d'envisager la conception de systèmes électroniques totalement autonomes. Cette possibilité, combinée à une demande forte en termes de capteurs autonomes de la part des secteurs industriel et biomédical, a conduit à une forte activité de recherche et développement de systèmes intelligents autoalimentés. Cependant la puissance délivrée par les microgénérateurs autonomes est encore limitée à quelques microwatts. Pour celà, de nouvelles méthodes de récupération d'énergie qui optimisent cette puissance permettraient l'ajout de nouvelles fonctions aux systèmes autonomes embarqués.

Cette thèse porte sur une étude théorique de la conversion de l'énergie mécanique des vibrations ambiantes en énergie électrique. Tout d'abord, une discussion est faite sur les avancées actuelles des technologies de récupération d'énergie ainsi que leur intérêt économique et social. En effet, deux modèles physiques théoriques sont retenus pour la récupération de l'énergie de vibration ambiante.

Dans une première partie, nous considérons un système de récupération d'énergie de vibration soumis à une excitation harmonique et exhibant des propriétés fractionnaires induites par les pertes dues à la résistance ohmique, aux courants de Foucault et au phénomène d'hystérésis. La méthode de la balance des harmoniques est utilisée dans le but de prédire la réponse analytique du système. Les résultats analytiques et ceux obtenus numériquement sont concordants permettant ainsi de justifier l'efficacité de la méthode analytique utilisée. D'une part, l'impact de l'ordre de la dérivée fractionnaire caractérisant l'effet mémoire qu'apporte l'inductance et de l'amplitude du couplage paramétrique induit par la variation du champ magnétique avec le temps sur les performances du système est analysé. Par la suite, l'effet de l'amortissement non-linéaire sur la puissance de sortie du système est présenté. D'autre part, la dynamique du système est examinée à travers le tracé, des diagrammes de bifurcations, des portraits de phases, des séries temporelles ainsi que des densités spectrales de puissance. Ces résultats sont corroborés par le test 0-1. A travers ces indicateurs, nous identifions les paramètres du système pour lesquels le système est chaotique, ce qui caractérise une récupération d'énergie maximale. De la réponse fréquentielle du système, nos résultats montrent que l'amplitude de résonance de la vibration électrique ainsi que la puissance générée par le

système augmente avec l'ordre de la dérivée fractionnaire. Nous montrons aussi que la puissance générée augmente également avec l'amplitude du couplage paramétrique. De plus, en remplaçant l'excitation harmonique par une excitation aléatoire, on constate que la puissance de sortie augmente avec l'intensité du bruit caractérisant l'environnement dans lequel fonctionnera le capteur.

Dans une deuxième partie, un modèle hybride soumis à un bruit blanc gaussien est présenté. Son comportement dynamique est étudié en utilisant une approche probabiliste. La méthode de la moyenne stochastique est utilisée pour prédire analytiquement la réponse stationnaire du système, ce qui a permis d'observer le phénomène de bifurcation stochastique. La concordance observée entre les résultats analytiques et ceux obtenus numériquement valide ainsi la méthode analytique utilisée. Les valeurs quadratiques moyennes de l'intensité du courant et de la tension électrique sont obtenues pour différentes intensités du bruit blanc et d'autres paramètres du système. Nous constatons, comme dans le premier modèle, une augmentation de la puissance de sortie moyenne avec l'intensité du bruit, montrant que les performances du système peuvent être améliorées par un choix approprié de l'environnement de fonctionnement et d'autres paramètres du système. Par ailleurs, en combinant un signal aléatoire avec une excitation harmonique, le phénomène de résonance stochastique est observé. Ce phénomène est renforcé avec l'augmentation de certains paramètres du système tels que, l'amplitude de l'excitation périodique, le coefficient de non linéarité quadratique et les termes de couplage, ce qui permet d'obtenir de larges amplitudes de vibrations et par conséquent, améliore l'énergie récoltée.

Les résultats présentés dans cette thèse peuvent fournir une idée théorique pour la conception et l'optimisation des systèmes, et permettre de faire un choix optimal de l'environnement dans lequel pourrait fonctionner le récupérateur d'énergie. Par ailleurs, Les résultats obtenus montrent la nécessité d'utiliser des composants exhibant des propriétés fractionnaires ainsi que la combinaison de plusieurs technologies dans le but de rendre plus performants les systèmes de récupérations d'énergie.

Mots clés: Système électromécanique, Dérivée fractionnaire, Couplage paramétrique, Bifurcation phénoménologique, Probabilité, Résonance stochastique.

General Introduction

The development in recent years of low-power electronics and the increasing need for autonomy energy of electronic microsystems have led to a renewal of research work on the harvesting of renewable micro-energy, including their presence in the human environment. Important scientific and technical challenges including the replacement of batteries with a low-power renewable energy harvesting system. These microsystems were initially powered by batteries. However, the batteries have a very limited life and are equipped with an energy reservoir. The main problem with the use of batteries as a source of energy is maintenance related to their periodic replacement and recharging. Several solutions have been envisaged to overcome this difficulty but which remain on the same concept as the conventional batteries, that is to say which are based on energy reservoirs. The first solution envisaged was the development of fuel cells, which are currently undergoing extensive research. The main difficulty of adopting its batteries is what are still expensive, difficult to miniaturize, and raises problems for the storage of hydrogen. A more radical solution is to use nuclear batteries. These batteries have remarkable characteristics that have thousands of times the energy density of Lithium-ion batteries. They are perfectly harmless. However, their major problem is the collection and reprocessing of spent batteries. Making these systems autonomous in terms of energy is at the heart of the researchers in charge of energy issues.

Our real environment is endowed with several sources of energy of which the best known are: mechanical vibrations energy, solar energy, wind energy, radiofrequency energy and thermal energy. The harvesting of these energies and their conversion into electricity seems to be an best solution to make the electronic systems autonomous.

There are many physical effects able to convert thermal, mechanical, solar and RF en-

ergy into micro – electric energy. Among all these effects that can be used in the energy harvesting technique, coupling effects in active materials (piezoelectric, thermoelectric and pyroelectric) are dominant in current research [1-4]. These are interdisciplinary techniques with a material science that have a higher development potential. Therefore, energy harvesting from mechanical vibrations is proposed as a solution to power these wireless sensors. Many devices are commonly used for vibration-based energy harvesting: electromechanical devices, piezoelectric devices and many others. Several authors have looked at the study of energy harvesting from mechanical vibrations through experimental and theoretical work.

While converting mechanical vibrations into electrical energy is not a new concept, the wide spread implementation of such systems has been the subject of much work. In order to move forward with this design methodology, accurate modeling techniques for energy harvesting systems are needed, this include; models of the energy harvester, the power converter, and the electronic load/energy storage unit. As pointed by Williams et al.[5], three transduction mechanisms are commonly used to converting vibrations mechanics to electricity, namely piezoelectric [6-9], electromagnetic [10] and electrostatic transduction [11, 12]. However many of the proposed harvesters are typically based on linear mechanical principles [5, 10]. Such devices give appreciable response amplitude only if the dominant ambient vibration frequency is closed to the resonance frequency of the harvester. However, in order to make the energy harvesters devices more optimal, nonlinearities are introduced through the electrical and mechanical elements such as diodes, resistors, capacitors, inductances, damping and springs.

Advances in material science and mathematics in conjunction with technological needs have triggered the use of material and electric components with fractional order physical properties. Fractional behavior of materials is a very interesting physical phenomenon and calculus theory based on it has been intensively studied since the 17th century. Fractional calculus has gained considerable importance during the recent times in the field of engineering modelling, design and control. In the field of electrical and electronics engineering there is a rapid import of concepts from fractional calculus to

explore their impact and determine the possible advantages of designing systems using their properties. Fractional calculus has been successfully applied to model viscoelasticity [13], economics problems [14], electric and magnetic phenomena [15, 16], electrochemical processes [17], bioengineering problems [13], social sciences and ecological interactions [16], distributed transmission lines [18], lossy capacitor [19], lossy coils [15], constant phase elements [20] and flexible structures [21]. The use of fractional calculus is encouraged in large part because of the reason that fewer parameters are sufficient in the fractional model to describe the dynamics of the physical system compared with the conventional models.

The conventional models used to describe the flux linking the coil and selfinductance fails in accurately describing the real behaviour of such circuits. The conventional model consisting of an inductor, an iron loss resistor and a copper resistor only provides a satisfactory description of coils with small eddy-current and hysteresis losses. Coils with significant losses are better described by the fractional model [15]. Currently, a great deal of research has been reported on fractional order inductance and its applications. Fouda et al., introduced the idea of fractional-order two-port networks with fractional order inductor and capacitors and its application to impedance and admittance parameters of fractional-order elements [22]. Machado and Galhano addressed the implementation of inductive elements of any fractional order based on the skin effect. It was demonstrated that by designing the variation of the conductor electrical conductivity we can get different fractional orders of the skin effect [23]. The concept of fractional order inductance is used in design of filters [24], the advantages of fractional order band pass filter over the integer order one are its sharper tuning characteristics and narrower bandwidth. Recently fractional order self and mutual inductance based linear variable differential transformer is designed and analysed in [25], this fractional order system provide higher sensitivity, reduced nonlinearity and increase in the stroke range as compared to the conventional system. This thesis investigates the impact of the fractional order derivative on the output voltage and power generated by the system through the analytical and numerical techniques.

The energy sources presented above are often insufficient to meet current needs and can be complementary, hence the importance of evaluating the interest of soliciting several for the same application. Indeed, in this millennium, the methodologies to harvest existing dissipated powers not only supply input energy to our sophisticated devices, but also contribute the current technological researches and developments. Single harvester generator or harvesting single power source may remain insufficient for the energy feed into the systems like electronic devices, biosensors, human, structural and machine health monitoring, and wireless sensor nodes. To overcome this problem, hybridization of energy harvesters (EHs) takes place to increase the limited energy generation of stand-alone EHs. From the model built in Ref. [26], we construct the hybrid model combining piezoelectric and electromagnetic mechanisms enhancing thereby the harvested energy. Another promising technique use in this work to improve the system performance is to combine the harmonic and random excitation which gives rise to the stochastic resonance phenomenon. This phenomenon (SR) gives the largest amplitude oscillation for a given excitation level, and reflects the transition in the system response from single potential well oscillations to double well vibration characteristics with hopping between the two potential wells.

In order to design energy harvesters capable of meeting current needs, The model must not only capture the general behavior of the energy harvester under ideal design conditions, but must also account for non-ideal effects, including changes in the vibration source and parasitic losses associated with the physical implementation of the system. The design procedure is explained, an electromechanical coupling model of the HEH is established. The energy harvesting characteristics are numerically simulated.

It is around of the problematic of design and optimization of the of the harvesters systems in this research field that this research work has been organized.

The first chapter describes the state of the art on the batteries and the energy harvesting devices by insisting on the works achieved in the vibrations energy harvesters. This chapter also replaces the energy harvesting from the electrostatic, electromagnetic and piezoelectric in their context by insisting on the motivations what have led at the

development of the energy harvesters allowing thereby to power wearable appliances.

The second chapter of the thesis is devoted to the mathematical modeling of the dynamics of two different models used in this thesis. The analytical and numerical techniques used are presented with detail in this chapter.

chapter three is devoted to the presentation of the main results of this thesis by showing on one hand the effect of a fractional inductance in the systems through the impact of the order of the fractional derivative. The stochastic bifurcation phenomenon and the stochastic resonance phenomena are discussed. A general conclusion from the thesis will establish the scientific breakthroughs gained during this work as well as the prospects for future work.

LITERATURE REVIEW ON ENERGY HARVESTERS AND PROBLEMS STATEMENTS

I.1 Introduction

This chapter highlights some of the most significant concepts developed in this thesis and presents the basic notions necessary for modeling the electromechanical energy harvesters. In recent years, the development of mobile wireless applications has grown remarkably. A challenge, emerged in the 90s, is to power these portable devices using resources in the human environment. In parallel, the development of communicating devices also has its own power supply problems, in particular related to battery change operations. The self-feeding of all these devices becomes possible. Thanks to the conjunction of the decline of the uses of electronic circuits, the possibility of producing efficient ambient energy harvesting and the progress made in the storage of electrical energy. Thus, after a brief review of the energy resources exploitable in the environment, we are interested in this first chapter to the different principles of conversion of mechanical energy, thermal and photovoltaic to exploitable electrical energy. To illustrate these different conversion principles, we rely on described systems in the literature. This chapter also aims to present the problematic of this thesis, and consequently, to position ourselves scientifically in relation to the work already carried out in this scientific community.

I.2 Motivations

The modern industrial world faces an increasing energy problem; fossil fuels are finite and environmentally costly, and alternative energy sources can not yet fully replace them. World consumption of energy is gradually increasing every year, and the main energy sources being consumed are non-renewable coal, gas and oil. The concept of energy harvesting generally relates to the process of using ambient energies, which are converted primarily into electrical energy, in order to power small and autonomous electronic devices. Energy harvesting has the potential to replace batteries for small, low power electronic devices. This energy can be then used either to improve the efficiency of existing technologies (e.g. the use of devices requiring no connection makes it possible on the one hand to eliminate expensive and cumbersome wiring, and on the other hand to be able to have the systems in any place).



Figure 1: Composition of toxic batteries (<http://phys.org>).

It can be noted that batteries present environmental problems, in particular with regard to the recycling of the materials they contain (Fig.1). Energy harvesting devices can also operate in harsher environments than batteries, which are for example very sensitive to temperature (Fig.2).

Fig.3 shows the improvement of the constituents performance of the wearable devices in the logarithmic scale between 1990-2003. It emerges from this figure that, the performance of batteries don't increases exponentially with the time, but seems to reach

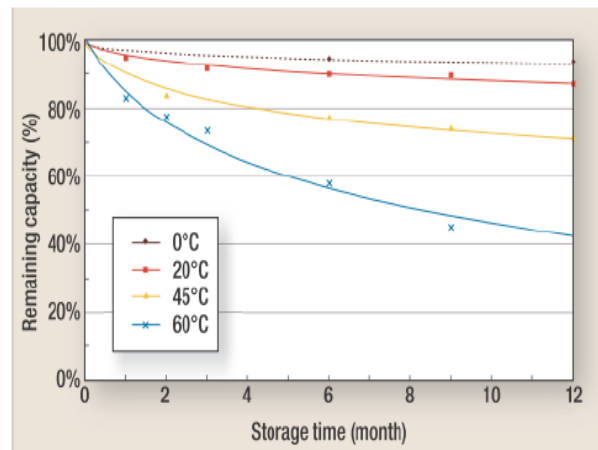


Figure 2: Self-discharge of Lithium-ion batteries according to the temperature of use [28].

a certain saturation. This trend renders necessary the research of the alternative energy source. It is in this context that we find the main motivation for this thesis.

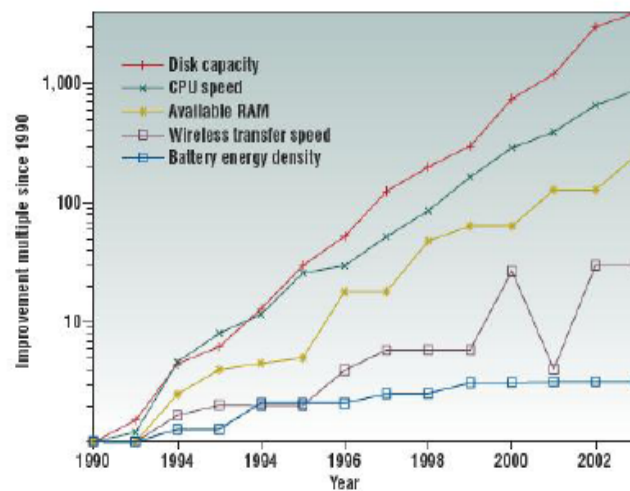


Figure 3: Improvement of the constituents performance of the wearable devices in the logarithmic scale between 1900 - 2003 [29]

I.3 Energy Sources and Energy Harvesting Technologies

Ambient energy harvesting, also known as energy scavenging, is the process where energy is obtained and converted from the environment and stored for use in electronic

applications. Usually this term is applied to energy harvesting for low power and small autonomous devices, such as wireless sensor networks, and portable electronic equipments. A variety of sources are available for energy scavenging, including solar power, ocean waves, piezoelectricity, thermoelectricity, and physical motions. For example, some systems convert random motions, including ocean waves, into useful electrical energy that can be used by oceanographic monitoring wireless sensor nodes for autonomous surveillance. This just shows that no single power source is sufficient for all applications, selection of power sources must be considered according to the application. Additionally, chemical and biological sources and radiation can be considered ambient energy sources. This subsection presents some sources of energy and presents various technologies used to convert energy.

I.3.1 Solar energy

This is certainly the most known of renewable energy sources [30]. Solar energy is uncontrollable, but it can be predicted through daily and seasonal patterns [31]. Solar power is transformed into electrical power using photovoltaic cells. The amount of out-



Figure 4: solar panels [32].

put power generated by a cell depends on the intensity of light as well as cell size and effectiveness, according to the photovoltaic principle [32]. To increase the output power, multiple cells are usually combined into modules, also known as solar panels (see Fig.4)

I.3.2 Wind Energy

Wind power has been known and exploited for thousands of years through windmills and navigation, for example. Today we can harness this energy with special propellers that store wind and machines that transform it into electrical energy (see Fig.5). Wind turbines are installed on land and at sea in places where the wind reaches a high and constant speed.



Figure 5: wind turbine [33].

I.3.3 Thermal energy

Theoretically, thermal energy would seem like the better solution when designing devices targeted to the industrial environment as wasted heat is present in abundance in all types of system. Conversion can be based on Seebeck effect and thermocouple, or exploiting the Pyroelectric effect (i.e. the property of certain materials to present a temporary voltage following a temperature change). The conversion efficiency of a thermal energy harvesting device is in any case related to Carnot's law

$$\eta = \frac{T_{max} - T_{min}}{T_{max}} \quad (1)$$

Where T_{max} and T_{min} are the extreme values of the temperature gradient to which the device is subjected, expressed in Kelvin. Application of Carnot Law usually yields higher values of efficiency compared to the actual ones, because of the characteristic efficiencies of the single devices that must be taken into account that are well below

the simple Carnots rule. Hence, at least for now, the attainable electrical power density turns out to be a small fraction of the one the material can offer with Carnot efficiency. Attempts to mechanically harvest energy through heat flow have also been reported, e.g., [34]. If the mechanical system experiences temperature variations, e.g., as in an airplane wing, the pyroelectric effect can be used to harvest energy. Sebald et al. [35] compare Seebeck harvesters and pyroelectric harvesters and explain the differences in efficiency between the two effects. In the case of a gradient, the use of the effect Seebeck on PN semiconductor junctions makes it possible to have thermoelectric devices making it possible to convert a temperature gradient into continuous electrical quantities (Figure 6).

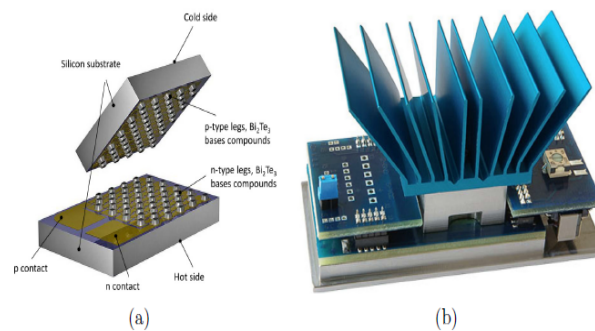


Figure 6: Example of thermoelectric generators: (a) principles and (b) realization [36].

I.3.4 RF-Based Sources

In the modern environment, there are multiple wireless sources of different frequencies radiating in all directions, such as TV, mobile phone, etc. So, it is easy to think that they would made a good source for energy harvesting purposes. For the conversion, an antenna or an array of antennae must be used: hence, frequency selection is an important consideration to be made in the design phase. The common choice would be Global System for Mobile communications (GSM), as mobile phone signals are prevalent and propagate well both in and out of buildings. Also, the distance from the RF source is a very important parameter, since the antenna dimension depend on it. The

extracted power range is wide as it is dependent on the aforementioned parameters. As an example, GSM 900, yields about $7\mu W/cm^3$.

I.3.5 Vibration energy

Indoor operating environments may have reliable and constant mechanical vibration sources for ambient energy scavenging. For example, indoor machinery sensors may have plentiful mechanical vibration energy that can be monitored and used reliably. Vibration energy harvesting devices can be either electromechanical or piezoelectric. Electromechanical harvesting devices, however, are more commonly researched and used. Energy withdrawal from vibrations could be based on the movement of a spring-mounted mass relative to its support frame. Mechanical acceleration is produced by vibrations that, in turn, causes the mass component to move and oscillate. This relative dislocation causes opposing frictional and damping forces to be applied against the mass, there by reducing and eventually extinguishing the oscillations. The damping force energy can be converted into electrical energy via an electric field (electrostatic), magnetic field (electromagnetic), or strain on a piezoelectric material. These energy conversion schemes can be extended and explained under the three listed subjects because, the nature of the conversion types differs even if the energy source is vibrating.

This part examines transduction methods used to convert mechanical vibrations into electrical energy in an energy harvesting system. Three types of transduction are examined in this paragraph; electrostatic, magnetic, and piezoelectric. The fundamental physics used to convert mechanical vibrations into electrical energy are reviewed for each method.

I.3.5.1 Electrostatic transduction

The electrostatic power generator consists of two conductors which move relative to one another. They are separated by a dielectric and create a capacitor. As the conductors move the energy stored in the capacitor changes, thus providing the mechanism for

mechanical to electrical energy conversion. A simple parallel plate capacitor, shown in Figure 7 can be used to illustrate the principle of electrostatic energy conversion. The capacitance of this structure is given by

$$C = \frac{\varepsilon_0 \varepsilon_r A}{e}, \quad (2)$$

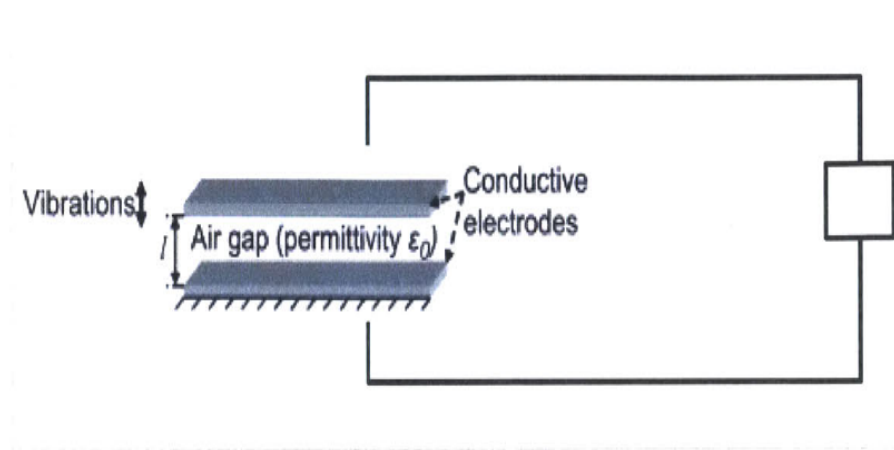


Figure 7: Electrostatic Energy Harvester [37].

where ε_0 is the permittivity of free space, ε_r is the relative dielectric permittivity, A is the area of the plate overlap, and e is the plate spacing. The voltage across the capacitor is given by

$$V = \frac{Q}{C}. \quad (3)$$

The electrical energy stored on the capacitor can be expressed as

$$E = \frac{Q^2}{2C}. \quad (4)$$

Electrostatic generators can be classified into three types: in-plane overlap (Figure 8(a)) varying the overlap area between two electrode plates, in-plane gap closing (Figure 8(b)) varying the gap between electrode plates and out-of-plane gap closing (Figure 8(c)) varying the gap between two large electrode plates.

These three types can be operated either in charge-constrained or voltage-constrained

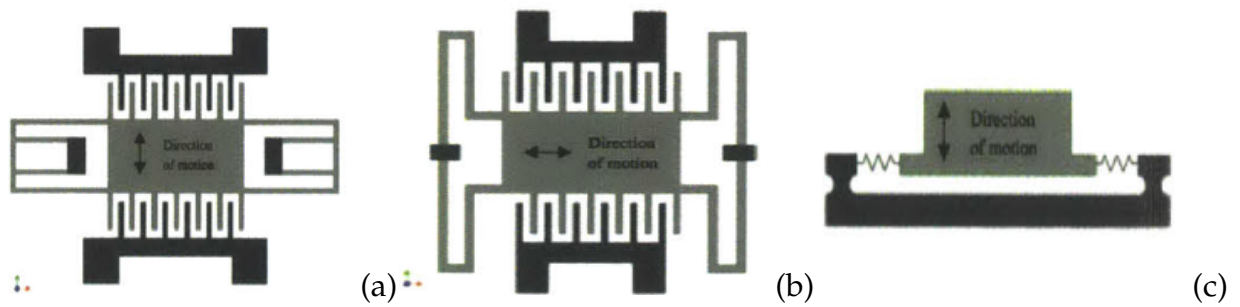


Figure 8: Three types of electrostatic generators [38]; (a) In-plane overlap, (b) In-plane gap closing, (c) Out-of-plane gap closing

cycles depending on the electric circuit used. In general, harvesters working in voltage constrained cycles provide more energy than those in charge constrained cycles. The primary disadvantage of electrostatic power generator is that they require a separate voltage source to initiate the conversion process because the capacitor must be charged up to an initial voltage for the conversion process to start.

I.3.5.1.1 State of the art of electrostatic system

The first category of the devices rely on an external bias to create a potential difference between the two parallel plates. In the second type of device, electrets are used to create a potential difference between the parallel plates. Electrets are essentially dielectric materials with permanent electrical polarization analogous to permanent magnet. It is well known in the literature that, micro-electromechanical system based electrostatic energy harvesters were firstly reported by Chandrakasan group at Massachusetts Institution of Technology (MIT) [12] and further developed by Roundy [39]. Meninger examined the energy conversion for both constant charge and constant voltage harvesters [12]. He determined that the constant voltage case was capable of producing more power, but required multiple external voltage sources. A hybrid design was proposed which increased the power capability of the constant charge case, and an in-plane overlap style transducer was designed. Simulation of this design produced output power of $8 \mu W$ at a vibration frequency of 2520 Hz.

Roundy performed a thorough examination of the three different variable capacitor

topologies and determined that the in-plane gap closing design was the most robust with output power comparable to the other topologies [40]. Through simulation, with an input acceleration of $2.25m/s^2$ at 120 Hz, Roundy calculated an optimal design could produce $110 \mu W$ output power and be confined to $1 cm^3$. The power estimate was made for a constant charge system, and does not take into account the power needed for the bias control circuitry. Peano [41] developed a nonlinear dynamic model for an in-plane overlap topology to be used for device optimization. For a $5 \mu m$ displacement at 911 Hz, it was shown that a device optimized for nonlinear operation could harvest $50 \mu W$, while a linearly optimized device could only harvest $5.8 \mu W$. Lo et. al [42] developed a parylene HT electret material with $3.69 mC/m^2$. Using an in-plane overlap topology, $5.6 \mu W$ of power has been demonstrated with a $2 mm_{pp}$ displacement at 50 Hz. The device is comprised of movable brass electrodes over a glass substrate. The total device size is approximately $25 mm^2$. A $16 \mu m$ thick Cyclic Transparent Optical Polymer (CYTOPTM) electret film was presented by Sakane [43] for use in a micromachined harvester. By doping the CYTOPTM, a charge of $1.5 mC/cm^2$ was achieved. When a $1.2 mm_{pp}$ displacement was applied at 20 Hz, an output power of $0.585 \mu W$ was delivered to an optimal resistive load of $4 M\Omega$. The total volume of this device was not clearly reported.

1.3.5.2 Piezoelectric transduction

The piezoelectric effect refers to a coupling between strain and polarization for certain materials due to their crystalline structure. When a material with piezoelectric properties is mechanically strained, either in compression or tension, an electric potential is induced in the material. This property, illustrated in Figure 9(a), is referred to as the direct piezoelectric effect. Piezoelectricity is a reciprocal property, meaning that an applied electric potential induces a mechanical strain in the material. This is referred to as the indirect piezoelectric effect and is shown in Figure 9(b). For harvesting vibration energy, the direct piezoelectric effect is utilized to convert energy from the mechanical domain to the electrical domain.

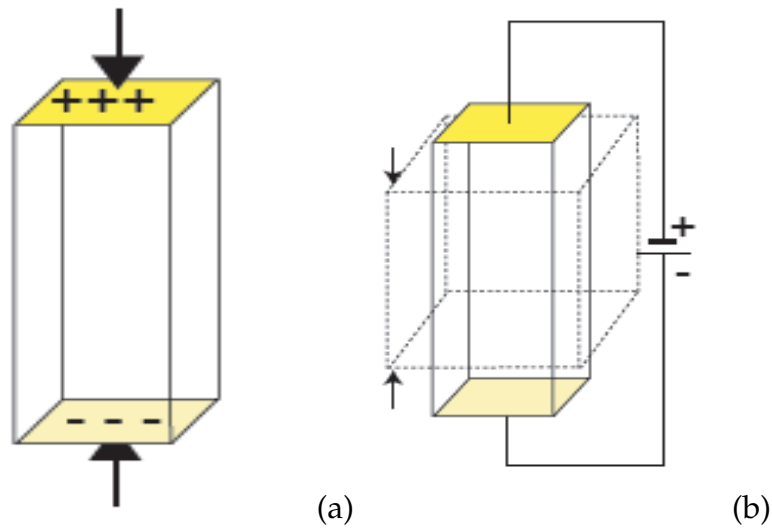


Figure 9: (a) The direct piezoelectric effect, (b) The indirect piezoelectric effect [46].

The presence of piezoelectric behavior in a material is determined by its crystal structure. Crystalline materials have atomic structures where the atoms are arranged in a periodic lattice. The smallest arrangement of atoms that can accurately represent the lattice is referred to as a unit cell [44]. In order for a material to exhibit piezoelectricity, the crystalline structure must be noncentrosymmetric, meaning that there is no center of symmetry within a unit cell. Of the 21 known noncentrosymmetric crystal configurations, 20 have been shown to possess piezoelectric properties. When a piezoelectric crystal is mechanically deformed, the lack of symmetry leads to the formation of electric dipoles which induce an electric field in the material [45]. Electrodes placed on the surface of the material experience a voltage differential as a result of the induced field. This effect was first demonstrated in quartz by Pierre and Jacques Curie in 1880. In addition to quartz, common piezoelectric materials include, lead zirconium titanate (PZT), aluminum nitride (AlN), zinc oxide (ZnO), and polyvinylidene fluoride (PVDF).

When using piezoelectric materials for vibration energy harvesting, there are two available modes of electromechanical coupling, namely the 31 and 33 modes. The numbers are used to represent the different modes, 1, 2 and 3, which refer to the orthogonal axes of a 3-dimensional coordinate system. By convention, the 3-direction refers to the direction of polarization. The 31 mode therefore describes a transducer where strain is

applied in the 1-direction, and the electric potential is generated in the 3-direction. Similarly, the 33 mode is characterized by strain in the 3-direction and an electric potential also in the 3-direction. Both modes, 31 and 33, are shown in Figure 10. The geometry of the piezoelectric material and placement of the electrodes will ultimately determine which electromechanical mode is harnessed for transduction.

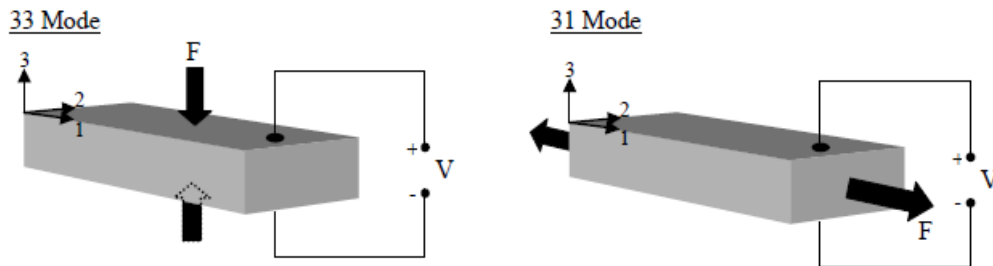


Figure 10: Illustration of 33 mode and 31 mode operation of piezoelectric material [47].

I.3.5.2.1 Linear Theory of Piezoelectricity

In linear piezoelectricity, the equations of linear elasticity are coupled to the charge equation of electrostatics by means of the piezoelectric constants. However, the electric variables are not purely static, but only quasi-static, because of the coupling to the dynamic mechanical equations. Thus, in order to provide an appropriate theoretical basis for the material covered in this standard, the relevant mechanical and electrical field variables will be briefly defined and the pertinent mechanical and electrical equations presented in this subsection.

The conservation of energy [48] for the linear piezoelectric continuum results in the first law of thermodynamics:

$$\dot{U} = T_{ij}\dot{S}_{ij} + E_i\dot{D}_i \quad (5)$$

where U is the stored energy density for the piezoelectric continuum. The electric enthalpy [49] density H is defined by

$$H = U - E_i D_i \quad (6)$$

and from Eqs.(5) and (6) there results

$$\dot{H} = T_{ij} \dot{S}_{ij} - D_i \dot{E}_i \quad (7)$$

Eq.(7) implies $H = H(S_{kl}, E_k)$ and from Eq.(7) and next consideration, there result

$$T_{ij} = \frac{\partial H}{\partial S_{ij}} \quad (8)$$

$$D_i = -\frac{\partial H}{\partial E_i} \quad (9)$$

where it should be noted that

$$\frac{\partial S_{ij}}{\partial S_{ji}} = 0, i \neq j \quad (10)$$

in taking the derivatives called for in Eq.(8). In linear piezoelectric theory the form taken by H is

$$H = \frac{1}{2} c_{ijkl}^E S_{ij} S_{kl} - e_{kij} E_k S_{ij} - \frac{1}{2} \varepsilon_{ij}^S E_i E_j \quad (11)$$

where c_{ijkl}^E , e_{kij} and ε_{ij}^S are the elastic, piezoelectric, and dielectric constants, respectively. In general there are 21 independent elastic constants, 18 independent piezoelectric constants, and 6 independent dielectric constants. From Eqs.(8), (9) and Eq.(11) with Eq.(10) there result the piezoelectric constitutive equations:

$$T_{ij} = c_{ijkl}^E S_{kl} - e_{kij} E_k \quad (12)$$

$$D_i = e_{ikl} S_{kl} + \varepsilon_{ij}^S E_k. \quad (13)$$

Table 1: Matrix Notation

ij or kl	p or q
11	1
22	2
33	3
23 or 32	4
31 or 13	5
12 or 21	6

where D is the electric displacement (charge per unit area, expressed in *Coulomb/m²*), E the electric field (V/m), T the stress (*N/m²*) and S the strain, c^E is the compliance when the electric field is constant (inverse of the Youngs modulus), e is the piezoelectric constant, and ε is the relative permittivity of the piezoelectric material. The subscripts i, j, k and l are tensor notations and take values of 1, 2 and 3.

A compressed matrix notation that replaces ij or kl in equation (12) and (13) by p or q is introduced to write the elastic and piezoelectric tensors in the form of a matrix. p and q take the values 1, 2, 3, 4, 5, and 6 according to Table 1. The identifications,

$$c_{ijkl}^E = c_{pq}^E, e_{ikl} = e_{ip}, T_{ij} = T_p \quad (14)$$

The matrix notation in Table 1 reduces equations (12) and (13) to

$$T_p = C_{pq}^E S_q - e_{kp} E_k \quad (15)$$

$$D_i = e_{iq} S_q + \varepsilon_{ik}^S E_k \quad (16)$$

where

$$S_{kl} = S_q \quad \text{when } k = l, q = 1, 2, 3 \quad (17)$$

$$2S_{kl} = S_q \quad \text{when } k \neq l, q = 4, 5, 6$$

The reduced equations (15) and (16) allow the constants to be expressed using the polarization of the piezoelectric material.

Figure 11 shows how to interpret the vectors in a piezoelectric material. The first

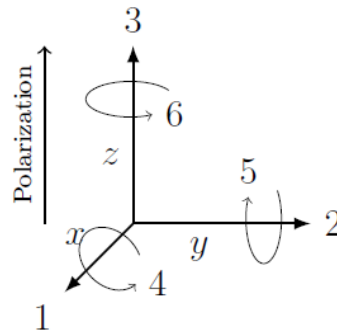


Figure 11: Definition of forces affecting a piezoelectric element relative to the polarization.

number in the subscript of the constants refers to the affected vector, and the second number refers to the applied vector; e.g., e_{33} refers to how the charge in the polarized vector 3 is affected by stress in the same vector (3). e_{31} refers to how the charge in the polarized vector 3 is affected by the stress applied to the orthogonal vector 1. It should be noted that when the compressed matrix notation is used, the transformation properties of the tensors become unclear. Hence, the tensor indices must be employed when coordinate transformations are to be made.

The mechanical model of the piezoelectric generator can be represented with the simple mass-spring system of Fig 12.

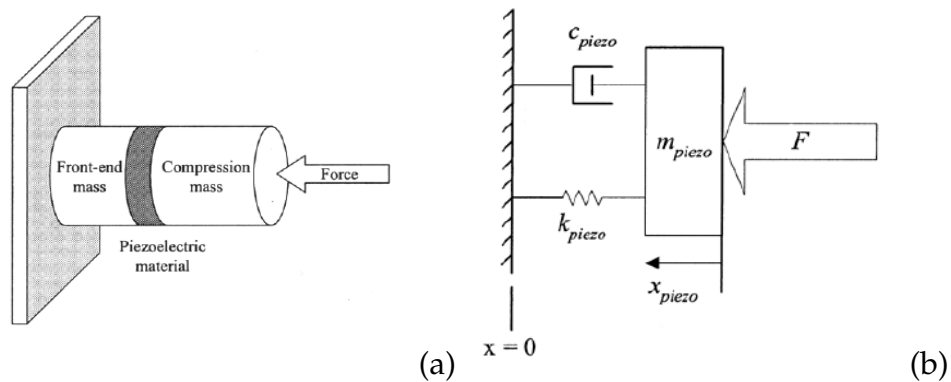
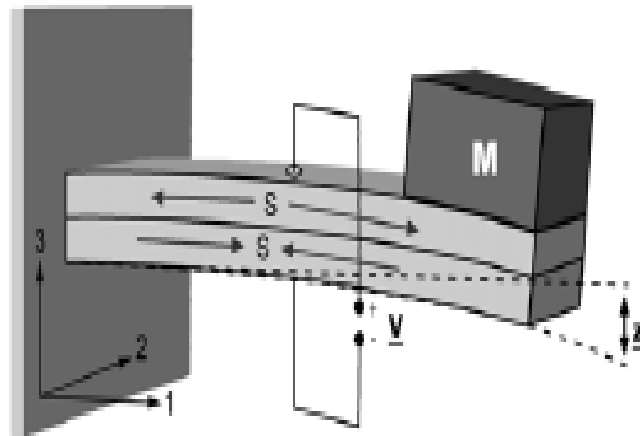


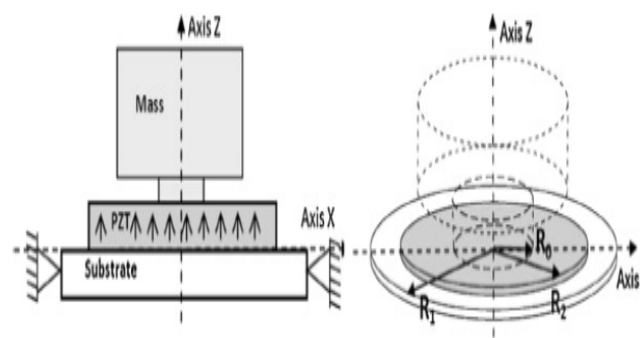
Figure 12: (a) Construction of the piezoelectric generator; (b) Mechanical model of the piezoelectric generator [51].

I.3.5.2.2 State of the art of piezoelectric system

Piezoelectric energy harvesting has been explored for a wide variety of applications. This section focuses on small (cm scale and down) piezoelectric energy harvesters and reviews work specifically designed for self powered systems. The majority of piezoelectric vibrational harvesters use a cantilever beam with piezoelectric materials on the top and bottom of the cantilever [52] with a proof mass at the tip of the cantilever [53-58] to tune it to a specific frequency.



(a)



(b)

Figure 13: (a) A two-layer bender mounted as a cantilever [59], (b) Piezoelectric diaphragm generator developed by Xu et al. [60]

In 2003, Roundy et al. [40](see figure 13(a)) designed a bimorph beam using a com-

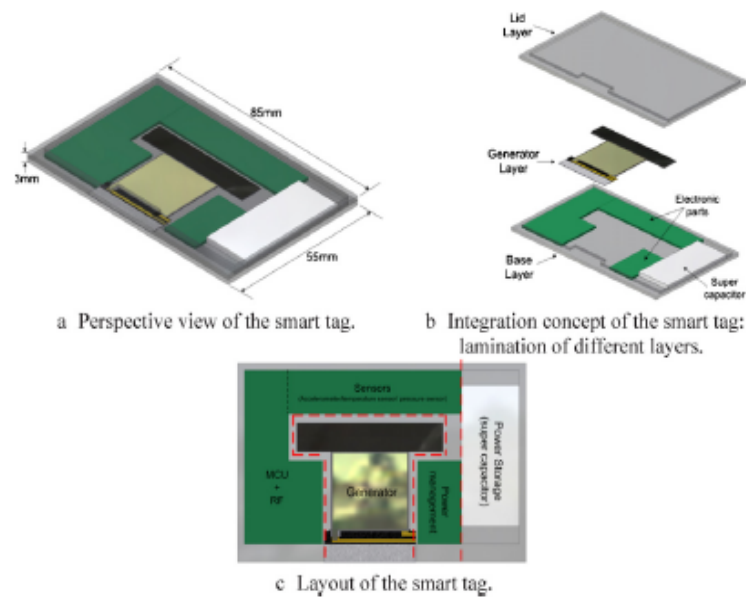


Figure 14: Overview of the smart tag. (a) Perspective view of the smart tag, (b) Integration concept of the smart tag: lamination of different layers, (c) Layout of the smart tag [61].

mercially available piezoelectric material, PSI-5A4E, from Piezo Systems Inc. The PZT cantilevered beam was 28 mm x 3 mm with a tungsten proof mass at the tip for adjusting the resonant frequency. The beam had top and bottom electrodes and operated in the 31 mode. From a base acceleration of 2.5 m/s^2 at 120 Hz, $365 \mu\text{W}$ was delivered to a resistive load. Xu et al. [60] have developed a piezoelectric generator of cylindrical shape of volume 0.23 cm^3 which recovers 12 mW at 113 Hz (Figure 13(b)), and for a vibration acceleration of 1 m/s^2 .

Zhu et al. [61] have proposed an example of the size of a credit card (see figure 14) designed to operate when subjected to vibrations of 67Hz and 3.9 m/s^2 , allows to recover a maximum power of $240 \mu\text{W}$.

Several examples have been reported that use piezoelectric harvesters mounted in shoe to harvest mechanical energy due to human walk or running [62-66]. A representative photograph of shoe-mounted piezoelectric energy harvesters is shown in Fig.15(a) [65]. Nathan et al. [66] designed a piezoelectric generator in shoe sole. Two methods have been used, explained in Figure 15(b), of piezoelectrically converting shoe power in

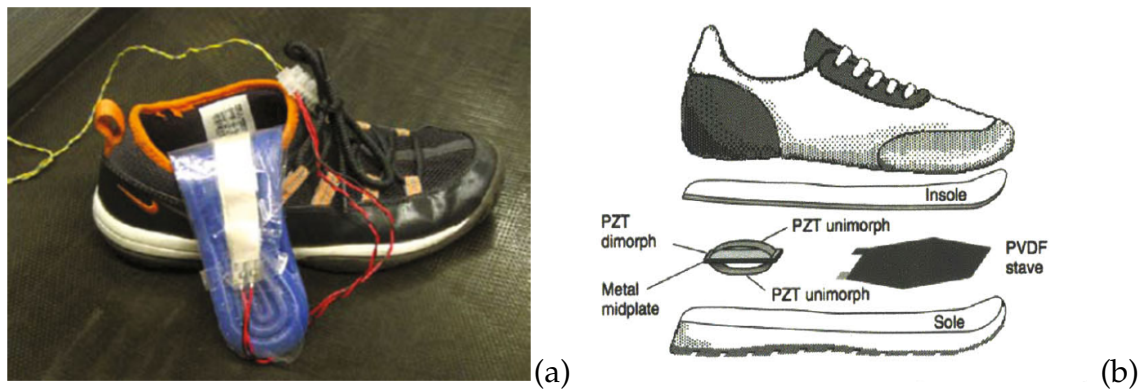


Figure 15: (a) Prototype of the piezoelectric film energy harvesting device inserted in a shoe [65], (b) Two approaches to harvest piezoelectric energy in shoes [66].

bending 3-1-mode operation. One way is to harvest the energy dissipated in bending the ball of the foot, using a polyvinylidene fluoride (PVDF) stave under the sole. The other way is to harvest foot strike energy by putting PZT dimorph under the heel. This device, called a dimorph, consists of two back-to-back, single-sided unimorphs. Although this application is very novel, its efficiency is relatively low. It can generate high voltage on the order of hundred V, but very low current on the order of 10^{-7} A. After trying different methods, they finally developed an off line, forwards witching converter, consisting of a small number of inexpensive, readily available components and materials.

I.3.5.3 Electromagnetic transduction

I.3.5.3.1 The basics or electromagnetic transduction

This technique uses a magnetic field to convert mechanical energy to electrical energy. The output power of electromagnetic vibration transducers is related to the particular design of the electromagnetic coupling. Hence factors like size, material properties and geometric configuration of magnet, coil and magnetic circuit play a vital key role in the design process. So far conclusions from literature are often based on very simplifying assumptions. Nevertheless the basic theory of magnetic induction is necessary in order to understand how the electrical energy can be extracted. In electromagnetic vibration transducers the transduction mechanism is based on Faradays law of induction. This

law states that any change of magnetic flux through a conductive loop of wire will cause a voltage to be induced in that loop.

Magnetic materials emanate magnetic fields, as shown for a typical bar magnet in Figure 16. By convention, these fields originate from the magnetic north pole and terminate at the magnetic south pole. The number of field lines passing normally through a surface within the field is defined as the magnetic flux, Φ_b , which has units of Webers.

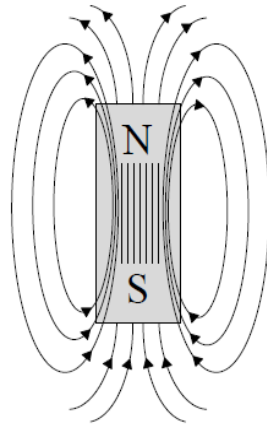


Figure 16: Bar magnet with magnetic field lines

The magnetic flux is defined as:

$$\Phi_{mag} = \int_A \vec{B} \cdot d\vec{A}, \quad (18)$$

where A indicates the area enclosed by the wire loop and B is the magnetic flux density. The induced voltage is the so-called electromotive force (V_m) which is given by:

$$V_m = -\frac{d\Phi_{mag}}{dt}. \quad (19)$$

The electrical and magnetic domains can be linked together through Faradays law of magnetic induction. When the N loops of a closed circuit are placed into a magnetic field, a voltage, (V_m), is induced equally to the time rate of change of the magnetic flux,

$$V_m = -N \frac{d\Phi_{mag}}{dt}. \quad (20)$$

Combining Eq.(18) and Eq.(20), the induced voltage can be expressed in terms of \vec{B} as

$$V_m = -N \frac{d}{dt} \int_A \vec{B} \cdot d\vec{A}. \quad (21)$$

Therefore, to induce a voltage in a closed circuit, either $\vec{B} \cdot d\vec{A}$, or both, must be functions of time.

Magnetic transducers convert vibration energy into electrical energy through magnetic induction described by Faradays law. Input vibration causes relative motion between a magnet and coil, which leads to a time-varying flux and induced voltage (V_m), defined by Equation 20. The voltage induced by the changing flux causes current to flow in the coil and delivers electrical energy to an external load.

If one substitutes the magnetic flux from Eq.18, then the induced voltage becomes:

$$V_m = -\left(\frac{d\vec{A}}{dt} \vec{B} + \frac{d\vec{B}}{dt} \vec{A}\right). \quad (22)$$

From this equation it is evident that for electromagnetic induction it does not matter whether the magnetic field is changing within a constant area or the area is changing within a constant magnetic field. This characteristic offers a wide range of possible implementations of the electromagnetic coupling. Two basic arrangements are shown in Fig.17. Both can be referred to the first term in the sum of equation (22). The coil in Fig.17a has a rectangular cross section with concentrated windings whereas the coil in Fig.17b has a circular cross section and the windings are spacious (more realistic case). These arrangements are often used for analytical evaluation due to the simplicity in calculation in contrast to arrangements where the (V_m) is produced through a diverging magnetic field according to the second term in the sum of equation (22). For coils with N windings the change of overlapping area follows $N \cdot \frac{dA}{dt} = Nl \frac{dz}{dt} = Nl\dot{z}$. Thus, (V_m) becomes:

$$V_m = -NBl\dot{z}. \quad (23)$$

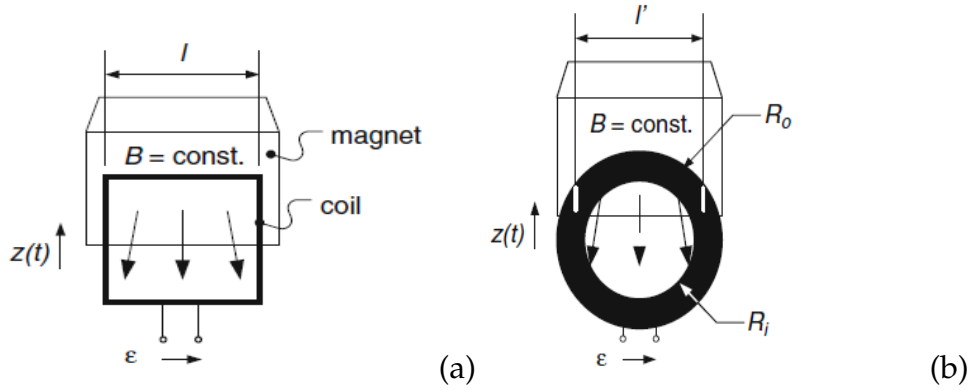


Figure 17: Popular models for linearized electromagnetic transducer analysis [67]. (a) rectangular cross section and concentrated windings, (b) circular cross section with spacious windings.

With the Lorentz force $F = q(\dot{z} \times B)$ (Force on point charge q in electromagnetic field) it is apparent that only wire segments orthogonal to the velocity are responsible for the (V_m) voltage. For coils with circular cross section the length l in Eq.(23) must be substituted by l' which can maximal be $(R_o + R_i)$. Note that this is only valid for small amplitudes in $z(t)$ or small changes of l' . Now Eq.(19) can be extended using the chain rule:

$$V_m = -\frac{d\Phi_{mag}}{dz} \cdot \frac{dz}{dt} = \kappa_t \dot{z}, \quad (24)$$

where κ_t is the transduction factor. The transduction factor equals the magnetic flux gradient and is assumed to be constant in the analytical treatment.

A common configuration used for magnetic transduction is shown in Figure 18. A permanent magnet, attached to the housing of the transducer with a mechanical spring, is suspended above an induction coil attached directly to the housing. Vibrations applied in the vertical-direction cause oscillations in the position of the magnet relative to the coil, which lead to a time-varying flux. A voltage is induced in the coils, and current flows to the electrical load. A similar configuration is possible where the magnet is stationary relative to the housing and the coils move in the presence of vibration.

The main benefit of magnetic transduction is the relatively high power densities that can be achieved. A wide variety of magnetic materials exist which exhibit very high

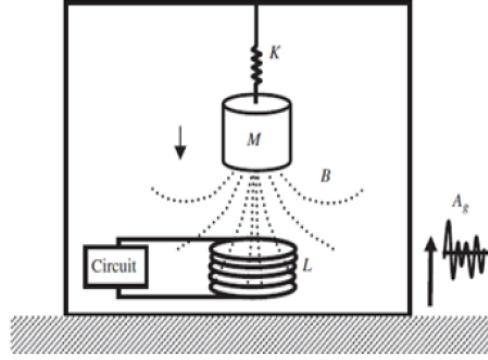


Figure 18: Electromagnetic Energy Harvester [68].

magnetic fields and provide good coupling between the mechanical and electrical energy domains. Unlike the capacitive method where an external bias is required to provide initial charge, magnetic transducers can operate without this constraint.

I.2.4.3.2 Transduction factor

Following Figure 19 shows the relative location and parameters of the magnet and induction coil. In this section, the magnetic field will be calculated based on magnetic dipole model. r_1 and r_2 are the inside and outside coil radius, respectively. h_c is the height of coil. The radial and axial positions of an arbitrary single wire of coil are r and z_1 , respectively. z_2 is the axial position of cylindrical magnet core. In this section we follow the strategy of Zhenlong et al. [69] to determine the expression of the coupling coefficient for a circular magnet., the electromotive force v_{mf} in Eq.(20) is rewritten as [70]

$$\begin{aligned}
 v_{mf} &= -\frac{d\Phi_{mag}}{dt} = -\frac{d\Phi_{mag}}{dz} \cdot \frac{dz}{dt} \\
 &= -\frac{AdB}{dz} \cdot \dot{z} = \kappa_t \cdot \dot{z}.
 \end{aligned}
 \tag{25}$$

where B is the magnetic flux density. A is the area enclosed by the wire loop, which is considered as a constant value. κ_t is called the electromagnetic coupling coefficient. The

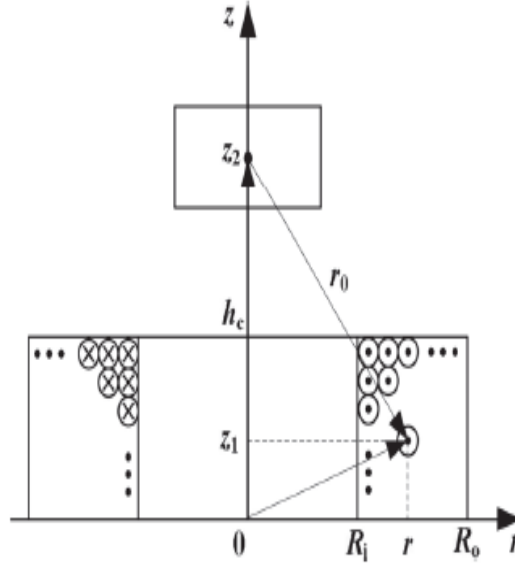


Figure 19: Relative location and parameters of the magnet and induction coil [69].

magnet is considered as a dipole with magnetic moment vector \vec{m}_2 [71], the magnetic field generated by the magnet can be expressed as

$$\vec{B} = -\frac{\mu_0}{4\pi} \left[\frac{\vec{m}_2}{r_0^3} - \frac{3r_0(\vec{m}_2 \cdot \vec{r}_0)}{r_0^5} \right] \quad (26)$$

where $\mu_0 = 4\pi \times 10^{-7} \text{ Hm}^{-1}$ is the permeability of vacuum. r_0 is the distance vector from center of the magnet to an arbitrary single wire. Assumed that the position coordinates of an arbitrary wire and magnet core are (r, z_1) and $(0, z_2)$ respectively. The corresponding expression of \vec{B} is

$$\vec{B} = \frac{B_r V_2}{4\pi} \cdot \frac{3(z_1 - z_2)r\vec{e}_r - [r^2 - 2(z_1 - z_2)^2]\vec{e}_z}{[r^2 + (z_1 - z_2)^2]^{5/2}} \quad (27)$$

where B_r and V_2 are the residual magnetic flux density and volume of the source magnet. \vec{e}_r and \vec{e}_z are the unit vectors along r - and z -axis, respectively.

As can be seen from Equation Eq.(25), the magnetic flux gradient along the z -axis direction is related to the induced voltage. For this reason, the magnetic flux density along the z -axis is the focus of research. The magnetic flux through the area enclosed by

the wire is

$$\Phi = \oint_S B dA = \frac{B_r V_2 r^2}{2[r^2 + (z_1 - z_2)^2]^{3/2}} \quad (28)$$

The average magnetic flux over the cross-section of the coil can be given as

$$\bar{\Phi} = \frac{1}{A_c} \int_0^{h_c} \int_{R_i}^{R_o} \Phi dr dz_1 \quad (29)$$

where $A_c = (R_o - R_i)h_c$ is the coil cross-sectional area. h_c , R_o , and R_i are the height, outer radius, and inner radius of the coil, respectively. Correspondingly, the total magnetic flux through the coil can be derived from $\Phi_{mag} = f_c N \bar{\Phi}$. $f_c = \frac{N A_w}{A_c}$ is the coil fill factor [50]. N is the number of turns in the coil. A_w is the cross-sectional area of single wire. Consequently, the electromotive force e_{mf} can be expressed as

$$v_{mf} = -\frac{d(f_c N \bar{\Phi})}{dz} = \kappa_t \dot{z} \quad (30)$$

where κ_t is

$$\kappa_t = -\frac{B_r V_2 f_c N}{2A_c} (\kappa_0^1 + \kappa_0^2) \quad (31)$$

where

$$\kappa_0^1 = \ln \frac{R_i + \sqrt{R_i^2 + (z_2 - h_c)^2}}{R_o + \sqrt{R_o^2 + (z_2 - h_c)^2}} + \ln \frac{R_o + \sqrt{R_o^2 + z_2^2}}{R_i + \sqrt{R_i^2 + z_2^2}}, \quad (32)$$

and

$$\kappa_0^2 = \frac{R_o}{\sqrt{R_o^2 + (z_2 - h_c)^2}} - \frac{R_o}{\sqrt{R_o^2 + z_2^2}} - \frac{R_i}{\sqrt{R_i^2 + (z_2 - h_c)^2}} + \frac{R_i}{\sqrt{R_i^2 + z_2^2}}. \quad (33)$$

It is assumed that the centers of the two magnets are always vertically aligned during the vibration of the hybrid energy harvester (HEH).

The electromagnetic energy harvester makes use of the relative motion between the

magnet and induction coil to change the vibration energy into electric power. In early works, the electromagnetic coupling and magnetic field distribution are not often concretized [72] or taken as linear electromagnetic coupling model [73].

The variation of dynamic magnetic field is highly nonlinear with respect to the gap between the magnet and coil. Consequently, the electromagnetic coupling is nonlinear [74, 75].

I.3.5.3.2 State of the art of electromagnetic transduction

Some of the first published work on magnetic transduction for vibration-based energy harvesting was performed by Williams et al. [5]. A device similar to that shown in Figure 20 was fabricated using a bulk S_mC_o magnet and a polyimide membrane for the spring. When the device was operated at its resonant frequency of 4.4 kHz with $0.5 \mu m$ vibration amplitude, a power of $0.3 \mu W$ was delivered to a 39Ω resistor. The volume of the device was approximated at $25 mm^3$.

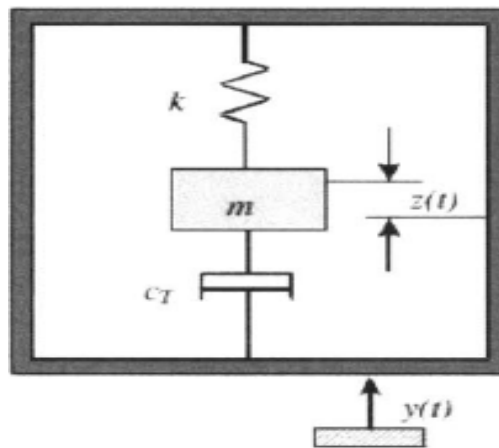
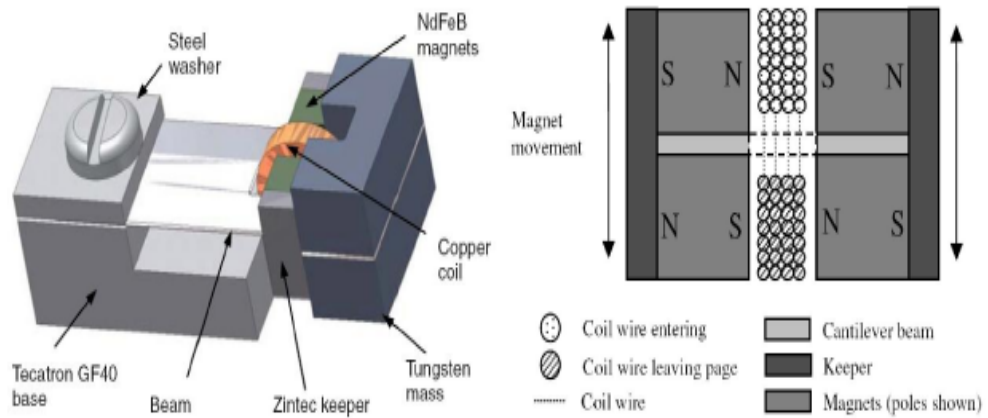
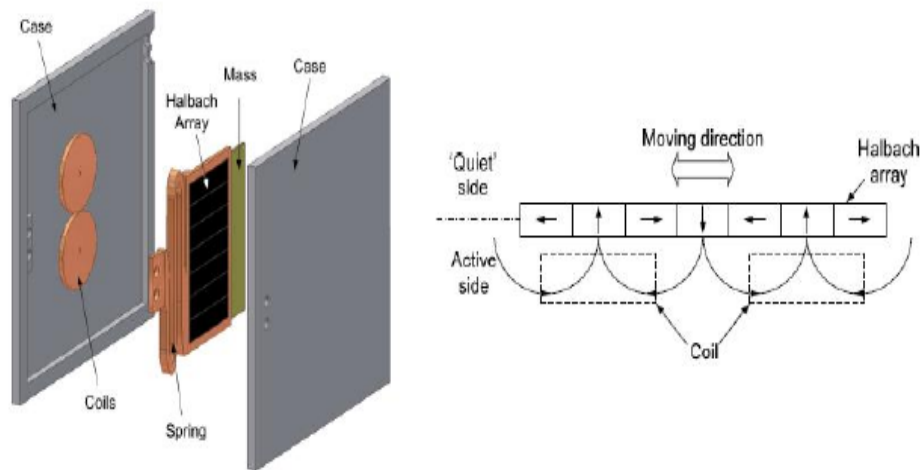


Figure 20: Schematic of a general energy harvesting device, which is a single-degree-of-freedom damped simple harmonic oscillator, as described by Williams and Yates [5].

With regard to macroscopic achievements, it was developed at the University of Southampton in 2001 several systems whose structure involves 2 or 4 permanent magnets fixed face to face at the free ends of a recessed mechanical beam, and a coil of copper taking place between the magnets within the magnetic field [76]. In 2004, Glynne-Jones



(a)



(b)

Figure 21: (a) Schematic design developed by Beeby et al. [78], (b) the electromagnetic generator developed by Zhu et al. [79]

et al. [77] recover with such a structure of 3.15 cm^3 mounted on the engine of a car, a maximum power of 3.9 mW and average of $157 \mu\text{W}$ on a journey of 1.24 km at an average speed of 25 km/h a miniaturized version of this system is developed in 2007 by Deeby et al. [78] of total volume 0.15 cm^3 generating $58 \mu\text{W}$ for ambient acceleration vibration $0.59 \text{ m}\cdot\text{s}^{-2}$ and frequency 52 Hz (Figure 21(a)). It is shown that this generator can power a wireless sensor system through the vibrations of an air conditioner or an industrial air compressor. Finally, Zhu et al. [79] developed in 2011 a new planar structure of 4 mm thick, based on an arrangement of magnets allowing a strong gradient of magnetic flux and reduced bulk (see Figure 21(b)). The generator harvested an average power of $120 \mu\text{W}$ at 44.9 Hz. The harvested of vibrations of large amplitudes including vibrations of the human body, was developed in 2006 by Sterken et al. [80]. It consists of a tube in which circulates one or more permanent magnets pushed or not at the ends of the tube, a coil is wound around the tube to recover the magnetic field variations. In 2008 Saha et al. [81] test a similar structure in a backpack during brisk walking or running: the generator with a volume of 12.4 cm^3 produces between 0.3 mW and 2.46 mW. In 2012, Rahimi et al. [82] developed a 4.5 cm^3 system including the electromagnetic generator, rectification circuit and storage capacity, delivering $11.6 \mu\text{W}$ at 12 Hz. Von Büren et al. [83] in 2007 showed a similar multipole structure (Figure 22) with a volume of 0.5 cm^3 recovering $35 \mu\text{W}$ on a suitable resistance when mounted under a knee during a walk.

As far as microscopic systems are concerned, a lot of work has been done. These systems are generally composed of a miniature magnet concentrating the dynamic mass of the system at the center of a planar spiral spring, or at the end of a silicon beam. One or more layers of planar coils are added on either side of this set. In 2007, Wang et al. [84] used a 0.32 cm^3 generator (figure 23)(a) and harvested $21.2 \mu\text{W}$ at 280 Hz and 8 ms^{-2} . The power harvested experimentally is 0.83 mW, for an external vibration amplitude $150 \mu\text{m}$. Water et al. [85] realized a 27 cm^3 generator consisting of a steel spring supporting a magnet with a coil harvested 1.2 mW(figure 23)(d). In 2008, Kulkarni et al. [86] produced 3 variants of electromagnetic silicone generators based on slightly differ-

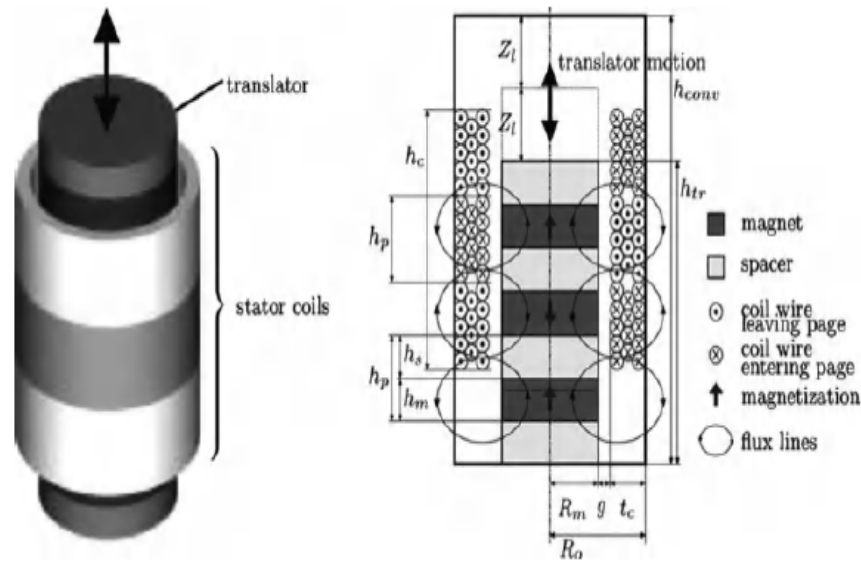


Figure 22: Electromagnetic generator developed by Von Büren et al. [83].

ent structures for a volume of 0.1 cm^3 . One of the variants consisting of an Neodymium Magnet (NdFeB) magnet on a beam moving between two planar coils (figure 23)(c) generates a maximum power of 586 nW at 60 Hz for an acceleration of 8.83 ms^{-2} . Owens et al. [87] discussed the effects of linear and nonlinear transduction and demonstrated that with a suitable design, nonlinear coupling is better than linear. Borowiec et al. [88] proposed a beam consisted of substrate and sandwiched with a tip mass which transduce the bending strains induced by the random horizontal displacement into electrical charge.

They analyzed the efficiency of this nonlinear device by focusing on the region of stochastic resonance where beam motion has a large amplitude. Nono et al. [89] used the Melnikov theory to discuss the performance of a bistable harvester by analyzing the critical condition for homoclinic bifurcation that could induce chaos in the system. Coccolo et al. [90] have studied the electrical response of a bistable system, by using a double-well Duffing oscillator, connected to a circuit through piezoceramic elements and driven by both a low and a high frequency forcing, where the high frequency forcing is the environmental vibration, while the low frequency is controlled by us. They showed that the response amplitude at the low-frequency increases, reaches a maxi-

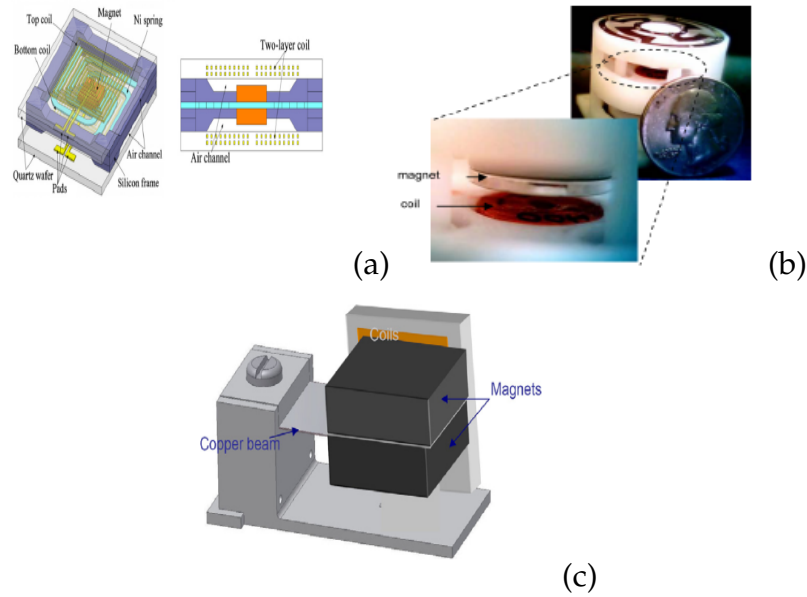


Figure 23: MEMS electromagnetic generators developed by (a) Wang et al. [84], (b) Water et al. [85], (c) Kulkarni et al. [86].

imum and then decreases to a certain range of the high frequency forcing. They also demonstrated in their work that by enhancing the oscillations, we can harvest more electric energy. Shahruz [91] shows that a bistable configuration of the potential energy of the system can be used to increase the output power. With a different perspective, Masana and Daqaq [92] proposed a comparative analysis of harvesters having bistable and mono-stable configuration of the potential energy, under harmonic excitation and demonstrated the effects of the potential shape on the performance of the system, for some ranges of frequencies. They concluded that mono-stable potential systems perform better than double-well systems for an excitation with a small amplitude. It is worth noting that, regardless of the type of transduction mechanism, any one exhibits advantage and disadvantage.

Table 2: Comparison of different types of technologies [93]

Types	Advantage	Disadvantages
Electrostatic	1) No need of smart material 2) Compatible with MEMS 3) High voltage generated	1) External voltage or charge source 2) Mechanical constraints needed 3) Capacitive
Piezoelectric	1) No external voltage source 2) Compatible with MEMS 3) High voltage generated 4) Compact configuration 5) High coupling in single crystal	1) Depolarization and aging problems 2) Brittleness in PZT 3) Poor coupling in piezo thin film 4) charge leakage 5) High output impedance
Electromagnetic	1) No need of smart material 2) No external voltage source	1) Difficult to integrate with MEMS 2) Bulky size 3) Small voltage generated

I.3.6 The advantages and disadvantages of different types of energy harvesting

Various studies have been able to summarize the advantages and disadvantages of the main modes Technologies implemented for energy recovery, by comparing for example, the ease of integration of electrostatic systems, the low voltages produced by electromagnetic generators or the high output impedance of piezoelectric generators. These general remarks are summarized in Table 2.

I.3.7 Power density of various technologies for energy harvesting

Comparing these different sources is tricky because dependent on many factors, and the application considered. Nevertheless, classical comparative studies have been able to compare the power densities of several classical sources. Results are listed in Table 3. It appears that the exploitation of energy from ambient vibrations makes it possible to potentially obtain the second highest energy density after solar energy. This source also has the advantage of being available in many fields of application, especially in industrial environments, or transport, where the use of autonomous sensor networks can be envisaged.

Table 3: Power density of various technologies for energy harvesting [93]

Technologie	Power density
Outdoor photovoltaic	15000 $\mu W/cm^2$
Indoor photovoltaic	100 $\mu W/cm^2$
Vibration (micro generator)	4 $\mu W/cm^3$ (human motion)
Vibrations (Small microwave oven)	116 $\mu W/cm^3$
Vibration (piezoelectric)	200 $\mu W/cm^3$
Piezoelectric (inserts in shoe)	330 $\mu W/cm^3$
Acoustic Noise	0.96 $\mu W/cm^3$
Thermoelectric	60 $\mu W/cm^2$

I.3.8 Summary of Power Scavenging Sources

Based on this survey, it was decided that solar energy and vibrations offered the most attractive energy scavenging solutions. Both solutions meet the power density requirement in environments that are of interest for wireless sensor networks. The question that must then be asked is: is it preferable to use a high energy density battery that would last the lifetime of the device, or to implement an energy scavenging solution? Figure 24 shows average power available from various battery chemistries (both rechargeable and non-rechargeable) versus lifetime of the device being powered.

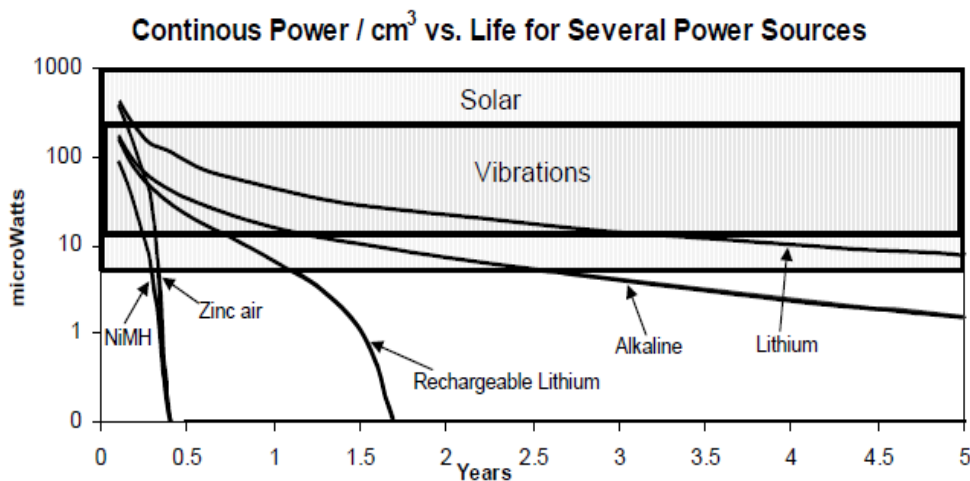


Figure 24: Power density versus lifetime for batteries, solar cells, and vibration generators [40].

The shaded boxes in the figure indicate the range of solar (lightly shaded) and vi-

bration (darkly shaded) power available. Solar and vibration power output are not a function of lifetime. The reason that both solar and vibrations are shown as a box in the graph is that different environmental conditions will result in different power levels. The bottom of the box for solar power indicates the amount of power per square centimeter available in normal office lighting. The top of this box roughly indicates the power available outdoors. Likewise, the area covered by the box for vibrations covers the range of vibration sources under consideration in this study. Some of the battery traces, lithium rechargeable and zinc-air for example, exhibit an inflection point. The reason is that both battery drain and leakage are considered. For longer lifetimes, leakage becomes more dominant for some battery chemistries. The location of the inflection roughly indicates when leakage is becoming the dominant factor in reducing the amount of energy stored in the battery. The graph indicates that if the desired lifetime of the device is in the range of 1 year or less, battery technology can provide enough energy for the wireless sensor nodes under consideration ($100 \mu W$ average power dissipation). However, if longer lifetimes are needed, as will usually be the case, then other options should be pursued. Also, it seems that for lifetimes of 5 years or more, a battery cannot provide the same level of power that solar cells or vibrations can provide even under poor circumstances. Therefore, battery technology will not meet the constraints of the project, and will not likely meet the constraints of very many wireless sensor node applications

I.3.9 Potential applications

Energy harvesters have many applications and most particularly in the micro-electromechanical system (MEMS) and in the many others domain. Indeed, use of energy harvesting helps to eliminate the need of battery replacement and maintenance and to prolong the lifetime of Wireless Sensors Nodes (WSN), this is rendered possible thanks to recent advance in wireless and micro electromechanical systems technology. There are many potential applications of MEMS vibration energy harvesters to power low-power

Wireless Sensors Node (WSNs) as indicated in Fig. 25.

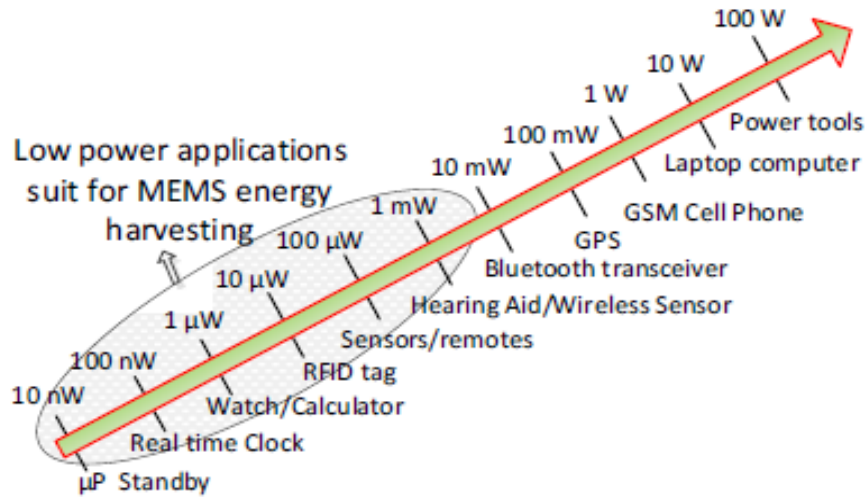


Figure 25: Power consumption of wireless sensor nodes [94].

The mechanical energy converted in the electricity through the PZT is used to stimulate the cardiac activity of the heart. Figure 26 shows an image of the ultra-flexible piezoelectric energy harvester incorporated on the heart. From the relaxation and expansion motion of the heart, the PZT nanogenerator can generate electrical energy and it can be stored inside a specifically designed battery in the pacemaker [95]

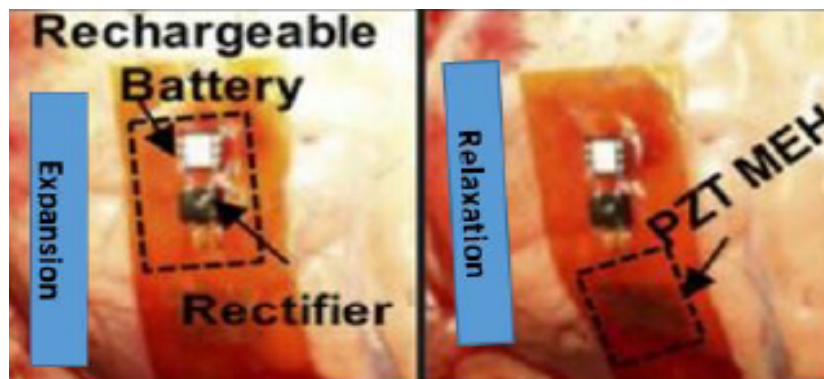


Figure 26: PEH for pacemaker. Expansion and relaxation of the pacemaker for the generation of voltage [95].

In addition to biomedical applications, energy harvesting from car-tire vibrations

to power tire pressure monitoring systems (TPMSs) is one of the most promising applications. As of September 2007, all cars sold in the United States must be equipped with a TPMS. In the Eurozone, from November 1st 2012 all cars must be installed with TPMS as well as all vehicles manufactured after November 1st 2014. Energy harvesting can still be used of Bridge stress monitoring [96], bridge health monitoring [97] or structural health monitoring [98] are other potential applications. Energy harvesters can be embedded into bridge or structural constructions to power these wireless monitoring sensors. Moreover, wearable sensors, and implantable sensors are other targets of MEMS vibration energy harvesters for applications [99, 100].

I.4 Fractional Property of Energy Harvesting Systems

The fractional calculus (FC) is a theory of integrals and derivatives of arbitrary real or even complex order. It is a generalization of the classical calculus and therefore preserves many of the basic properties. As an intensively developing area of the calculus during the last couple decades it offers tremendous new features for research and thus becomes more and more in use in various applications.

I.4.1 State of the art of fractional calculus

The beginning of the fractional calculus is considered to be the Leibniz's letter to L'Hospital in 1695, where the notation for differentiation of non-integer order $\frac{1}{2}$ is discussed. In addition, Leibniz writes: " Thus it follows that $d^{\frac{1}{2}}$ will be equal to $x\sqrt{dx} : x$. This is an apparent paradox from which, one day, useful consequences will be drawn" (see Miller et al. [101]).

Nowadays, not only fractions but also arbitrary real and even complex numbers are considered as order of differentiation. Nevertheless, the name fractional calculus is kept for the general theory.

A lot of contributions to the theory of fractional calculus up to the middle of the

20th century, of famous mathematicians are known: Laplace (1912), Fourier (1822), Abel (1823), Liouville (1832), Riemann (1847), Grunward (1867), Letnikov (1868), Heaviside (1892), Weyl (1917), Erdélyi (1939) and many others (see Gorenflo et al. [102]). However, this topic is a matter of particular interest just the last thirty years. The first specialized conference on fractional calculus and its applications in 1974 at the University of New Haven, USA, initiated the up-to-date books of Oldmam et al. [103], Miller et al. [101], Podlubny [104], etc.

I.4.2 Fractional theory

Following [15], the conventional derivative can be extended to non-integer derivative orders by using the following Fourier transform:

$$\mathfrak{S}\{f(t)\} = \underline{f}(\omega) = \int_{-\infty}^{+\infty} f(t)e^{-j\omega t} dt, \quad (34)$$

$$\mathfrak{S}^{-1}\{\underline{f}(\omega)\} = \frac{1}{2\pi} \int_{-\infty}^{+\infty} \underline{f}(\omega)e^{j\omega t} dt.$$

Letting

$$\mathfrak{S}\left\{\frac{d^n f(t)}{dt^n}\right\} = (j\omega)^n \mathfrak{S}\{f(t)\}, \quad (35)$$

the fractional derivative of order q with $q \in \mathfrak{R}$ is defined as

$$\frac{d^q f(t)}{dt^q} = \mathfrak{S}^{-1}\{(j\omega)^q \mathfrak{S}\{f(t)\}\}. \quad (36)$$

Equations (34) and (36) are suitable only to a limited extent for realistically calculating a fractional derivative. If the integral exists, the following is equally valid:

$$\frac{d^q f(t)}{dt^q} = \frac{1}{\Gamma(1-q)} \int_{-\infty}^t \frac{f'(\tau)}{(1-\tau)^q} d\tau, \quad q \in [0, 1[, \quad (37)$$

$$\frac{d^q f(t)}{dt^q} = \frac{1}{\Gamma(2-q)} \int_{-\infty}^t \frac{f''(\tau)}{(1-\tau)^q} d\tau, \quad q \in [1, 2[.$$

This definition includes the classical integer derivatives and satisfies the semigroup condition

$$\frac{d^q}{dt^q} \left(\frac{d^p f(t)}{dt^p} \right) = \frac{d^p}{dt^p} \left(\frac{d^q f(t)}{dt^q} \right) = \frac{d^{p+q} f(t)}{dt^{p+q}}, \quad (38)$$

as well as the translation invariance which plays a major role in science applications

$$\frac{d^q f(t)}{dt^q} = g(t) \Leftrightarrow \frac{d^q f(t - \tau)}{dt^q} = g(t - \tau). \quad (39)$$

Further, equation (37) proves the linear behaviour of the fractional derivative [103, 104]. In contrast to an integer derivative, a fractional derivative is a global operator. This means that not only the actual values of the function to be derived but also its entire past history have to be included in the actual value of the derivative. This can be well demonstrated by means of a step. Comparable to an integer derivative, the fractional derivative of a constant function $f(t) = c$ gives

$$\frac{d^{1/2} f(t)}{dt^{1/2}} = \frac{1}{\Gamma(1 - \frac{1}{2})} \int_{-\infty}^t \frac{0}{(t - \tau)^{1/2}} d\tau = 0. \quad (40)$$

A step $f(t) = c \cdot \sigma(t)$ yields,

$$\frac{d^{1/2} f(t)}{dt^{1/2}} = \frac{c}{\Gamma(\frac{1}{2})} \int_{-\infty}^t \frac{\delta(\tau)}{(t - \tau)^{1/2}} d\tau = \begin{cases} 0, & t < 0 \\ \frac{c}{\Gamma(\frac{1}{2})\sqrt{t}}, & t > 0. \end{cases} \quad (41)$$

Figure 27 shows that the step applied at the time instant $t = 0$ determines the history of the fractional derivative also for $t > 0$. This clearly distinguishes the fractional from the integer derivatives.

Further examples of fractional derivatives are

$$\frac{d^q e^{bt}}{dt^q} = b^q e^{bt}, \quad (42)$$

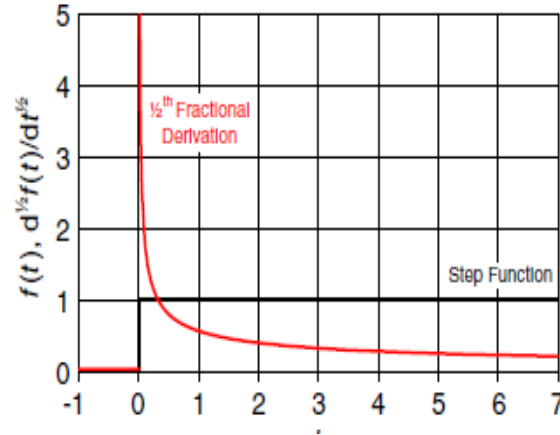


Figure 27: The fractional derivative is a global operator [15].

$$\frac{d^q \sin(bt)}{dt^q} = b^q \sin\left(bt + \frac{\pi}{2}q\right), b > 0. \quad (43)$$

The handling of fractional derivatives in the time domain may involve some effort. In the frequency domain, however, they can be easily applied. According to the definition given by equation (36), the following applies:

$$\mathfrak{S} \left\{ \frac{d^q f(t)}{dt^q} \right\} = (j\omega)^q \mathfrak{S} \{f(t)\} = (j\omega)^q \underline{f}(\omega). \quad (44)$$

Three main definitions have been established for mathematical analysis of fractional order systems [106]

i) Grünwald-Letnikov definition

$${}_a D_t^\alpha f(t) = \lim_{h \rightarrow 0} h^{-\alpha} \sum_{i=0}^{\left(\frac{t-a}{h}\right)} (-1)^i \binom{\alpha}{i} f(t - ih). \quad (45)$$

ii) Riemann-Liouville definition suppose that $\alpha > 0, t > a, \alpha, a \in \mathfrak{R}$. Then

$${}_a D_t^\alpha f(t) = \frac{1}{\Gamma(n - \alpha)} \int_a^t (\tau - t)^{n-\alpha-1} \left(-\frac{d}{d\tau}\right)^n f(\tau) d\tau \quad (46)$$

iii) Caputo definition suppose that $\alpha > 0, t > a, \alpha, a \in \mathfrak{R}$. Then

$$D_t^\alpha f(t) = \frac{1}{\Gamma(n - \alpha)} \int_a^t \frac{f^n(\tau)}{(t - \tau)^{\alpha+1-n}} d\tau, n - 1 < \alpha < n \in N. \quad (47)$$

where $\Gamma(\cdot)$ is the gamma function. The Caputo definition is suitable for the analysis of physical systems because it provides initial conditions, which physically can be explained [106]. Moreover, from an analytical point of view, it is quite simple to integrate.

I.4.3 Elements with fractional order physical properties

Recent research contributions have shown evidence of mechanical elements and electrical components whose dynamics is well described by fractional order differential equations or fractional order power law. In fact, considerable amount of research in fractional calculus has been published in engineering and applied science literature.

I.4.3.1 Fractional resistor

Following [105], physical quantities are the electric field ε , the magnetic field B , the electric flux density D , the magnetic field intensity H and electric current density J . Consider a lossy material in the form of a cylinder of length l and cross section S of area A . Assume a constant electric field in the direction of the axis of the cylinder z . The voltage $v(t)$ between the ends of the cylinder is

$$v(t) = \int_0^l \varepsilon \cdot z ds = l\varepsilon \cdot z, \quad (48)$$

whereas the total current $i(t)$ is

$$i(t) = \int_S J \cdot z ds \quad (49)$$

with

$$J(x, t) = \sigma_\alpha D_t^{1-\alpha} \varepsilon(x, t), 0 < \alpha \leq 1. \quad (50)$$

Assume (50) is valid. We have

$$i(t) = A\sigma_\alpha D_t^{1-\alpha} \varepsilon.z. \quad (51)$$

Hence

$$i(t) = \frac{A\sigma_\alpha}{l} D_t^{1-\alpha} v(t), \quad (52)$$

let $R_\alpha = \frac{l}{A\sigma_\alpha}$. It follows that the fractional resistor satisfies the Curie's law

$$i(t) = \frac{1}{R_\alpha} D_t^{1-\alpha} v(t). \quad (53)$$

Notice that if $\alpha = 1$, we have the classical law $v = Ri$.

I.4.3.2 Fractional capacitor

Following [105], consider two parallel plates confining a lossy material. Both plates have charge of equal magnitude but opposite sign. If distance between the plates is small compared with their size, there is no charge in the region between the plates. Charge will reside mostly in the inner surfaces of the plates. The electric field is normal to the plates away from the edges, say in the x direction, and zero in the interior of the plates. Consequently, in the region between the plates the first Maxwell's equation

$$\nabla \cdot D = \rho, \quad (54)$$

becomes

$$\nabla \cdot D = 0. \quad (55)$$

We propose the constitutive law

$$D = \epsilon_\beta D_t^{1-\beta} \varepsilon, 0 < \beta \leq 1. \quad (56)$$

Since $\varepsilon = -\nabla\phi$, the potential $\phi(x, y, z) \equiv \phi(x)$ solves the equation

$$D_x D_t^{1-\beta} D_x \phi = 0. \quad (57)$$

We have

$$D_x \left(\frac{1}{\Gamma(\beta)} t^{\beta-1} D_x \phi \right) = 0, \quad (58)$$

and for $t > 0$, $D^2\phi = 0$.

Let the plates be at $x = a$ and $x = b$. As customary, suppose that the potentials are constant on each plate and are $\phi(a) = v_a$ and $\phi(b) = v_b$. Then

$$\phi(x) = \frac{(v_b - v_a) + bv_a - av_b}{b - a}, \quad (59)$$

and the electric field

$$\varepsilon = \frac{v_{ab}}{b - a}, \quad (60)$$

where, $v_{ab} = v_b - v_a$.

Now choose δ such that $\delta \ll |b - a|$ and construct the cylindrical surface S_C , with axis in the x -direction. The plane top and bottom, of area A , are at $x = a + \frac{\delta}{2}$ and $x = a - \frac{\delta}{2}$. From the integral form of equation (54) in the region confined by S_C we obtain

$$qA = \int_{S_C} D \cdot n ds, \quad (61)$$

where q is the constant surface density of charge, positive on $x = a$. Let $v(t) = v_{ab}H(t)$ and $Q(t)$ the total charge on the plate at $x = a$, namely $Q(t) = qAH(t)$. From (56) and (60) we have

$$Q = \frac{\epsilon_\beta A}{b - a} D_t^{1-\beta} v. \quad (62)$$

We are led to a generalized governing equation of a capacitor

$$Q(t) = C_\beta D_t^{1-\beta} v(t), \quad (63)$$

$$\text{with } C_\beta = \frac{\epsilon_\beta A}{b-a}.$$

I.4.3.3 Fractional inductor

Following [105], For later reference let us recall Ampere's law and Faraday's law of induction. Namely

$$i(t) = \oint_C H \cdot tdl, \quad (64)$$

$$\oint_C \varepsilon \cdot tdl = -\frac{d}{dt} \int_S B \cdot nds. \quad (65)$$

The corresponding generalized constitutive relation between the magnetic field intensity H and the magnetic field B is

$$\mu_\gamma H = D_t^{1-\gamma} B, 0 < \gamma \leq 1. \quad (66)$$

For the inductor it is considered a toroidal frame of rectangular cross section. The inner and outer radii of the frame are r_1 and r_2 respectively, and the height is h . A coil consisting of n turns of wire is tightly wound on the frame. There is a current of magnitude $i(t)$, $t \geq 0$ in the conducting wire.

Set cylindrical coordinates such that the z -axis is the axis of symmetry and the frame is located between $r = r_1$ and $r = r_2$. Let C_r be a circular path within the toroidal frame of radius r with $r_1 < r < r_2$. As customary, we assume axis symmetry so that the magnetic field $B \equiv B(r, z, t)$ only depends on r , z , and t . By Ampere's law applied to the surface of the disk bounded by C_r , we have

$$ni(t) = D_t^{1-\gamma} \int_{C_r} B \cdot tdl, \quad (67)$$

where t is the unit tangent to C_r .

Substituting B from (67) we obtain

$$\mu_\gamma n i(t) = D_t^{1-\gamma} \int_{C_r} B \cdot t dl. \quad (68)$$

After application of the Riemann-Liouville integral of order $1 - \gamma$ we are led to

$$\mu_\gamma n J_t^{1-\gamma} i(t) = \int_{C_r} B \cdot t dl. \quad (69)$$

If B is the magnitude of the magnetic field in the direction of t , then

$$\int_{C_r} B \cdot t dl = \int_0^{2\pi} B(r, z, t) dl = 2\pi r B(r, z, t). \quad (70)$$

So

$$B(r, z, t) = \frac{\mu_\gamma n}{2\pi r} J_t^{1-\gamma} i(t). \quad (71)$$

Let us apply Faraday's law to one such surface S . Then the normal to this surface is $n = t$. So if $v_S(t)$ is the induced voltage

$$\begin{aligned} v_S(t) &= -\frac{d}{dt} \int_S B \cdot n ds \\ &= -\frac{d}{dt} \int_0^h \int_{r_1}^{r_2} B(r, z, t) dr dz \\ &= -\frac{\mu_\gamma n}{2\pi} \int_0^h \int_{r_1}^{r_2} \frac{1}{r} dr dz \frac{d}{dt} J_t^{1-\gamma} i(t) \\ &= -\frac{\mu_\gamma n h}{2\pi} \log\left(\frac{r_2}{r_1}\right) D_t^\gamma i(t). \end{aligned} \quad (72)$$

Let v be the total voltage dropped. Since there are n such coils, we have

$$v(t) = L_\gamma D_t^\gamma i(t), \quad (73)$$

Table 4: Fractional and classical governing equations of circuit components

Component	Fractional Equation	Classical Equation
Resistor	$i(t) = \frac{1}{R_\alpha} D_t^{1-\alpha} v(t)$	$i(t) = \frac{1}{R} v(t)$
Capacitor	$Q(t) = C_\beta D_t^{1-\beta} v(t)$	$Q(t) = C v(t)$
Inductor	$v(t) = L_\gamma D_t^{1-\gamma} i(t)$	$v(t) = L D_t[i(t)]$

with $L_\gamma = \frac{\mu_\gamma n}{2\pi} \log\left(\frac{r_2}{r_1}\right)$.

Equation (73) is a generalization of the governing equation of an inductor. Table 4 summarizes the equations obtained in the previous section. In the second column the fractional generalizations are shown, while the third column presents the limit behavior of the fractional models. As expected the classical governing equations, representing ideal components of a circuit, are obtained.

Some models of fractional coils have been modeled using massive ferromagnetic nuclei. Its structures are presented in Fig.28

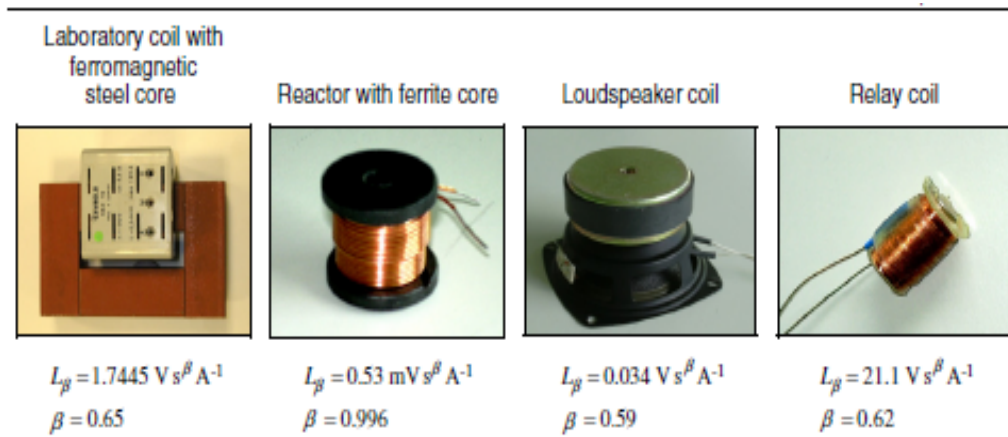


Figure 28: Modelling of coils using fractional derivatives (derivation of order β , lossy inductance L_β) [105].

I.4.3.4 Literature review of the fractional models

Recent studies brought FC into attention revealing that many physical phenomena in nature exhibit fractional behavior and can be modeled by fractional differential Equations. The importance of fractional order models is that they yield a more accurate description and give a deeper insight into the physical processes underlying a long range

memory behavior.

Many recent studies revealed that FO nonlinear dynamical systems, in various applications, display rich and complex behaviors. Bagley et al. [109, 110, 111] pointed out that half-order fractional derivative models can quite well describe the frequency dependence damping of viscoelastic materials. Kelly et al. [112] have applied the fractional Kelvin model to predict the seismic response of natural rubber bearings. Markris et al. [113] presented a fractional derivative Maxwell model for a viscous damper and validated their model using experimental results. Cao et al. [114] recently considered an energy harvesting system with fractional order viscoelastic material. They showed that the fractional order property of the material enhances high-energy chaotic motion as well as inter-well periodic oscillation. Kwuimi et al. [115] proposed an electromechanical energy harvesting system with a fractional order current voltage relationship for the electrical circuit and fractional power law in the restoring force of its mechanical part. The authors showed that under a single-well potential configuration, for a small amplitude of the perturbation, as the order of derivative increases, the resonant amplitude of mechanical vibration decreases while the bending degree remains fairly constant. For a large amplitude of the perturbation, the output power increased, this is due to the hardening effects. However, under a double-well configuration, the fractional power stiffness strongly affects the crossing well dynamics and consequently the output electrical power. Ducharne et al. [116] built and energy harvesting devices based on piezoelectric Ericsson cycles in a piezoceramic material. They showed that by coupling an electric field and mechanical excitation on Ericsson-based cycles, the amplitude of the harvested energy can be highly increased, and can reach a maximum close to 100 times its initial value. Ngueuteu et al. [117] considered an electromechanical system having a fractional order capacitor and modeled by a fractional-order Duffing-quintic equation. They studied its dynamics and synchronization, and concluded that the fractional order component can strongly affect the performance of the system, especially the route to chaos and the onset of synchronization. Atanackovic et al. [118] considered the forced oscillations of a rod having fractional order viscoelastic physical properties, Deng et al.

[119] and Hosseini et al. [120] considered the stochastic analysis of column of viscoelastic material. They concluded that for both white noise and colored noise, the fractional order μ of viscoelastic materials plays an important role in the system stability.

I.5 Hybrid systems

The synthesis of the energy harvesting potential in the human environment that we have just established makes it possible to highlight the difficulty of converting the ambient resources and the low levels of recoverable powers by different transducers such as electromagnetic, thermoelectricity, photovoltaic et c. These resources are often insufficient to meet current needs, and they can be complementary hence the importance of evaluating the interest of soliciting several for the same application.

Hybrid systems consist of the combination of two or more complementary technologies to increase the supply of energy. Energy sources such as the sun and the wind do not deliver constant power, and their combination can lead to more significant and continuous electricity generation. Hybrid systems operate such that batteries are charged by solar panels (during the day) and by the wind generator (when there is wind) [121].

Gergaud [122], showed the relevance of multi-source production (wind and photovoltaic technology) on the design of a coupled decentralized electricity generation system network and can be autonomous. Even if the energy sources of the sources envisaged are less correlated than wind and sun, we hope to enjoy the same benefits in low power energy harvesting. We present here a state of the art of systems low power hybrids described in literature.

I.5.1 State of the Art on hybrid Systems

A prototype was developed by superimposing a photovoltaic cell on the TEG [123]. The hybridization of these two resources made it possible to reduce the size and the overall weight of the system (Figure 29 (a)) thus to improve the power density of the generator. This hybrid generator recovers an average power of 1 mW for a consumption

of the EEG of about 0.8 mW. Following this first application, a new hybrid generator (TEG + PV) integrated into the clothing and used to feed an electrocardiogram (ECG) [124] (Figure 29 (b)) is proposed. The power levels recovered by the generator and consumed by the ECG are similar to those of the previous application. The association of a TEG with a PV cell is also discussed in [125] to increase the autonomy of a laptop. The TEG recovers the heat of the microprocessor, and the PV generator the surrounding light.

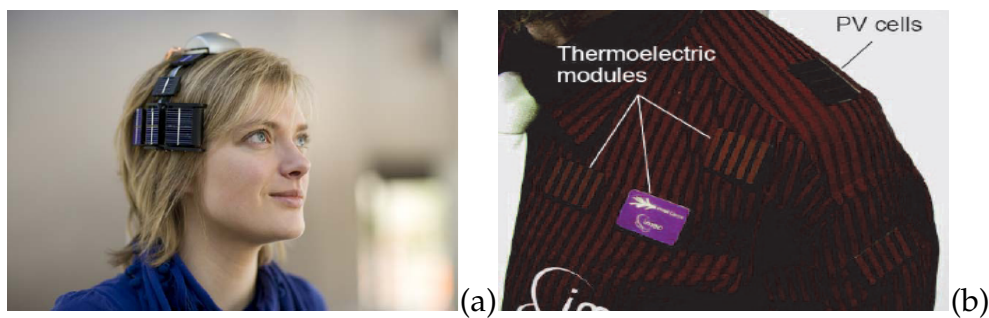


Figure 29: (a) Wearable wireless EEG system with hybrid power supply [123], (b) Hybrid generator for feeding an ECG [124].

Many other work on hybrid systems has been proposed. For examples, Wang et al. [126] developed a Piezoelectric and electromagnetic hybrid energy harvester for powering wireless sensor nodes in smart grid. The authors showed that from current-carrying conductor of 2.5 A at 50 Hz, the proposed harvester combining piezoelectric components and electromagnetic elements can generate up to $295.3\mu W$. Zhenlong et al. [69] presented a novel tunable multi-frequency hybrid energy harvester. It comes out from their studies that the magnitude and direction of magnetic force have significant effect on the performance of the system. Friswell et al. [127] proposed a hybrid cantilever beam harvester with piezoelectric and electrostatic transducers for narrow band base excitation using an applied DC voltage as a control parameter to change the resonant frequency of the harvester to ensure resonance as the excitation frequency varies. Wacharasindhu et al. [128] proposed a micro machine energy harvester from a keyboard typing motions, using combined electromagnetic and piezoelectric conversion. Bin et al. [129] built a hybrid energy harvester combined piezoelectric with electromag-

netic mechanism to scavenge energy from external vibration. They explored the effect of the relative position of the coils and magnets on the PZT cantilever end and the poling direction of magnets on the output voltage of the harvested energy. Karami et al. [130] proposed a hybrid model using piezoelectric and electromagnetic induction effect. They showed that electromechanical coupling has a strong impact upon the system performance. Mokem et al. [131] investigated the dynamics of sandwiched buckled beam with axial compressive force under Gaussian white noise energy harvesting system. The authors showed the optimization of the harvested energy when the stochastic resonance phenomenon occurs.

I.6 Aims of this thesis

In the energy harvesting research field, the main challenge is to enhance the system performance. This thesis is organized around the two bases models whose the first is built by Siewe et al. [132] to demonstrate chaotic motion, and the second by Wen et al. [26] as the energy harvesting device.

In the goal to use the model built by Siewe et al [132] as a electromagnetic energy scavenging device, we introduced a fractional inductance on the model proposed in [132] in order to study its impact on the power generated by the system. moreover, we consider that the magnetic field varies with time. This give rise to a parametric coupling which could play an important role in the improvement of the output power. We explain the behavior of this energy harvester, particularly in the chaotic regime. This study of the system behavior allows us to bound the regions of control parameters where the system displays desired chaotic oscillations and thus characterize the maximal harvestable power for this particular architecture.

The second model of this thesis is based on the model firstly built by Wen et al. [26, 27]. The aim here is to optimize the among of energy harvested by the system [26] and consequently, extended its application field. To reach our objective, we start by considering the nonlinear damping which was absent in original model (Ref.[26, 27]).

Besides, By combining the determinist and random excitation, the stochastic resonance phenomenon could occur and improves the harvested energy. Always in the purpose to overcome some limits observed in the Wen model [26, 27], we built the hybrid model which combines piezoelectric and electromagnetic transduction. The comparison between the output power generated by the harvester without magnetic energy and hybrid model proposed could show the interest to build the hybrid system.

I.7 Conclusion

In this chapter, a detailed review of ambient energy sources and some transduction mechanisms were presented in order to understand the concepts and techniques of energy harvesting. A lot of models to convert ambient energy to electricity have been presented.. However, many studies have shown that several physical phenomena are described through systems exhibiting fractional properties. A state of the art on fractional physical elements has been presented. In Chapter II, we will present a modeling of the different study models as well as the analytical and numerical methods used in this thesis.

METHODOLOGY: MODELING AND NUMERICAL METHODS

II.1 Introduction

In the previous chapter, we have presented the objectives of our thesis. This chapter is devoted to presenting electromechanical harvesters to show the vibration energy harvesting of electromagnetic and piezoelectric types as well as their mathematical modelings. Two situations are discussed in this chapter; (1) the effect of a fractional inductance on the system as well as the impact of parametric coupling, (2) we are interested in comparing the performance of conversion mechanisms through a hybrid model. In the last part, we present the analytical and numerical techniques used in this thesis.

II.2 Nonlinear Electromechanical Energy Harvesters with Fractional Inductance

II.2.1 Governing equations

The scheme of the investigated system is shown in Fig.30 and called electromagnetic transducer. This transducer represents the simplest class of electromechanical system with featuring complex dynamics, because it only records vertical component of ground or support motion under low frequencies. Electromechanical device modeling leads usually to nonlinear systems.

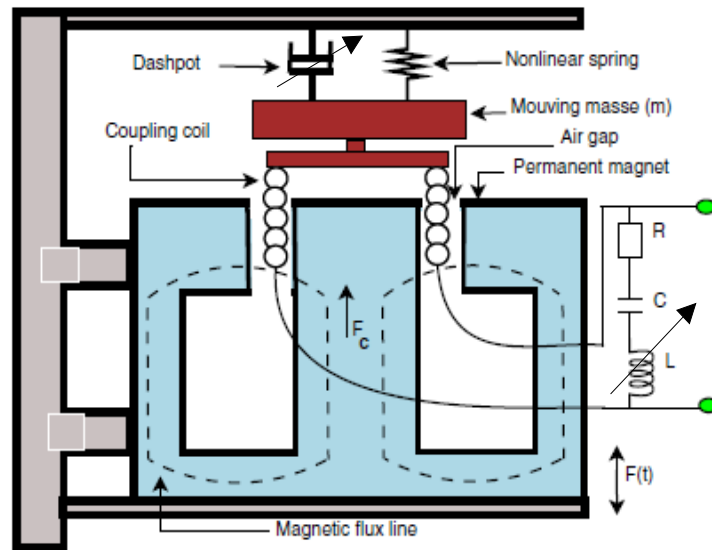


Figure 30: Schematic model with the associated electric circuit [132].

Electrical subsystem

The model shown in Figure 30 is an electrical oscillator coupled through a magnet. The electrical part consists of a linear resistor (LR), a linear condenser (LC) and an fractional inductor L, all connected in series. The voltage of the condenser is a linear function of the instantaneous electrical charge and is expressed by

$$v_c = \frac{q}{C} \quad (74)$$

where C is the linear value of the capacitor. The current-voltage characteristics of the resistor is defined as

$$v_R = R\dot{q}, \quad (75)$$

where q is the instantaneous electrical charge and the dot over a quantity denotes the time derivative ($\dot{q} = \frac{dq}{dt} = i$, where i is the current). R is the resistance in the electrical part, and C is the linear part of the capacitive characteristic.

Existence of ideal inductance in reality is merely a hypothesis. Inductance for real

time application is built by conductor loops or coils. The ideal relation between the current through and voltage across the inductor $v(t) = L \frac{di}{dt}$ does not describe the real time inductance accurately. Several methods were proposed in the literature to model an inductor taking into account the losses due to ohmic resistance, eddy-current and hysteresis. In the field of mechanics the behaviour of magnetic core coils is comparable to that of viscoelastic materials [15] and this motivated to use fractional calculus to model coils. In [15] fractional derivatives are used for modelling coils and showed that such models provide clearly more realistic description than the conventional model. the current-voltage relation of a coil whose current-voltage characteristic has fractional order has been presented in chapter I in section I.4 (see Eq.73). Thus, the current-voltage characteristics of the fractional inductor is used in this thesis is defined by

$$v_k(t) = L_\kappa \frac{d^\kappa i}{dt^\kappa}, \quad (76)$$

Where L_κ is the value of the equivalent inductance, i is the harvest current, t is the time and κ is the degree of derivation between 0 and 1, ($\kappa = 1$ for an ideal inductor).

Fractional order inductance is extensively used in circuit design and simulation in recent times [107]. Fractional order inductances are realized using impedance converter circuit and a fractional element [108]. This author have been realized fractional inductor (FI) using a two-terminal Fractional capacitor (FC) for the first time in a generalized impedance converter (GIC) circuit.

Mechanical subsystem

The mechanical part is composed of a large suspended mass; its motion is determined by the inherent forces of the mass-spring system and the natural forces acting on the system. Let the time-dependent ground motion be $F(t)$, which is due to the motion of the seismic wave. We make the natural assumption that damping forces (friction, air resistance, etc.) are present, and the associated spring is nonlinear with non linear stiffness.

Eq.(77) reports the equation of the nonlinear spring

$$k(y) = k_0 + k_1y^2, \tag{77}$$

where k_0 is the linear mechanical stiffness and k_1 is the nonlinear stiffness that arises due to the stretching of each springs neutral axis, which results from the boundary conditions. The restoring force due to non linear spring stiffness is given by

$$f_r(y) = k_0y + k_1y^3. \tag{78}$$

As pointed by Nguyen et al. [133], damping is important to the bandwidth because it strongly affects the jump frequencies in frequency sweeps. Therefore, understanding the behavior of damping against a variety of working conditions is needed for device performance prediction. The common model with a linear damping force misses essential physics in the device. Motivated by this, we introduce instead nonlinear damping-force models in the form of polynomials in velocity and displacement ([133]).

$$f_d(\dot{y}) = c_1\dot{y} + \sum_{i=1}^N c_{2i+1}(\dot{y})^{2i+1}, \tag{79}$$

where \dot{y} is the velocity of the mass, c_1 and c_{2i+1} are the linear and nonlinear damping coefficients respectively.

Several studies have been made theoretically and numerically the effect of a polynomial dissipation in a model of energy harvesting. Nguyen et al. [133] have experimentally validated a polynomial dissipation model by showing that a high velocity expansion could successfully replicate the experimental results. A systematic experiment was set up and revealed the dependency of the effective damping coefficient on excitation level and bias voltage. Zaitsev et al. [134] have studied experimentally a model of nonlinear dissipation. It follows from the model that nonlinear damping plays an important role in the dynamics of the micro-mechanical beam oscillator. they proposed many methods for experimental evaluation of the contribution of the nonlinear

damping were proposed, applicable at different experimental situations. These methods were compared experimentally and shown to provide similar results. The experimental values of the nonlinear damping constant are non-negligible for all the beams measured.

The nonlinear damping introduced in this system is important insofar as it has been shown that it can improve efficiency in the context of EHS [135, 136] Moreover, it is close to the reality because experimental studies have been done recently or it appears that nonlinear dissipation is the one, that offers better performances in terms of optimization. This form has been adopted from the analytic and experimental work on modeling of the nonlinear damping in a micro-mechanical oscillator in ref [133, 134].

In the mechanical part, the Laplace force $\vec{F}_c = i \vec{l} \wedge \vec{B}$, where l is the length of the coil winding lying in the magnetic field \vec{B} with a moving rod to which a body of each mass m is attached. Since $i \vec{l}$ is orthogonal to \vec{B} and $i = \dot{q}$ we have $F_c(\dot{q}) = lB\dot{q}$.

In the electrical part, the *Lorentz* electromotive force for the expressed is derived thanks to the *Lenz* law and the *Faraday* formula $e = -\vec{l} \cdot (\vec{B} \wedge \dot{y} \vec{k})$. Since $(\vec{l}, \vec{B}, \dot{y})$ is direct, one has $e(\dot{y}) = F_c(\dot{y}) = -lB\dot{y}$.

To derive the equations of motion of the electromechanical device show in Fig.30, let us use the Kirchhoff's law for the electrical part and the second Newton's law of dynamics for the mechanical part. The electromechanical system obeys to the following dimensional two coupled differential equations

$$\begin{aligned} m\ddot{y} &= -m\ddot{f}_s(t) - f_d(\dot{y}) - f_r(y) + F_c(\dot{q}) \\ v_k(t) + v_R + v_C &= F_c(\dot{y}) \end{aligned} \tag{80}$$

Here m is the mass of the oscillator, $f_d(\dot{y})$ is the damping force for the device (due, for example, to friction, air resistance, or transduction of power) in this thesis, we took $N = 1$ in the equation (79). $f_r(y)$ is the restoring force for the oscillator (due, for example, to spring-like mechanical forces and electrostatic forces) and $f_s(t)$ is the displacement of the base of the oscillator due to vibration.

Substituting Eqs.(74)-(79) into (80), we have:

$$\begin{aligned}
 m\ddot{y} + c_1\dot{y} + c_3\dot{y}^3 + k_0y + k_1y^3 - lB\dot{q} &= -m\ddot{f}_s(t) \\
 L_k D_t^{\kappa+1}q + R\dot{q} + \frac{q}{C} + lB\dot{y} &= 0
 \end{aligned}
 \tag{81}$$

where l is the length of the electrical wire inside the magnetic field B , c_1 is the linear damping constant, c_3 is the nonlinear cubic damping constants, k_0 is the linear spring constant and k_3 is the nonlinear cubic spring constant, y and q are the displacement of the mass and charge respectively and $(\dot{\cdot}) = \frac{d}{dt}$.

Some clarifications regarding Eq.(81) are in order. The term $c_1\dot{y}$ is the linear dissipation. An additional dissipation term proportional to the cubed velocity $c_3\dot{y}^3$, has been added artificially. Such term, although not easily derived using the analysis sketched above, may be required to describe some macroscopic friction mechanisms [137, 138], such as losses associated with nonlinear mechanical components. It will be shown below that the impact of this term on the behavior of the system.

The electromagnetic energy harvester makes use of the relative motion between the magnet and induction coil to change the vibration energy into electric power. In early works, the electromagnetic coupling and magnetic field distribution are not often concretized [72] or taken as linear electromagnetic coupling model [73]. The variation of dynamic magnetic field is highly nonlinear with respect to the gap between the magnet and coil. Consequently, the electromagnetic coupling is nonlinear [74, 75].

In certain circumstances, some parameters of the self-sustained electromechanical device can vary with time because of the functioning constraints. This is particularly the case for the parameters of the electromagnetic coupling: i.e., time variations of the magnetic field B and the region of electromagnetic action. We assume that the time variation is periodic with frequency $2\omega_1$. So that, B and l can be explained as

$$\begin{aligned}
 B(t) &= B_0(1 + \gamma\cos(2\omega_1t)) \\
 l(t) &= l_0(1 + \gamma\cos(2\omega_1t)).
 \end{aligned}
 \tag{82}$$

B_0 is the highest intensity that the field B reaches and l is the length of the electrical wire inside the magnetic field B_0 . γ is the amplitude of the parametric coupling with

$0 < \gamma \leq 1$. The variation of the coupling coefficients is considered for the engineering purpose.

In the context of coupled parametrically excited systems, Yamapi et al. [139, 140] studied recently the dynamics of the forced parametric nonlinear electromechanical system consisting of an electrical Duffing oscillator coupled magnetically and parametrically to a linear mechanical oscillator. The frequency response and stability boundaries of harmonic oscillatory states have derived. Effects of the parametric modulation of the coupling coefficient on frequency response-curves and stability boundaries are analyzed. Various types of bifurcation structures were reported using numerical simulations of the equations of motion. Our goal in this thesis is to analyze the effects of parametric coupling on dynamics, oscillatory states and bifurcation sequences of the nonlinear electromechanical system. It is for this reason that only one form of temporal variation of the equation (82) is considered, Eq.(81) become

$$\begin{aligned} m\ddot{y} + c_1\dot{y} + c_3y^3 + k_0y + k_1y^3 - lB_0 (1 + \gamma \cos(2\omega_1 t)) \dot{q} &= -m\ddot{f}_s(t) \\ L_k D_t^{\kappa+1} q + R\dot{q} + \frac{q}{C} + lB_0 (1 + \gamma \cos(2\omega_1 t)) \dot{y} &= 0 \end{aligned} \tag{83}$$

Using the following transformation of coordinates $\omega_0^2 = \frac{k_0}{m}$, $y = lx$, $q = Q_0z$, $\alpha = \kappa + 1$ and by letting the time variable $t = \frac{\tau}{\omega_0}$, the dimensionless equation is given by:

$$\begin{aligned} \ddot{x} + \mu_1\dot{x} + \mu_3\dot{x}^3 + \varrho x + \lambda x^3 - \vartheta_m(1 + \gamma \cos(2\omega\tau))\dot{z} &= f(\tau), \\ \dot{z} + \beta D_\tau^\alpha z + \mu_e z + \vartheta_e(1 + \gamma \cos(2\omega\tau))\dot{x} &= 0 \end{aligned} \tag{84}$$

with

$$\begin{aligned} f(\tau) = -\ddot{f}_s(\tau), \omega = \frac{\omega_1}{\omega_0}, \mu_1 = \frac{c_1\omega_0}{k_0}, \mu_3 = \frac{l^2 c_3 \omega_0^3}{k_1}, \vartheta_e = \frac{l^2 B_0}{Q_0 R} \\ \lambda = \frac{l^2 k_1}{\omega_e^2 m}, \vartheta_m = \frac{B_0 \omega_0^3 Q_0}{k_0}, \mu_e = \frac{1}{\omega_0 RC}, \beta = \frac{\omega_0^\kappa L_k}{R}, L_\kappa = \omega_0^{1-\kappa} L. \end{aligned}$$

x and z are the dimensionless displacement and current respectively. The dot, as in x and z , will indicate differentiation with respect to time. ϑ_i are parameters of the coupling

terms, λ is parameter due to nonlinear stiffness, μ_i and γ_e are damping coefficients, γ_e is the parametric coupling amplitude and L is the conventional value of inductance in Henry. The external ground motion is assumed to be stochastic or periodic ($f_s(\tau) = \frac{E_0}{\omega^2} \cos(\omega\tau)$), where E_0 and ω being respectively, the amplitude and frequency of the harmonic excitation.

The nonlinearity observed in the spring stiffness involves a potential $V(x)$ expressed as follow:

$$V(x) = \frac{\varrho}{2}x^2 + \frac{1}{4}\mu_3x^4, \mu_3 > 0, \tag{85}$$

so that $V(x)$ is monostable for $\varrho \geq 0$ ($x_{01} = 0$) and bistable for $\varrho < 0$ ($x_{02} = \pm \sqrt{-\frac{\varrho}{\mu_3}}$).

II.2.2 Harmonic balance method

Harmonic balance is a method used to calculate the steady-state response of nonlinear differential equations and is mostly applied to nonlinear electrical circuits. It is a frequency domain method for calculating the steady state, as opposed to the various time-domain steady state methods. The name "harmonic balance" is descriptive of the method, which starts with Kirchhoff's Current Law written in the frequency domain and a chosen number of harmonics. A sinusoidal signal applied to a nonlinear component in a system will generate harmonics of the fundamental frequency. Effectively the method assumes the solution can be represented by a linear combination of sinusoids, then balances current and voltage sinusoids to satisfy Kirchhoff's law. The method is commonly used to simulate circuits which include nonlinear elements, and is most applicable to systems with feedback in which limit cycles occur.

The essence of the method is to replace the nonlinear forces in the oscillating systems by specially constructed linear functions, so that the theory of linear differential equations may be employed to find approximate solutions of the non-linear systems. The linear functions are constructed by a special method, known as harmonic lineariza-

tion. Let the given nonlinear function be

$$F(x, \dot{x}) \equiv \epsilon f(x, \dot{x}), \dot{x} = \frac{dx}{dt} \quad (86)$$

where ϵ is a small parameter. Harmonic linearization is the replacement of $F(x, \dot{x})$ by the linear function

$$F_l(x, \dot{x}) = k^0 x + \lambda^0 \dot{x}, \quad (87)$$

where the parameters k^0 and λ^0 are computed by the formulas

$$\begin{aligned} k^0(a) &= \frac{\epsilon}{\pi a} \int_0^{2\pi} f(a \cos \varphi, -a\omega \sin \varphi) \cos \varphi d\varphi, \\ \lambda^0(a) &= -\frac{\epsilon}{\pi a \omega} \int_0^{2\pi} f(a \cos \varphi, -a\omega \sin \varphi) \sin \varphi d\varphi, \end{aligned} \quad (88)$$

$$\varphi = \omega t + \theta.$$

If $x = a \cos(\omega t + \theta)$, $a = \text{const}$, $\omega = \text{const}$, $\theta = \text{const}$. The non-linear force $F(x, \dot{x})$ is a periodic function of time, and its Fourier series expansion contains, generally speaking, an infinite number of harmonics, having the frequencies $n\omega$, $n = 1, 2, \dots$, i.e. it is in the form

$$F(x, \dot{x}) = \sum_{n=0}^{\infty} F_n \cos(n\omega t + \theta_n) \quad (89)$$

The term $F_1 \cos(\omega t + \theta_1)$ is called the fundamental harmonic of the expansion (89). The amplitude and the phase of the linear function F_l coincide with the respective characteristics of the fundamental harmonic of the non-linear force. For the differential equation

$$\ddot{x} + \omega^2 x + F(x, \dot{x}) = 0, \quad (90)$$

which is typical in the theory of quasi-linear oscillations, the harmonic balance method consists in replacing by the linear function instead of equation (90), one then considers

the equation

$$\ddot{x} + \lambda^0 \dot{x} + k^1 x = 0, \tag{91}$$

where $k^1 = \omega^2 + k^0$. It is usual to call F_l the equivalent linear force, λ^0 the equivalent damping coefficient and k^1 the equivalent elasticity coefficient. It has been proved that if the non-linear equation (90) has a solution of the form

$$x = a \cos(\omega t + \theta), \tag{92}$$

where

$$\dot{a} = O(\epsilon), \dot{\omega} = O(\epsilon), \tag{93}$$

then the order of the difference between the solutions of (90) and (91) is ϵ^2 . In the harmonic balance method the frequency of the oscillation depends on the amplitude a (through the quantities k^0 and λ^0). The harmonic balance method is used to find periodic and quasi-periodic oscillations, periodic and quasi-periodic conditions in automatic control theory, as well as stationary conditions, and in the studies of their stability [142, 143].

II.2.3 Amplitude equation

We use the harmonic balance method describe in the next subsection to provide the analytical solution of the model equation. To achieve our objective, we assume that the approximative solution of the system (Eq.(84)) is defined as follows:

$$\begin{aligned} x(\tau) &= A \cos(\omega\tau + \varphi_1) \quad (a) \\ z(\tau) &= B \cos(\omega\tau + \varphi_2) \quad (b) \end{aligned} \tag{94}$$

where

$$A = \sqrt{A_1^2 + A_2^2} \quad \text{and} \quad B = \sqrt{B_1^2 + B_2^2} \quad (95)$$

are the amplitude of the mechanical and the electrical subsystem.

It is known in the literature that, there are many definitions of the fractional derivative. In this work, we used the Caputo's definition [141] given as:

$$\frac{d^\alpha z}{d\tau^\alpha} = D_\tau^\alpha[z(\tau)] = \frac{1}{\Gamma(1-\alpha)} \int_0^\tau (\tau-s)^{-\alpha} \dot{z}(s) ds. \quad (96)$$

where $0 < \alpha \leq 1$, while $\Gamma(\cdot)$ is the gamma function.

Substituting Eq.94(b) into Eq.(96), we obtain:

$$D_\tau^\alpha[B\cos(\omega\tau + \varphi_2)] = D_\tau^\alpha[\varsigma_1 \cos(\omega\tau) - \varsigma_2 \sin(\omega\tau)] \quad (97)$$

with

$$\varsigma_1 = B\cos\varphi_2 \quad ; \quad \varsigma_2 = B\sin\varphi_2, \quad (98)$$

By using the following approximation,

$$z(\tau-s) = B\cos(\omega(\tau-s) + \varphi_2) = B\cos(\theta_2 - \omega s), \quad (99)$$

with

$$\theta_2 = \omega\tau + \varphi_2.$$

Eq.(97) becomes:

$$D_\tau^\alpha[z(\tau)] = \frac{1}{\Gamma(1-\alpha)} \frac{d}{d\tau} \left[B\cos\theta_2 \int_0^\tau \frac{\cos\omega s}{s^\alpha} ds + B\sin\theta_2 \int_0^\tau \frac{\sin\omega s}{s^\alpha} ds \right] \quad (100)$$

By letting $u = \omega s$, we obtain the following expression:

$$D_\tau^\alpha[z(\tau)] = \frac{\omega^\alpha}{\Gamma(1-\alpha)} [-(\varsigma_1 J_1 + \varsigma_2 J_2) \sin\omega\tau + (\varsigma_1 J_2 - \varsigma_2 J_1) \cos\omega\tau] \quad (101)$$

with J_1 and J_2 are defined as [144-147]

$$J_1 = \int_0^\tau \frac{\cos u}{u^\alpha} du = \Gamma(1 - \alpha)\omega^{\alpha-1} \sin\left(\frac{\alpha\pi}{2}\right), \quad (102)$$

$$J_2 = \int_0^\tau \frac{\sin u}{u^\alpha} du = \Gamma(1 - \alpha)\omega^{\alpha-1} \cos\left(\frac{\alpha\pi}{2}\right). \quad (103)$$

Inserting Eq.(102) and Eq.(103) into Eq.(97) we have:

$$D_\tau^\alpha[z(\tau)] = \omega^\alpha(B_1 \cos(\omega\tau) + B_2 \sin(\omega\tau))\left(\cos\left(\frac{\alpha\pi}{2}\right) - \sin\left(\frac{\alpha\pi}{2}\right)\right). \quad (104)$$

Substituting Eq.(104) and Eq.(94) into Eq.(84) and equating the coefficients of the terms containing only $\sin(\omega\tau)$ and $\cos(\omega\tau)$ separately to zero, we obtain the following equations:

$$\begin{aligned} \left(\varrho - \omega^2 + \frac{3}{4}\lambda A^2\right) A_1 + (\mu_1\omega + \frac{3}{4}\mu_3\omega^3 A^2)A_2 + \zeta_2 B_2 - E_0 &= 0, \\ (-\mu_1\omega - \frac{3}{4}\mu_3\omega^3 A^2)A_1 + \left(\varrho - \omega^2 + \frac{3}{4}\lambda A^2\right) A_2 - \zeta_1 B_1 &= 0, \\ \delta B_1 + \omega B_2 + \frac{\vartheta_e \zeta_2}{\vartheta_m^3} A_2 &= 0, \\ -\omega B_1 + \delta B_2 - \frac{\vartheta_e \zeta_1}{\vartheta_m} A_1 &= 0 \end{aligned} \quad (105)$$

where

$$\begin{aligned} \delta &= \beta\omega^\alpha\left(\cos\left(\frac{\alpha\pi}{2}\right) - \sin\left(\frac{\alpha\pi}{2}\right)\right) + \mu_e, \\ \zeta_1 &= \vartheta_m\omega\left(1 - \frac{\gamma}{2}\right), \zeta_2 = \vartheta_m\omega\left(1 + \frac{\gamma}{2}\right). \end{aligned}$$

Using some mathematics tools, the solution of Eq.(105), give rise to the amplitudes equation given as:

$$r_{10} A^{10} + r_8 A^8 + r_6 A^6 + r_4 A^4 + r_2 A^2 + r_1 = 0 \quad (106)$$

and

$$B^2 = b_4 A^4 + b_2 A^2 + b_0 \quad (107)$$

with

$$\begin{aligned}
r_{10} &= (\omega^6 \mu_3^2 + \lambda^2)^2, \\
r_8 &= -\frac{8}{3} \omega^3 \mu_3 (\omega^6 \mu_3^2 + \lambda^2) (\eta_1 - \eta_4 - \lambda (\eta_2 - \eta_3)), \\
r_6 &= \frac{16}{9} \omega^6 (\eta_1^2 - 4 \eta_1 \eta_4 + 2 \eta_2 \eta_3 + \eta_4^2) \mu_3^2 - \frac{32}{9} \lambda \omega^3 (\eta_2 + \eta_3) (\eta_1 - \eta_4) \mu_3 \\
&\quad - \frac{16}{9} \lambda^2 (2 \eta_1 \eta_4 - \eta_2^2 - 4 \eta_2 \eta_3 - \eta_3^2), \\
r_4 &= -\frac{16}{9} \omega^6 E_0^2 \mu_3^2 + \frac{128}{27} \omega^3 (\eta_1 - \eta_4) (\eta_1 \eta_4 - \eta_2 \eta_3) \mu_3 - \frac{16}{27} \lambda (8 (\eta_2 + \eta_3) (\eta_1 \eta_4 - \eta_2 \eta_3) + 3 \lambda E_0^2), \\
r_2 &= \frac{256}{81} \eta_1^2 \eta_4^2 + \left(\frac{128}{27} \omega^3 E_0^2 \mu_3 - \frac{512}{81} \eta_2 \eta_3 \eta_4 \right) \eta_1 + \frac{256}{81} \eta_2^2 \eta_3^2 - \frac{128}{27} \eta_2 \lambda E_0^2, \\
r_1 &= -\frac{256}{81} E_0^2 (\eta_1^2 + \eta_2^2), \\
\xi &= 12 ((-\eta_1 + \eta_4) \mu_3 \omega^3 + \eta_2 \lambda + \eta_3 \lambda) A^2 - 16 (\eta_1 \eta_4 - \eta_2 \eta_3) + 9 (\omega^6 \mu_3^2 + \lambda^2) A^4,
\end{aligned}$$

$$b_0 = \frac{256(\eta_1^2 \zeta_2^2 + \eta_2 \zeta_1^2) \vartheta_e^2 E_0^2}{(\delta^2 + \omega^2) \xi^2 \vartheta_m^2},$$

$$b_2 = \frac{384(\eta_2 \lambda \zeta_1^2 - \eta_1 \omega^3 \zeta_2^2 \mu_3) \vartheta_e^2 E_0^2}{(\delta^2 + \omega^2) \xi^2 \vartheta_m^2},$$

$$b_4 = \frac{144(\eta_2^2 \omega^6 \mu_3 + \lambda^2 \zeta_1^2) \vartheta_e^2 E_0^2}{(\delta^2 + \omega^2) \xi^2 \vartheta_m^2}$$

and

$$\eta_1 = -\omega \mu_1 - \frac{\zeta_1^2 \omega \vartheta_e}{\vartheta_m (\delta^2 + \omega^2)},$$

$$\eta_2 = -\omega^2 + \varrho - \frac{\zeta_1 \vartheta_e \delta \zeta_2}{\vartheta_m (\delta^2 + \omega^2)},$$

$$\eta_3 = -\omega^2 + \varrho - \frac{\zeta_1 \vartheta_e \delta \zeta_2}{\vartheta_m (\delta^2 + \omega^2)},$$

$$\eta_4 = -\omega \mu_1 - \frac{\zeta_2^2 \omega \vartheta_e}{\vartheta_m (\delta^2 + \omega^2)}.$$

Eqs.(106) and (107) are the equations of the amplitudes of harmonic oscillatory states.

An expression for this power is derived by integrating the dimensionless form of the

Table 5: Parameters

Parameter	Value	Unit
c_1	0.55	Ns/m
c_3	2.5	Ns^3/m^3
k_0	25	N/m
k_1	90	N/m
L	1.34	H
R	20.5	Ω
m	1.082	kg
l	0.17	m
C	0.01052	F

instantaneous power $P = \mu_e(\dot{z})^2$. The average output power is estimated using this formula:

$$P_{max} = \frac{\mu_e}{2T} \int_0^T \left(\frac{dz}{dt}\right)^2 dt, \quad (108)$$

where $T = \frac{2\pi}{\omega}$ is the period of the excitation source and an ideal transducer with zero internal resistance is presumed. The physical parameters used in the simulation are given in Table 5.

In equation (84), the efficiency conversion of energies dispersed in the environment by the energy harvesting devices such as the electromechanical systems is the one of the fundamental elements for evaluating the systems performance. Thus, the efficiency conversion of the scavenger is defined as follows:

$$\eta = \frac{p_e}{p_m} \times 100[\%] \quad (109)$$

where p_e and p_m are respectively, the electrical and the mechanical power effective value. Let us notice that the power effective value is defined as:

$$p_t = \sqrt{\frac{1}{T} \int_0^T (p_t^{ins})^2 dt} \quad (110)$$

where p_t^{ins} is the instantaneous power and T is the time.

II.3 Hybrid Electromagnetic and Piezoelectric Vibration Energy Harvester with Gaussian white Noise Excitation

At present, the hybridization of resources for low power applications is finally little discussed in the literature. We therefore chose to study a multi-source system used two energy transduction mechanism to know electromagnetic and piezoelectric. At these two mechanisms, we will associate a storage element, here an inductance.

II.3.1 Description and modelling of the hybrid model

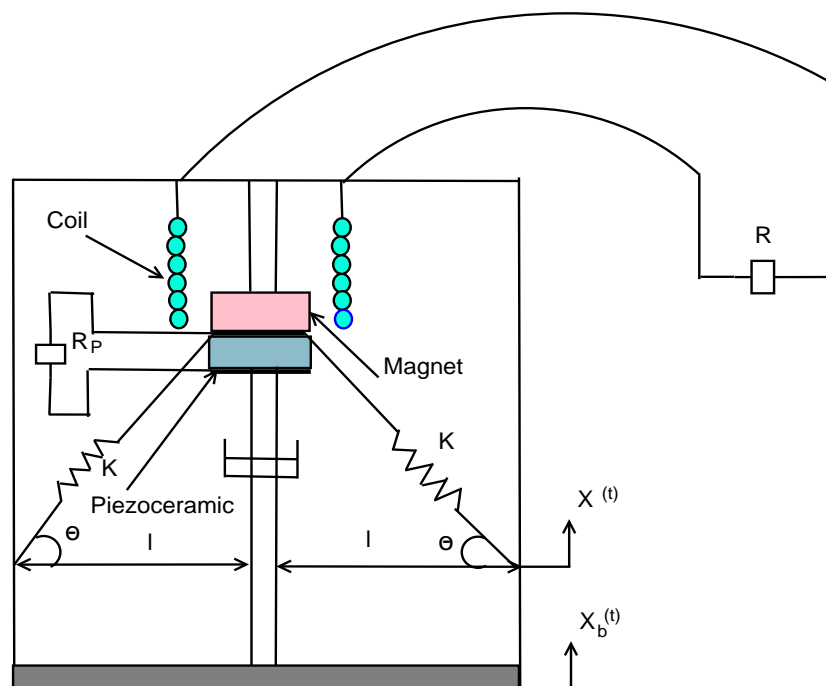


Figure 31: Schematic of the hybrid energy harvester

The traditional PE and EM energy harvester consists of a piezoelectric element and an electromagnetic element. In the PE element, the piezoceramic material is excited at the vibratory mass which modifies the stress distribution of the PZT layer, there by generating the output power via the piezoelectric effect. Electromagnetic output power is

mainly obtained by placing a coil near the magnet, due to Faraday's law on electromagnetic induction. In order to generate a non-linear PE and EM hybrid energy harvester, two springs are used, located symmetrically on the PE element and the ground (see Fig.31). Introducing of spring as a nonlinear component in a hybrid piezoelectric and electromagnetic energy harvester will produce a linear factor α_1 and a nonlinear factor α_3 based on the reference [126]. The mechanical part is composed of the mass m , the nonlinear spring and nonlinear damping.

II.3.1.1 Static analysis of the oblique springs

This section focuses on a static analysis of the two oblique springs and shows how the arrangement results in a negative stiffness mechanism. Figure 32 shows a possible arrangement of the mass spring-damper. It consists of two linear oblique springs connected to a mass and a damper. Unlike a linear system, when the springs are unextended, they are inclined at an angle $\pm\theta$ to the line $x = 0$. Although the springs provide

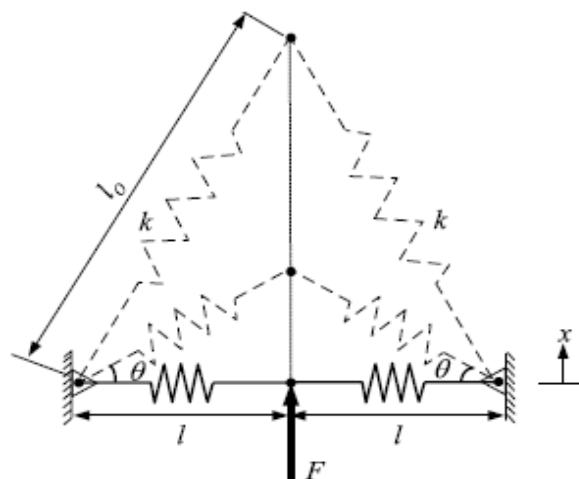


Figure 32: The force acting on the oblique spring

a linear restoring force along their axes, this particular arrangement yields a non-linear restoring force in the x -direction. The purpose of this mechanism is to steepen the gradient of the displacement curve as a function of time so as to approximate a square wave. The purpose of this arrangement is to aims to obtain a bistable potential that allows to

obtain large oscillations, because it allows to harvest the maximum energy.

The total axial component of the spring force F at any displacement x is such that

$$F = 2\widetilde{f}_{\Delta} \quad (111)$$

where \widetilde{f}_{Δ} is the axial component of each spring force. The total axial restoring force as a function of x is given by

$$\widetilde{f}_{\Delta} = 2k(\sqrt{x^2 + l^2} - l_0) \sin \theta \quad (112)$$

where $\sqrt{x^2 + l^2}$ is the length of the spring, l_0 is the original length of the spring and θ is the inclination of the spring with respect to the origin. Referring to Fig.32,

$$\sin \theta = \frac{x}{\sqrt{x^2 + l^2}}. \quad (113)$$

Substituting this into (112) gives

$$F = 2k\left(1 - \frac{l_0}{\sqrt{x^2 + l^2}}\right)x. \quad (114)$$

The total elastic potential energy, $U(x)$ is given by

$$U(x) = 2\left(\frac{1}{2}k(\sqrt{x^2 + l^2} - l_0)^2\right). \quad (115)$$

II.3.1.2 Governing equations

The Newton's equation in standard form describes this displacement $x(t)$; there by, a differential equation of second order is given by:

$$m\ddot{x}(t) = -\frac{dU(x(t))}{dx(t)} - f_d(\dot{x}(t)) - \Gamma_1(v(t)) - \Gamma_2(i(t)) - m\ddot{x}_b(t) \quad (116)$$

Where;

- $U(x(t))$ corresponds to the non dimensionless potential given by Eq.(115),

- $f_d(\dot{x}(t))$ corresponds to non linear dissipative force given by Eq.(79),
- $\Gamma_1(v(t))$ corresponds to force of reaction caused by piezoelectric transduction mechanism expressed by $\Gamma_1(v(t)) = \eta v(t)$,
- $\Gamma_2(i(t))$ corresponds to force of reaction caused by electromagnetic transduction mechanism expressed by $\Gamma_2(i(t)) = \theta_m i(t)$,
- $m\ddot{x}_b(t)$ corresponds to the vibration force.

Using the Kirchhoff's laws and combining the constitutive equations of electromagnetic and piezoelectric we have,

$$\begin{aligned} C_p \dot{v}(t) + \frac{1}{R_p} v(t) - \eta \dot{x}(t) &= 0 \\ L \dot{i}(t) + (R_c + R_m) i(t) - \theta_m \dot{x}(t) &= 0. \end{aligned} \quad (117)$$

So, the equations of the hybrid system of figure 32 are given by

$$\begin{aligned} m\ddot{x}(t) + c_1 \dot{x}(t) + c_3 (\dot{x}(t))^3 + 2k \left(1 - \frac{l_0}{\sqrt{x(t)^2 + l^2}}\right) x(t) + \eta v(t) + \theta_m i(t) &= -m\ddot{x}_b(t) \\ C_p \dot{v}(t) + \frac{1}{R_p} v(t) - \eta \dot{x}(t) &= 0 \\ L \dot{i}(t) + (R_c + R_m) i(t) - \theta_m \dot{x}(t) &= 0 \end{aligned} \quad (118)$$

where $x(t)$ is the displacement of the mass magnet, m is the mass, k is the spring stiffness, c_1 and c_3 are the linear and nonlinear damping coefficients, l_0 is the original length of the spring, l is the distance between the center and the edge of the frame, v is the voltage across the load resistance, C_p is the capacitance of the piezoceramic, R_p and R_m are load resistance of PE and EM element respectively, R_c and L refer to the resistance and inductance of coils, θ_m and η are the PE and EM transfer factors, respectively, \ddot{x}_b is the base displacement. Using the following transformation of coordinate $X = \frac{x}{l_0}$ and $\gamma = \frac{l}{l_0}$, Eq.(118) can be rewritten as:

$$\begin{aligned}
 \ddot{X} + \frac{c_1}{m}\dot{X} + \frac{c_3 l_0^2}{m}\dot{X}^3 + \frac{2k}{m}\left(1 - \frac{1}{\sqrt{X^2 + \gamma^2}}\right)X + \frac{\eta}{l_0 m}v + \frac{\theta_0}{l_0 m}i &= -\frac{\ddot{x}_b}{l_0} \\
 \dot{v} + \frac{1}{C_p R_p}v - \frac{\eta l_0}{C_p}\dot{X} &= 0 \\
 \dot{i} + \frac{R}{L}i - \frac{\theta_m l_0}{L}\dot{X} &= 0,
 \end{aligned} \tag{119}$$

where $(\dot{}) = \frac{d}{dt}$.

The dimensionless potential energy is

$$U(X) = \frac{2k}{m}(\sqrt{X^2 + \gamma^2} - 1)^2. \tag{120}$$

The equilibrium positions of the mechanical system are given by

$$\widetilde{X}_1 = \sqrt{1 - \gamma^2}\{stable\}, \tag{121}$$

$$\widetilde{X}_2 = -\sqrt{1 - \gamma^2}\{stable\}, \tag{122}$$

$$\widetilde{X}_3 = 0\{unstable\}. \tag{123}$$

If the amplitude of the motion is small, the system will oscillate about one of its stable equilibrium positions depending on the initial conditions. If the amplitude is large, the system starts to oscillate between the two stable equilibrium positions, which can also be described as cross-well motion.

In this work, we consider the weak amplitude of vibration. In this case, the non-linear term in Eq.(119) can be expanded into the Taylor series at equilibrium $(X_0, 0)$. Introducing the new variable $X = z - X_0$, with $X_0 = \widetilde{X}_1$ is the positive stable static equilibrium position given by the Eq.(121), this term expressed as

$$\begin{aligned}
 \frac{1}{\sqrt{\gamma^2 + (z + X_0)^2}} &= \frac{1}{\sqrt{\gamma^2 + X_0^2}} - \frac{X_0}{(\gamma^2 + X_0^2)^{\frac{3}{2}}}z + \frac{-\frac{1}{2(\gamma^2 + X_0^2)} + \frac{3}{2}\frac{X_0^2}{(\gamma^2 + X_0^2)^2}}{\frac{1}{(\gamma^2 + X_0^2)^{\frac{5}{2}}}}z^2 \\
 &+ \frac{\frac{3}{2}\frac{X_0}{(\gamma^2 + X_0^2)^2} - \frac{5}{2}\frac{X_0^3}{(\gamma^2 + X_0^2)^3}}{\frac{1}{(\gamma^2 + X_0^2)^{\frac{7}{2}}}}z^3 + 0(z^4)
 \end{aligned} \tag{124}$$

substituting $X_0 = \sqrt{1 - \gamma^2}$, Eq.(124) is rewritten as

$$\frac{1}{\sqrt{\gamma^2 + (z + X_0)^2}} = 1 - \sqrt{1 - \gamma^2}z + (1 - \frac{3}{2})z^2 + (\frac{3}{2}\sqrt{1 - \gamma^2} - \frac{5}{2}(1 - \gamma^2)^{\frac{3}{2}})z^3 + 0(z^4). \tag{125}$$

Using the following transformation of coordinates

$$\omega_1^2 = \frac{2|k|(1 - \gamma^2)}{m}, z = z_0z, i = i_0\rho, v = v_0y \tag{126}$$

and by letting the time variable $t = \frac{\tau}{\omega_1}$, By omitting higher order terms in the resulting expanding expression, the dimensionless equation (Eq.(119)) is given by:

$$\begin{aligned}
 \ddot{z} + \zeta_1\dot{z} + \zeta_3z^3 + \omega_1^2z + \alpha_2z^2 + \alpha_3z^3 + \zeta_m\rho + \zeta_e y &= \xi(\tau)(a), \\
 \dot{y} + \lambda y - \vartheta_p\dot{z} &= 0(b), \\
 \dot{\rho} + \beta\rho - \vartheta_e\dot{z} &= 0(c),
 \end{aligned} \tag{127}$$

where

$$\begin{aligned}
 \zeta_1 &= \frac{c_1\omega_1}{2|k|(1 - \gamma^2)}, \zeta_3 = \frac{(z_0l_0)^2c_3\omega_1^3}{2|k|(1 - \gamma^2)}, \vartheta_e = \frac{\theta_m l_0 z_0}{i_0 L} \\
 \lambda &= \frac{1}{\omega_1 C_p R_p}, \zeta_m = -\frac{\theta_m i_0}{2z_0 l_0 |k|(1 - \gamma^2)}, \zeta_e = -\frac{\eta v_0}{2z_0 l_0 |k|(1 - \gamma^2)}, \\
 \beta &= \frac{R_c + R_m}{\omega_1 L}, \vartheta_p = \frac{\eta l_0 z_0}{v_0 C_p}, \alpha_3 = \frac{z_0^2 \gamma^2 (5\gamma^2 - 4)}{\gamma^2 - 1}, \alpha_2 = \frac{3z_0 \gamma^2}{2\sqrt{1 - \gamma^2}}.
 \end{aligned}$$

$\xi(\tau) = -\frac{\ddot{x}_b}{2|k|l_0(1-\gamma^2)}$ is the Gaussian white noise verifying the statistic properties:

$$\langle \xi(\tau)\xi(t+\tau') \rangle = 2D\delta(\tau), \quad (128)$$

$$\langle \xi(\tau) \rangle = 0,$$

where $2D$ is the intensity of noise and $\delta(\tau)$, the Dirac function. The variables z , y and ρ are the dimensionless displacement, voltage and current respectively. The dot in z , y and ρ indicates differentiation with respect to the time. ϑ_p , ϑ_e , ζ_e and ζ_m are parameters of the coupling terms, α_2 is the coefficient of quadratic nonlinearity, α_3 is the coefficient of cubic nonlinearity, ζ_1 and ζ_3 are damping coefficients, λ is the impedance of the (PE) system, β is the ratio of the resistance and inductance and $\omega_1 = 1$.

The non-dimensionless potential $U(z)$ is defined as

$$U(z) = \frac{\omega_1^2}{2}z + \frac{1}{3}\alpha_2z^3 + \frac{1}{4}\alpha_3z^4. \quad (129)$$

This potential $U(z)$ depends on the values of the parameters α_3 , α_2 and ω_1 .

II.3.2 Stochastic averaging method and stochastic p-bifurcation

II.3.2.1 Stochastic averaging method

A stochastic averaging analysis involves both stochastic averaging and deterministic averaging that can be carried out in either order. The stochastic averaging accounts for the averaged effects of random excitations multiplied by correlated response, and physically wide-band random excitations are replaced by mathematically Gaussian white noise excitations. Thus, the slowly varying response quantities are approximated by a vector of diffusive Markov process and the Fokker-Planck-Kolmogorov (FPK) equation method can be applied to them. Following [148], the original method of stochastic averaging was introduced by Stratonovich [149]. It may be viewed as an extension of the deterministic averaging procedure of Bogoliubov and Mitropolsky [143], method is ap-

plicable to lightly damped systems with small nonlinearities under broadband random excitations of small magnitudes.

This method, known as the classical or standard stochastic averaging (CSA) as to its deterministic counterpart the effects of some nonlinear inertia terms and nonlinear stiffness terms, such as the cubic displacement terms, in the governing second order differential equation of motion of a sdof system are absent in the approximate solutions. The implication is that the effects of these nonlinear terms on the stochastic system can not be studied by applying the classical stochastic averaging (CSA) method. It was suggested (see, for examples, page 149 of Ref [150], page 125 of Ref [151], and page 191 of Ref [152]) that in order to reveal the effects of these nonlinear terms a second order averaging is required.

A closer examination of the equations in standard form for such a system reveals that while it is true that the influence, of the nonlinear inertia terms and nonlinear stiffness terms, such as the cubic displacement terms of a sdof system, on the amplitude solution is absent, the influence of these nonlinear terms is present in the phase solution. Thus, the influence of these nonlinear terms on the response statistics is retained since the latter are functions of both amplitude and phase.

In the following the CSA method is introduced first. The procedure of application of the CSA method is illustrated with several examples. Consider a set of differential equations in standard form

$$\frac{dz_j}{dt} = \varepsilon f_j(Z, t) + \varepsilon \frac{1}{2} g_{jr}(Z, t) \xi_r(t), \tag{130}$$

$$j = 1, 2, \dots, n; r = 1, 2, \dots, m.$$

where ε is a small positive parameter Z is an- n -dimension random vector process of response state and z_j is its j 'th component; f_j and g_{jr} are deterministic nonlinear functions, while $\xi_r(t)$ is the r 'th component of the stationary random excitation vector $\varepsilon(t)$. Elements of the latter vector are of zero mean and have cross correlation matrix $\Gamma(\tau)$

whose elements are

$$\Gamma_{rv}(\tau) = \langle \varepsilon_r(t), \varepsilon_v(t + \tau) \rangle . \quad (131)$$

If the maximum of correlation times of the random excitations is much smaller than the minimum of the relaxation times of the mdof system, then it can be shown that [155] the state vector Z weakly converges to a diffusive Markov vector $Z^{(0)}$ with transition probability density $p(Z^{(0)}, t | Z_0^{(0)}, t_0)$ or simply p , where the subscript 0 denotes at time t_0 . The governing FPK equation is

$$\frac{\partial P}{\partial t} = -\varepsilon \frac{\partial(a_j P)}{\partial Z_j^{(0)}} + \frac{\varepsilon}{2} \frac{\partial^2(b_{jk} P)}{\partial Z_j^{(0)} \partial Z_k^{(0)}}, \quad (132)$$

where the drift and diffusion coefficients, a_j and b_{jk} are given, respectively by

$$a_j(Z^{(0)}) = T_s^{av} \{ \langle f_j(Z^{(0)}, s) \rangle + I_{av} \}, \quad (133)$$

in which

$$I_{av} = \int_{-\infty}^0 \left\langle \frac{\partial g_{jr}(Z^{(0)}, s)}{\partial Z_k^{(0)}} g_{kv}(Z^{(0)}, s + v) \xi_r(s) \xi_v(s + \tau) \right\rangle d\tau \quad (134)$$

and

$$b_{jk}(Z^{(0)}) = T_s^{av} \left\{ \int_{-\infty}^{+\infty} \langle g_{kv}(Z^{(0)}, s + \tau) \xi_r(s) \xi_v(s + \tau) \rangle d\tau \right\}, \quad (135)$$

in which $T_s^{av} \{ \cdot \}$ denotes deterministic averaging of the enclosing quantity with respect to time s . That is,

$$T_{t_0}^{av} = \lim_{T \rightarrow \infty} \frac{1}{T} \left\{ \int_{t_0}^{t_0+T} \{ \cdot \} dt \right\} \quad (136)$$

in which the integration is performed over explicit time t . If the quantities in Eqs. (133) and (135) are periodic, with period T_0 for example, then Eq. (136) becomes

$$T_{t_0}^{av} = \frac{1}{T_0} \left\{ \int_{t_0}^{t_0+T_0} \{.\} dt \right\} \quad (137)$$

and the results are independent of t_0 . The implication of Eq.(137) is that if the function $f_1(Z^{(0)}, s)$, for example, contains a periodic term, such as $\sin\left(\frac{2\pi t}{T_0}\right)$ its effect on the response will be zero after the deterministic averaging. The integral on the right-hand-side (RHS) of Eq.(133) is related to the Wong and Zakari (WZ) or Stratonovich (S) correction term and therefore Eqs.(132), (133) and (135) are to be interpreted in the Itô's sense.

The Markov vector process $Z^{(0)}$ can be described by the following set of Itô stochastic differential equations

$$dz_j^{(0)} = \varepsilon m_j(Z^{(0)})dt + \varepsilon \frac{1}{2} \sigma_{jr}(Z^{(0)})dW_r(t) \quad (138)$$

where the unit Wiener processes are defined by

$$dW_r(t) = \xi_r(t)dt \quad (139)$$

The drift coefficients m_j and diffusion coefficients σ_{jr} of the Itô equation, (138) are related to a_j and b_{jk} of the Fokker-Planck-Kolmogorov (FPK) equation, (132) by

$$m_j(Z^{(0)}) = a_j(Z^{(0)}), \quad (140)$$

$$\sigma_{jr}(Z^{(0)})\sigma_{kr}(Z^{(0)}) = b_{jk}(Z^{(0)}). \quad (141)$$

In the Itô equations, (138), the diffusion matrix $[\sigma]$ may not be unique though the matrix product $[\sigma][\sigma]^T$ and the diffusion matrix $[b]$ of FPK equation, (132) are unique. The exact response statistics of the approximate solution of the given system defined by Eq.(130) can be obtained from either the FPK equation (132) or Itô equations (138).

II.3.2.2 Probability density

The fluctuating quantities considered as excitations in many mechanical systems cannot always be adequately modeled by deterministic time functions. In fact, there are several natural phenomena that vary in a random manner due to the effect of many unknown factors, that fluctuate randomly over a wide band of frequencies and have to be considered as stochastic functions of time, defined only in probabilistic terms [153]. Dynamic systems in such environments are subject to stochastic excitations. Then, in order to examine their response and stability, a probabilistic approach employing the theory of stochastic bifurcation is essential. The main purpose of this heading is to provide the statistic response of the harvester through the Fokker -PlanckKomogorov equation using the stochastic averaging technique developed by Stratonovich [154].

To achieve our objective, it is judicious to find the Ito stochastic differential equations associated with the system Eq.(127). In the quasiharmonic regime, on assumption that noise intensity is small, we introduce change of variables [153]

$$\begin{aligned} z(\tau) &= a(\tau) \cos(\varphi), \\ \dot{z}(\tau) &= -a(\tau) \omega_0 \sin(\varphi), \end{aligned} \tag{142}$$

where $\varphi = \omega_0\tau + \theta(\tau)$, $a(\tau)$ is amplitude of mechanical subsystem. Substituting Eq.(142) into Eq.127(b) and (c), we have:

$$y(\tau) = C_1(\tau)e^{-\lambda\tau} + \frac{a\vartheta_p\omega_0}{\lambda^2 + \omega_0^2}(\omega_0 \cos \varphi - \lambda \sin \varphi), \tag{143}$$

$$\rho(\tau) = C_2(\tau)e^{-\beta\tau} + \frac{a\vartheta_e\omega_0}{\beta^2 + \omega_0^2}(\omega_0 \cos \varphi - \beta \sin \varphi). \tag{144}$$

Where the first term and the second term in the right hand are the general solution of the associated homogeneous equation and the special solution, respectively. For the stationary responses concerned here, however, the general solution $C_1(\tau) \exp(-\lambda\tau)$ and $C_2(\tau) \exp(-\beta\tau)$ almost has not any influence due to the exponential decay nature. The

steady-state of Eq.(143) and Eq.(144) are given by:

$$y(\tau) = \frac{a\vartheta_p\omega_0}{\lambda^2 + \omega_0^2}(\omega_0 \cos \varphi - \lambda \sin \varphi) \quad (145)$$

and

$$\rho(\tau) = \frac{a\vartheta_e\omega_0}{\beta^2 + \omega_0^2}(\omega_0 \cos \varphi - \beta \sin \varphi). \quad (146)$$

From Eq.(145),

$$\omega_0 \cos \varphi - \lambda \sin \varphi = \sqrt{\lambda^2 + \omega_0^2} \left(\frac{\omega_0}{\sqrt{\lambda^2 + \omega_0^2}} \cos \varphi - \frac{\lambda}{\sqrt{\lambda^2 + \omega_0^2}} \sin \varphi \right) \quad (147)$$

who can still put himself in the form

$$\omega_0 \cos \varphi - \lambda \sin \varphi = \sqrt{\lambda^2 + \omega_0^2} (\cos \Theta \cos \varphi - \sin \Theta \sin \varphi) \quad (148)$$

with

$$\cos \Theta = \frac{\omega_0}{\sqrt{\lambda^2 + \omega_0^2}} \quad \text{and} \quad \sin \Theta = \frac{\lambda}{\sqrt{\lambda^2 + \omega_0^2}}. \quad (149)$$

Finally,

$$\omega_0 \cos \varphi - \lambda \sin \varphi = \sqrt{\lambda^2 + \omega_0^2} \cos(\Theta + \varphi). \quad (150)$$

Thus

$$y(\tau) = \frac{a\vartheta_p\omega_0}{\lambda^2 + \omega_0^2} \sqrt{\lambda^2 + \omega_0^2} \cos\left(\varphi + \tan^{-1}\left(\frac{\lambda}{\omega_0}\right)\right). \quad (151)$$

In the steady state, the amplitude of the voltage expressed as follow:

$$V_0 = \frac{a\vartheta_p\omega_0}{\lambda^2 + \omega_0^2} \times \sqrt{\lambda^2 + \omega_0^2} = \frac{a\vartheta_p\omega_0}{\sqrt{\lambda^2 + \omega_0^2}}. \quad (152)$$

Similarly, Eq.(146) in the steady state, the amplitude of the steady state current is

$$I_0 = \frac{a\vartheta_e\omega_0}{\beta^2 + \omega_0^2} \times \sqrt{\beta^2 + \omega_0^2} = \frac{a\vartheta_e\omega_0}{\sqrt{\beta^2 + \omega_0^2}}. \quad (153)$$

Substituting Eq.(145), Eq.(146) and Eq.(142) into Eq.(127) by letting $\omega_1 = \omega_0$ we obtain:

$$\begin{aligned} \dot{a} = & -\zeta_1 a \sin^2 \varphi - \zeta_3 \omega_0^2 a^3 \sin^4 \varphi + \frac{\alpha_2 a^2 \sin \varphi \cos^2 \varphi}{\omega_0} + \frac{\alpha_3 a^3 \sin \varphi \cos^3 \varphi}{\omega_0} + \frac{\zeta_e \omega_0 \vartheta_p a \sin \varphi \cos \varphi}{\lambda^2 + \omega_0^2} \\ & - \frac{\zeta_e \vartheta_p \lambda a \sin^2 \varphi}{\lambda^2 + \omega_0^2} + \frac{\zeta_m \omega_0 \vartheta_e a \sin \varphi \cos \varphi}{\beta^2 + \omega_0^2} - \frac{\zeta_m \vartheta_e \beta a \sin^2 \varphi}{\beta^2 + \omega_0^2} - \frac{\sin \varphi \xi(\tau)}{\omega_0}, \end{aligned} \quad (154)$$

$$\begin{aligned} \dot{\theta} = & -\zeta_1 \cos \varphi \sin \varphi - \zeta_3 \omega_0^2 a^2 \cos \varphi \sin^3 \varphi + \frac{\alpha_2 a \cos^3 \varphi}{\omega_0} + \frac{\alpha_3 a^2 \cos^4 \varphi}{\omega_0} + \frac{\zeta_e \omega_0 \vartheta_p \cos^2 \varphi}{\lambda^2 + \omega_0^2} \\ & - \frac{\zeta_e \vartheta_p \lambda \cos \varphi \sin \varphi}{\lambda^2 + \omega_0^2} + \frac{\zeta_m \omega_0 \vartheta_e \cos^2 \varphi}{\beta^2 + \omega_0^2} - \frac{\zeta_m \vartheta_e \beta \cos \varphi \sin \varphi}{\beta^2 + \omega_0^2} - \frac{\cos \varphi \xi(\tau)}{\omega_0 a}. \end{aligned} \quad (155)$$

Thus, after applying the deterministic averaging method to Eq.(154) and (155), we obtained the following approximated system:

$$\begin{aligned} \dot{a} = & -\frac{3}{8} \zeta_3 \omega_0^2 a^3 - \frac{1}{2} \left(\frac{\lambda^2 \varsigma_1 + \lambda \varsigma_2 + \varsigma_3}{(\lambda^2 + \omega_0^2)(\beta^2 + \omega_0^2)} \right) a - \frac{\sin \varphi \xi(\tau)}{\omega_0}, \\ \dot{\theta} = & \frac{3}{8} \frac{\alpha_3 a^2}{\omega_0} + \frac{1}{2} \frac{\omega_0 (\vartheta_p \zeta_e (\beta^2 + \omega_0^2) + \vartheta_m \zeta_m (\lambda^2 + \omega_0^2))}{(\lambda^2 + \omega_0^2)(\beta^2 + \omega_0^2)} - \frac{\cos \varphi \xi(\tau)}{a \omega_0} \end{aligned} \quad (156)$$

with

$$\varsigma_1 = \zeta_m \beta \vartheta_e + (\beta^2 + \omega_0^2) \zeta_1,$$

$$\varsigma_2 = (\beta^2 + \omega_0^2) \zeta_e \vartheta_p,$$

$$\varsigma_3 = \zeta_m \beta \vartheta_e \omega_0^2 + (\beta^2 \omega_0^2 + \omega_0^4) \zeta_1.$$

By applying the stochastic averaging method [156, 149], we can obtain the following stochastic equations for a and θ :

$$da = \left(-\frac{3}{8}\zeta_3\omega_0^2a^3 - \frac{1}{2}\left(\frac{\lambda^2\zeta_1 + \lambda\zeta_2 + \zeta_3}{(\lambda^2 + \omega_0^2)(\beta^2 + \omega_0^2)}\right)a + \frac{D}{2\omega_0^2a} \right) d\tau + \sqrt{\frac{D}{\omega_0^2}}d\eta_1(\tau) (a) \quad (157)$$

$$d\theta = \left(\frac{3}{8}\frac{\alpha_3a^2}{\omega_0} + \frac{1}{2}\frac{\omega_0(\vartheta_p\zeta_e(\beta^2 + \omega_0^2) + \vartheta_m\zeta_m(\lambda^2 + \omega_0^2))}{(\lambda^2 + \omega_0^2)(\beta^2 + \omega_0^2)} \right) d\tau + \sqrt{\frac{D}{\omega_0^2a^2}}d\eta_2(\tau) (b)$$

where $\eta_1(\tau)$ and $\eta_2(\tau)$ are two independent normalized Wiener processes. It is worth pointing out that a and θ are independent, allowing us further to develop a probability density for amplitude a , rather than a joint density for θ . The probability density $p(a, \tau)$ of the instantaneous amplitude a satisfied the Fokker-Planck-Kolmogorov equations [157, 158]:

$$\frac{\partial}{\partial \tau} p(a, \tau) = -\frac{\partial}{\partial a} \left[\left(\chi_1 + \frac{D}{2\omega_0^2a} \right) p(a, \tau) \right] + \frac{1}{2} \frac{\partial^2}{\partial a^2} \left[p(a, \tau) \left(\frac{D}{\omega_0^2} \right) \right] \quad (158)$$

In the context of energy harvesting systems, we are primarily interested in the long-term system behavior. Thus, the stationary solutions of Eq.(158) of mechanical part is obtained as:

$$p(a) = N_1 a \exp \left(-\frac{1}{16D} (3\zeta_3\omega_0^4a^4 + K_0a^2) \right), \quad (159)$$

where N_1 is the normalization constant expressed by

$$N_1 = \left| \frac{3\sqrt{D}\zeta_3\omega_0^4}{\sqrt{\pi D} \exp\left(\frac{1}{192} \frac{K_0^2}{D\zeta_3\omega_0^4}\right) \left(1 - \operatorname{erf}\left(\frac{K_0}{8\sqrt{3}\omega_0^2\sqrt{D}\zeta_3}\right)\right)} \right|, \quad (160)$$

with

$$K_0 = K_1 + K_2 + K_3$$

and

$$K_1 = \frac{8\omega_0^2\lambda^2(\zeta_m\beta\vartheta_e + (\beta^2 + \omega_0^2)\zeta_1)}{(\beta^2 + \omega_0^2)(\lambda^2 + \omega_0^2)},$$

$$K_2 = \frac{8\omega_0^2\lambda(\beta^2 + \omega_0^2)\zeta_e\vartheta_p}{(\beta^2 + \omega_0^2)(\lambda^2 + \omega_0^2)},$$

$$K_3 = \frac{8\omega_0^2(\zeta_m\beta\vartheta_e\omega_0^2 + (\beta^2\omega_0^2 + \omega_0^4)\zeta_1)}{(\beta^2 + \omega_0^2)(\lambda^2 + \omega_0^2)}.$$

Eq.?? can be rewritten in the potential form:

$$da = \left(-\frac{dU(a)}{da}\right) + \sqrt{\frac{D}{\omega_0^2}}d\eta_1(\tau)(a) \quad (161)$$

where $U(a)$ denote the effective potential of mechanical subsystem given by:

$$U(a) = -\frac{3}{32}\zeta_3\omega_0^2a^4 - \frac{1}{4}\left(\frac{\lambda^2\zeta_1 + \lambda\zeta_2 + \zeta_3}{(\lambda^2 + \omega_0^2)(\beta^2 + \omega_0^2)}\right)a^2 + \frac{D \ln(a)}{2\omega_0^2}. \quad (162)$$

Through a transformation from variables (a, θ) to the original variables (z, \dot{z}) , an expression for the stationary density function of (z, \dot{z}) can be derived from Eq.(159) as

$$p(z, \dot{z}) = \frac{1}{2\pi\omega_0 a}p(a), \quad (163)$$

by letting $a = z^2 + \frac{\dot{z}^2}{\omega_0^2}$, Eq.(163) becomes

$$p(z, \dot{z}) = \frac{N_1}{2\pi\omega_0} \exp\left(-\frac{1}{16D}\left(3\zeta_3\omega_0^4\left(z^2 + \frac{\dot{z}^2}{\omega_0^2}\right)^4 + K_0\left(z^2 + \frac{\dot{z}^2}{\omega_0^2}\right)^2\right)\right). \quad (164)$$

Thus, the expected value of the mean square voltage of the piezoelectric circuit and electric current of the magnetic circuit can be calculated following this formula:

$$\langle y^2 \rangle = \langle V_0^2 \rangle = \frac{\vartheta_p^2\omega_0^2}{\lambda^2 + \omega_0^2} \langle a^2 \rangle \quad (165)$$

with

$$\langle a^2 \rangle = \int_0^{+\infty} a^2 p(a) da. \quad (166)$$

Substituting Eq.(166) into Eq.(165), we obtain:

$$\langle y^2 \rangle = \frac{\vartheta_p^2 \omega_0^2}{\lambda^2 + \omega_0^2} \int_0^{+\infty} a^2 p(a) da = \frac{\vartheta_p^2 \sqrt{D} N_1 \Lambda}{2\sqrt{\pi}(\lambda^2 + \omega_0^2) K_4^2}. \quad (167)$$

Similarly

$$\langle \rho^2 \rangle = \frac{\vartheta_e^2 \omega_0^2}{\beta^2 + \omega_0^2} \int_0^{+\infty} a^2 p(a) da = \frac{\vartheta_e^2 \sqrt{D} N_1 \Lambda}{2\sqrt{\pi}(\beta^2 + \omega_0^2) K_4^2} \quad (168)$$

with

$$\Lambda = \pi K_0 \sqrt{K_4} \exp\left(\frac{1}{64} \frac{K_0^2}{DK_4}\right) \left(\operatorname{erf}\left(\frac{1}{8} \frac{K_0}{\sqrt{K_4 D}}\right) - 1\right) + 8\sqrt{\pi D} K_4 \quad (169)$$

and

$$K_4 = 3\zeta_3 \omega_0^4.$$

The average output power harvested by the hybrid system is estimated using this formula:

$$P_{hybrid} = \frac{\beta}{2T} \int_0^T y^2 d\tau + \frac{\lambda}{2T} \int_0^T \rho^2 d\tau. \quad (170)$$

Using the expressions of the mean square voltage of the piezoelectric circuit and electric current of the magnetic circuit, Eq.(170) become

$$P_{hybrid} = \beta \langle \rho^2 \rangle + \lambda \langle y^2 \rangle. \quad (171)$$

II.3.2.3 Stochastic bifurcations

Contrarily to the determinist bifurcation, stochastic bifurcation is characterized with a qualitative change of the stationary probability distribution (e.g. a transition from uni-modal to bimodal and vis versa) called phenomenological (p) bifurcation, or a sudden change of the lyapunov exponent called dinamical (D) bifurcation. It is also judicious to notice that, D bifurcation is a dynamical concept, which is similar in nature to determin-

Table 6: Parameters

Parameter	Value	Unit
c_1	0.001	Ns/m
c_3	4.5	Ns^3/m^3
k	0.05	N/m
L	10	H
R	20.5	Ω
m	0.04	kg
l_0	0.075	m
c_p	0.00005	F
R_p	10000	Ω
η	0.00025	N/V
z_0	0.017	m
l	0.0735	m
v_0	0.1	V

istic bifurcations, while p bifurcation is a static concept. This section aims at finding the condition for which we can observe the phenomenon of stochastic p-bifurcation of the harvester. By letting $\frac{\partial p(a)}{\partial a} = 0$, the extrema of the distribution Eq.(159) are the roots of equations:

$$1 - \frac{3}{4} \frac{\zeta_3 \omega_0^4 a_m^4}{D} - \frac{1}{8} \frac{K_0 a_m^2}{D} = 0 \quad (172)$$

a_m is the amplitude corresponding to the extremum of distribution Eq.(172) and m is the index number of the extremum. For a suitable choice of system parameters, the probability density function of the harvester can present one or two positive extrema (one minimum and one maximum). By taking $\zeta_3 > 0$, the positive root of Eq.(172) is $\sqrt{\frac{1}{12} \frac{-K_0 + \sqrt{192D\zeta_3\omega_0^4 + K_0^2}}{\zeta_3\omega_0^4}}$, and then the probability density function in Eq.(159) has a maximum. However, by taking $\zeta_3 < 0$, there are two real positive roots of Eq.(172) for a convenient choice of system parameters:

$\sqrt{\frac{1}{12} \frac{-K_0 + \sqrt{192D\zeta_3\omega_0^4 + K_0^2}}{\zeta_3\omega_0^4}}$ and $\sqrt{-\frac{1}{12} \frac{K_0 + \sqrt{192D\zeta_3\omega_0^4 + K_0^2}}{\zeta_3\omega_0^4}}$ whose the shape is similar to a crater.

The physical parameters used in the simulation are given in Tables 6.

II.4 Numerical simulation techniques

The numerical simulations of the deterministic and stochastic nonlinear differential equations are in the center of many of the advanced scientific computations. In the goal to predict the system response of the different models proposed in this thesis, we integrate numerically the mathematical models of the different physical models proposed. This heading, present the different numerical technique used.

II.4.1 Algorithms of the numerical simulations

II.4.1.1 Fourth-order Runge-Kutta (RK4) algorithm for ordinary differential equations

In numerical analysis, the Runge-Kutta methods are an important family of implicit and explicit iterative methods for the approximation of solution of ODEs. These techniques were co-developed in 1901 by the German mathematicians Carl Runge and Martin Wilhelm Kutta [159] to solve ODE numerically. In the Runge-Kutta family, the most used method is the fourth-order one, which extends the idea of the mid-point method. Consider an initial value problem specified as follows

$$\frac{\partial u}{\partial t} = f(t, u), u(t_0) = u_0 \quad (173)$$

Here, u is an unknown function of time t which we would like to approximate. To have the quantity u at time $t + \Delta t$ (Δt being the time step) knowing its value at time t , the

RK4 method process as follows:

$$\begin{aligned}
 u(t + \Delta t) &= u(t) + \frac{1}{6}(K_1 + 2K_2 + 2K_3 + K_4) \\
 K_1 &= \Delta t f(t, u); K_2 = \Delta t f\left(t + \frac{\Delta t}{2}, u + \frac{K_1}{2}\right); \\
 K_3 &= \Delta t f\left(t + \frac{\Delta t}{2}, u + \frac{K_2}{2}\right); \\
 K_4 &= \Delta t f(t + \Delta t, u + K_3)
 \end{aligned} \tag{174}$$

The RK4 presented above can be easily extended to a set of ODEs and for instance, in this thesis, the differential equations describing the time evolution of nonlinear electromechanical energy harvester will be solved numerically in that way.

II.4.1.2 Euler-Maruyama algorithm

Following [160], the probabilistic response of multidimensional vibration system under noisy random excitations in general can be considered to be governed by the following set of first-order stochastic differential equations:

$$\dot{X}(t) = f(X(t)) + g(X(t))\xi(t) \tag{175}$$

where $X(t)$ is the random response vector process, $f(X(t))$ and $g(X(t))$ are determinist function vector. $\xi(t)$ is a noisy random vector.

A scale autonomous Stochastic Differential Equations (SDE) can be rewritten in the integral form as:

$$\dot{X}(t) = X_0 + \int_0^t f(X(s))ds + \int_0^t g(X(s))d\xi(s), 0 \leq t \leq T \tag{176}$$

Here, f and g are scalar functions and the initial condition X_0 is a random variable. The second integral on the right-hand side of Eq.(176) is to be taken with respect to

Brownian motion, as discussed in the previous section, and we assume that the Itô version is used. The solution $X(t)$ is a random variable for each t . We do not attempt to explain further what it means for $X(t)$ to be a solution to Eq.(176) instead we define a numerical method for solving Eq.(176), and we may then regard the solution $X(t)$ as the random variable that arises when we take the zero step size limit in the numerical method. It is usual to rewrite Eq.(176) in differential equation form as:

$$dX(t) = f(X(t))dt + g(X(t))d\xi(t), X(0) = X_0, 0 \leq t \leq T \quad (177)$$

This is nothing more than a compact way of saying that $X(t)$ solves Eq.(176). To keep with convention, we will emphasize the SDE form Eq.(177) rather than the integral form Eq.(176). (Note that we are not allowed to write $\frac{d\xi(t)}{dt}$, since Brownian motion is nowhere differentiable with probability 1). If $g \equiv 0$ and X_0 is constant, then the problem becomes deterministic, and Eq.(177) reduces to the ordinary differential equation

$$\frac{dX(t)}{dt} = f(X(t)) \quad (178)$$

with $X(0) = X_0$. To apply a numerical method to Eq.(177) over $[0, T]$, we first discretize the interval. Let $\Delta t = \frac{T}{L}$ for some positive integer L , and $\tau_j = j\Delta t$. Our numerical approximation to $X(\tau_j)$ will be denoted X_j . The Euler-Maruyama (EM) method takes the form:

$$X_j = X_{j-1} + f(X_{j-1})\Delta t + g(X_{j-1})(W(\tau_j) - W(\tau_{j-1})), j = 1, 2, \dots, L \quad (179)$$

To understand where Eq.(179) comes from, notice from the integral form Eq.(176) that

$$X(\tau_j) = X(\tau_{j-1}) + \int_{\tau_{j-1}}^{\tau_j} f(X(s))ds + \int_{\tau_{j-1}}^{\tau_j} g(X(s))dW(s) \quad (180)$$

Each of the three terms on the right-hand side of Eq.(179) approximates the corre-

sponding term on the right-hand side of Eq.(180). We also note that in the deterministic case ($g \equiv 0$ and X_0 constant), Eq.(179) reduces to Euler's method. The Euler algorithm or more precisely the Euler-Maruyama algorithm is a generic algorithm generally used for stochastic differential equation simulations [161].

II.4.1.3 Box-Muller algorithm

The Box-Muller algorithm is an important tool to generate two independent standard Wiener processes ξ_1 and ξ_2 . To do this, we consider four independent random number between 0 and 1 with equal probability a_1, a_2, b_1 and b_2 . Then, the two independent standard Wiener processes are generate as

$$\xi_1 = \sqrt{-4\Delta t \ln(a_1)} \cos(2\pi b_1) \quad \text{and} \quad \xi_2 = \sqrt{-4\Delta t \ln(a_2)} \cos(2\pi b_2). \quad (181)$$

II.4.1.4 Algorithm for generating standard Wiener process

We consider a standard Wiener process (or standard Brownian motion) $\psi(t)$ that depends continuously on $t \in [0, T]$ and satisfies the above mentioned properties. For computational purposes, it is useful to consider discretized Brownian motion, where $\psi(t)$ is specified at discrete t values, i.e. the interval $[0, T]$ is divided into a segments $0 = t_0 < t_1 < \dots < t_{N-1} < t_N = T$. We thus set $\Delta t = T/N$ for some positive integer N and let $\psi(t_i)$ with $t_i = i\Delta t, \psi_0 = \psi(t_0) = 0$. The simulation of discretized Brownian motion over $[0, T]$ is as follows: (1) Generate a new random number r from the standard normal distribution; (2) set i to $i+1$; (3) set $\psi(t_i) = \psi(t_{i-1}) + r\sqrt{\Delta t}$; (4) if $i \leq N$, iterate from steps (1).

II.4.2 Stochastic resonance phenomenon

Stochastic resonance (SR) is a counter-intuitive phenomenon where the presence of noise in a nonlinear system is essential for optimal system performance. It cannot occur in a linear system (linear in this sense means that the output of the system is a linear

transformation of the input of the system). It occurs in many systems including neurons, electronic circuits and the energy harvesting systems. Many aspects have been hotly debated by scientists for nearly 30 years, with one of the main questions being whether biological neurons use stochastic resonance [162]. The term stochastic resonance was first used in the context of noise enhanced signal processing in 1980 by Roberto Benzi [162], at the NATO International School of Climatology to explain the periodicity of earths ice ages. It is well known in the literature that, the eccentricity of the orbit of the earth varies with a periodicity of about 10^5 years, but according to current theories the variation is not strong enough to cause a dramatic climate change. Stochastic resonance (SN) is a physical phenomenon where large vibration occurs when a weak sinusoidal force is applied to a bi-stable or tri-stable system. The phenomenon of the stochastic resonance requires three basic ingredients: (a) an energetic activation barrier such as the double or triple potential well of a bi-stable system or tri-stable, (b) a weak coherent input such as a periodic signal, and (c) a source of noise that is inherent to the system. Given these features, the response of the system undergoes resonance-like behaviors as a function of the noise level, hence the name stochastic resonance. There are a lot of technique to characterize the SN [163] such as Signal-to-noise ratio (SNR), Mean Residence Time (TMR) and probability distribution of residence times ($P(\text{TR})$).

II.4.3 Mathematical formula for determining the mean amplitude response in this thesis

Most studies of vibration energy harvesters have considered either sinusoidal excitations and Gaussian white noise excitations. This is the case of the study conducted in this thesis. Stochastic averaging method is mainly due to the reduction of dimensions of the FPK equation while the essential behavior of the system is retained. It is a convenient approximation approach to predict the stationary response of nonlinear stochastic systems. For the stochastic system described by Eq.(127) the extrema of the probability density function are the continuation of the limit cycles of the corresponding

deterministic system [164]. Noise can shift the frequency of limit cycles [165], increase the spectral bandwidth and induce a rapid decay of the limit cycle's auto-correlation [166]; such quasi-cycles are described by circular orbits whose radius is modulated by an Ornstein-Uhlenbeck process [167]. Stationary states could be viewed as a formal approximation of sample paths that stay close to the limit cycle.

In this subsection we discuss the impact of the combination of the deterministic and random signal on the system performance. The deterministic excitation is expressed as $(E_0 \cos(\omega\tau))$. It is well known in the literature that the adding of the coherent signal to the random excitation can give rise to the stochastic resonance phenomenon which can increase the bandwidth of the harvester and consequently, improve the system performance [168, 169]. Let us remind that the system of equation obtained in the second model are nonlinear and should exhibit many frequency components. For the large value of time ($\tau \mapsto \infty$), the asymptotic solution of Eq.127(a) can be given as follows:

$$\langle z(\tau) \rangle_{as} = \sum_j x_m(j\Omega) \cos[j\Omega\tau - \varphi_m(j\Omega)] \quad (182)$$

where j is the positive real number, $x_m(j\Omega)$ and $\varphi_m(j\Omega)$ are the mean response amplitude and phase lag respectively at the frequency $j\Omega$. In this manuscript, we limit the study in the first harmonic i.e. $j = 1$. The mean amplitude response is defined as [131, 168]:

$$z_m(\omega) = \sqrt{A_s^2 + A_c^2} \quad (183)$$

where A_s and A_c are the sine and cosine components of the Fourier coefficients defined by:

$$A_c = \frac{2}{nT} \int_0^{nT} x(\tau) \cos(\omega\tau) d\tau \quad (184)$$

$$A_s = \frac{2}{nT} \int_0^{nT} x(\tau) \sin(\omega\tau) d\tau \quad (185)$$

where n is the integer number. In this work, $n = 300$, while $T = \frac{2\pi}{\omega}$ is the period of the harmonic excitation. In the purpose to know the degree of optimization of the hybrid model with respect to the piezoelectric circuit, we compute the increase rate using this formula:

$$op_{max} = \frac{P_{hybrid} - P_{piezoelectric}}{P_{piezoelectric}} \times 100[\%] \quad (186)$$

where P_{hybrid} and $P_{piezoelectric}$ are the output power harvested by the hybrid system and piezoelectric circuit. In the simulation, we took 100 realizations.

II.4.4 Bifurcation diagram, Poincaré maps, time history and power spectral density

The definition of bifurcation diagram is based on the sudden change of topological properties of the phase portraits. It indicates a range where values can be found to obtain regular or chaotic behavior. An understanding of the way in which dynamical systems evolve in time is facilitated by considering the concepts of phase space and time series. These concepts were developed in the late 19th century by Ludwig Boltzmann, Henri Poincaré and Willard Gibbs [170]. Phase portraits are basically used to appreciate the shape of trajectories in the phase space on which the system evolves in time. They may be sufficient to state whether the dynamic is regular or not. Nevertheless, they are not practical when the phase space is of dimension greater than two. Moreover, we cannot easily distinguish roughly between chaotic states and some quasi-periodic ones using only phase portraits. The power spectral density is also useful here to determine, in particular, the aspect of the energy in the case of regular periodic motion. A broad one shows chaotic motion.

II.4.5 Bifurcation diagrams

A dynamical system, in the abstract sense, consists of two things: a set of states through which we can describe the evolution of a system, and a rule for that evolution. Although this viewpoint is very general and may be applied to almost any system that evolves with time, often the fruitful and conclusive results are achievable when we pose some mathematical structure on the dynamical system, for example, we often assume the set of states form a linear space with nice geometric properties and the rule of evolution has some order of regularity on that space. The prominent examples of such dynamical systems are amply found in physics, where we use differential equations to describe the physical variables change in time. In this note, we specially focus on dynamical systems that can be represented as

$$\dot{x} = f(x), \quad (187)$$

where x is the state, an element of the state space $S \subset \mathfrak{R}^n$, and $f : S \mapsto \mathfrak{R}^n$ is a vector field on the state space. Occasionally, we will specify some regularity conditions for f like being smooth or a few times differentiable. We also consider dynamical systems given by the discrete–time map

$$\dot{x}^{t+1} = T(x^t), t \in Z \quad (188)$$

where x belongs to the state space $S \subset \mathfrak{R}^n$, $T : S \mapsto S$ is the dynamic map and t is the discrete time index. Just like the continuous-time system in (187), we may need to make some extra assumptions on T . The discrete time representation of dynamical system does not often show up in physical systems, but we can use it to represent continuous–time systems, for example, through discrete-time sampling. This representation also has the benefit of being more practical because the data collected from dynamical systems almost always comes in discrete–time samples.

Bifurcation analysis is the study of changes in the qualitative behavior of all the tra-

jectories due to the changes in vector field f or the map T . For example, if we add some forcing term to the vector field f , a stable fixed point might turn unstable or a limit cycle might appear out of the blue. A physical example is the evolution of incompressible flows given by Navier-Stokes equations: increasing the Reynolds number may fundamentally change the flow solution from steady to unsteady, or from laminar to turbulent.

Here is the traditional approach to study of dynamical systems: We first discover or construct a model for the system in the form of (187) or (188). Sometimes, if we are very lucky, we can come up with analytical (or approximate) solutions and use them to analyze the dynamics, by which, we usually mean finding the attractors, invariant manifolds, imminent bifurcations and so on. A lot of times, this is not possible and we have to use various estimates or approximation techniques to evaluate the qualitative behavior of the system, for example, construct Lyapunov functions to prove the stability of a fixed point. But most of the times, if we want a quantitative analysis or prediction, we have to employ numerical computation and then extract information by looking at a collection of trajectories in the state space.

This approach has contributed the most to our knowledge of dynamical and physical systems around us, but it is falling short in treating the high-dimensional systems that have arisen in various areas of science and technology. A set of classic examples, which regularly arises in physics, is the set of systems that are governed by partial differential equations. In these systems, the state space is infinite-dimensional and the numerical models that we use may have up to billions of degrees of freedom. Some examples of more recent interest include climate system of the earth, smart cars and buildings, power networks, and biological systems with interacting components like neural networks. The first problem with the traditional approach is that simulating the evolution of trajectories for these systems is just devastating due to the large size of the problem. Moreover, unlike the two- or three-dimensional system, the geometric objects in the state space are difficult to realize and utilize. The second problem is the uncertainty in the models or even the sheer lack of a model for simulation or analysis. As a result, the field of dynamical analysis has started shifting toward a less model-based and more

data-driven perspective.

II.4.6 Poincaré maps

Poincaré map section is a tool for graphical study of dynamic properties in the phase space. So we can analyze the dynamic systems by studying their section of punched. Making a Poincaré map section amounts to cutting the trajectory in the phase space, in order to study the intersections of this trajectory with, for example in dimension three, a plane. If the plane is suitably chosen, the trajectory will cross in the same direction at a sequence of instants not necessarily constant, at points p_k . We will retain, in numerical calculus that the coordinate points p_k in the plan. We then go from a dynamic system in continuous time to a dynamic system with discrete time. This makes it possible to reduce the size of the system by one unit, which contributes to savings in computation time. Thus, the Poincaré map section makes it possible to distinguish.

II.4.7 Power Spectral Density

Spectral analysis considers the problem of determining the spectral content (i.e., the distribution of power over frequency) of a time series from a finite set of measurements, by means of either nonparametric or parametric techniques. The power spectral density is also useful here to determine, in particular, the aspect of the energy in the case of regular periodic motion. Spectral analysis finds applications in many diverse fields. In vibration monitoring, the spectral content of measured signals give information on the wear and other characteristics of mechanical parts under study. In economics, meteorology, astronomy and several other fields, the spectral analysis may reveal hidden periodicity in the studied data, which are to be associated with cyclic behavior or recurring processes. In speech analysis, spectral models of voice signals are useful in better understanding the speech production process, and in addition can be used for both speech synthesis (or compression) and speech recognition. In radar and sonar systems, the spectral contents of the received signals provide information on the location

of the sources (or targets) situated in the field of view. In medicine, spectral analysis of various signals measured from a patient, such as electrocardiogram (ECG) or electroencephalogram (EEG) signals, can provide useful material for diagnosis. In seismology, the spectral analysis of the signals recorded prior to and during a seismic event (such as a volcano eruption or an earthquake) gives useful information on the ground movement associated with such events and may help in predicting them. Seismic spectral estimation is also used to predict subsurface geologic structure in gas and oil exploration.

II.4.8 phase space and time series methods

An understanding of the way in which dynamical systems evolve in time is facilitated by considering the concepts of phase space and time series. These concepts were developed in the late 19th century by Ludwig Boltzmann, Henri Poincaré and Willard Gibbs [170]. Phase space is a very efficient tool in the study of dynamical systems in the sense that it presents the global behavior of these systems. Although time history hardly reveals any qualitative features of the system dynamics, it provides a foundation for the study of the qualitative behavior of the dynamics of the systems. The phase space method is a technique for constructing and analyzing solutions of dynamical systems by solving time-dependent differential equations. It is a space in which all possible state of the system are represented, corresponding to one unique point in the phase space. The method consists of first rewriting the equations as a system of differential equations that are first-order in time, by introducing additional variables. The original and the new variables form a vector in the phase space. The solution then becomes a curve in the phase space, parameterized by time. The curve is usually called a trajectory or an orbit where the horizontal axis gives the position and the vertical one the velocity. This phase-space trajectory of a dynamical system can be used as an indicator to determine whether its motion is chaotic. Beside, a time series is a sequence of data points, measured typically at successive points in time spaced at uniform time intervals. Time series are very frequently plotted via line charts. The horizontal axis presents the time

while the vertical one is the position.

When we consider the possible forms trajectories can take in a two-dimensional phase space, we see that they are very limited: we can have fixed points, curves that end at or spiral toward or away from fixed points (without crossing each other), perhaps closed loops (which describe periodic orbits), or simply families of curves that neither terminate nor cross. Under suitable conditions these lead to an extremely strong dependence on initial conditions and the resulting chaotic motion is called deterministic chaos.

II.4.9 The 0-1 test for chaos

Recently a new test for chaos has been developed by Gottwadt and Melbourne [171]. It is used in this work to corroborate the result given by the bifurcation diagram. Unlike the usual method that is the calculi of the maximum exponent of Lyapunov, this method is applied directly to the data series and there is no construction of the phase space. Most often, the dimension at the origin of the dynamic system and the form of the equations intervening in it are not important. In input, we have the series of the data and in exit we have 0 and 1, depending on the case of the non-chaotic or chaotic dynamics respectively. The 0-1 test is also applicable to graphs, ordinary equations, partial differential equations. This test is general and applicable to all systems.

To quantify the results obtained, we use the 0 – 1 test for chaos detection [171, 172]. This test combines both spectral and statistical properties of the system and can distinguish different types of dynamics of the system by computing a number $K \in \{0, 1\}$. First of all, a change coordinates (x, \dot{x}) to a new set (p, q_1) is required

$$p(n) = \sum_{j=1}^n \tilde{x}_j \cos(jc), q_1(n) = \sum_{j=1}^n \tilde{x}_j \sin(jc) \quad (189)$$

where $\tilde{x} = [\tilde{x}_1, \tilde{x}_2, \tilde{x}_3, \tilde{x}_4, \dots]$ is the discrete time series sampled from the originally simulated x using one-fourth of excitation period, while c is a constant ($c \in [0, \pi]$). The Mean Square Displacement (MSD) is defined as in ref.[173, 174]:

$$MSD(c, j) = \frac{1}{n-j} \sum_{i=1}^{n-j} \{ [p(i+j) - p(i)]^2 + [q_1(i+j) - q_1(i)]^2 \} \quad (190)$$

where j is the integer number varying as follows:

$$\frac{n}{100} \leq j \leq \frac{n}{10}.$$

Thus, the asymptotic growth rate of MSD is given as:

$$K(c) = \frac{Cov [j, MSD(c, j)]}{\sqrt{Cov [j, j] \cdot Cov [MSD(c, j), MSD(c, j)]}} \quad (191)$$

where $Cov(x, u)$ is the covariance of the series x, u . In this thesis, we let ($x = j$ and $u = MSD(c, j)$). The covariance of x, u is defined as:

$$cov [x, u] = \frac{1}{N} \sum_{n=1}^N (x(n) - \bar{x})(u(n) - \bar{u}) \quad (192)$$

where \bar{x} and \bar{u} are the average value of x and u , N is the element number of \bar{x} and \bar{u} are given by:

$$\bar{x} = \frac{1}{N} \sum_{n=1}^N x(n), \bar{u} = \frac{1}{N} \sum_{n=1}^N u(n). \quad (193)$$

II.5 Discrete schematic of the different models

II.5.1 Investigating Bifurcations and Chaos in Nonlinear electromechanical energy harvesters with fractional inductance

The numerical schematic of the first model use the Runge-Kutta algorithm. By letting

$$\begin{aligned}
\dot{x} &= u \\
\dot{u} &= -\mu_1 u - \mu_3 u^3 - \rho x - \lambda x^3 + \vartheta_m(1 + \gamma \cos(2\omega\tau))v + E_0 \cos(\omega\tau) \\
\dot{z} &= v \\
\dot{v} &= -\frac{1}{\beta}(v + \mu_e z + \vartheta_e(1 + \gamma \cos(2\omega\tau))u).
\end{aligned} \tag{194}$$

The discrete equations can be written as:

$$\begin{aligned}
x_{k+1} &= x_k + \frac{1}{6}(l_1 + 2l_2 + 2l_3 + l_4) \\
u_{k+1} &= u_k + \frac{1}{6}(p_1 + 2p_2 + 2p_3 + p_4) \\
z_{k+1} &= z_k + \frac{1}{6}(k_1 + 2k_2 + 2k_3 + k_4) \\
v_{k+1} &= v_k + \frac{1}{6}(r_1 + 2r_2 + 2r_3 + r_4).
\end{aligned} \tag{195}$$

II.5.2 Discrete schematic of the nonlinear analysis of a Nonlinear electromechanical energy harvesters with fractional

In the goal to provide the discrete schematic of Eq.(84), it is necessary to decompose the system (Eq.(84)) into a set of equations of lower degree:

$$D_{\tau}^1 x(\tau) = u(\tau)$$

$$D_{\tau}^1 u(\tau) = -\mu_1 u(\tau) - \mu_3 u(\tau)^3 - \varrho x(\tau) - \lambda x(\tau)^3 + \vartheta_m (1 + \gamma \cos(2\omega\tau)) z(\tau) + E_0 \cos(\omega\tau)$$

$$D_{\tau}^k z(\tau) = y(\tau)$$

$$D_{\tau}^1 z(\tau) = -\beta y(\tau) - \mu_e z(\tau) - \vartheta_e (1 + \gamma \cos(2\omega\tau)) u(\tau). \quad (196)$$

The Newton-Leipnikov methods are an important family of implicit and explicit iterative methods for the approximation of solution of (FO). From Eq.(84), the discrete equations are given by

$$x(k) = x(t_{k-1}) + u(t_{k-1})h \quad (197)$$

$$y(t_{k-1}) = [z(t_{k-1}) + \sum_{i=1}^{n-1} c_j^{(\alpha)} z(t_{k-1})] h^{-\alpha} \quad (198)$$

$$u(t_k) = [-\mu_1 u(t_{k-1}) - \mu_p u(t_{k-1})^p - \varrho x(t_{k-1}) - \lambda x(t_{k-1})^3] \quad (199)$$

$$+ \vartheta_m (1 + \gamma \cos(2\omega(t_{k-1}))) z(t_k) + E_0 \cos(\omega(t_{k-1})) h + u(t_{k-1})$$

$$z(t_k) = z(t_{k-1}) + (-\beta y(t_{k-1}) - \mu_e z(t_{k-1}) - \vartheta_e (1 + \gamma \cos(2\omega(t_{k-1})))) h \quad (200)$$

where h is the integration step and the coefficients $c_j^{(\alpha)}$ satisfy the following recursive relations:

$$c_0^{(\alpha)} = 1, c_j^{(\alpha)} = \left(1 - \frac{1 + \alpha}{j}\right) c_{j-1}^{(\alpha)}. \quad (201)$$

II.5.3 Discrete schematic of the probabilistic distribution and stochastic P-bifurcation of a hybrid energy harvester under Gaussian white noise

We also use in this model, the Euler algorithm. By introducing the new variable $\dot{z} = u$, Eq.(127), the general form of nonlinear stochastic differential equations can be rewritten in the form

$$\begin{aligned} \dot{z} &= u \\ \dot{u} &= -\zeta_1 u - \zeta_3 u^3 - \omega_1^2 z - \alpha_2 z^2 - \alpha_3 z^3 - \zeta_e y - \zeta_m \rho + \sqrt{2D}\xi(\tau) \end{aligned} \quad (202)$$

$$\dot{y} = -\lambda y + \vartheta_p u$$

$$\dot{\rho} = -\beta \rho + \vartheta_e u.$$

The discrete equations can be written as:

$$\begin{aligned} z_{n+1} &= z_n + u_n \Delta\tau \\ u_{n+1} &= u_n - (\zeta_1 u_n + \zeta_3 u_n^3 + \omega_1^2 z_n + \alpha_2 z_n^2 + \alpha_3 z_n^3 + \zeta_e y_n + \zeta_m \rho_n) \Delta\tau + \xi_n(\tau), \\ y_{n+1} &= y_n + (-\lambda y_n + \vartheta_p u_n) \Delta\tau, \\ \rho_{n+1} &= \rho_n + (-\beta \rho_n + \vartheta_e u_n) \Delta\tau, \end{aligned} \quad (203)$$

where ξ_n is a sequence of random numbers distributed normally by the Box-Mueller

algorithm.

II.6 Conclusion

In this chapter we have presented different mathematical techniques and numerical methods used to study the dynamic behavior of the Energy harvesters model proposed in this thesis. We have presented some analytical and numerical methods used. These methods are used to obtain the results presented in chapter III. we used the harmonic balance method to approximate the analytical amplitude response of the fractional model. Besides, the stochastic average method is used to build the Fokker-Planck-Kolmogorov equation which is necessary to study the P-bifurcation phenomenon in the hybrid model under white noise. For the numerical simulations, RK4 algorithm has been described in the case of harmonic perturbations whereas the Euler forward procedure with Box-Muller algorithm was used in that of the stochastic disturbances. The next chapter deals with the results and discussions.

RESULTS AND DISCUSSION

III.1 Introduction

In this chapter, we present and discuss the main results of our work using numerical simulations. The first part examines the impact of the fractional inductance, the non-linear damping as well as the amplitude of the parametric coupling on the output power. Then, we deal with the effect of external white noise excitation on the non-linear dynamics of the system through the mean square response. A second section is dedicated to the study of stochastic bifurcation under Gaussian white noise through the hybrid model, a comparison of the different output power generated by the system is presented. Finally, we study the phenomenon of stochastic p-bifurcation and stochastic resonance.

III.2 Nonlinear Electromechanical Energy Harvesters with Fractional Inductance

III.2.1 Potential configuration

This potential $V(x)$ depends on the values of the parameters μ_3 and σ . We can have a mono-stable or a bistable configuration according to the system parameters. Fig.33 shows the potential of the mechanical part under two configurations: mono-stable and bistable for two values of linear coefficient of the stiffness. In the following, we discuss the system performance under these two configurations.

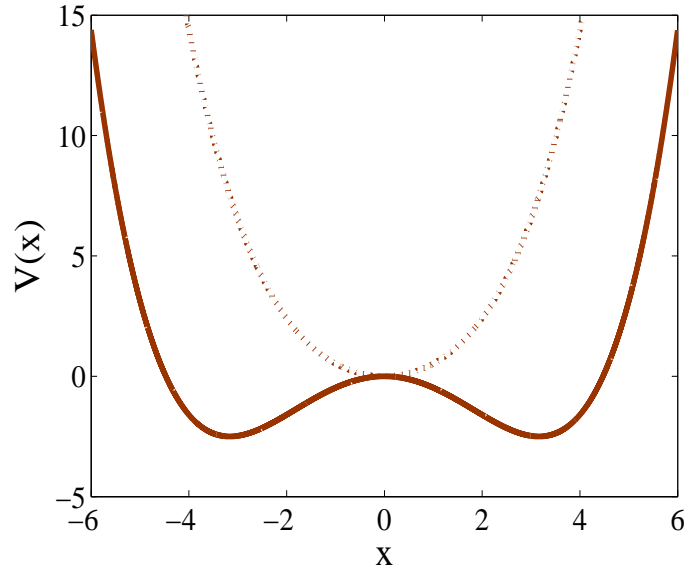


Figure 33: Potential of the system (84) for $\lambda = 0.1$, the dot line obtained for $\varrho = 1.0$ and solid line for $\varrho = -1.0$.

III.2.2 Amplitudes of the harmonic oscillatory states

We must recall that the analytical analysis of the amplitude of harmonic oscillatory states is described by Eqs.(106) and (107). Our aim is to analyse the effects of the higher nonlinearity and fractional properties on the dynamics response of the electromechanical energy harvesters.

Figs.34(a) and (c) show the comparison between the results obtained from analytical and numerical investigations. From these figures we notice the agreement between the two results. The effects of the fractional derivative κ on the amplitude are depicted in Figs.34(b) and 34(d). We notice that, the amplitude of the mechanical vibration are almost unchanged when κ increases (see Fig.34(b)). However, in Fig.34(d), we observe that, the enhancing of the fractional order derivative leads to increase the output power change. We displayed on Figs.35(a)-(d), the mechanical and electrical response versus frequency ω . In Figs.35(a) and 35(c), the impact of the amplitude of the parametric coupling is presented. We notice in Fig.35(a) that when γ increases, the the response of mechanical part is not change. However, in Fig.35(c), an increase of γ leads to enhance

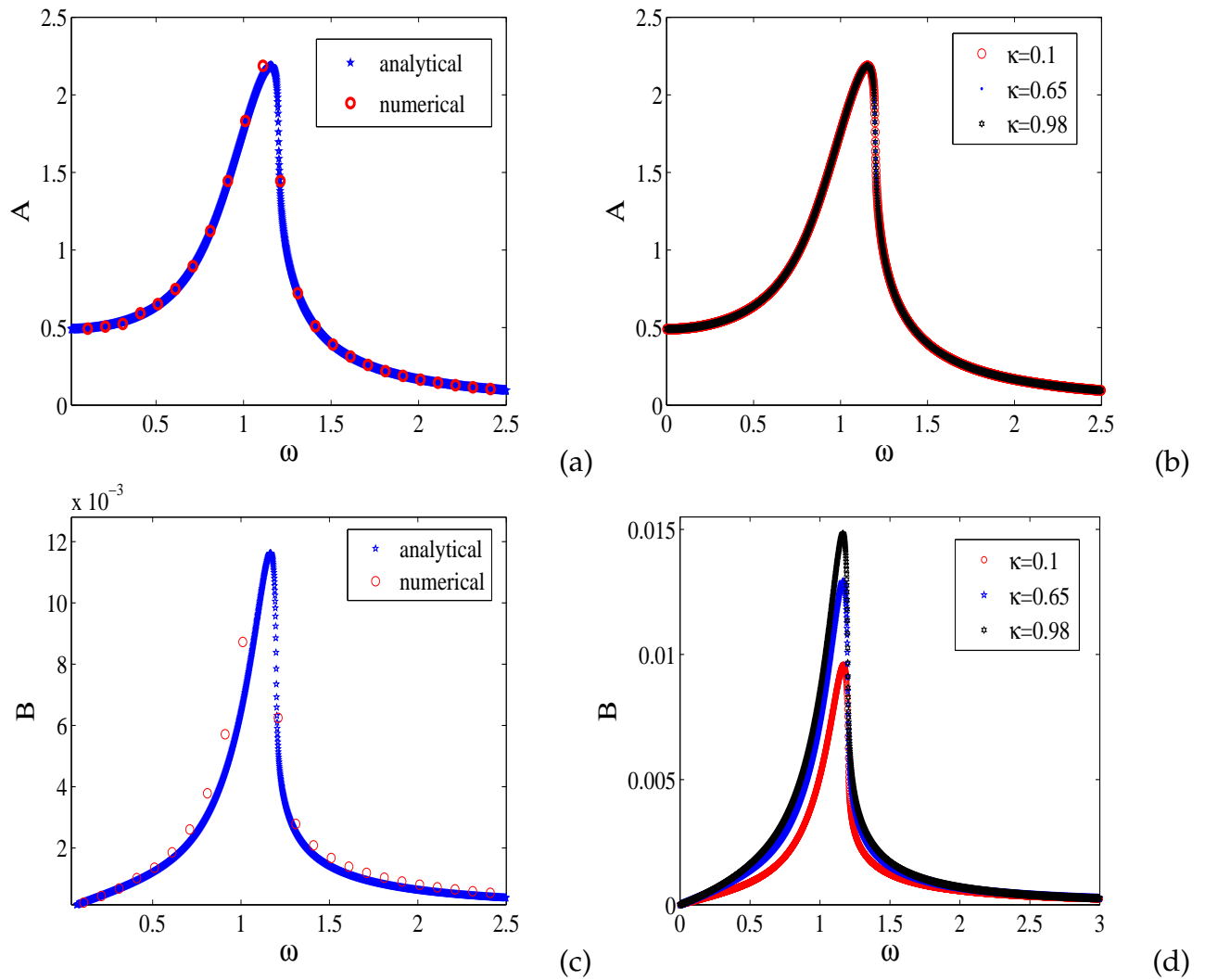


Figure 34: Amplitudes response-curves of the driving frequency ω and $E_0 = 0.5$, $\kappa = 0.25$ with the parameters $\lambda = 0.1$, $\mu_1 = 0.1$, $\mu_3 = 0.018$, $\gamma = 0.5$, $\vartheta_m = 0.76$, $\vartheta_e = 0.0056$, $\mu_e = 0.96$ and $\varrho = 1.0$.

the output charge, and consequently, an enhancing of the output power. Figs.35(c) and 35(d) show the impact of the linear ($\mu_1 \neq 0, \mu_3 = 0$), cubic ($\mu_3 \neq 0, \mu_1 = 0$) and polynomial damping ($\mu_1 \neq 0, \mu_3 \neq 0$) upon the electrical response. It emerges from these results that, the cubic and polynomial damping induced a reducing of harvested energy. Fig.36 show the impact of κ, γ, λ and damping upon the output power. We notice in Figs.36(a)-(b) that, when κ and γ increase, the output power increases. Similar result is observed in Fig.36(c). When the coefficient of the cubic nonlinearly increases. However, in Fig.36(d), an increase of the degree of the damping gives rise to the small output power.

We show in Fig.37, the comparison between the mechanical and electrical power for three value of γ . We notice in Figs.37(a-c) that for a fixed value of the γ , the resonance occurs for the same value of the frequency. For $\gamma = 0.9$, the real maximum electric power is obtained at $\omega = 1.17Hz$ and is about $2.7mW$, for the corresponding input power(the mechanical power) equal to $0.19W$. We show in Fig.37(d) the efficiency conversion of the system. We notice that an increase of the γ leads to the increase of efficiency. We also notice in this figure that the efficiency is optimum when the resonance phenomenon occurs ($\omega = 1.17Hz$), this give rise to the maximum charge and output power (Figs.37(a) and (c)).

Several works have been published in the field of energy harvesting using electromechanical system. However, several authors have been used the standards materials [176, 177] and other, the materials exhibiting the fractional properties. In contrarily in the previous works [178, 115], a novelty of this present work is the introduction of the fractional inductor in the electrical subsystem. Kwuimi et al.[115] have been showed that for some value of amplitude of the excitation force, the voltage present the antagonistic phenomenon ie an increase of fractional order derivative leading to increase or decrease the output voltage. In addition, Oumbé et al.[178] have been showed that, Energy harvesting system with fractional order viscoelastic properties has better performance at resonance. Indeed, small value of fractional derivative leads to large value of the maximum output voltage. On major observation in our study reveal that, the system

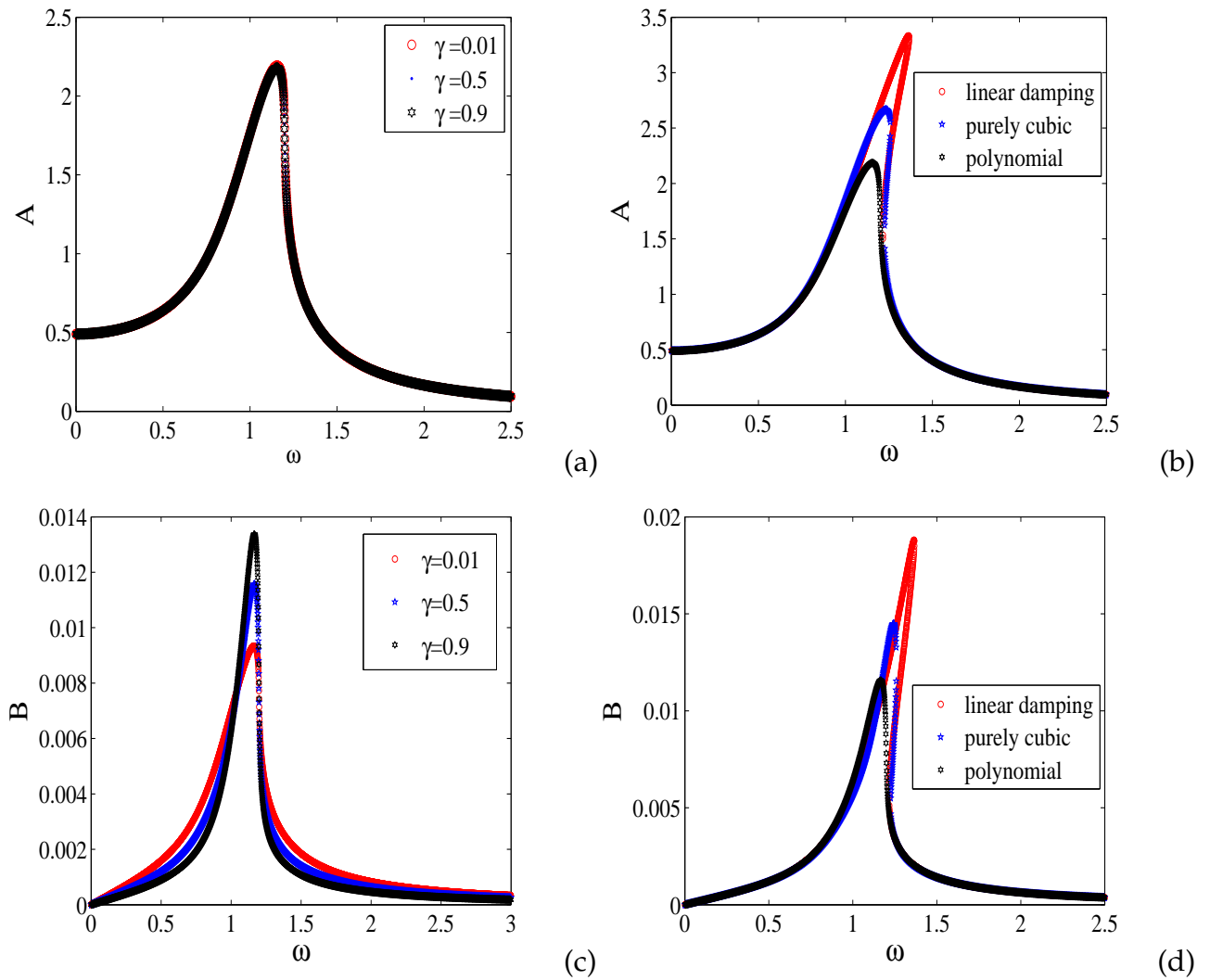


Figure 35: Amplitudes response-curves of the driving frequency ω and $E_0 = 0.5$, $\kappa = 0.25$ with the parameters $\lambda = 0.1$, $\mu_1 = 0.1$, $\mu_3 = 0.018$, $\gamma = 0.5$, $\vartheta_m = 0.76$, $\vartheta_e = 0.0056$, $\mu_e = 0.96$ and $\varrho = 1.0$.

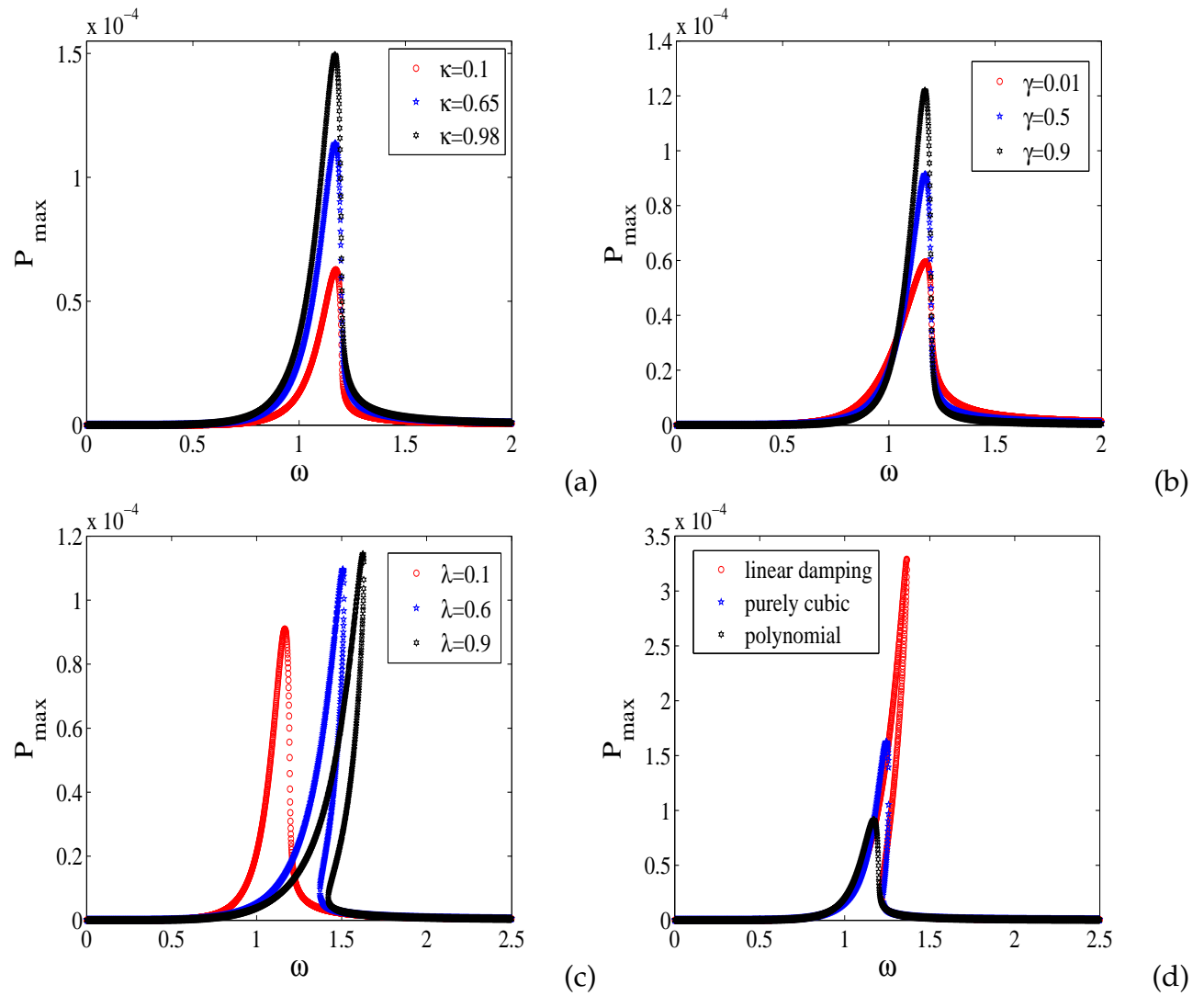


Figure 36: Output electric power as function of the driving frequency with the parameters $\lambda = 0.1$, $\mu_1 = 0.1$, $\mu_3 = 0.018$, $\gamma = 0.5$, $\vartheta_m = 0.76$, $\vartheta_e = 0.0056$, $\mu_e = 0.96$, $\varrho = 1$, $E_0 = 0.5$ and $\kappa = 0.25$.

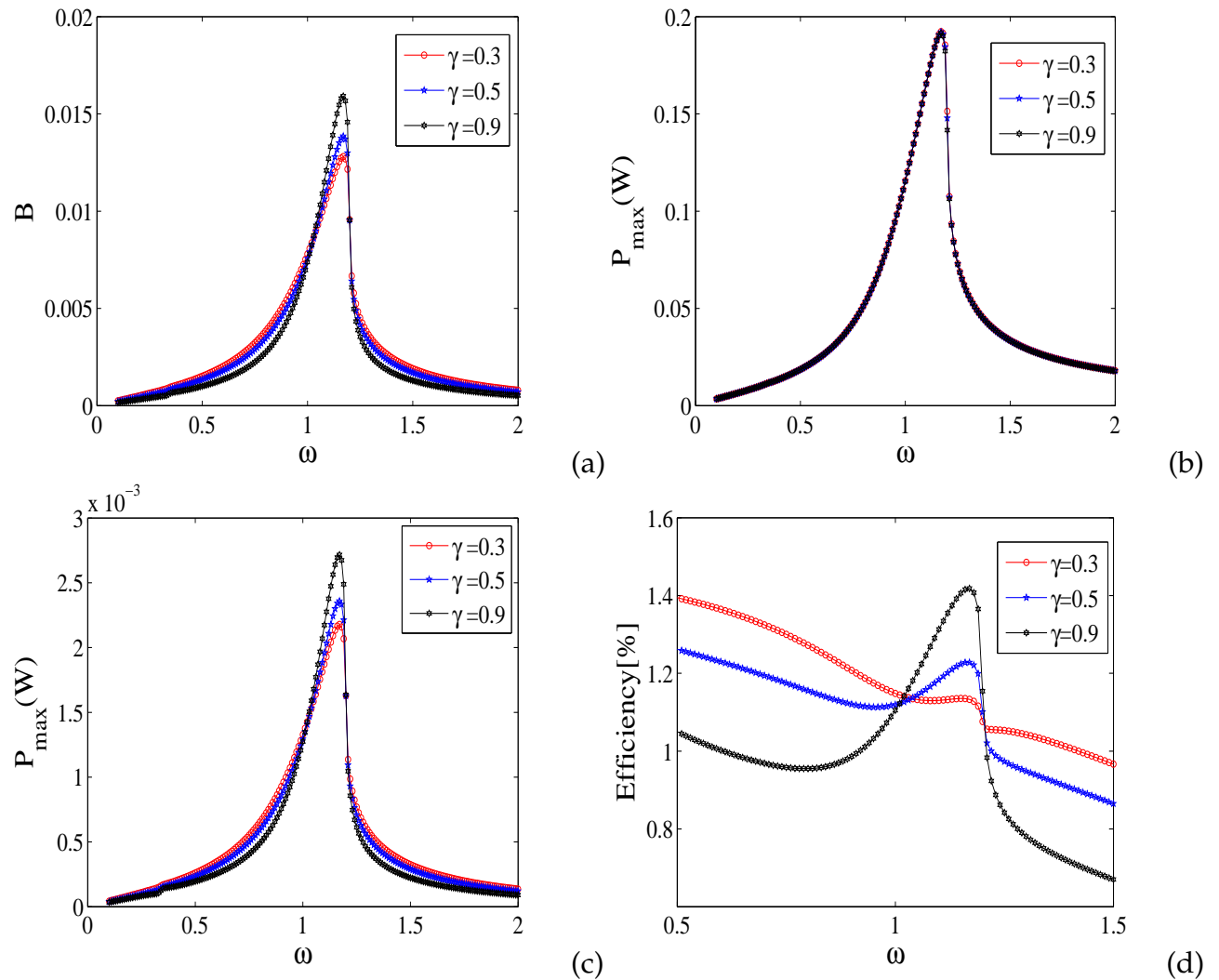


Figure 37: Effects on the amplitude of parametric coupling γ on the amplitude response curve B and output power with the parameters $\lambda = 0.1$, $\mu_1 = 0.1$, $\mu_3 = 0.018$, $\vartheta_m = 0.76$, $\vartheta_e = 0.0056$, $\mu_e = 0.96$, $\varrho = 1$, $E_0 = 0.5$ and $\kappa = 1.0$. (a) amplitude response B , (b) mechanical input, (c) output electric power and (d) efficiency.

performance is optimum for the high value of the fractional order derivative (see Fig.36). However, for $\kappa \in]0, 1[$, while the output power increase when κ go up, the standards inductor ($\kappa = 1$) is better than the inductor exhibiting the fractional properties. It would be advantageous in this research field, to use a standard inductance. The performance of the system depends on the degree of nonlinear damping. In addition, the steady-state solution under the same conditions except $\mu_3 = 0$ (i.e., no nonlinear damping) is also plotted in Fig.35. We notice that, the existence of non-negligible nonlinear damping has a strong impact on the frequency response of the system, specifically on the locations of the jump points. In particular, for the polynomial damping only the cubic term provides power harvested while the linear term is considered as a loss. When a polynomial damping is taken into account only, the cubic term is considered as power harvested. As shown in Figure 36(d), the polynomial damping allows us to store less energy than the linear and the cubic damping. This is due to the fact that the linear term is loss power. The effects of the amplitude of the parametric modulation are found in the response curves and output power. The amplitude of the parametric coupling can contribute to increase the harvested output voltage. The performance of the system depends also on the degree of nonlinearity of the potential and the electrical dissipation.

III.2.3 Numerical simulation of bifurcation diagram, 0–1 test, Poincaré maps, Times History and Power Spectral Density

This section discusses numerical simulations of an incommensurate fractional-order system. The dynamic behaviors of the system, are analyzed by evaluating the phase portrait, bifurcation diagrams, power spectral density and 0 – 1 test.

The main purpose of this section is to show the qualitative behavior of the solution of the extended electromechanical model. The system generates a complex behavior that directly depends on the amplitude and frequency of the modulated force. We now use the numerical simulations for examining the complicated behavior of Eq.(84). The initial conditions used in the numerical simulation are ($x(0) = 1.0, \dot{x}(0) = 0.0, z(0) = 0.0$).

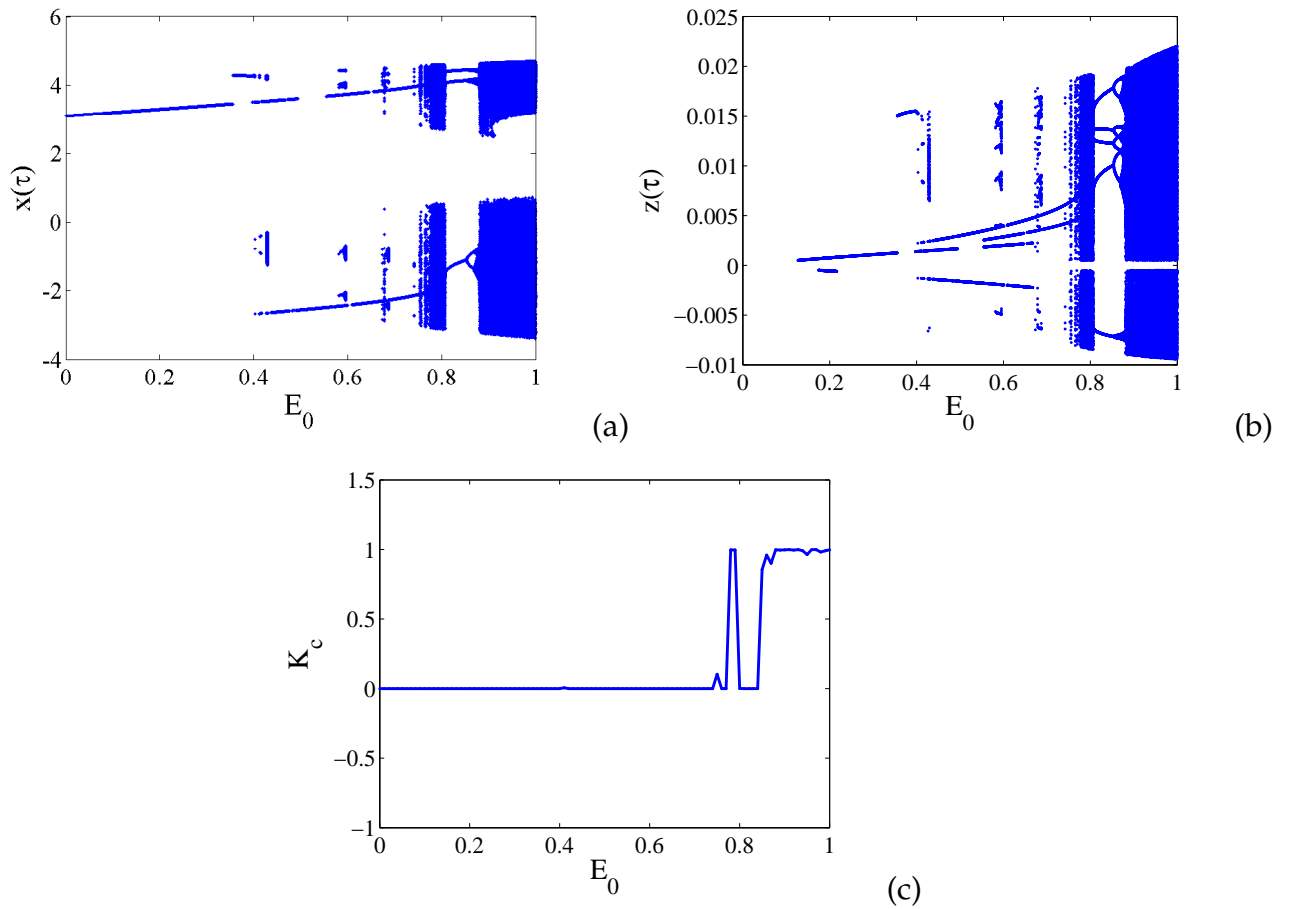


Figure 38: Bifurcation diagram (a)-(b) and asymptotic growth rate k_c (c) curves for system (84) for E_0 varying with the parameters $\lambda = 0.1$, $\mu_1 = 0.1$, $\mu_3 = 0.018$, $\gamma = 0.5$, $\vartheta_m = 0.76$, $\vartheta_e = 0.0056$, $\mu_e = 0.96$, $\omega = 1.0$, $\varrho = -1.0$ and $\kappa = 1.0$.

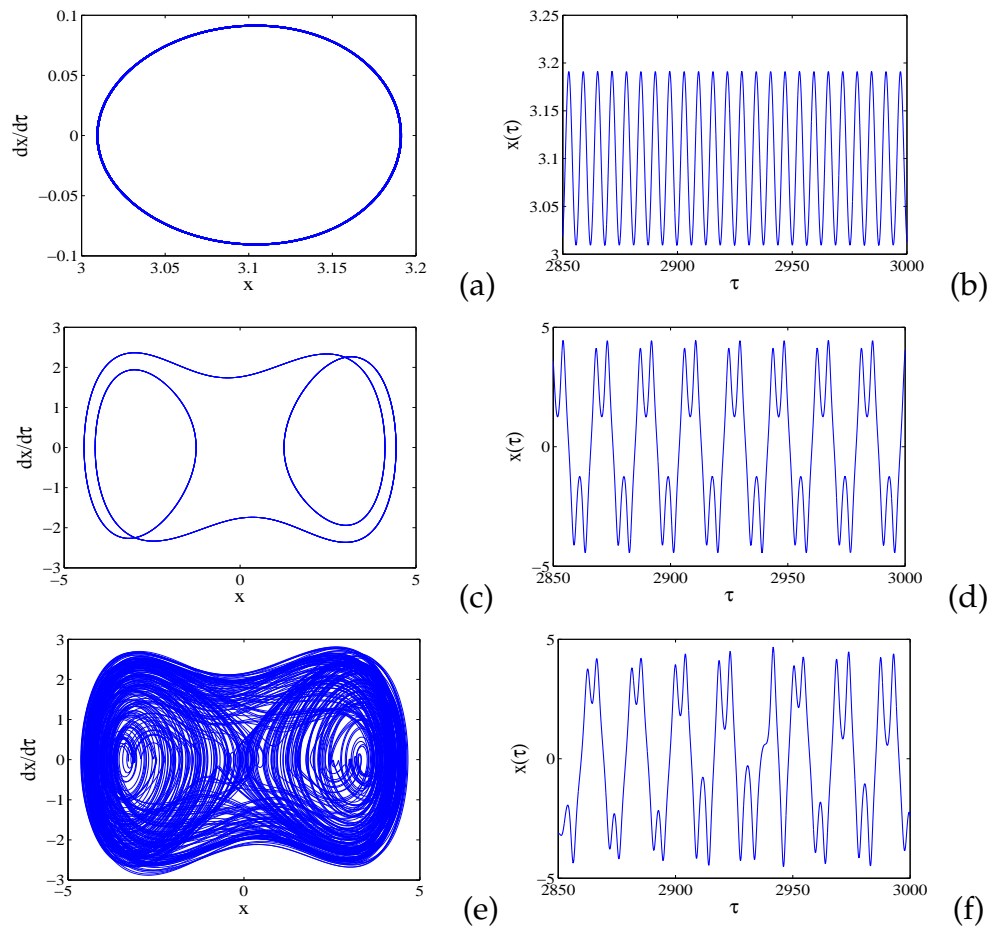


Figure 39: Phase portrait and times history of the bistable mechanical system for $\kappa = 1$; (a-b) $E_0 = 0.0911$; (c-d) $E_0 = 0.83$; (e-f) $E_0 = 0.92$. The parameters used are : $\lambda = 0.1$, $\mu_1 = 0.1$, $\mu_3 = 0.018$, $\gamma = 0.5$, $\vartheta_m = 0.76$, $\vartheta_e = 0.0056$, $\mu_e = 0.96$, $\varrho = -1.0$ and $\omega = 1.0$.

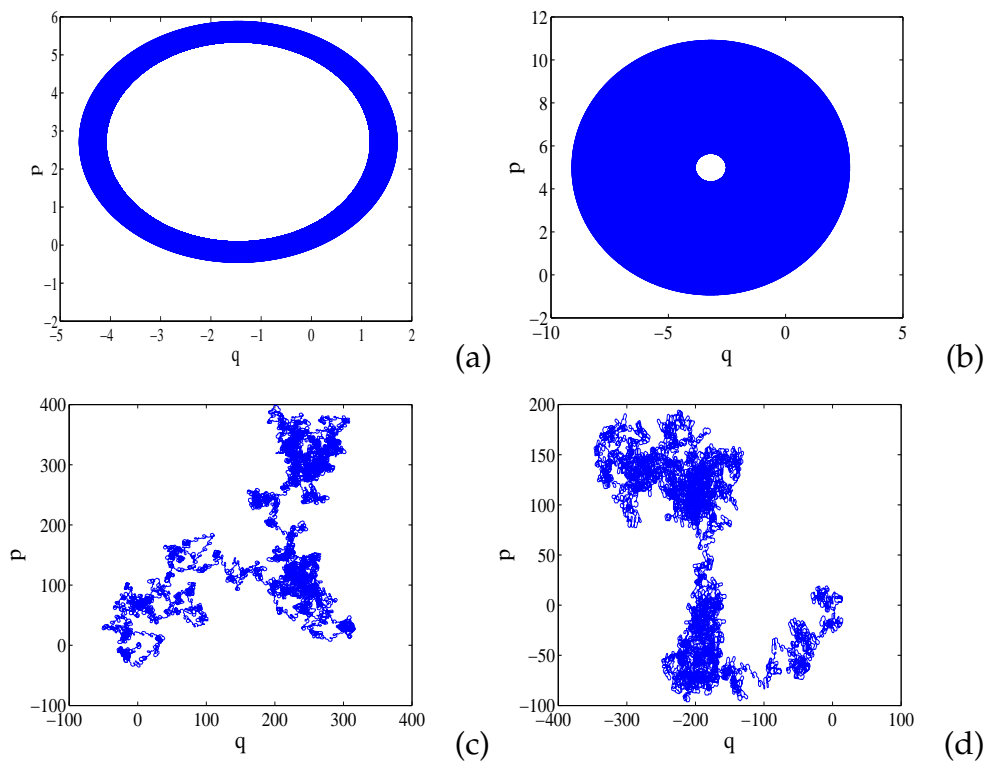


Figure 40: Phase portraits of the mechanical part for crossing well dynamics as function of E_0 for $\kappa = 1$ and the value of Fig.38: (a) $E_0 = 0.09$, (b) $E_0 = 0.8$, (c) $E_0 = 0.9$, (d) $E_0 = 0.96$, with the parameters $\lambda = 0.1$, $\mu_1 = 0.1$, $\mu_3 = 0.018$, $\gamma = 0.5$, $\vartheta_m = 0.76$, $\vartheta_e = 0.0056$, $\mu_e = 0.96$, $\omega = 1.0$, $\varrho = -1.0$ and $\kappa = 1.0$.

The fourth-order Runge-Kutta algorithm is used to check the threshold of harmonic excitation amplitude for onset of possible chaos obtained for system (84). Fig.38 shows a representative bifurcation diagram and the variation of the corresponding 0 – 1 test versus the amplitude E_0 of mechanical part. A bifurcation diagram is displayed in Fig.38(a), showing the dependence of the system response when E_0 increases. We observe in this figure the regions corresponding to regular motion ($E_0 \in [0, 0.78]$), the region corresponding to period-3 orbit ($E_0 \in [0.8, 0.88]$) and regions corresponding to the chaotic states ($E_0 \in [0.78, 0.799] \cup [0.88, 1]$). In the goal to validate the result obtained in Fig.38(a), the 0-1 test is provided (Fig.38(b)). The result obtained (Fig.38(b)) confirms this obtained via the bifurcation diagram (Fig.38(a)).

The results are presented on the portraits and times series, which are generated by sampling the system stroboscopically with a fixed period as mentioned before. The portraits for different values of parameter E_0 are shown in figure 39. It is seen from these figures that the motion of the system is periodic when $E_0 = 0.0911$ and chaotic when $E_0 = 0.92$. Explicitly it may be seen from figure 39 that, (1) when $E_0 = 0.0911$, the portrait is closed curved and as shown in figure 38(a), the systems motion is quasi-periodic. (2) when $E_0 = 0.83$, the portrait is still a closed curve, but the curve has a double well, and as shown in figure 38(a), the system shows a two-frequency quasi-periodic motion. (3) when $E_0 = 0.92$, relative to figure 38(a), the portrait is a strange attractor, and chaotic motion takes place in the system.

The phase portrait provided in Fig.40, allow us to know the different regimes in which the system involves. We observe a diffusive (Figs.40(c)- 40(d)) and bounded dynamic (Figs.40(a)-(b)) of the $p(n)$ and $q_1(n)$ in the phase space (p, q_1) . Let us notice that, a diffuse dynamic of $p(n)$ and $q_1(n)$ corresponds to the chaotic motion, which increases the bandwidth of oscillator there by allowing to enhance to output power. However, when the dynamic of $p(n)$ and $q_1(n)$ is bounded in the phase space, the motion is regular. In such condition, the energy storage by the mechanical oscillator is concentrated within its harmonic or super-harmonic.

We provide in Fig.41-43, the poincaré map, the time series and its corresponding

power spectral density (PSD). We notice in Figs.41(a) and 41(c) that the regular motion. These result are confirmed in Figs.41(b) and 41(d) by plotting PSD. Only one peak located to the dimensionless frequency ($f_{pic} = 0.16$) is observed for the mechanical subsystem. However, in Fig.41(d) three peaks are observed. In Figs.42(a) and 42(c), the motion of the system is quasi-period characterized by three harmonics. The agreement between these results and those obtained in Fig.42(b) is observed. Fig.42(d) shows tree peaks. In this condition, the energy harvested by the system is high than obtained when the dynamic of the system is periodic. In Figs.43(b) and 43(d), the system exhibits the chaotic motion giving rise to the large bandwidth of the frequency allowing to harvest more energy. These latters results are confirmed in Figs.43(b) and 43(d) which present many harmonics.

III.2.4 Numerical simulation of the system Performance under the Gaussian white Noise

The harmonic excitation is used in the previous section to investigate the system response. However, in the real environment, wave oscillations, atmospheric turbulence and seismic shocks, the vibration source are not harmonic but exists under a random form ref[179, 180, 182]. Thus we replace in the previous section, the harmonic excitation by a Gaussian white noise verifying the statistic properties:

$$\langle \xi(\tau)\xi(t + \tau') \rangle = 2D\delta(\tau), \tag{204}$$

$$\langle \xi(\tau) \rangle = 0,$$

where $2D$ is the intensity of noise and $\delta(\tau)$, the Dirac function. The impact of fractional order derivative κ and γ upon the output power expressed in terms of mean square voltage $\langle z^2 \rangle$ and mean displacement is presented in Figs.44(a)-(d). Let us notice that in Figs.44(a)-(b), when $x \simeq 0$, the system oscillates by hopping symmetrically through the potential barrier. However, $x \simeq 1$ indicates that the oscillating system is strapped in

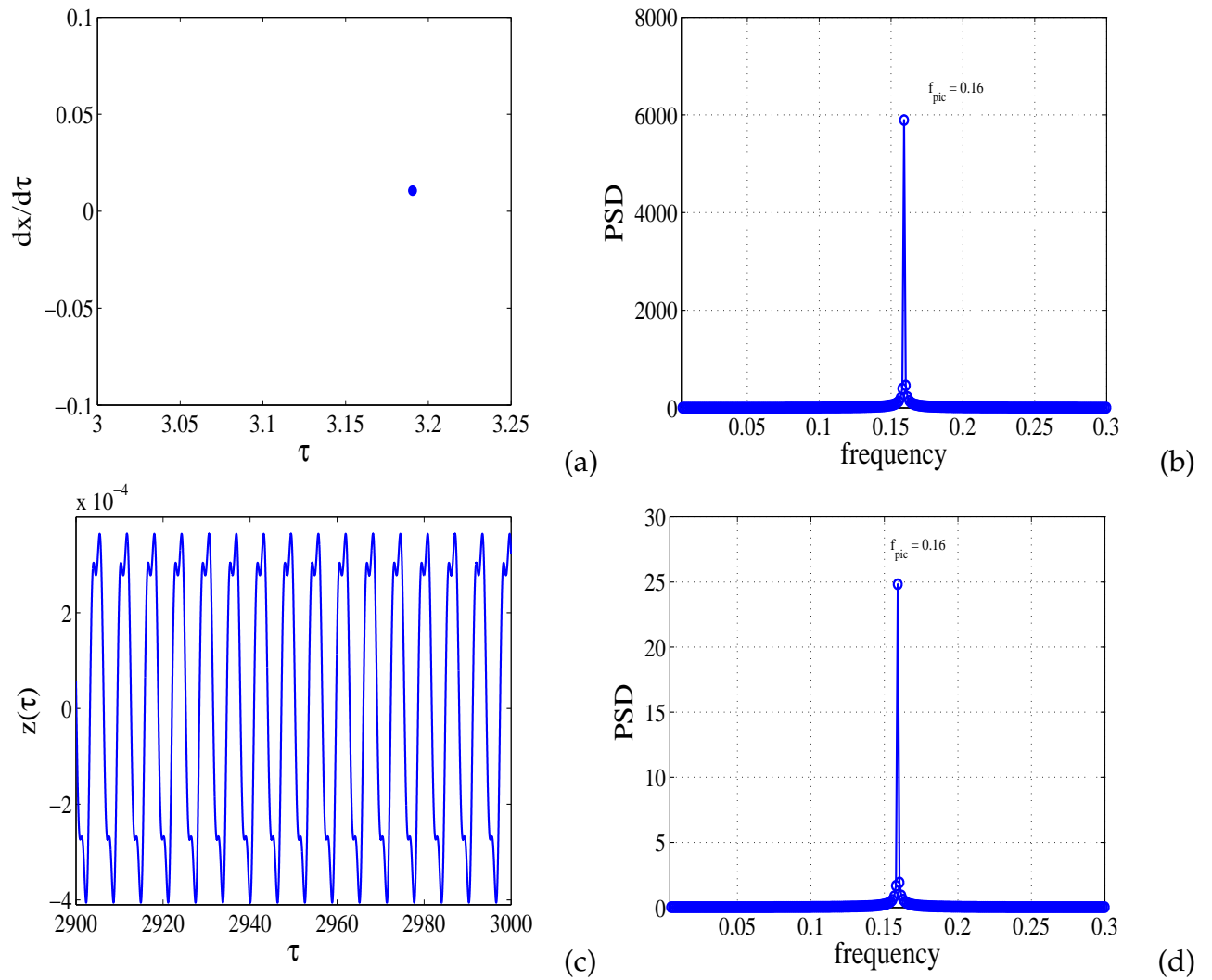


Figure 41: Poincaré maps, time history and power spectral density from system (84) for $\kappa = 1$ and $E_0 = 0.0911$ with the parameters: $\lambda = 0.1$, $\mu_1 = 0.1$, $\mu_3 = 0.018$, $\gamma = 0.5$, $\vartheta_m = 0.76$, $\vartheta_e = 0.0056$, $\mu_e = 0.96$, $\varrho = -1.0$ and $\omega = 1.0$.

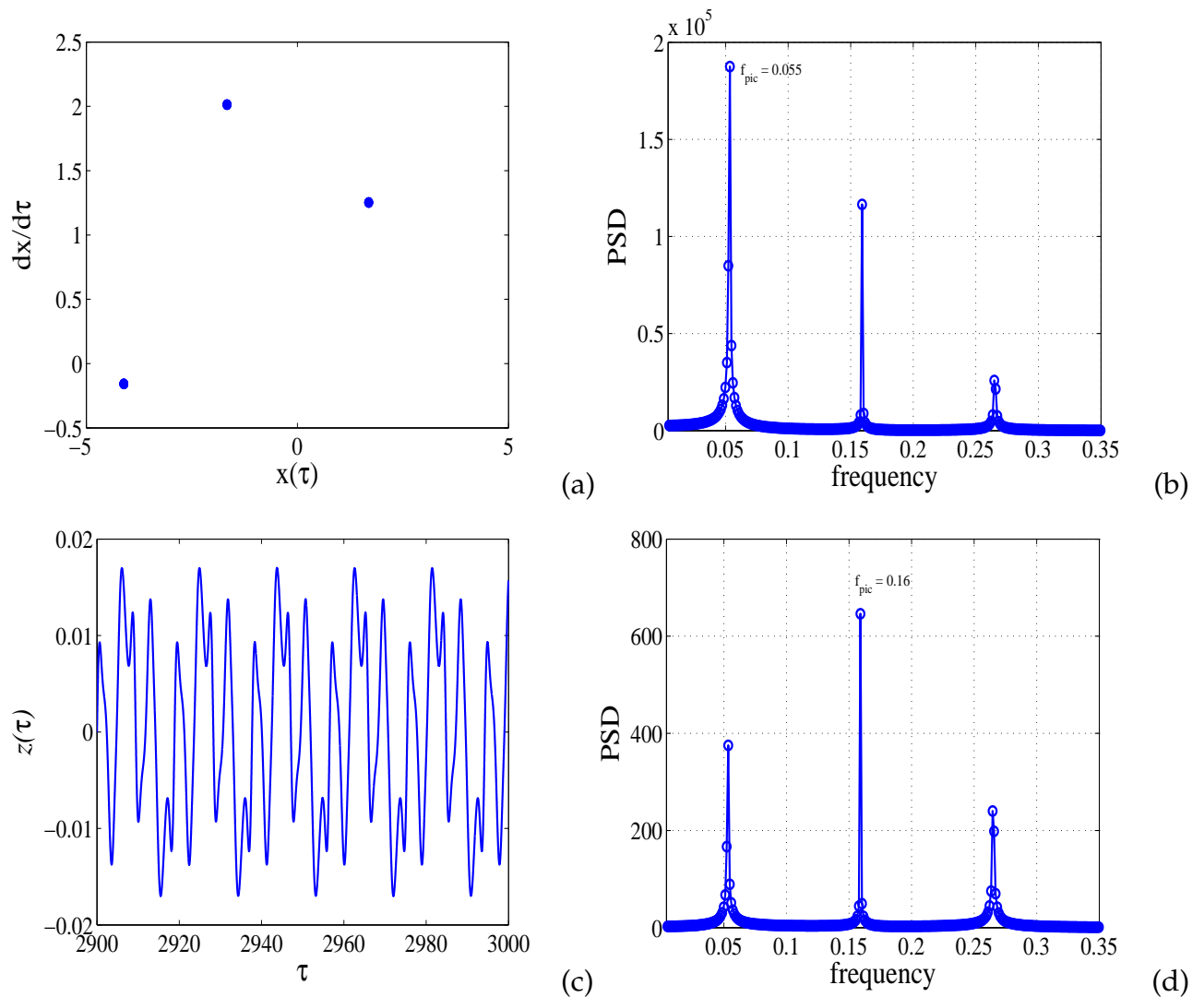


Figure 42: Poincaré maps, time history and power spectral density from system (84) for $\kappa = 1$ and $E_0 = 0.8284$ with the parameters: $\lambda = 0.1$, $\mu_1 = 0.1$, $\mu_3 = 0.018$, $\gamma = 0.5$, $\vartheta_m = 0.76$, $\vartheta_e = 0.0056$, $\mu_e = 0.96$, $\varrho = -1.0$ and $\omega = 1.0$.

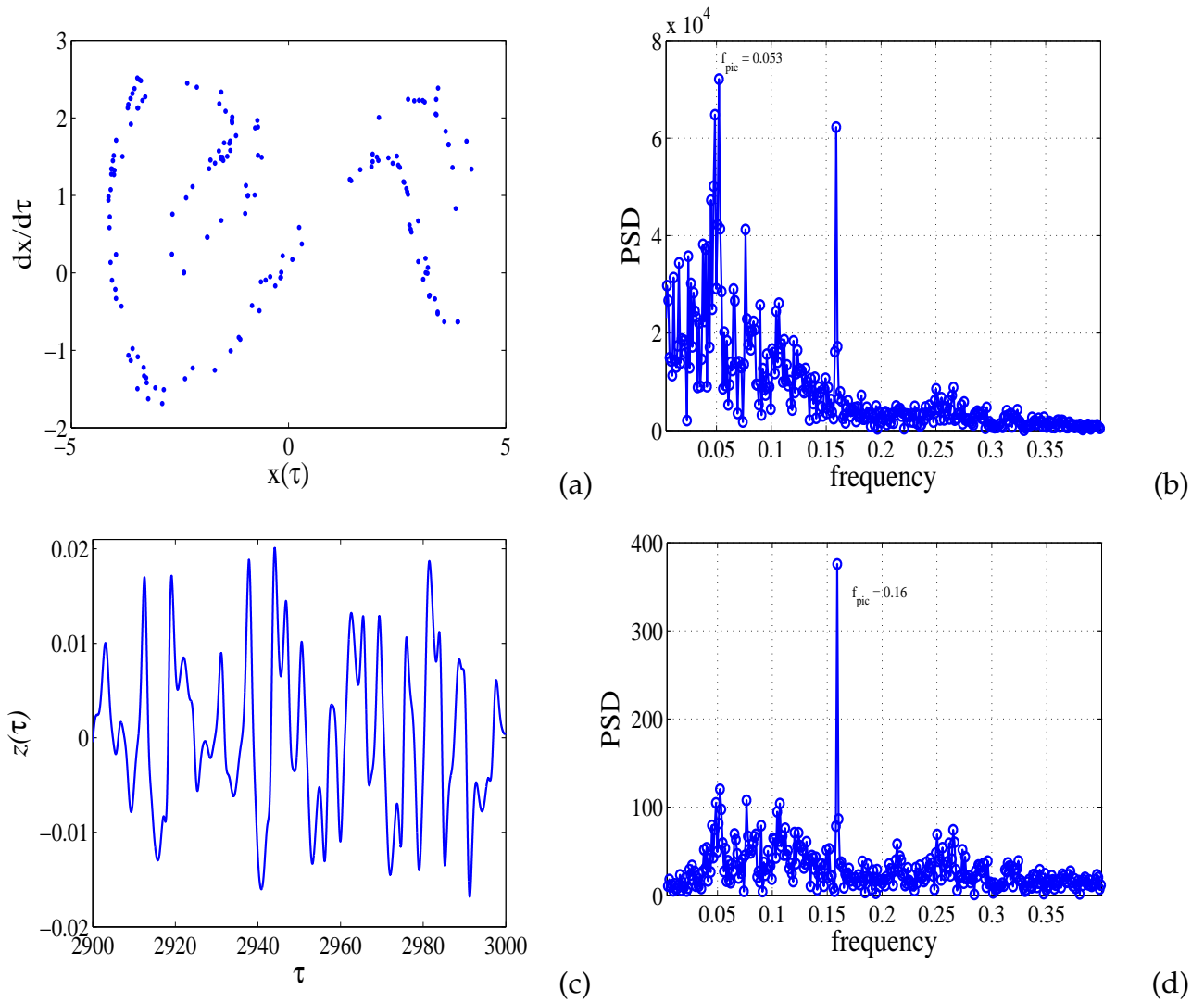


Figure 43: Poincaré maps, time history and power spectral density from system (84) for $\kappa = 1$ and $E_0 = 0.9318$ with the parameters: $\lambda = 0.1$, $\mu_1 = 0.1$, $\mu_3 = 0.018$, $\gamma = 0.5$, $\vartheta_m = 0.76$, $\vartheta_e = 0.0056$, $\mu_e = 0.96$, $\varrho = -1.0$ and $\omega = 1.0$.

one of the potential wells. Figs.44(c)-(d), the output power versus noise intensity for three values of fractional order derivative κ and amplitude of the parametric coupling γ . Because of the increased values of mean square current there will be enhancement of the energy harvested. The value of the noise intensity at which the mean square current begins to increase rapidly can be adjusted by varying the parameters κ and γ . Or for a given noise intensity the parameters κ and γ can be suitably found to maximize the value of the harvested power.

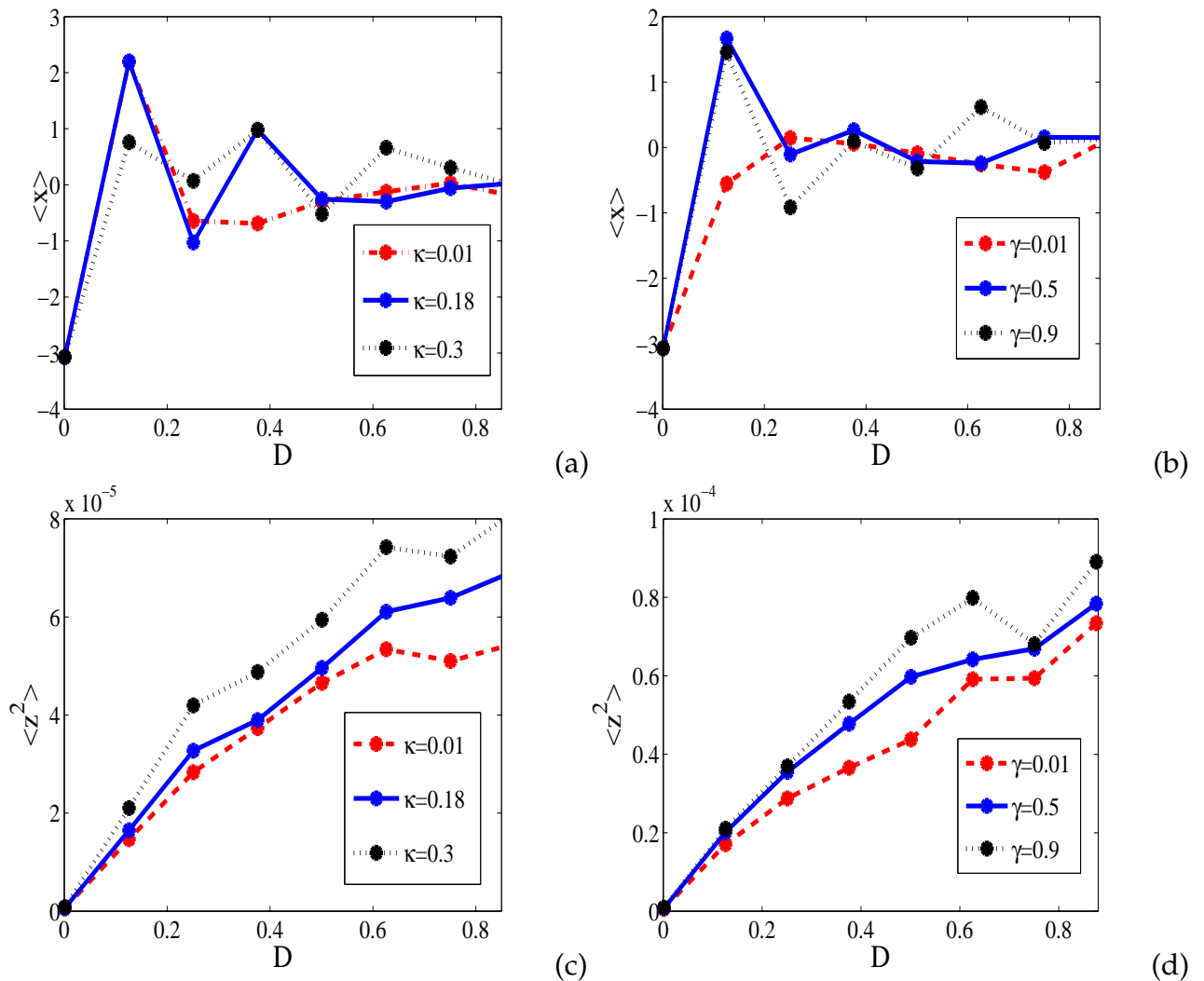


Figure 44: Means square of the system with the parameters $\lambda = 0.1, \mu_1 = 0.1, \mu_3 = 0.018, \vartheta_m = 0.76, \vartheta_e = 0.0056, \mu_e = 0.96, \varrho = -1.0$ and $\omega = 1.0$.

III.2.5 Discussion

The harmonic balance method (HBM) is the one of the best approximative analytical method of the coupled dynamical system. It is advantageous for providing an efficient analytical framework to assess steady-state dynamics. The inconvenient is inherent in the assumption that the system response is the superposition of a number of harmonics, and therefore the fidelity of the method is limited to the size of the truncated series. The nonlinear damping enhances the bandwidth of the harvester by reducing the maximal amplitude of the vibration.

The conventional models used to describe the flux linking the coil and self inductance fails in accurately describing the real behaviour of such circuits. The conventional model consisting of an inductor, an iron loss resistor and a copper resistor only provides a satisfactory description of coils with small eddy-current and hysteresis losses. Coils with significant losses are better described by the fractional model [15]. Currently, a great deal of research has been reported on fractional order inductance and its applications.

The utilization of the inductance exhibiting fractional properties in the energy scavenging research field is a promising solution to optimize the harvested energy [115]. For the best choice of the self inductance, the energy harvested by the system can be improved.

In contrast to the usual technique of evaluating the Maximum Lyapunov Exponent that requires phase-space reconstruction, the $0 - 1$ test is a method is applied directly to the times series data. The input is the time series data and the output is 0 or 1 depending on whether the dynamics is regular or chaotic.

The numerical simulation showed that the dynamical system behavior can be periodic and chaotic according to the value of external loading. In the chaotic regime, the vibration amplitude is large than this observed in regular.

III.3 Numerical simulation of the probabilistic distribution and stochastic P-bifurcation of a hybrid energy harvester with Gaussian white noise excitation

III.3.1 Potential configuration and bifurcation diagram

As we said above, the phenomenon of the stochastic resonance requires three basic ingredients among which an energetic activation barrier such as the double potential well of a bi-stable system. We can have a mono-stable or a bistable configuration according the sign of the nonlinear cubic term, the potential energy presents two configurations: monostable and bistable several patterns of potential are shown in Fig.45.

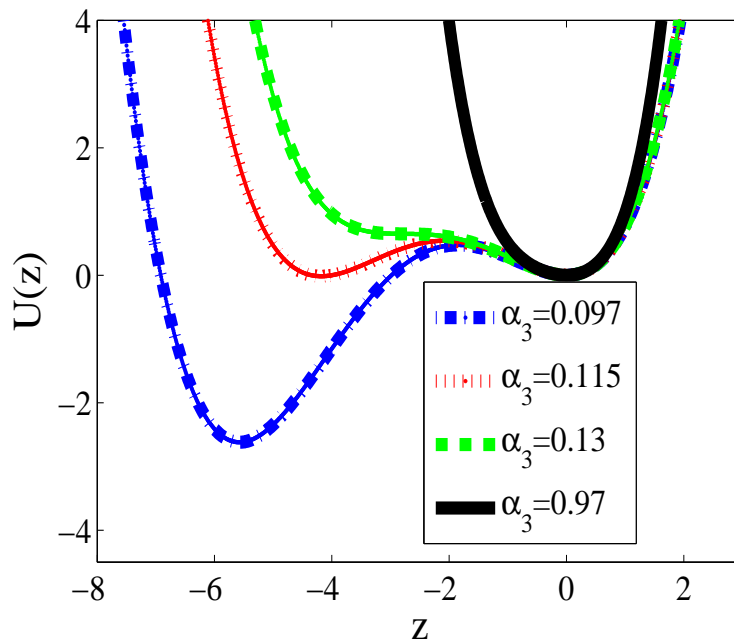


Figure 45: One-dimensional potential governed by Eq.(129) with parameters $\omega_1 = 1$, $\alpha_2 = 0.72$ and metastable potentials $\alpha_3 = 0.13$, symmetric bistable potentials $\alpha_3 = 0.115$ and asymmetric bistable potentials $\alpha_3 = 0.097$.

Here, following [181], activation energy may be denoted as the minimum energy necessary for a specific event to occur (for example for switching between two station-

ary states or limit cycle oscillation (LCO). The activation energy can be pictured as an energy hill that must be overcome in order to get to the valley of stability on the other side. Fig.46 represents the effective potential under varying, the amplitude of mechanical subsystem for three values of noise intensity D . It shows a single-well potential with an unstable equilibrium point (a_1) and a stable point (a_2). When the system is trapped in the unstable equilibrium point, the effective potential $U(a)$ moves from the left to the right and vice-versa depending on the initial condition. We also observe that when the intensity of Gaussian white noise D increases, the depth or the height of the barrier ΔU decreases. For a suitable choice of system parameters, the probability density function of the harvester can present one or two positive extrema (one minimum and one maximum).

Limit cycle oscillations (LCO) of an energy harvester was exploited for enhancing piezoelectric power generation. The extremely large amplitudes characteristic of these LCO was recorded as greatly increasing the efficacy of piezoelectric transduction. The LCO mechanism leads to both stable and unstable states that might be useful in a piezoelectric system designed for energy harvesting, so that large-amplitude response can be obtained. Stable LCO of acceptable amplitude in nonlinear piezoelectric systems can provide an important source of persistent electrical power. The goal is then to lower the threshold condition leading to LCO, and giving the condition for living a less desirable LCO for a more one.

By taking $\zeta_3 > 0$, the positive root of Eq.(172) is $\sqrt{\frac{1 - K_0 + \sqrt{192D\zeta_3\omega_0^4 + K_0^2}}{12 \zeta_3\omega_0^4}}$, and then the probability density function in Eq.(163) has a maximum (Fig.47(b)). However, by taking $\zeta_3 < 0$, there are two real positive roots of Eq.(172) for a convenient choice of system parameters: $\sqrt{\frac{1 - K_0 + \sqrt{192D\zeta_3\omega_0^4 + K_0^2}}{12 \zeta_3\omega_0^4}}$ and $\sqrt{\frac{1 - K_0 - \sqrt{192D\zeta_3\omega_0^4 + K_0^2}}{12 \zeta_3\omega_0^4}}$ whose the shape is similar to a crater, and then the probability density function $P(a)$ presented in Fig.47(b) has one maximum and one minimum respectively. Thus, a transition from a craterlike distribution to the unimodal distribution observed in Fig.47(b) can be defined as a type of P-bifurcation.

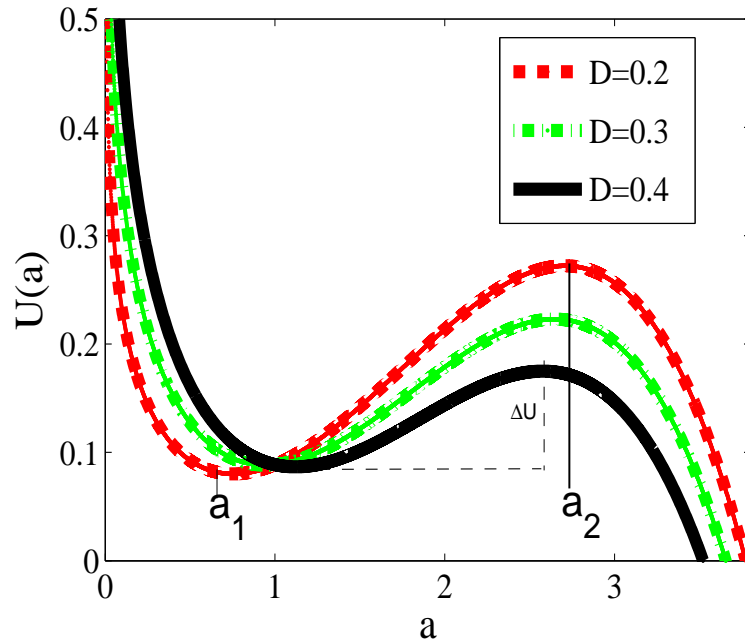


Figure 46: Effective potential $U(a)$ versus amplitude a for various values of noise intensity

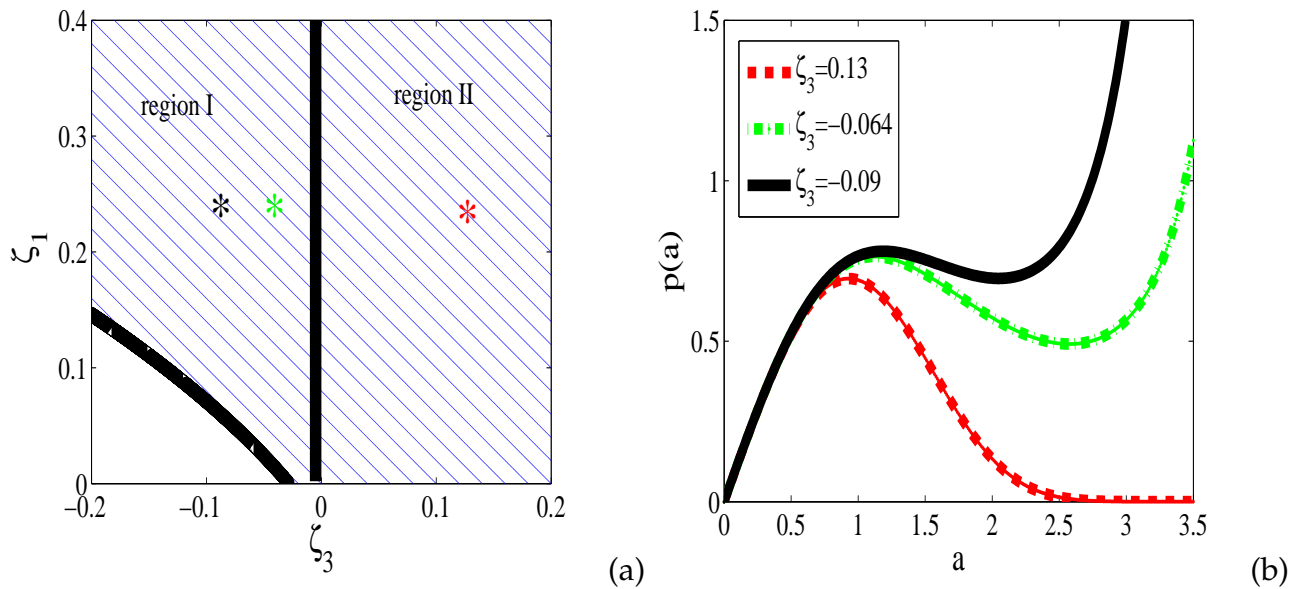


Figure 47: (a) Bifurcation diagram of Eq.(172) in the parameter plane (μ_3, μ_1) , (b) Stationary probability density of amplitude for three value of ζ_3 . The other parameters used are given as: $\zeta_1 = 0.25$, $\alpha_1 = 0.72$, $\alpha_3 = 0.97$, $\zeta_e = 0.84$, $\lambda = 2.0$, $\zeta_m = 0.057$, $\vartheta_p = 0.38$, $\beta = 2.05$, $\omega_0 = 1.0$, $\vartheta_e = 0.05$ and $D = 0.4$.

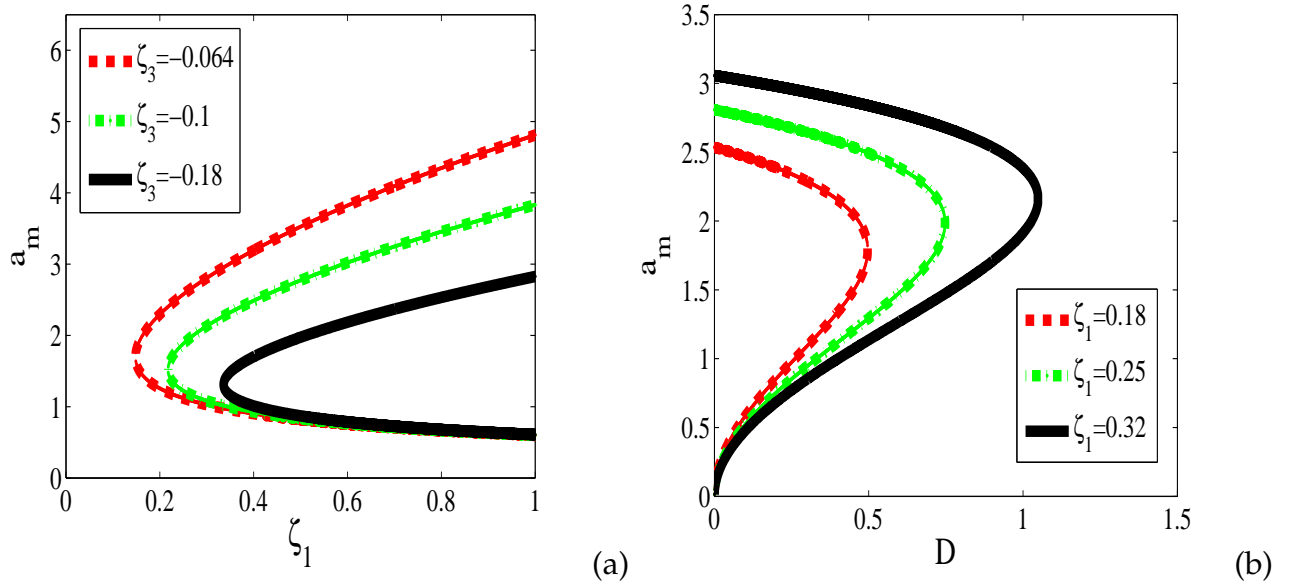


Figure 48: (a) Amplitude response of mechanical subsystem versus ζ_1 for $D=0.4$, (b) Amplitude response of mechanical subsystem versus D for $\zeta_3 = -0.064$. The parameters are the same as those in Fig.47.

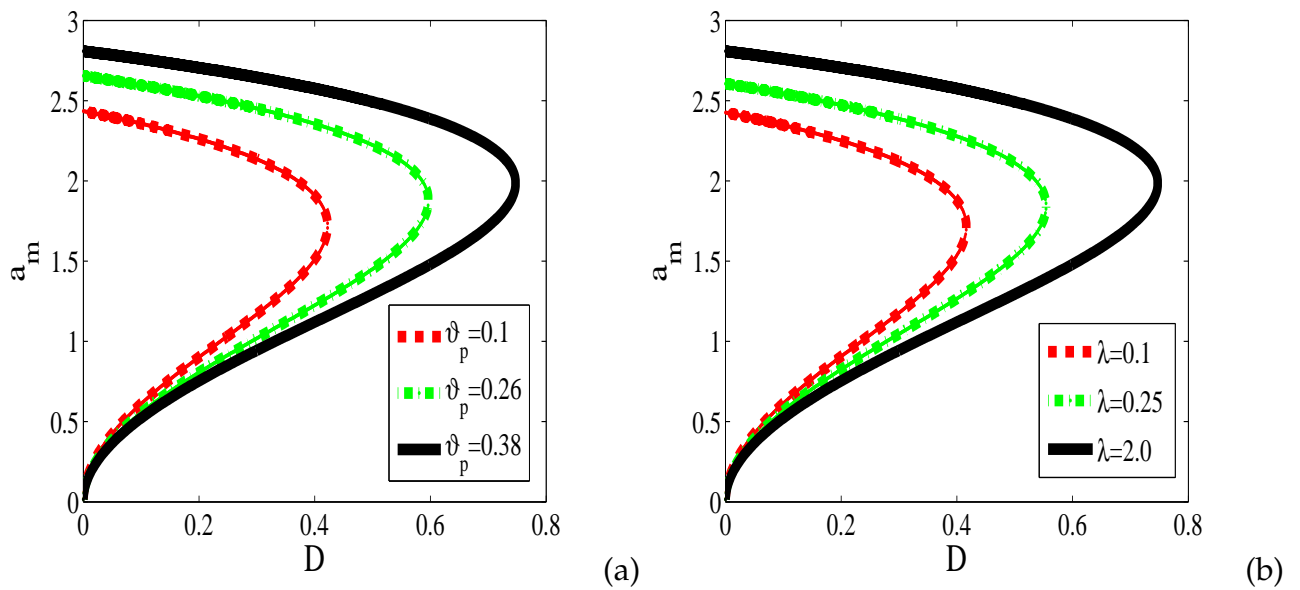


Figure 49: Amplitude response of mechanical subsystem versus noise intensity D for various (a) electro-magnetic coupling coefficient ϑ_p , (b) impedance λ . The parameters are the same as those in Fig.47.

We plotted in figure(47(a)), the bifurcation diagram of Eq.(172), for a fixed value of the noise intensity D . However, in region I, two positive roots are observed and give rise to the craterlike distribution. In region II, we have only one positive root, the distribution is unimodal.

Fig.48(a)-(b) show the amplitudes of the mechanical subsystem, when varying the noise intensity and for three fixed values of ζ_1 and ζ_3 . In Fig.48(a), we observe that, an increase of ζ_3 lead to decrease the maximum amplitude. However, an opposite phenomenon is observed in Fig.48(b) when ζ_1 increase: an increase of ζ_1 leads to increase the maximum amplitude. In Figure 49, a similar behavior to that of figure 48(a) is observed.

III.3.2 Numerical simulation of the probability density of the system

With the goal to verify the efficiency of the analytical technique used, the numerical simulation of the system Eq.(127) is made.

In this heading, we numerically and analytically plotted in Fig.50, the probability density of mechanical subsystem for two values of noise intensity D and electrical impedance λ . We notice in Figs.50(a) and (b) that, when D increase, the peak of the probability density function decreases. However, when the electrical impedance λ increases, the peak of probability density increases by shifting towards the weak amplitude values of (Figs.50(c-d)). Within this framework, when the probability density reaches his maximum for a fixed value of electrical impedance coefficient, the amplitude a and the accumulated energies of the ambient energy collector are higher than those received in any oscillation. The agreement between the numerical and analytical simulation justifies the efficiency of the analytical technique used.

In Figs.51(a) and (b), we studied the impact of a linear and nonlinear damping coefficient ζ_1 and ζ_3 on probability density function $P(a)$. One can observe in Fig.51(a) that, the probability distribution has only one maximum situated in the vicinity of zero for the high value of ζ_1 . In Fig.51(b), one interesting phenomenon is observed when we enhance ζ_3 . A transition from a craterlike distribution to an unimodal distribution

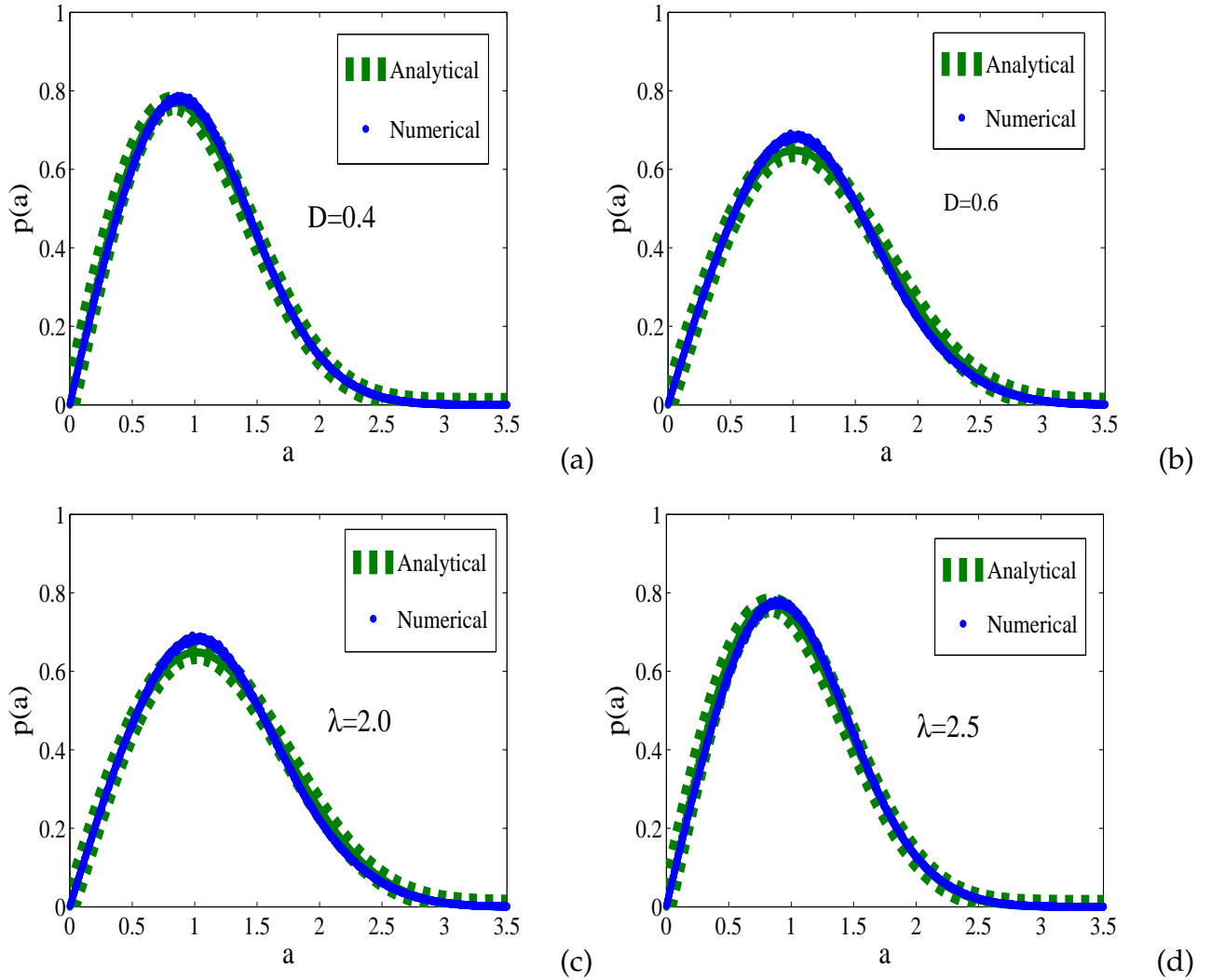


Figure 50: Stationary probability density of mechanical subsystem for different values of electrical impedance λ . The other parameters used are given as : $\zeta_1 = 0.25$, $\zeta_3 = 0.064$, $\alpha_1 = 0.72$, $\alpha_3 = 0.97$, $\zeta_e = 0.84$, $\zeta_m = 0.057$, $\vartheta_p = 0.38$, $\beta = 2.05$, $\omega_0 = 1.0$, $\vartheta_e = 0.05$. The initial conditions: $(z(0), \frac{dz(0)}{d\tau}, y(0), \rho(0)) = (0, 0, 0, 0)$.

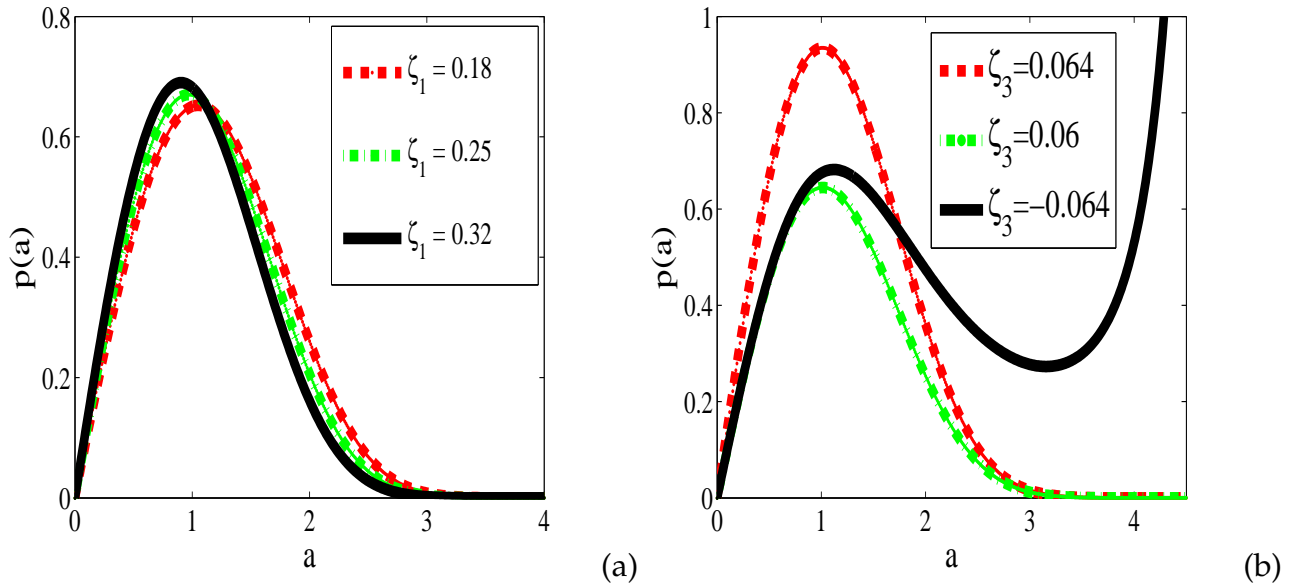


Figure 51: Stationary probability density function of mechanical system: (a) for different values of linear damping with $\zeta_3 = 0.064$, (b) for different values of nonlinear damping with $\zeta_1 = 0.25$. The other parameters used are given as : $\alpha_1 = 0.72$, $\alpha_3 = 0.97$, $\zeta_e = 0.84$, $\lambda = 2.0$, $\zeta_m = 0.057$, $\vartheta_p = 0.38$, $\beta = 2.05$, $\omega_0 = 1.0$, $\vartheta_e = 0.05$ and $D = 0.4$.

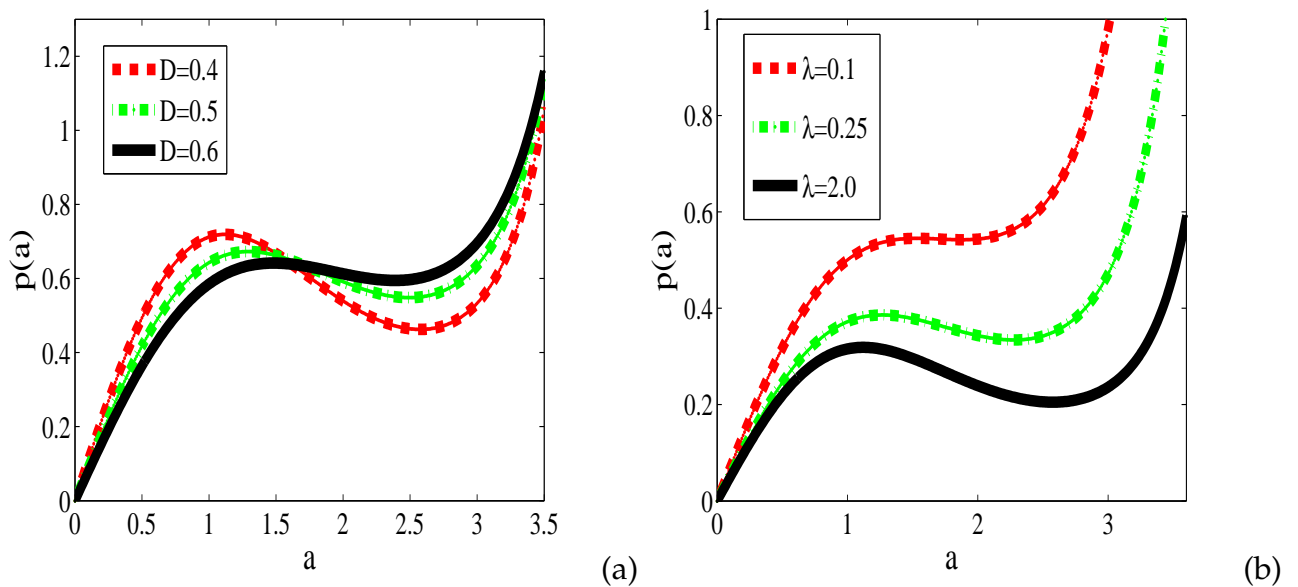


Figure 52: Stationary probability density function of mechanical system: (a) for different values of noise intensity D with $\lambda = 2.0$, (b) for different values of impedance λ with $D = 0.4$. The other parameters used are given as : $\zeta_1 = 0.25$, $\zeta_3 = -0.064$, $\alpha_1 = 0.72$, $\alpha_3 = 0.97$, $\zeta_e = 0.84$, $\zeta_m = 0.057$, $\vartheta_p = 0.38$, $\beta = 2.05$, $\omega_0 = 1.0$, $\vartheta_e = 0.05$.

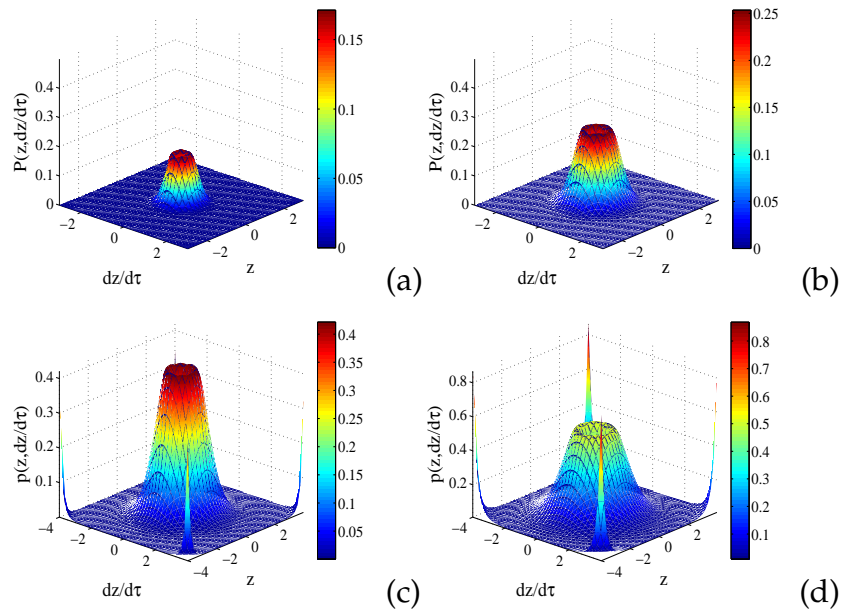


Figure 53: Stationary probability density of the system in 3D representation for: (a) $D = 0.09$; (b) $D = 0.2$; (c) $D = 0.4$; (d) $D = 0.6$. The other parameters used are given as : $\zeta_1 = 0.25$, $\zeta_3 = -0.064$, $\alpha_1 = 0.72$, $\alpha_3 = 0.97$, $\zeta_e = 0.84$, $\zeta_m = 0.057$, $\vartheta_p = 0.38$, $\beta = 2.05$, $\omega_0 = 1.0$, $\vartheta_e = 0.05$ and $\lambda = 2.0$.

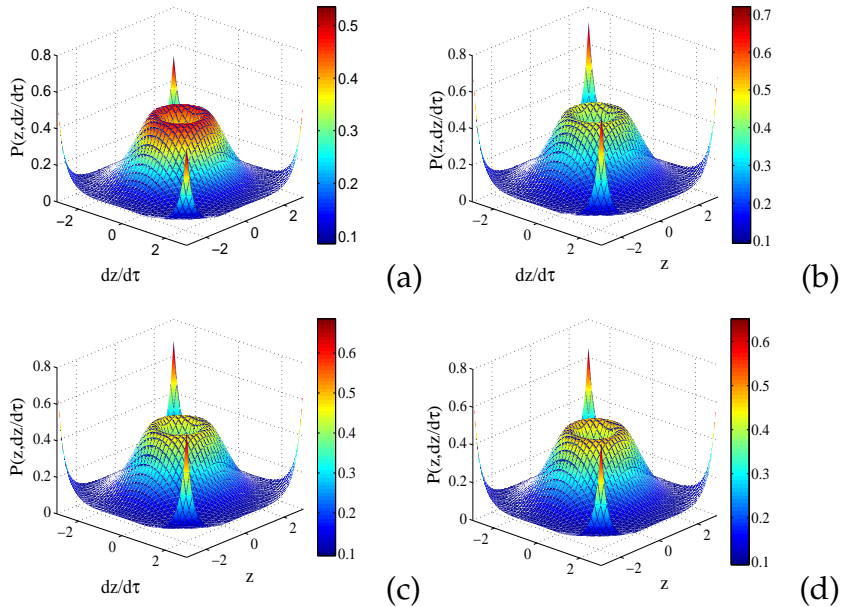


Figure 54: Stationary probability density of the system in 3D representation for: (a) $\vartheta_e = 0.01$; (b) $\vartheta_e = 0.05$; (c) $\vartheta_e = 0.1$; (d) $\vartheta_e = 0.15$. The other parameters used are given as : $\zeta_1 = 0.25$, $\zeta_3 = -0.064$, $\alpha_1 = 0.72$, $\alpha_3 = 0.97$, $\zeta_e = 0.84$, $\zeta_m = 0.057$, $\beta = 2.05$, $\omega_0 = 1.0$, $\vartheta_p = 0.38$, $\lambda = 2.0$ and $D = 0.4$.

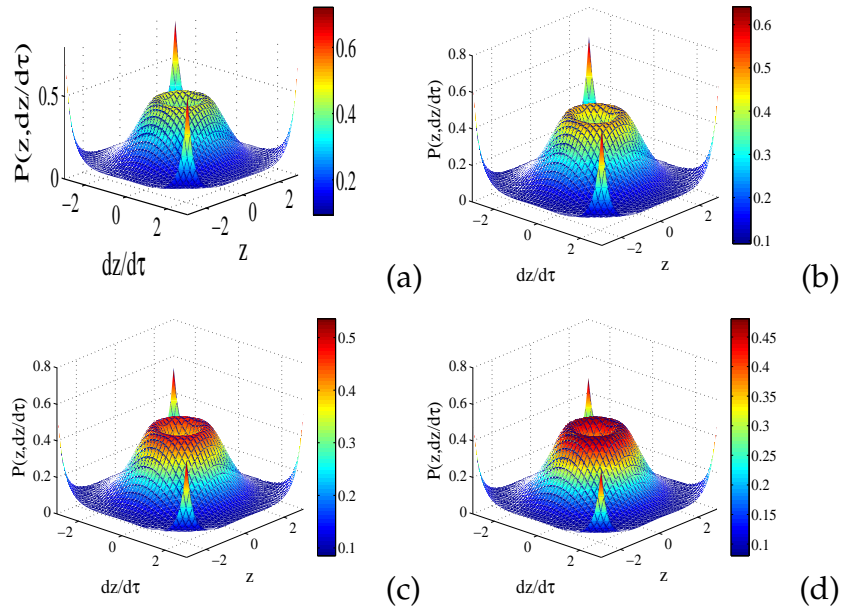


Figure 55: Stationary probability density of the system in 3D representation for: (a) $\vartheta_p = 0.05$; (b) $\vartheta_p = 0.18$; (c) $\vartheta_p = 0.38$; (d) $\vartheta_p = 0.5$. The other parameters used are given as : $\zeta_1 = 0.25$, $\zeta_3 = -0.064$, $\alpha_1 = 0.72$, $\alpha_3 = 0.97$, $\zeta_e = 0.84$, $\zeta_m = 0.057$, $\beta = 2.05$, $\omega_0 = 1.0$, $\vartheta_e = 0.05$, $\lambda = 2.0$ and $D=0.4$.

occurs. We also observe in these figure (Fig.51(b)) that, the increasing of ζ_3 leads to the enhancement of the probability density function by shifting its maximum towards small amplitude values. This means that the system energy could be optimized for the small values of linear and non- linear damping coefficient. In Figs.52(a) and (b), we studied the impact of a noise intensity D and impedance λ on probability density function $P(a)$ for $\zeta_3 < 0$. One can observed in Fig.52(a) that, the amplitude distribution has only one minimum situated in the vicinity of zero for the high value of D . However, beyond the peak, the probability density function decreases when D increases. In Fig.52(b), an enhancement of impedance λ leads to decrease, the maximum value of peak and increases its maximum.

The joint stationary probability density (normalized $p(z, \dot{z})$) of the mass displacement and velocity amplitudes of Eq.(164) are shown in Figs.53-(55). In Figs.53(a)-(b), the unimodal distribution is observed. However, in Figs.53(c)-(d), the craterlike distribution characterized by one maximum and one minimum is observed. From Figs.54 and 55, the influences of the coupling parameters on the the joint stationary probability

density have been investigated. The joint stationary probability density decreases as the values of ϑ_e increases as shown in Fig. 54 and and electro-magnetic coupling coefficient ϑ_p (see figure 55). As we have seen in this study, noise can stabilize unstable equilibria and shift bifurcations, i.e., the parameter value at which the dynamics changes qualitatively. Noise can also lead to transitions between coexisting deterministic stable states or attractors such as in birhythmic or bistable system. Fokker-Planck equation allows the analytic derivation of activation energies associated to the switching between different attractors.

III.3.3 Mean Square Current and voltage

In this section, we use equations Eq.(165)- Eq.(168) giving respectively the expressions of the mean square values of the voltage for the piezoelectric circuit $\langle y^2 \rangle$ and mean square values of the instantaneous electrical current for the magnetic circuit $\langle \rho^2 \rangle$. We provided in Figs.56(a)-(b), the mean square values of the instantaneous electrical current for the magnetic circuit $\langle \rho^2 \rangle$ and mean square voltage versus coupling coefficient of the piezoelectric circuit ϑ_p and the magnetic circuit ϑ_e for three values of the noise intensity. In Fig.56(a), we observed that, the output power in terms of mean square voltage increases when the noise intensity increases. Similar result is observed in Fig.56(b) when the noise intensity increase. We plotted in Figs.57(a)-(b),the output power versus D for three values of the ϑ_e and ϑ_p . We notice in these figures that, an increase of ϑ_e and ϑ_p leads to increase of the output power.

Fig.58 demonstrates the mean square electric current $\langle \rho^2 \rangle$ and mean square (PE) voltage $\langle y^2 \rangle$ as function of noise intensity D for different system parameters. As the noise intensity D increases, the mean square electric current $\langle \rho^2 \rangle$ and mean square voltage $\langle y^2 \rangle$ increases monotonously. In Figs.58(a-b), the mean square electric current $\langle \rho^2 \rangle$ and mean square (PE) voltage $\langle y^2 \rangle$ decreases with increases of damping coefficient ζ_3 . The mean square electric current $\langle \rho^2 \rangle$ decrease as the values of β increases as shown in Fig.58(c). Finally, The mean square voltage $\langle y^2 \rangle$ decrease as the

values of λ increases as shown in Fig.58(d).

Fig.59 demonstrates the total mean output power of hybrid energy harvester P_{hybrid} as function of noise intensity D for two coupling parameters. As the noise intensity D increases, the total mean output power of hybrid energy harvester increases monotonously. In Figs.59(a)-(b), the total mean output power harvested by the hybrid system increases with increases of coupling coefficient ϑ_e and ϑ_p . In Figs. 60(a-b), we observe the similar results. the total mean output power of hybrid energy harvester P_{hybrid} as function of coupling parameters. the mean output power of hybrid increases with increases of noise intensity D.

The mean square values of the current and the voltage in the piezoelectric layers are calculated from the PDFs and are shown respectively in Figs.(56)-(57) as a function of white noise intensity . It is seen from the figures that the mean square value of the current and voltage with an increase in the excitation intensity. It has been shown that this increase depends on large limit cycle oscillations (LCO) and bimodality of the PDF. Large limit cycle oscillations (LCO) can be used for energy harvesting [183], by providing an important source of persistent electrical power [184]. Some authors have demonstrated the advantage of energy harvesting from LCO on high-energy orbits [185]. Because of the increased values of mean square voltage there will be enhancement of the energy harvested. The value of the noise intensity at which the mean square voltage begins to increase rapidly can be adjusted by varying the parameters ϑ_e and ϑ_p . Or for a given noise intensity the parameters ϑ_e and ϑ_p can be suitably found to maximize the voltage mean square value in the piezoelectric layers.

III.3.4 Stochastic Resonance

In the above study we have pointed out that the energy harvesting system is a bistable system driven by a harvestable noise source. In addition, for an energy harvesting system located in certain zone such as the industrial zones where large rotating machines are observed as well as large cars entering and leaving the factory, the energy harvester

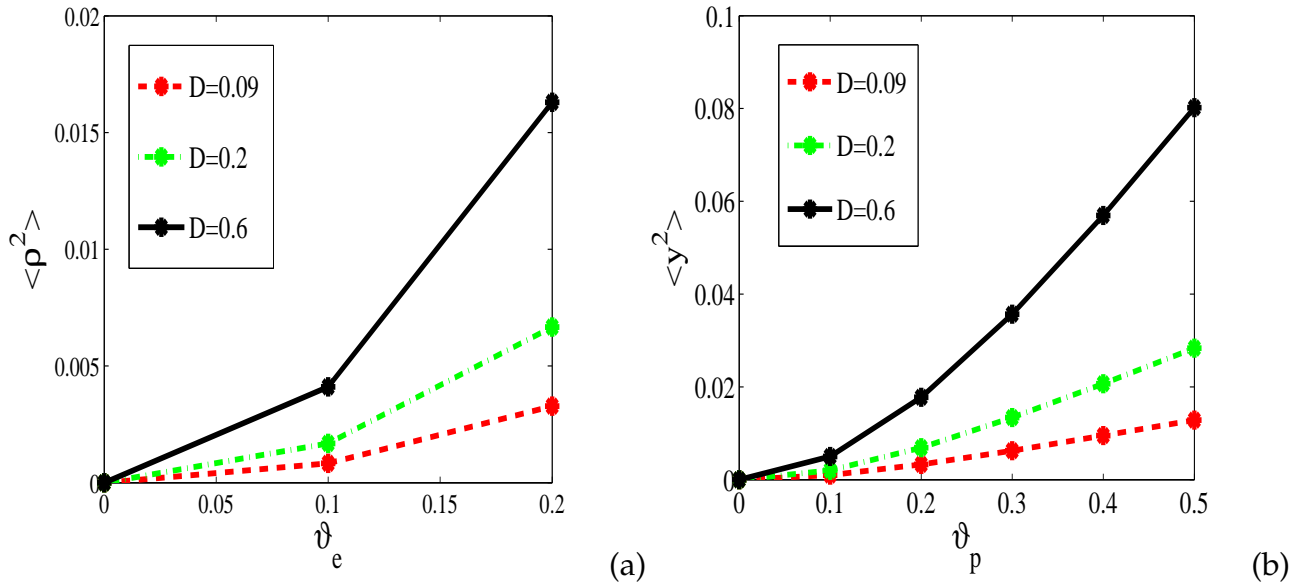


Figure 56: (a) Evolution of mean square current of magnetic circuit versus ϑ_e for $\vartheta_p = 0.38$; (b) Evolution of mean square voltage of piezoelectric circuit versus ϑ_p for $\vartheta_e = 0.05$. The other parameters are given as: $\zeta_1 = 0.25$, $\zeta_3 = 0.064$, $\alpha_1 = 0.72$, $\alpha_3 = 0.115$, $\zeta_e = 0.84$, $\zeta_m = 0.057$, $\beta = 2.05$, $\omega_0 = 1.0$ and $\lambda = 2.0$.

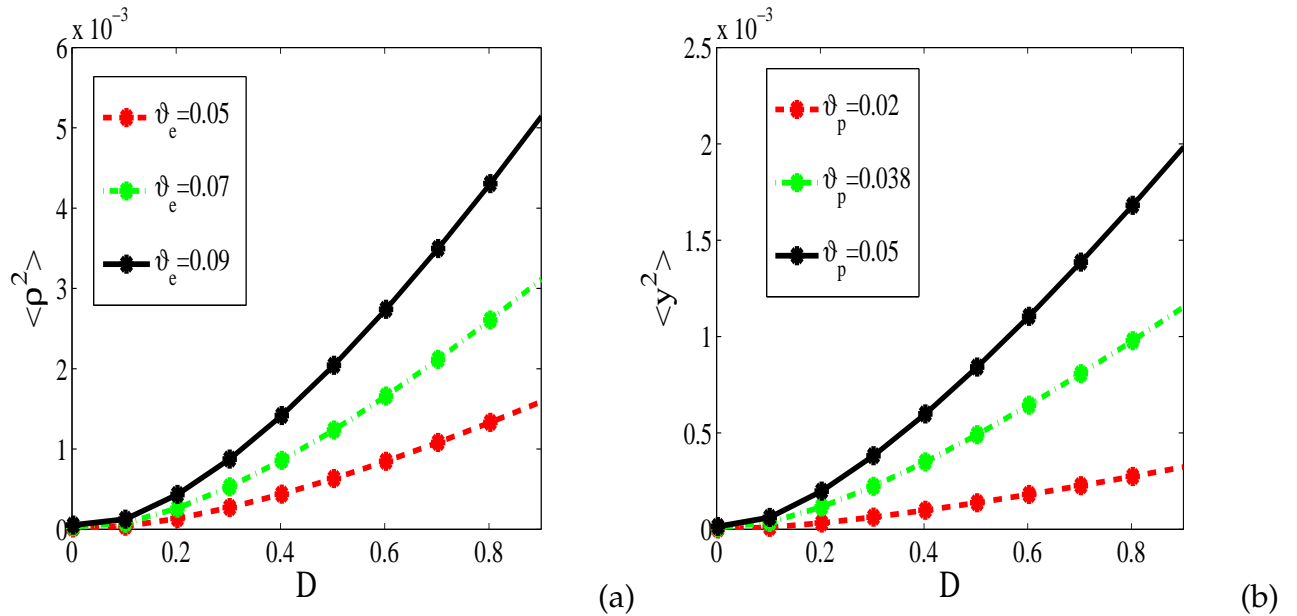


Figure 57: (a) Evolution of mean square current of magnetic circuit versus noise intensity D for $\vartheta_p = 0.38$; (b) Evolution of mean square voltage of piezoelectric circuit versus noise intensity D for $\vartheta_e = 0.05$. The other parameters used are given as: $\zeta_1 = 0.25$, $\zeta_3 = 0.064$, $\alpha_1 = 0.72$, $\alpha_3 = 0.115$, $\zeta_e = 0.84$, $\zeta_m = 0.057$, $\beta = 2.05$, $\omega_0 = 1.0$ and $\lambda = 2.0$.

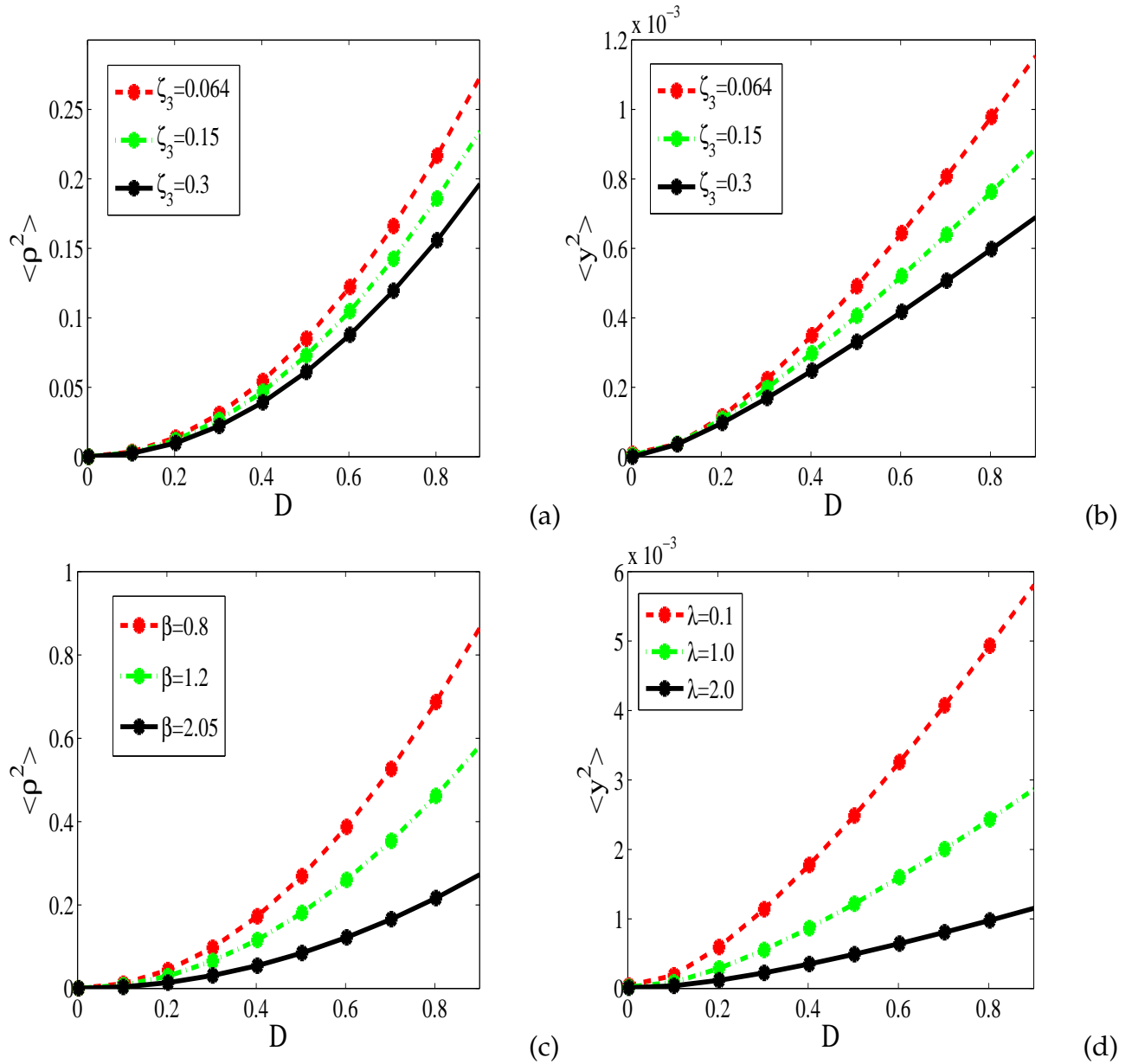


Figure 58: The mean square value $\langle \rho^2 \rangle$ of the electric current and mean square value $\langle y^2 \rangle$ of the voltage versus noise intensity D for various (a)-(b) nonlinear damping coefficient ζ_3 , (c) resistance and inductance ratio β , (d) impedance of the (PE) system λ .

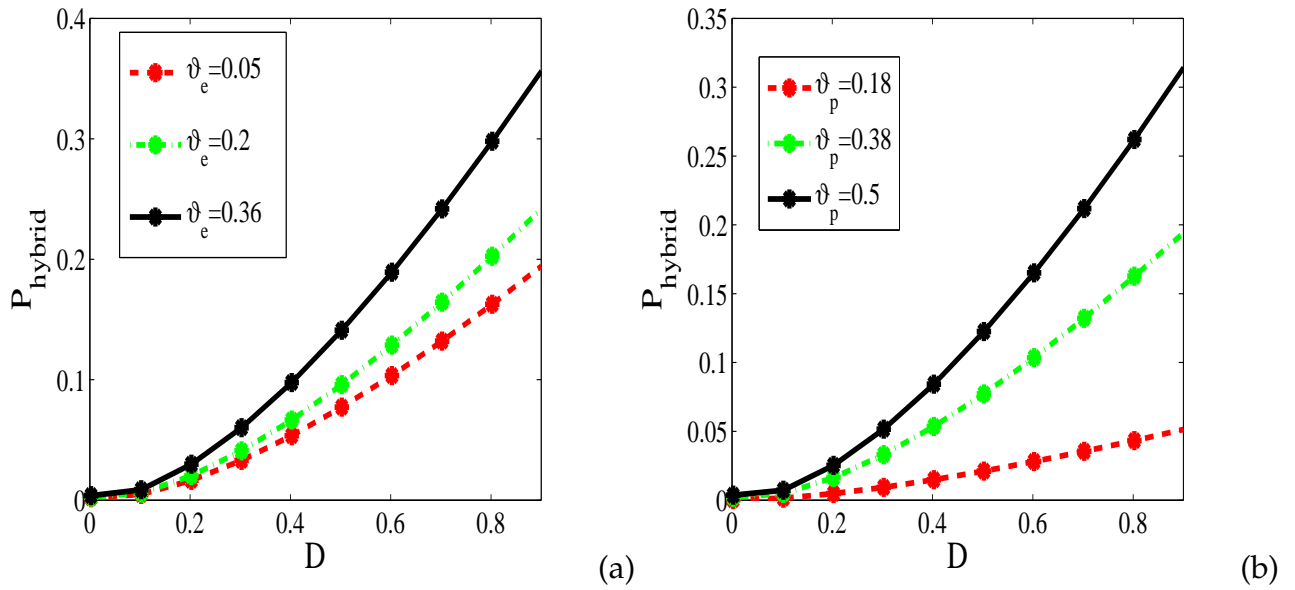


Figure 59: Output power harvested by the hybrid system as function of the driving noise intensity with the parameters $\zeta_1 = 0.25$, $\zeta_3 = 0.064$, $\alpha_1 = 0.72$, $\alpha_3 = 0.115$, $\zeta_e = 0.84$, $\zeta_m = 0.057$, $\beta = 2.05$, $\omega_0 = 1.0$ and $\lambda = 2.0$.

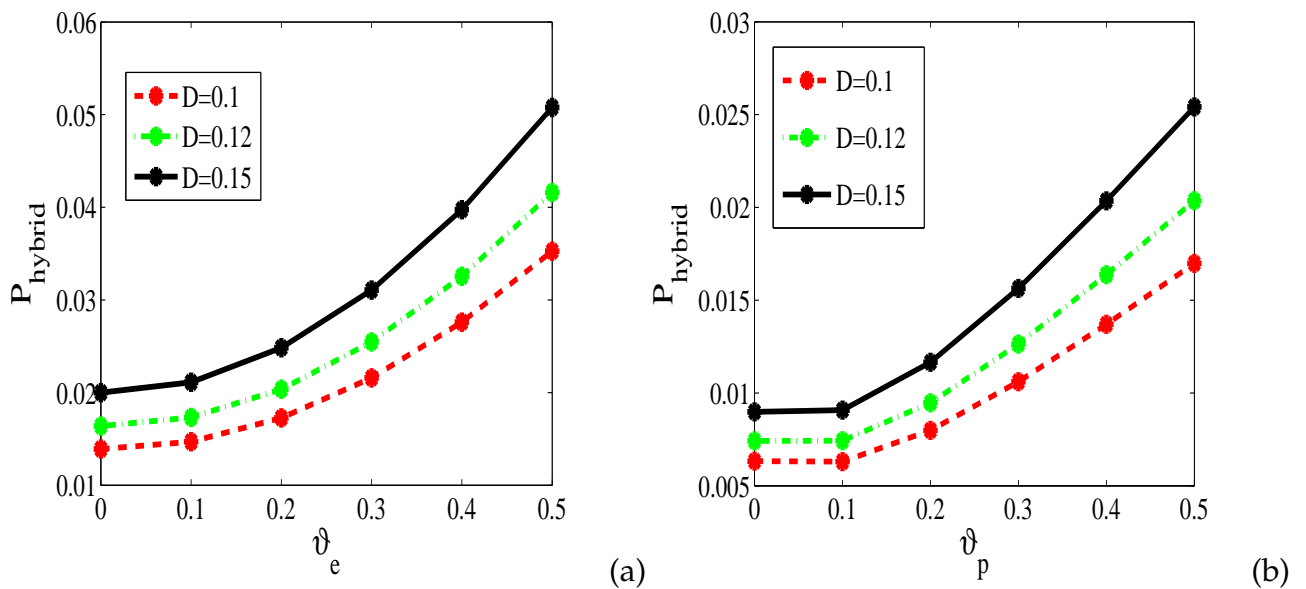


Figure 60: (a) Evolution of output power harvested by the hybrid system versus ϑ_e for $\vartheta_p = 0.38$; (b) Evolution of output power harvested by the hybrid system versus ϑ_p for $\vartheta_e = 0.05$. The other parameters are given as: $\zeta_1 = 0.25$, $\zeta_3 = 0.064$, $\alpha_1 = 0.72$, $\alpha_3 = 0.115$, $\zeta_e = 0.84$, $\zeta_m = 0.057$, $\beta = 2.05$, $\omega_0 = 1.0$ and $\lambda = 2.0$.

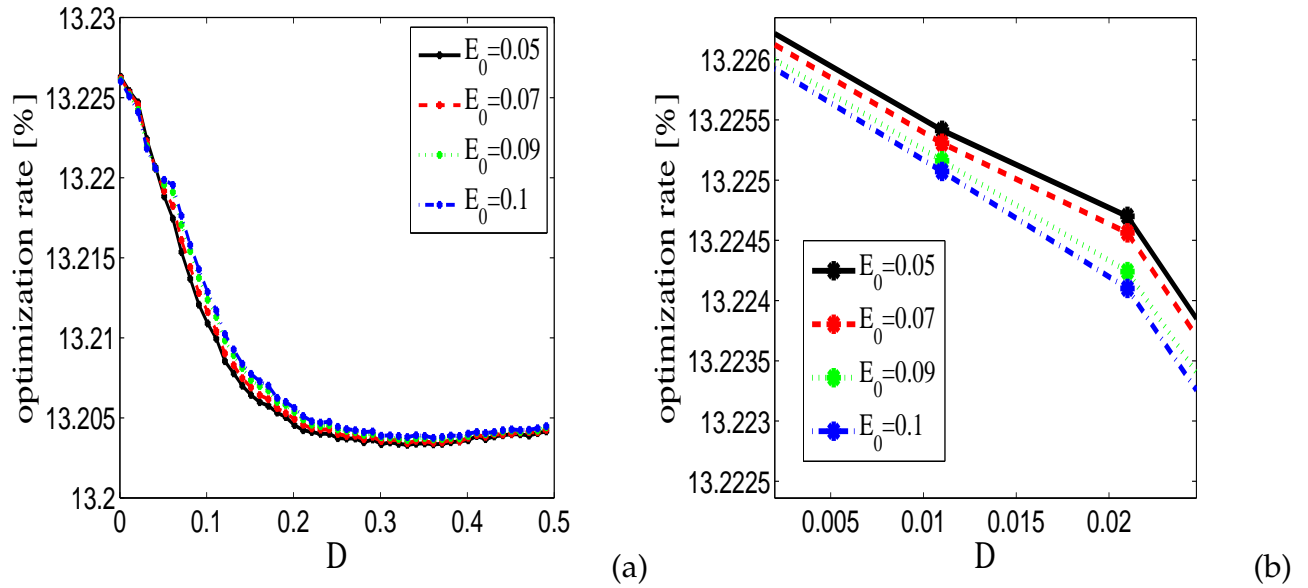


Figure 61: Increase rate op_{max} versus noise intensity, (a) overall view; (b) detailed view for $\zeta_1 = 0.25$, $\zeta_3 = 0.064$, $\alpha_1 = 0.72$, $\alpha_3 = 0.115$, $\zeta_e = 0.84$, $\zeta_m = 0.057$, $\vartheta_p = 0.38$, $\beta = 2.05$, $\vartheta_e = 0.05$ and $\lambda = 2.0$ and $\omega = 0.35$.

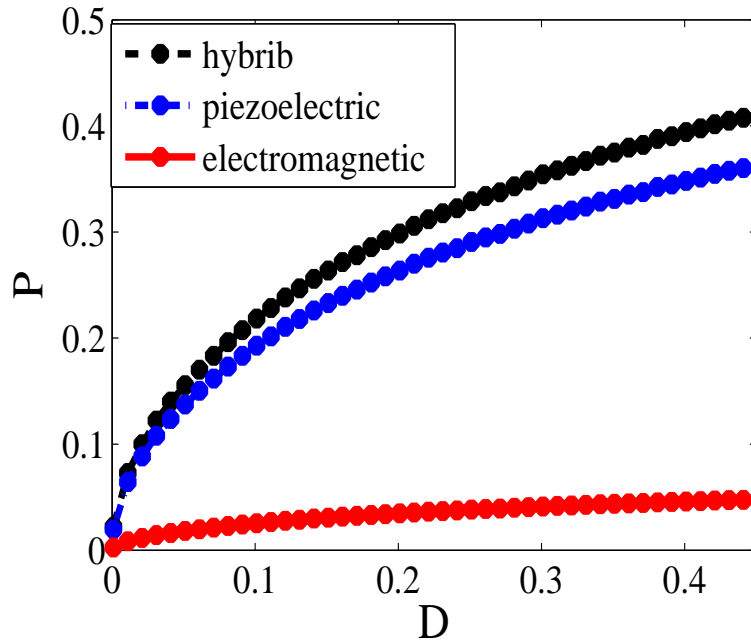


Figure 62: Comparison of the output power with $E_0 = 0.05$; with the parameters $\zeta_1 = 0.25$, $\zeta_3 = 0.064$, $\alpha_1 = 0.72$, $\alpha_3 = 0.115$, $\zeta_e = 0.84$, $\zeta_m = 0.057$, $\vartheta_p = 0.38$, $\beta = 2.05$, $\vartheta_e = 0.05$ and $\lambda = 2.0$ and $\omega = 0.35$.

could be subjected to the combination of the harmonic and random excitation. In order to improve vibrational energy harvesting, theoretical studies have clearly shown that the phenomenon of stochastic resonance can be used to generate large-amplitude vibrations [186]. Stochastic resonance applied to harvesting requires three basic ingredients: an energetic activation barrier such as the double well potential of a bistable system, a weak but coherent control input in the form of a periodic signal, and a source of ambient vibration that is inherent to the system to be harvested [187, 188, 189]. In these cases, one wants to measure the response of the system in the presence of the input $E_0 \cos \omega \tau$ compared to the case when the system is solely subject to a random term.

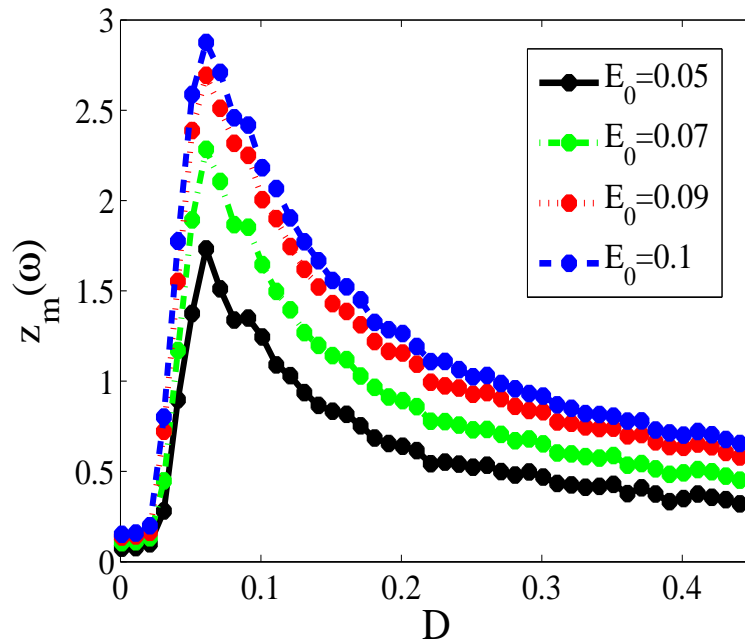


Figure 63: Mean response amplitude versus noise intensity D ; with the parameters $\zeta_1 = 0.25$, $\zeta_3 = 0.064$, $\alpha_1 = 0.72$, $\alpha_3 = 0.115$, $\zeta_e = 0.84$, $\zeta_m = 0.057$, $\vartheta_p = 0.38$, $\beta = 2.05$, $\vartheta_e = 0.05$ and $\lambda = 2.0$ and $\omega = 0.35$.

We depicted in Fig.61, the increase rate op_{max} versus D , for four values of amplitudes of the harmonic excitation E_0 . This figure reveals that, an increase of E_0 leads to decrease the op_{max} . In addition, we also observed in this figure that, regardless of the value of the harmonic excitation, when the noise intensity is large, op_{max} decreases and tends towards the constant value.

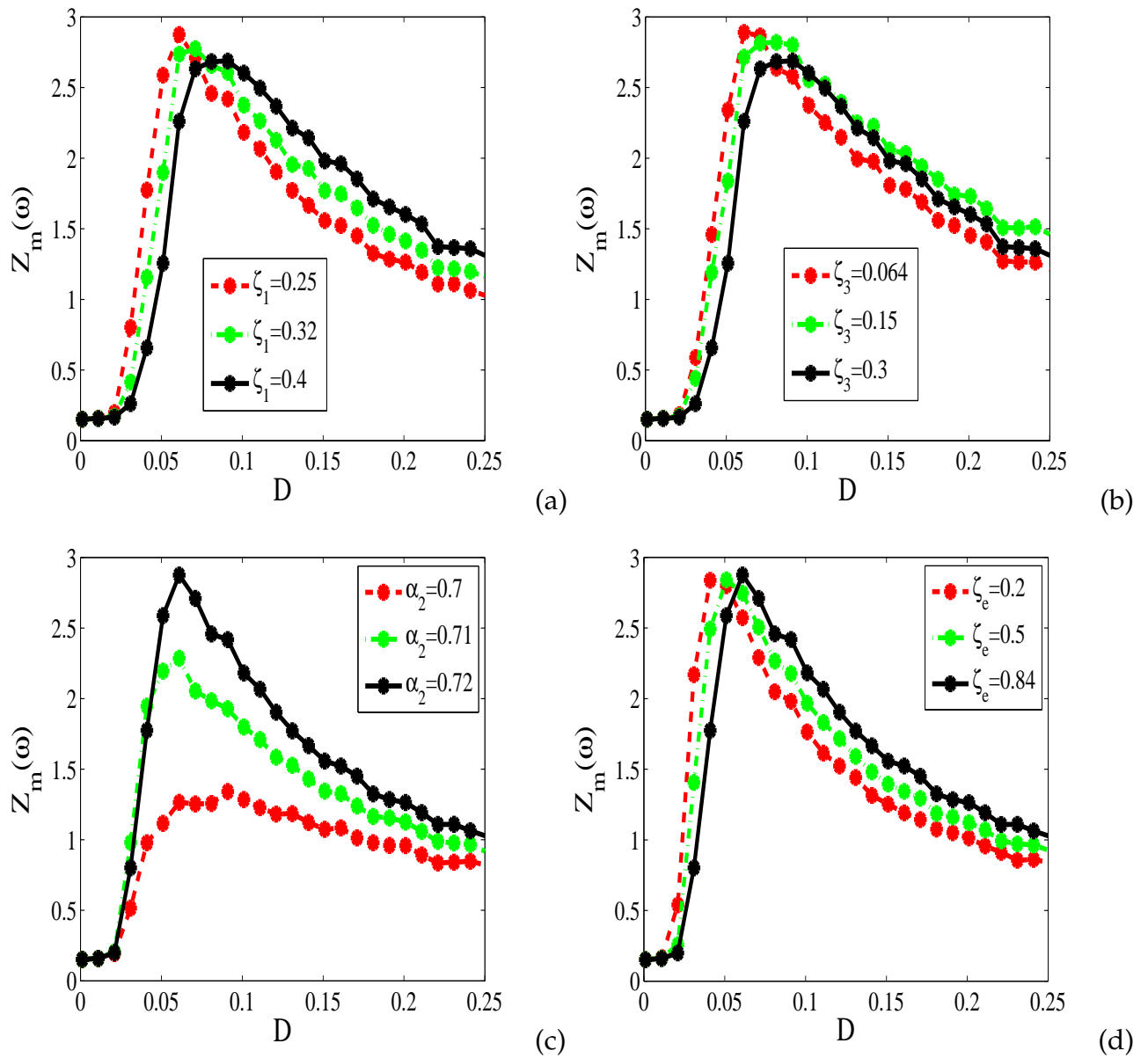


Figure 64: Mean response amplitude versus noise intensity D for various (a) linear damping ζ_1 , (b) nonlinear damping ζ_3 , (c) quadratic nonlinear coefficient α_2 and (d) electro-magnetic coupling coefficient ζ_e .

We provided in Figs.62 and 63, the comparison between the output power harvested respectively in the piezoelectric circuit, the electromagnetic circuit and the overall system and the mean amplitude response versus noise intensity D . We notice in Fig.62 that, the energy harvested by the hybrid model is higher than that harvested by the piezoelectric or electromagnetic circuit (Fig.62). Fig.63 show the mean amplitude response versus noise intensity D , for four values of the amplitude of the harmonic excitation E_0 . One observes that, for some values of amplitude of the noise excitation, the mean amplitude response presents a maximum. This maximum is a signature of the stochastic resonance, which gives the largest oscillation amplitude for a given excitation level, and reflects the transition in the system response from single well to double well oscillations. In addition, we can note in this figure (Fig.63) that, the maximum amplitude response is obtained for the highest amplitude of the harmonic excitation.

3.3.4.1 Effect of parameters on stochastic resonance

With the deduced analytical expression of the mean response amplitude in the bistable stage of the vibrational energy harvesting system, the mean response amplitude as a function of noise intensity D with different system parameters are shown in Figs.64. From Figs.63 and 64, there is a maximum in the mean response amplitude. It means that there is an optimal noise intensity D at which the mean response amplitude of the system is maximum that identifies as characteristic of the stochastic resonance phenomenon.

An increase in the maximum of the mean response amplitude means that the stochastic resonance phenomenon is enhanced, and vice versa. In Figs. 64(a)-(b), the maximum of the mean response amplitude decreases on increasing linear damping coefficient ζ_1 and nonlinear damping coefficient ζ_3 . Meanwhile, the positions of the maximum are shifted to the larger value of noise intensity D . From Fig.64(c), the maximum of the mean response amplitude increases on increasing quadratic nonlinear coefficient α_2 . The positions of the maximum are shifted to the smaller value of noise intensity D . Fig. 64(d) shows that the impacts of electro-magnetic coupling coefficient ζ_e on the maximum of the mean response amplitude is very small. However the locations of the maximum

value are shifted to the larger value of noise intensity D .

In Fig. (63) and (64), we observe the stochastic resonance phenomenon which gives the largest oscillation amplitude for a given excitation level, and reflects the transition in the system response from single well to double well oscillations characteristics; with hoppings between the two potential wells. We also notice from figure 64(c)-(d) that, an increase of the quadratic nonlinear coefficient α_2 and electromechanical coupling term ζ_e leads to the increases of the mean amplitude response before the stochastic resonance as concluded from analytical study. However, the mean amplitude response is enhanced. Its maximum value slightly shifts towards the high value of noise intensity D . We also notice from figure 64(a)-(b) that, an increase of the nonlinear damping term ζ_1 and cubic damping term ζ_3 leads to the decreases of the mean amplitude response the stochastic resonance. Noise may play a very constructive role in energy harvesting. It may enhance a system's sensitivity to a small periodic deterministic signal by amplifying it. Stochastic resonance is the physical phenomenon through which the throughput of energy within an oscillator excited by a modulating excitation source can be boosted by adding a small stochastic perturbation [190]. For energy harvesting from noise, it was confirmed that active power can be increased at stochastic resonance, in the same way of the relationship between energy and phase at an appropriate [191]. Experiments have validated this observation, showing that the response can indeed be amplified and indicate that the available power generated under stochastic resonance is noticeably higher than the power that can be collected under other harvesting conditions [187].

The curve of the mean output power increases with increasing noise intensity, electromechanical coupling coefficient and electro-magnetic coupling coefficient. That is, these parameters play an active role in improving the performance of the energy harvester. This is of great significance to energy harvesting because these parameters are important to characterize performance of nonlinear vibration energy harvester under random excitations. While the curve of the mean output power decreases as there damping coefficients increases. For the proposed harvester, the present work opens up another possible way to increase the harvested energy from ambient environment via the exploitation

of the stochastic resonance phenomenon. The stochastic resonance phenomenon is enhanced on increasing, quadratic nonlinear coefficient and coupling terms. While the stochastic resonance phenomenon is weakened on increasing damping coefficient.

In this section, the dynamic behavior of the hybrid energy harvester under Gaussian white noise using probabilistic approach is investigated. By applying a stochastic averaging method on this system, the stochastic response is obtained. The results obtained show that, the shape of the statistic response strongly depends on the coefficient of the nonlinear damping. The impact of the system parameters is investigated with detail. The obtained results show that, when the coupling coefficients and noise intensity increase, the harvested energy is improved. In addition, the stochastic bifurcation phenomenon characterized by the qualitative change of the stationary probability density is observed and allows to obtain the best value of the bifurcation parameter for which the harvester presents a high limit cycle. Besides, combining the harmonic force to the random signal, the stochastic resonance phenomenon occurs and improves the system performance. The comparison between the harvested energy by the hybrid model to that harvested by the piezoelectric model is investigated. The impact of the amplitude of the harmonic excitation is investigated on the system performance. The results obtained in this manuscript show the interest to build the hybrid harvester.

III.3.5 Discussion

While, most studies of vibration energy harvesters have considered sinusoidal excitations. It would be judicious to consider the finite bandwidth random vibrations, i.e., external Gaussian white noise. Stochastic averaging could be used to study the effect of the gaussian white noise on the performance of the nonlinear hybrid energy harvesters. Stochastic averaging method is mainly due to the reduction of dimensions of the Fokker-Planck-Kolmogorov equation while the essential behavior of the system is retained. It is a convenient approximation approach to predict the stationary response of nonlinear stochastic systems. For an energy harvesting system located in certain zone such as the

industrial zones where large rotating machines are observed as well as large cars entering and leaving the factory, the energy harvester could be subjected to the combination of the coherent (harmonic) and random excitation.

In fig.58, we observe the stochastic resonance phenomenon which gives the largest oscillation amplitude for a given excitation level, and reflects the transition in the system response from single well to double well oscillations characteristics; with hoppings between the two potential wells.

Noise may play a very constructive role in energy harvesting. It may enhance a systems sensitivity to a small periodic deterministic signal by amplifying it. Stochastic resonance is the physical phenomenon through which the throughput of energy within an oscillator excited by a modulating excitation source can be boosted by adding a small stochastic perturbation. For energy harvesting from noise, it was confirmed that active power can be increased at stochastic resonance, in the same way of the relationship between energy and phase at an appropriate.

Experiments have validated this observation, showing that the response can indeed be amplified and indicate that the available power generated under stochastic resonance is noticeably higher than the power that can be collected under other harvesting conditions [192].

III.4 Conclusion

This chapter presents the results of the study of the dynamic behavior of they models proposed in this thesis. Through the first model, the combined effect of the fractional derivative order, the amplitude of the parametric coupling in the model, we have shown that the model under these parameters presents some nonlinear phenomena such as the jump phenomenon, the aperiodic phenomenon and the chaotic behavior. These results show that fractional inductance and parametric coupling increase output power. We also studied the influence of Gaussian white noise in our model. We got a beneficial role from this noise. For this second model, we showed that the power harvest by the

hybrid system was high. The combined effect of a Gaussian white noise and a periodic excitation in our model has a beneficial role on the system performance. The harvested energy is very significative for the high value of the amplitude of the periodic excitation.

General Conclusion

Main results

In this thesis, two physical models of the vibrations energy harvesters, subjected to the periodic and stochastic excitation have been proposed in the goal to harness ambient vibration energy. A detailed review of ambient energy sources and some transduction mechanisms were presented in order to understand the concepts and techniques of energy harvesting.

- Firstly, we investigate the impact of fractional inductance and parametric coupling in the energy harvester system. The analytical investigation is carried out by using harmonic balance method. Using the Newton-Leipnik algorithm, the analytical results obtained are checked. The agreement between these two methods justified the efficiency of the proposed technique. The impact of fractional inductance and parametric coupling upon the system's performance is discuss with detail showing the optimization of output voltage and power of the system for a fixed value of the control parameter E_0 . We follow our investigation by discussing the influence of the nonlinear damping (μ_3) on the system response. The result obtained show a decrease of the output power for the large values of nonlinear damping. In the numerical simulation, the presence, of chaotic vibrations involves an enhancing of the bandwidth frequency of the harvester there by increasing the level of harvested energy.

- Secondly, we investigate the probabilistic distribution and stochastic P-bifurcation of a hybrid energy harvester under gaussian white noise. A two dimensional model have been proposed and the main dimensionless equations governing the dynamical of structure are derived. By applying the method of stochastic averaging based on a per-

turbation technique, we have obtained the stationary probability density function of mechanical amplitude. One type of qualitative change was found namely the p-bifurcation when certain system parameters vary. The stochastic p-bifurcation based on this qualitative change of the shape of probability density function is observed. We also discuss the extrema of the distribution. The probability density which has been obtained via the stochastic averaging method was numerically checked through the Euler algorithm. The agreement between numerical and analytical results justifies the efficiency of the used analytical technique.

Thereafter, we investigate hybridization of two energy harvesting transduction mechanisms and vibration source, in order to achieve greater power generation. The comparison between the output power generated by the piezoelectric circuit, electromagnetic circuit and the hybrid model is made. As indicated, it is seen that hybrid energy harvesters generate greater power outputs than their single harvester components, and that the combination of noisy and periodic vibrating sources could induce high output power. Combining the noise signal with harmonic signal, the phenomenon of stochastic resonance is observed which gives rise to the large amplitude of vibrations and consequently, optimize the output power. The results presented in this thesis can provide a theoretical idea for the design and optimization of the systems, and allow making an optimal choice of the environment in which the energy harvesters could function. Moreover, the results obtained show the need to use materials exhibiting fractional properties as well as the combination of several technologies in order to make the energy harvesting systems more efficient.

Perspectives

Like future work based in this thesis, we have:

- The achievement of experimental study in order to verify the theoretical results,
- The study by taking a higher order dissipation in the presence of a colored noise,
- The synchronization of several energy harvesters.

Bibliography

- [1] K. A. C. Chennault, N. Thambi and A. M. Sastry, Powering MEMS portable devices a review of non-regenerative and regenerative power supply systems with special emphasis on piezoelectric energy harvesting systems, *Smart Materials and Structures*, Vol. 17, 043001 (2008).
- [2] S. B. Riffat and X. L. Ma, Thermoelectrics; A review of present and potential applications, *Applied Thermal Engineering*, Vol. 23, 913 (2003).
- [3] Y. G. Deng and J. Liu, Recent advances in direct solar thermal power generation, *Journal of Renewable and Sustainable Energy*, Vol. 1, 052701 (2009).
- [4] S. R. Antonal and H. A. Sodano, A review of power harvesting using piezoelectric materials (2003-2006), *Smart Materials and Structures*, Vol. 16, R1 (2007).
- [5] C. B. Williams and R. B. Yates, Analysis of a micro-electric generator for microsystems, *Sensors and Actuators A: Physical*, Vol. 52, 8 (1996).
- [6] A. Erturk and D. J. Inman, A Distributed Parameter Electromechanical Model for Cantilevered Piezoelectric Energy Harvesters, *Journal of Vibration and Acoustics*, Vol. 130, 041002 (2008).
- [7] H. A. Sodano, D. J. Inman and G. Park, A review of power harvesting from vibration using piezoelectric materials, *The Shock and Vibration Digest*, Vol. 36, 197 (2004).
- [8] G. Sebald, H. Kuwano, D. Guyomar and B. Ducharne, Experimental Duffing Oscillator for broadband piezoelectric energy harvesting, *Smart Materials and Structures*, Vol. 20, 102001 (2011) .

- [9] M. A. Ahmad and H. N. Alshareef, Modeling the Power Output of Piezoelectric Energy Harvesters, *Journal of Electronic Materials*, Vol. 40, 1477 (2011).
- [10] C. R. Saha, T. O'Donnell, H. Loder, S. Beeby and J. Tudor, Optimization of an Electromagnetic Energy Harvesty Device, *IEEE Transactions On Magnetics*, Vol. 42, 3509 (2006).
- [11] P. D. Mitcheson, P. Miao, B. H. Stark, E. M. Yeatman, A. S. Holmes and T. C. Green, MEMS electrostatic micropower generator for low frequency operation, *Sensors and Actuators A Physical*, Vol. 115, 523 (2004).
- [12] S. Meninger, J. O. MurMiranda, R. Amirtharajah, A. P. Chandrakasan and J. H. Lang, Vibration to electric energy conversion, *IEEE Transactions on Very Large Scale Integration (VLSI) Systems*, Vol. 9, 64 (2001).
- [13] I. Petráš, An effective numerical method and its utilization to solution of fractional models used in bioengineering applications, *Advances in Difference Equations*, (2011).
- [14] W. C. Chen, Nonlinear dynamics and chaos in a fractional-order financial system, *Chaos, Solitons and Fractals*, Vol. 36, 1305 (2008).
- [15] I. Schäfer and K. Krüger, Modelling of lossy coils using fractional derivatives, *Journal of Physics D: Applied Physics*, Vol. 41, 045001 (2008).
- [16] S. Westerlund and L. Ekstam, Capacitor theory, *IEEE Transactions on Dielectrics and Electrical Insulation*, Vol. 1, 826 (1994).
- [17] I. S. Jesus and J. A. T. Machado, Development of fractional order capacitors based on electrolyte processes, *Nonlinear Dynamics*, Vol. 56, 45 (2009).
- [18] C. Yang and Y. Shang, Characterisation of CMOS material, *IEEE Transactions on Electron Devices*, Vol. 62, 3012 (2015).

- [19] S. Westerlund and L. Ekstam, Capacitor theory, *IEEE Transactions on Dielectrics and Electrical Insulation*, Vol. 1, (1984).
- [20] J. Bisquert, G. Garcia-Belmonte, P. Bueno, E. Longo and L. O. S. Bulhoes, Impedance of constant phase element (CPE)-blocked diffusion in film electrodes, *Journal of Electroanalytical Chemistry*, Vol. 452, 229 (1998).
- [21] P. Veeraian, U. Gandhi and U. Mangalanathan, Analysis of fractional order inductive transducers, *The European Physical Journal Special Topics*, Vol. 226, 3851 (2018).
- [22] M. E. Fouda, A. S. Elwakil, A. G. Radwan and B. J. Maundy, Fractional-Order Two-Port Networks, *Hindawi Publishing Corporation*, Vol. 2016, (2016).
- [23] A. T. Machado and A. M. S. F. Galhano, Fractional order inductive phenomena based on the skin effect, *Nonlinear Dynamics*, Vol. 68, 107 (2012).
- [24] M. C. Tripathy, D. Mondal, K. Biswas and S. Sen, Experimental studies on realization of fractional inductors and fractional-order bandpass filters, *International Journal of Circuit Theory and Applications*, Vol. 43, 1183 (2015).
- [25] P. Veeraian, U. Gandhi and U. Mangalanathan, Fractional order Linear Variable Differential Transformer: Design and analysis, *International Journal of Electronics and Communications*, Vol. 79, 141 (2017).
- [26] J. Wen-An and C. Li-Qun, Snap-through piezoelectric energy harvesting, *Journal of Sound and Vibration*, Vol. 333, 4314 (2014).
- [27] J. Wen-An and C. Li-Qun, Stochastic averaging of energy harvesting systems, *International Journal of Non-Linear Mechanics*, Vol. 86, 174 (2016).
- [28] J. VanZwol's, Designing battery packs for thermal extremes, *Power Electronics Technology*, Vol. 2006, 40 (2006).

- [29] J. A. Paradiso and T. Starner, Energy Scavenging for Mobile and Wireless Electronics, *IEEE Pervasive Computing*, Vol. 4, 18 (2005).
- [30] R. Shad, D. Steingart, L. Frechette, P. Wright and J. Rabaey, Power Sources for Wireless Sensor Networks, *Springer-Verlag Berlin Heidelberg New York* 2920, Vol. 1 (2004).
- [31] S. M. Mousavi, E. S. Mostafavi and P. Jiao, Next generation prediction model for daily solar radiation on horizontal surface using a hybrid neural network and simulated annealing method, *Energy Conversion and Management*, Vol. 153, 671 (2017).
- [32] V. A. Milichko, A. S. Shalin, I. S. Mukhin, A. E. Kovrov, A. A. Krasilin, A. V. Vinogradov, P. A. Belov, and C. R. Simovski, Solar photovoltaics: current state and trends, *Physics-Uspeski*, Vol. 59, 727 (2016).
- [33] Wind, Global water and power—solutions for a renewable future, <http://globalwaterandpower.com/wind/>, site visited (2009).
- [34] M. Ujihara, G. Carman and D. Lee, Thermal energy harvesting device using ferromagnetic materials, *Applied Physics Letters*, Vol. 91, 093508 (2007).
- [35] G. Sebald, D. Guyomar and A. Agbossou, On thermoelectric and pyroelectric energy harvesting, *Smart Materials and Structures*, Vol. 18, 125006 (2009).
- [36] Micropelt Energy Harvesting Thermal Generators-TE-Power Plus, [http : //www.micropelt.com/applications/te_ power_ plus.php](http://www.micropelt.com/applications/te_power_plus.php).
- [37] M. Lallart, S. Pruvost and D. Guyomar, Electrostatic energy harvesting enhancement using variable equivalent Permittivity, *Physics Letters A*, Vol. 375, 3921 (2011).
- [38] S. P. Beeby, M. J. Tudor, and N. M. White, Energy harvesting vibration sources for microsystems applications, *Measurement science and technology*, Vol. 17, R175 (2006).

- [39] S. Roundy, K. S. J. Pister and P. K. Wright, Micro-electrostatic vibration-to-electricity converters, *ASME International Mechanical Engineering Congress and Exposition*, (2002).
- [40] S. Roundy, P. K. Wight and J. Rabaey, A study of low level vibrations as a power source for wireless sensor nodes, *Computer Communications*, Vol. 26, 1131 (2003).
- [41] F. Peano and T. Tambosso, Design and optimization of a mems electret-based capacitive energy scavenger, *Journal of Microelectromechanical Systems*, Vol.14, 429 (2005).
- [42] H. Lo and Y. Tai, Parylene-based electret power generators, *Journal of Micromechanics and Microengineering*, Vol. 18, 104006 (2008).
- [43] Y. Sakane, Y. Suzuki, and N. Kasagi, The development of a high-performance perfluorinated polymer electret and its application to micro power generation, *Journal of Micromechanics and Microengineering*, Vol. 18, 104011 (2008).
- [44] R. Pierret, *Semiconductor Device Fundamentals*, New York: Addison-Wesley Publishing Company, (1996).
- [45] R. Solecki and R. J. Conant, *Advanced Mechanics of Materials*, New York: Oxford University Press, (2003).
- [46] B. Gusarov, PVDF piezoelectric polymers: Characterization and application to thermal energy harvesting, *Doctorate of Philosophy, Alpes*, (2015).
- [47] S. Roundy, Energy Scavenging for Wireless Sensor Nodes with a Focus on Vibration to Electricity Conversions, *Doctorate of Philosophy, Berkeley*, (2003).
- [48] H. F. Tiersten, *Linear Piezoelectric Plate Vibrations*, New York: Plenum Press, (1969).
- [49] W. P. Mason, *Piezoelectric Crystals and Their Application to Ultrasonics*, New York: Van Nostrand, (1950).

- [50] S. Priya, D. J. Inman, *Energy Harvesting Technologies*, Springer: Berlin, Germany, (2009).
- [51] C. Keawboonchuay and T. Engel, Electrical power generation characteristics of piezoelectric generator under quasi-static and dynamic stress conditions *Industrial Electronics, IEEE Transactions Ultrason. Ferroelectric Freq. Control*, Vol. 50, 82 (2003).
- [52] A. Khaligh, P. Zeng and C. Zheng, Kinetic Energy Harvesting Using Piezoelectric and Electromagnetic Technologies State of the Art, *IEEE Transactions on Industrial Electronics*, Vol. 57, 850 (2010).
- [53] L. Zhou, J. Sun, X. Zheng, S. Deng, J. Zhao, S. Peng, Y. Zhang, X. Wang and H. Cheng, A model for the energy harvesting performance of shear mode piezoelectric cantilever, *Sensors and Actuators A: Physical*, Vol. 179, 185 (2012).
- [54] Z. Y. Wen, D. L. Li, Z. G. Shang, X. Q. Zhao, L. C. Deng and G. X. Luo, A mems piezoelectric cantilever beam array for vibration energy harvesting, *Key Engineering Materials*, Vol. 562, 1052 (2013).
- [55] J. W. Cryns, B. K. Hatchell, E. S. Rojas and K. L. Silvers, Experimental analysis of a piezoelectric energy harvesting system for harmonic, random, and sine on random vibration, *Advances in Acoustics and Vibration*, (2013).
- [56] J. Ajitsaria, S. Y. Choe, D. Shen and D. J. Kim, Modeling and analysis of a bi-morph piezoelectric cantilever beam for voltage generation, *Smart Materials and Structures*, Vol. 16, 447 (2007).
- [57] R. Ly, M. Rguiti, S. D Astorg, A. Hajjaji, C. Courtois and A. Leriche, Modeling and characterization of piezoelectric cantilever bending sensor for energy harvesting, *Sensors and Actuators A: Physical*, Vol. 168, 95 (2011).

- [58] L. Zhou, J. Sun, X. J. Zheng, S. F. Deng, J. H. Zhao, S. T. Peng, Y. Zhang, X. Y. Wang, H. B. Cheng, A model for the energy harvesting performance of shear mode piezoelectric cantilever, *Sensors and Actuators A: Physical*, Vol. 179, 185 (2012).
- [59] S. Roundy and P. K. Wright, A piezoelectric vibration based generator for wireless electronics, *Smart Materials and Structures*, Vol. 13, 1131 (2004).
- [60] X. Chen, T. Yang, W. Wang and X. Yao, Vibration energy harvesting with a clamped piezoelectric circular diaphragm, *Ceramics International*, Vol. 38, S271 (2012).
- [61] D. Zhu, S. Beeby, M. J. Tudor and N. R. Harris, A credit card sized self-powered smart sensor node, *Sensors and Actuators A: Physical*, Vol. 169, 317 (2011).
- [62] J. G. Rocha, L. M. Goncalves, P. F. Rocha, M. P. Silva and S. Lanceros-Mendez, Energy harvesting from piezoelectric materials fully integrated in footwear, *IEEE Transactions On Industrial Electronics*, Vol. 57, 813 (2010).
- [63] L. Moro and D. Benasciutti, Harvested power and sensitivity analysis of vibrating shoe mounted piezoelectric cantilevers, *Smart Materials and Structures*, Vol. 19, 115011 (2010).
- [64] W. R. Ledoux and H. J. Hillstrom, Acceleration of the calcaneus at heel strike in neutrally aligned and pes planus feet, *Clin Biomech*, Vol. 16, 608 (2001).
- [65] L. Mateu and F. Moll, Appropriate charge control of the storage capacitor in a piezoelectric energy harvesting device for discontinuous load operation, *Sensors and Actuators A: Physical*, Vol. 132, 302 (2006).
- [66] S. N. Shenck and J. A. Paradiso, Energy scavenging with shoe-mounted piezoelectrics, *IEEE Micro*, Vol. 21, 30 (2001).
- [67] D. Spreemann and Y. Manoli, Electromagnetic Vibration Energy Harvesting Devices, *Springer Series in Advanced Microelectronics*, (2012).

- [68] M. Shi, Energy Harvesting from Wind-Induced Vibration of Suspension Bridges, *Doctorate of Philosophy, Massachusetts Institute of Technology*, (2013).
- [69] Z. Xu, X. Shan, D. Chen and T. Xie, A Novel Tunable Multi-Frequency Hybrid Vibration Energy Harvester Using Piezoelectric and Electromagnetic Conversion Mechanisms, *Applied Sciences*, Vol. 6, 10 (2016).
- [70] D. Spreemann, D. Hoffmann, B. Folkmer and Y. Manoli, Numerical optimization approach for resonant electromagnetic vibration transducer designed for random vibration, *Journal of Micromechanics and Microengineering*, Vol. 18 (2008).
- [71] K. W. Yung, P. B. Landecker and D. D. Villani, An analytic solution for the force between two magnetic dipoles, *Magnetic and Electrical Separation*, Vol. 9, 39 (1998).
- [72] C. R. Saha, T. O'Donnell, H. Loder, S. Beeby and J. Tudor, Optimization of an electromagnetic energy harvesting device, *IEEE Transactions on Magnetics*, Vol. 42, 3509 (2006).
- [73] Z. Wang, B. Wang, M. Wang, H. Zhang and W. Huang, Model and experimental study of permanent magnet vibration-to-electrical power generator, *IEEE Transactions on Application Supercon*, Vol. 20, 1110 (2010).
- [74] B. A. M. Owens and B. P. Mann, Linear and nonlinear electromagnetic coupling models in vibration-based energy harvesting, *Journal of Bifurcation and Chaos*, Vol. 331, 922 (2011).
- [75] A. A. G. Bernal, L. L. E. García, The modelling of an electromagnetic energy harvesting architecture, *Applied Mathematical Modelling*, Vol. 36, 4728 (2011).
- [76] M. El-hami, P. G. Jones, N. M. White, M. Hill, S. Beeby, E. James, A. D Brown and J. N Ross, Design and fabrication of a new vibration-based electromechanical power generator, *Sensors and Actuators A: Physical*, Vol. 92, 335 (2001).
- [77] P. G. Jones, An electromagnetic, vibration-powered generator for intelligent sensor systems, *Sensors and Actuators A: Physical*, Vol. 110, 344 (2004).

- [78] S. P. Beeby, R. N. Torah, M. J. Tudor, P G. Jones, T. O'Donnell, C. R. Saha and S. Roy, A micro electromagnetic generator for vibration energy harvesting, *Journal of Micromechanics and Microengineering*, Vol. 17, 1257 (2007).
- [79] D. Zhu, S. P. Beeby, M. J. Tudor and N. R. Harris, A planar electromagnetic vibration energy harvester with a Halbach array, *In Power MEMS*, (2011).
- [80] T. Sterken, P. Fiorini and R. Puers, Motion-based generators for industrial applications, *The Symposium on Design, Test, Integration and Packaging of MEMS/MOEMS, Stresa, Italy*, (2006).
- [81] C. R. Saha, T. O Donnell, N. Wang and P. McCloskey, Electromagnetic generator for harvesting energy from human motion, *Sensors and Actuators A: Physical*, Vol. 47, 248 (2008).
- [82] A. Rahimi, Ö. Zorlu, A. Muhtaroglu and H. Klah, A Compact Electromagnetic Vibration Harvesting System with High Performance Interface Electronics, *In Eurosensors XXV*, Vol. 25, 215 (2011).
- [83] T. Von Büren and G. Tröster, Design and optimization of a linear vibration driven electromagnetic micro-power generator, *Sensors and Actuators A: Physical*, Vol. 135, 765 (2007).
- [84] P. Wang, H. Liu, X. Dai, Z. Yang, Z. Wang and X. Zhao, Design, simulation, fabrication and characterization of a micro electromagnetic vibration energy harvester with sandwiched structure and air channel, *Microelectronics Journal*, Vol. 43, 154 (2012).
- [85] R. L. Waters, B. Chisum, H. Jazo, M. Fralick, S. Diego and N. Warfare, Advanced Integrated Circuits, and Costa Mesa: Development of an Electro-Magnetic Transducer for Energy Harvesting of Kinetic Energy and its Applicability to a MEMS scale Device, *In Nanopower*, Vol. 1 (2008).

- [86] S. Kulkarni, E. Koukharenko, R. Torah, J. Tudor, S. Beeby, T. O'Donnell and S. Roy, Design, fabrication and test of integrated micro-scale vibration-based electromagnetic generator, *Sensors and Actuators A: Physical*, Vol. 145, 336 (2008).
- [87] B. A. Owens and B. P. Mann, Linear and nonlinear electromagnetic coupling models in vibration-based energy harvesting, *Journal of Sound and Vibration*, Vol. 331, 922 (2012).
- [88] M. Borowiec, G. Litak, M. I. Friswell, S. F. Ali, S. Adhikari, A. W. Lees and O. Bilgen, Energy harvesting in piezoelectric systems driven by random excitations, *International Journal of Structural Stability and Dynamics*, Vol. 13, 1340006 (2013).
- [89] C. N. Dueyou Buckjohn, M. Siewe Siewe, I. S. Mokem Fokou, C. Tchawoua and T. C. Kofane, Investigating bifurcations and chaos in magnetopiezoelectric vibrating energy harvesters using Melnikov theory, *Physica Scripta*, Vol. 88, 015006 (2013).
- [90] M. Coccolo, G. Litak, M. J. Seoane and A. F. S. Miguel, Energy harvesting enhancement by vibrational resonance, *International Journal of Bifurcation and Chaos*, Vol. 24, 1430019 (2014).
- [91] S. M. Shahruz, Design of mechanical band-pass filters for energy scavenging, *Journal of Sound and Vibration*, Vol. 292, 987 (2006).
- [92] R. Masana and M. F. Daqaq, Relative performance of a vibratory energy harvester in mono- and bistable potentials, *Journal of Sound and Vibration*, Vol. 330, 6036 (2011).
- [93] Yildiz, Zhu, Pecan and Guo, Potential Ambient Energy Harvesting Systems and Techniques, *IEEE Journal of Solid-State Circuits*, Vol. 33, 687 (2007).
- [94] Infinite Power Solutions, *THINERGY micro-energy cell (MEC) product overview*, *Technology Representative*, Vol. 6, 14 (2012).

- [95] J. Li and X. Wang, Research Update, Materials design of implantable nanogenerators for biomechanical energy harvesting, *APL Materials*, Vol. 5, 073801 (2017).
- [96] E. Sazonov, H. Li, D. Curry and P. Pillay, Self-powered sensors for monitoring of highway bridges, *Sensors Journal, IEEE*, Vol. 9, 1422 (2009).
- [97] A. M. Hedayetullah, Analysis of piezoelectric energy harvesting for bridge health monitoring systems, *Doctorate of Philosophy, University of Wales Swansea*, (2010).
- [98] G. Park, T. Rosing, M. Todd, C. Farrar and W. Hodgkiss, Energy harvesting for structural health monitoring sensor networks, *Journal of Infrastructure Systems*, Vol. 14, 64 (2008).
- [99] E. Romero, R. O. Warrington and M. R. Neuman, Energy scavenging sources for biomedical sensors, *Physiol Meas*, Vol. 30, R35 (2009).
- [100] P. Mitcheson, Energy harvesting for human wearable and implantable biosensors, *biosensors*, Vol. 6, 3432 (2010).
- [101] K. Miller and B. Ross, An introduction to the fractional calculus and fractional differential Equations, *John Willey Some line, New York*, (1993).
- [102] R. Gorenflo and H. Mainardi, Essentials of fractional calculus, *Preprint submitted to MaPhySto Center*, (2000).
- [103] K. Oldham and J. Spanier, The fractional calculus, *Academic Press, New York London*, (1974).
- [104] I. Podlubny, Fractional differential equations, *Academic Press, San Diego*, (1999).
- [105] M. A. Moreles and R. Lainez, Mathematical modelling of fractional order circuits, *physics Class-ph*, (2016).

- [106] L. Debnath, Recent applications of fractional calculus to science and engineering, *International Journal of Mathematics and Mathematical Sciences*, Vol. 54, 3413 (2003).
- [107] A. Soltan, A. G. Radwan and A. M. Soliman, Analysis of fractional order inductive transducers, *International Journal of Circuit Theory and Applications*, Vol. 44, 1 (2015).
- [108] M. C. Tripathy, D. Mondal, K. Biswas and S. Sen, Experimental studies on realization of fractional inductors and fractional-order bandpass-filters, *International Journal of Circuit Theory and Applications*, Vol. 43, 1183 (2015).
- [109] R. L. Bagley and P. J. Torvik, A theoretical basis for the application of fractional calculus to viscoelasticity, *Journal of Rheology*, Vol. 27, 201 (1983).
- [110] R. L. Bagley and P. J. Torvik, Fractional calculus a different approach to the analysis of viscoelastically damped structures, *AIAA Journal*, Vol. 21, 741 (1983).
- [111] R. L. Bagley and P. J. Torvik, Fractional calculus in the transient analysis of viscoelastically damped structures, *AIAA Journal*, Vol. 23, 918 (1985).
- [112] C. G. Koh and J.M. Kelly, Application of fractional derivatives to seismic analysis of base-isolated models, *Earthquake Engineering and Structural*, Vol. 19, 229 (1990).
- [113] N. Makris and M. C. Constantinou, Spring-viscous damper systems for combined seismic and vibration isolation, *Earthquake Engineering and Structural*, Vol. 21, 649 (1992).
- [114] J. Cao, S. Zhou, D.J. Inman and Y. Chen, Chaos in the fractionally damped broadband piezoelectric energy generator, *Nonlinear Dynamics*, Vol. 80, 1705 (2014).
- [115] C. A. K. Kwuimy, G. Litak and C. Nataraj, Nonlinear analysis of energy harvesting systems with fractional order physical properties, *Nonlinear Dynamics*, Vol. 80, 491 (2015).

- [116] B. Zhang, B. Ducharne, D. Guyomar and G. Sebald, Energy harvesting based on piezoelectric Ericsson cycles in a piezoceramic material, *The European Physical Journal Special Topics*, Vol. 222, 1733 (2013).
- [117] G. M. Ngueuteu and P. Woafu, Dynamics and synchronization analysis of coupled fractional-order nonlinear electromechanical systems, *Mechanics Research Communications*, Vol. 46, 20 (2012).
- [118] T. M. Atanackovic, S. Pilipovic and D. Zorica, Forced oscillations of a body attached to a viscoelastic rod of fractional derivative type, *International Journal of Engineering Science*, Vol. 64, 54 (2013).
- [119] J. Deng, W. C. Xie and M. D. Pandey, Higher-order stochastic averaging to study stability of a fractional viscoelastic column, *Journal of Sound and Vibration*, Vol. 333, 6121 (2014).
- [120] S. M. Hosseini, H. Kalhori, A. Shooshtari and S. N. Mahmoodi, Analytical solution for nonlinear forced response of a viscoelastic piezoelectric cantilever beam resting on a nonlinear elastic foundation to an external harmonic excitation, *Composites Part B: Engineering*, Vol. 67, 464 (2014).
- [121] E. Lorenz, G. Araujo, A. Cuevas, Solar Electricity: Engineering of Photovoltaic Systems, *Engineering Transportation*, (1994).
- [122] Gergaud O., Energy Modeling and Economic Optimization of a Network-Associated Solar and Photovoltaic Generation System Associated with an Accumulator, *Doctorate of Philosophy, Cachan ENS*, (2002).
- [123] V. M. Bavel, V. Leonov, R. F. Yazicioglu, T. Torfs, C. V. Hoof, E. N. Posthuma and R. J. M. Vullers, Wearable Battery-free Wireless 2-Channel EEG Systems Powered by Energy Scavengers, *Sensors Transducers Journal*, Vol. 94, 103 (2008).

- [124] V. Leonov, T. Torfs, C. Van Hoof and R. J. M. Vullers, Smart Wireless Sensors Integrated in Clothing: An Electrocardiography System in a Shirt Powered Using Human Body Heat, *Sensors Transducers Journal*, Vol. 107, 165 (2009).
- [125] A. Muhtaroglu, A. Yokochi and A. Vonjouanne, Integration of thermoelectrics and photovoltaics as auxiliary power sources in mobile computing applications, *Journal of Power Sources*, Vol. 177, 239 (2008).
- [126] C. Wang, C. Yanlong and X. Jin, Piezoelectric and electromagnetic hybrid energy harvester for powering wireless sensor nodes in smart grid, *Journal of Mechanical Science and Technology*, Vol. 29, 4313 (2015).
- [127] B. H. Madinei, K. H. Haddad, S. Adhikari and M. I. Friswell, Shock Vibration, Aircraft/Aerospace, Energy Harvesting, Acoustics Optics, *Proceedings of the 35th IMAC*, Vol. 9 (2017).
- [128] T. Wacharasindhu and J. W. Kwon, A micromachined energy harvester from a keyboard using combined electromagnetic and pieoelectrique conversion, *Journal of Micromechanics and Microengineering*, Vol. 18, 104016 (2008).
- [129] B. Lee and L. Wei, Hybrid energy harvester based on piezoelectric and electromagnetic mechanisms, *Journal of Micro/Nanolithography, MEMS, and MOEMS*, Vol. 9, 023002 (2010).
- [130] M. A. Karami and D. J. Inman, Equivalent damping and frequency change for linear hybrid vibrational energy harvesting systems, *Journal of Sound and Vibration*, Vol. 330, 5583 (2011).
- [131] F. I. S. Mokem, D. B. C. Nono, S. M. Siewe and C. Tchawoua, Probabilistic behavior analysis of a sandwiched buckled beam under Gaussian white noise with energy harvesting perspectives, *Chaos Solitons Fractals*, Vol. 92, 101 (2016).

- [132] M. S. Siewe, C. N. D. Buckjohn: Heteroclinic motion and energy transfer in coupled oscillator with nonlinear magnetic coupling, *Nonlinear Dynamics*, Vol. 77, 297 (2014).
- [133] C. H. Nguyen, D. S. Nguyen and E. Halvorsen, Experimental Validation of Damping Model for a MEMS Bistable Electrostatic Energy Harvester, *Journal of Physics: Conference Series*, Vol. 557, 012114 (2014).
- [134] S. Zaitsev, O. Shtempluck, E. Buks and O. Gottlieb, Nonlinear damping in a micro-mechanical oscillator, *Nonlinear Dynamics*, Vol. 67, 859 (2012) .
- [135] M. G. Tehrani, L. Simeone and S. J. Elliot, Energy harvesting using nonlinear damping, *in: ENOC Conference, Wien*, (2014).
- [136] M. G. Tehrani and S. J. Elliot, Extending the dynamic range of an energy harvester using nonlinear damping, *Journal of Sound and Vibration*, Vol. 333, 623 (2014).
- [137] B. Ravindra and A. K. Mallik, Role of nonlinear dissipation in soft Duffing oscillators, *Physical Review E*, Vol. 49, 4950 (1994).
- [138] M. A. F. Sanjuan, The effect of nonlinear damping on the universal escape oscillator, *International Journal of Bifurcation and Chaos*, Vol. 9, 735 (1999).
- [139] R. Yamapi, J. B. Chabi Orou and P. Woafu, Harmonic Dynamics and Transition to Chaos in a Nonlinear Electromechanical System with Parametric Coupling, *Physica Scripta*, Vol. 67, 269 (2003).
- [140] R. Yamapi and S. Bowong, Dynamics and chaos control of the self-sustained electromechanical device with and without discontinuity, *Communications in Nonlinear Science and Numerical Simulation*, Vol. 11, 355 (2006).
- [141] K. S. Miller and B. Ross, An Introduction to the Fractional Calculus and Fractional Differential Equations, *Wiley, New York*, (1993).

- [142] N. M. Krylov and N. N. Bogolyubov, Introduction to non-linear mechanics, *Princeton University Press*, (1947).
- [143] N. N. Bogoliubov and Y. A. Mitropolsky, Asymptotic Methods in the Theory of Nonlinear Oscillations, *Gordon and Breach, New York*, (1961).
- [144] L. Chen and W. Zhu, Stochastic jump and bifurcation of duffing oscillator with fractional derivative damping under combined harmonic and white noise excitations, *International Journal of Non-Linear Mechanics*, Vol. 46, 1324 (2011).
- [145] A. Leung and Z. Guo, Forward residue harmonic balance for autonomous and non-autonomous systems with fractional derivative damping, *Communications in Nonlinear Science and Numerical Simulations*, Vol. 16, 2169 (2011).
- [146] A. Leung, H. Yang and Z. Guo, The residue harmonic balance for fractional order van der Pol like oscillators, *Journal of Sound and Vibration*, Vol. 331, 1115 (2012).
- [147] M. Xiao, W. X. Zheng and J. Cao, Approximate expressions of a fractional order van der pol oscillator by the residue harmonic balance method, *Mathematics and Computers in Simulation*, Vol. 9, 1 (2013).
- [148] W. S. Cho, Nonlinear random vibration analytical techniques and applications, *New York: CRC Press Taylor and Francis Group*, (2012).
- [149] R. L. Stratonovich, Topics in the Theory of Random Noise, *vol.II*, *Gordon and Breach, New York*, (1967).
- [150] R. A. Ibrahim, Parametric Random Vibration, *Chapter5*, *John Wiley and Sons Inc, New York*, (1985).
- [151] J. B. Roberts and P. D. Spanos, Stochastic averaging: An approximate method of solving random vibration problems, *International Journal of Non-Linear Mechanics*, Vol. 21, 111 (1986).

- [152] W. Q. Zhu, Stochastic averaging methods in random vibration, *Applied Mechanics Reviews*, Vol. 41, 189 (1988).
- [153] N. S. Namachchivaya, Stochastic bifurcation, *Applied Mathematics and Computers*, Vol. 38, 10159 (1990).
- [154] R. L. Stratonovich, Topics in the theory of random noise volume I: general theory of random processes nonlinear transformations of signals and noise, *Gordon and Breach, New York*, (1963).
- [155] R. Z. Khasminskii, A limit theorem for the solution of differential equations with random right hand sides, *Theory of Probability and Its Applications*, Vol. 11, 390 (1966).
- [156] V. S. Anishchenko, V. Astakhov, A. Neiman, T. Vadivasova and L. Schimansky-Geier, *Tutorial and Modern Developments*, Springer, Berlin, (2007).
- [157] H. Risken and T. Frank, The Fokker-Planck Equation: Methods of Solution and Applications, *Springer Science Business Media*, (1996).
- [158] M. I. Freidlin and A. D. Wenzel, Random Perturbations in Dynamical Systems, *Springer, New York*, (1984).
- [159] E. Hairer and G. Wanner, Solving Ordinary Differential Equations II, *Springer-Verlag, Berlin Heidelberg New York*, (1991).
- [160] J. H. Desmond, An Algorithmic Introduction to Numerical Simulation of Stochastic Differential Equations, *SIAM Review*, Vol. 43, 525 (2001).
- [161] T. Raul and C. Pere, Stochastic Numerical Methods, An Introduction for Students and Scientists, *Wiley-VCH Verlag GmbH, Weinheim*, (2014).
- [162] R. Benzi, A. Sutera and A. Vulpiani, The mechanism of stochastic resonance, *Journal of Physics A : Mathematical and General*, Vol. 14, L453 (1981).

- [163] S. Arathi, S. Rajasekar, J. Kurths, Characteristics of stochastic resonance in asymmetric dufing oscillator, *International Journal of Bifurcation and Chaos*, Vol. 21, 2729 (2011).
- [164] H. Crauel and M. Gundlach, Bifurcations of one-dimensional stochastic differential equations, *Stochastic dynamics*, New York: Springer-Verlag, (1999).
- [165] H. Gang, T. Ditzinger, C. Z. Ning and H. Haken, Stochastic resonance without external periodic force, *Physical Review Letters*, Vol. 71, 807 (1993).
- [166] G. Burgers, The El Niño stochastic oscillator, *Climate Dynamics*, Vol. 15, 521 (1999).
- [167] G. E. Uhlenbeck and L. S. Ornstein, On the Theory of the Brownian Motion, *Physical Review E*, Vol. 36, 823 (1930).
- [168] J. H. Yang, M. A. F. Sanjuan, H. G. Liu, G. Litak and X. Li, Stochastic P-bifurcation and stochastic resonance in a noisy bistable fractional-order system, *Communications in Non-linear Science and Numerical Simulation*, Vol. 41, 104 (2016).
- [169] R. N. Mantegna, B. Spagnolo, L. Testa and M. Trapanese, Stochastic resonance in magnetic systems described by Preisach hysteresis model, *Journal of Applied Physics*, Vol. 97, 10E519 (2005).
- [170] F. Diacu, The solution of the n-body problems, *The Mathematical Intelligencer*, Vol. 18, 66 (1996).
- [171] G. A. Gottwald and I. Melbourne, Comment on Reliability of the 0–1 test for chaos, *Proceedings of the Royal Society of London, Series A*, Vol. 460, 603 (2004).
- [172] G. Litak, A. Syta, M. Budhraj, and L. M. Saha, Detection of the chaotic behaviour of a bouncing ball by the 0–1 test, *Chaos, Solitons and Fractals*, Vol. 42, 1511 (2009).

- [173] L. Petrás, Fractional-order Nonlinear Systems, Modelling analysis and Simulation, *Higher Education Press, Beijing*, (2011).
- [174] G. Litak, D. Bernardini, A. Syta and A. Rysak, Analysis of chaotic non-isothermal solutions of thermomechanical shape memory oscillators, *Proceedings of the Institution of Mechanical Engineers, Part K: Journal of Multi-body Dynamics*, Vol. 222, 1637 (2013).
- [175] J. F. Heagy, T. L. Carroll and L. M. Pecora, Synchronous chaos in coupled oscillator systems, *Physical Review E*, Vol. 50, 1874 (1994).
- [176] E. B. Tchawou Tchuisseu and P. Wofo, Harvesting energy using a magnetic mass and a sliding behaviour, *Nonlinear Engineering*, Vol. 3, 89 (2014).
- [177] G. T. Oumbé Tékam, E. T. Tchuisseu, C. A. K. Kwuimy and P. Wofo, Analysis of an electromechanical energy harvester system with geometric and ferroresonant nonlinearities, *Nonlinear Dynamics*, Vol. 76, 1561 (2014).
- [178] G. T. Oumbé Tékam, C. A. K. Kwuimy and P. Wofo, Analysis of tristable energy harvesting system having fractional order viscoelastic material, *Chaos: An Interdisciplinary Journal of Nonlinear Science*, Vol. 25, 013112 (2015).
- [179] F. Rudiner, Tuned mass damper with fractional derivative damping, *Engineering Structures*, Vol. 28, 1774 (2006).
- [180] P. Kumar, S. Narayanan, S. Adhikari and M. I. Friswell, Fokker-planck equation analysis of randomly excited nonlinear energy harvester, *Journal of Sound and Vibration*, Vol. 333, 2040 (2014).
- [181] S. David, A. S. Janice, Density functional theory: A practical introduction, *John Wiley and Sons Inc : Hoboken*, (2009).
- [182] P. jung and F. Marchelsoni, Energetics of Stochastic resonance, *chaos*, Vol. 21, 047516 (2011).

- [183] B. Jae-Sung and J. I. Daniel, A preliminary study on piezo-aeroelastic energy harvesting using a nonlinear trailing-edge flap, *International Journal of Aeronautical and Space Sciences*, Vol. 16, 407 (2015).
- [184] A. Erturk, W. G. R. Vieira, C. D. J. Marqui and D. J. Inman, On the energy harvesting potential of piezoaeroelastic systems, *Applied Physics Letters*, Vol. 96, 184103 (2010).
- [185] Z. Dan and E. Evan, Energy harvesting from self-sustained aeroelastic limit cycle oscillations of rectangular wings, *Applied Physics Letters*, Vol. 105, 103903 (2014).
- [186] C. R. McInnes, D. G. Gorman and M. P. Cartmell, Enhanced vibrational energy harvesting using nonlinear stochastic resonance, *Journal of Sound and Vibration*, Vol. 318, 655 (2008).
- [187] R. Zheng, K. Nakano, H. Hu, D. Su and M. P. Cartmell, An application of stochastic resonance for energy harvesting in a bistable vibrating system, *Journal of Sound and Vibration*, Vol. 333, 2568 (2014).
- [188] L. Gammaitoni, P. Hanggi, P. Jung and F. Marchesoni, Stochastic resonance, *Reviews of Modern Physics*, Vol. 70, 223 (1998).
- [189] R. Ray and S. Sengupta, Stochastic resonance in under damped, bistable systems, *Physics Letters A*, Vol. 353, 364 (2006).
- [190] S. Herrmann, P. Imkeller, I. Pavlyukevich and D. Peithmann, Stochastic Resonance: A Mathematical Approach in the Small Noise Limit, *American mathematical Society*, (2013).
- [191] M. Kubota, T. Ryo and H. Takashi, Active and Reactive Power in Stochastic Resonance for Energy Harvesting, *IEICE TRANSACTIONS on Fundamentals of Electronics, Communications and Computer Sciences*, Vol. 98, 1537 (2015).

-
- [192] Y. Zhang, R. Zheng, T. Kaizuka, D. Su, K. Nakano and M. P. Cartmell, Broad-band vibration energy harvesting by application of stochastic resonance from rotational environments, *The European Physical Journal Special Topics*, Vol. 224, 2687 (2015).

List of Publications

1-O. Foupouapouognigni, C. Nono Dueyou Buckjohn, M. Siewe Siewe, C. Tchawoua. *Nonlinear electromechanical energy harvesters with fractional inductance*. *Chaos, Solitons and Fractals* **103**, 12–22 (2017).

2-O. Foupouapouognigni, C. Nono Dueyou Buckjohn, M. Siewe Siewe, C. Tchawoua. *Hybrid electromagnetic and piezoelectric vibration energy harvester with Gaussian white noise excitation*. *Physica A* **509**, 346–360 (2018).

Other Publications

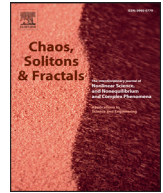
1-O. Foupouapouognigni, M. Siewe Siewe, C. Tchawoua. *Parametric Resonance and Homoclinic Chaos in a Bullard-type Dynamo*. *Theory, Applications and Future Directions*, Nova Science Publishers, Inc. , 183–200 (2013).



Contents lists available at ScienceDirect

Chaos, Solitons and Fractals

Nonlinear Science, and Nonequilibrium and Complex Phenomena

journal homepage: www.elsevier.com/locate/chaos

Frontiers

Nonlinear electromechanical energy harvesters with fractional inductance



O. Foupouapouognigni, C. Nono Dueyou Buckjohn, M. Siewe Siewe*, C. Tchawoua

Université de Yaoundé I, Faculté des sciences, Département de Physique, Laboratoire de Mécanique, BP: 812 Yaoundé-Cameroun, Cameroun

ARTICLE INFO

Article history:

Received 9 October 2016

Revised 10 April 2017

Accepted 15 May 2017

Keywords:

Electromechanical system

Energy harvesters

Fractional inductance

Parametric coupling

0-1 test

ABSTRACT

In this paper, an electromechanical energy harvesting system exhibiting the fractional properties and subjected to the harmonic excitation is investigated. The main objective of this paper is to discuss the system performance with parametric coupling and fractional derivative. The dynamic of the system is presented, plotting bifurcation diagram, poincaré map, power spectral density and phase portrait. These results are confirmed by using 0 – 1 test. The harmonic balance method is used with the goal to provide the analytical response of the electromechanical system. The numerical simulation validates the results obtained by this analytical technique. In addition, replacing the harmonic by the random excitation, the impact of noise intensity, the fractional order derivatives κ and the amplitude of the parametric coupling γ is investigated in detail. It points out from these results that for the best choice of D , κ and γ , the output power can be improved.

© 2017 Elsevier Ltd. All rights reserved.

1. Introduction

In the past two decades, fractional calculus has attracted the attention of scientists and engineering, resulting to the development of many applications [1–3]. However, this field of research did not grow until recently, largely because the underlying mathematics was difficult. Thanks to the many methods for approximation of the fractional derivative and integral available in the literature nowadays, this barrier is considerably eliminated. Thus, fractional-order systems have been intensively studied in various areas namely, in biology, physics, chemistry, traffic systems, genetic algorithms and control systems [4–13]. Indeed, the concept of fractional derivative goes back to discussing that Leibniz and l'Hospital had over three under years ago about the half order derivatives. The interest accorded to this term is due to the experiments investigations which had shown, fractional order derivative appears to render real phenomena meaningful. For instance, in mechanical engineering, one used it to model viscoelastic properties in the physical system.

In physics, most particularly in the domain of energy harvesting, scientific research is mainly focused on enhancing the efficiency of the system. Many researchers groups [14–17] had consid-

ered nonlinear effects to reach widening the frequency bandwidth of the system. C.Nono et al. [19] used the Melnikov theory to discuss the performance of a bistable harvester by analyzing the critical condition for homoclinic bifurcation that could induce chaos in the system. Owens and Mann [20] discussed the effects of linear and nonlinear transduction and demonstrated that with a suitable design, nonlinear coupling is better than linear. Borowiec et al. [21] proposed a beam consisted of substrate and sandwiched with a tip mass which transduce the bending strains induced by the random horizontal displacement into electrical charge. They analyzed the efficiency of this nonlinear device by focusing on the region of stochastic resonance where beam motion has a large amplitude. Coccolo et al. [22] have studied the electrical response of a bistable system, by using a double-well Duffing oscillator, connected to a circuit through piezoceramic elements and driven by both a low and a high frequency forcing, where the high frequency forcing is the environmental vibration, while the low frequency is controlled by us. They showed that the response amplitude at the low-frequency increases, reaches a maximum and then decreases to a certain range of the high frequency forcing. They also demonstrated in their work that by enhancing the oscillations, we can harvest more electric energy.

Recently, a large amount of work in engineering vibrations showed that long-memory factor exists in many practical systems, which are difficult to be accurately described by integer-order models [23–28]. Bagley and Torvik [29–31] pointed out that half-order fractional derivative models can quite well describe the fre-

* Corresponding author.

E-mail addresses: oumarfoupouagnigni@yahoo.fr (O. Foupouapouognigni), bucknono@yahoo.fr (C. Nono Dueyou Buckjohn), martinsiewesiewe@yahoo.fr (M. Siewe Siewe), ctchawoua@yahoo.fr (C. Tchawoua).

quency dependence damping of viscoelastic materials. Kelly et al. [32] have applied the fractional Kelvin model to predict the seismic response of natural rubber bearings. Markris et al. [33] presented a fractional derivative Maxwell model for a viscous damper and validated their model using experimental results. Cao et al. [34] recently considered an energy harvesting system with fractional order viscoelastic material. They showed that the fractional order property of the material enhances high-energy chaotic motion as well as inter-well periodic oscillation. Kitio et al. [35] proposed an electromechanical energy harvesting system with a fractional order current voltage relationship for the electrical circuit and fractional power law in the restoring force of its mechanical part. They authors showed that under a single-well potential configuration, for a small amplitude of the perturbation, as the order of derivative increases, the resonant amplitude of mechanical vibration decreases while the bending degree remains fairly constant. For a large amplitude of the perturbation, the output power increased, this is due to the hardening effects. However, under a double-well configuration, the fractional power stiffness strongly affects the crossing well dynamics and consequently the output electrical power. Ducharme et al. [36] built and energy harvesting devices based on piezoelectric Ericsson cycles in a piezoceramic material. They showed that by coupling an electric field and mechanical excitation on Ericsson-based cycles, the amplitude of the harvested energy can be highly increased, and can reach a maximum close to 100 times its initial value. Several electromechanical models have been the subject of such study, in particular this of Oumbé et al. [37]. In this work, the authors studied the effect of a nonlinear inductance induced by the saturation of the magnetic circuit. Siewe et al. [38] worked on an unsaturated magnetic circuit where they focused on the study of dynamics of the model (study of chaos via the Melnikov method) and the energy transfer from the mechanical to electrical subsystem without interesting to the impact of inductance upon system performance. The present work is based on this model. An originality of this work comes from the fact that we have taken into account the fractional character of the inductance [35,39]. In this previous work, the authors assume that the inductance is linear and the magnetic field through the air-gap of the permanent magnet varies with the coil position. In this case, the voltage through the self is defined as $U = L \frac{di}{dt}$. Let us notice that in the experimental investigation, the coil exhibit the fractional properties [39]. Thus, the relationship between the current and voltage is defined as follows [35] $U_L = L \frac{d^{\kappa} i}{dt^{\kappa}}$. The one of the purpose of this present paper is to investigate the impact of fractional inductance on the model propose in Ref. [38].

As pointed by Yamapi et al. [40,41], in certain circumstances, some parameters of the electromechanical device can vary with time because of the functioning constraints. This is particularly the case for the parameters of the electromagnetic coupling. In this present work, we consider that the magnetic field varies with time. This give rise to a parametric coupling which could play an important role in the improvement of the output power. The remain of the manuscript is organized as follows: Section 2 is devoted to the description of the system by a system equation. In Section 3, we evaluate analytical and numerically, the mechanical and electrical response of the system. This section is followed by the numerical simulation in Section 4. In Appendix, we have the conclusion.

2. The model and governing equations

As pointed by siewe et al. [38], the electromechanical device shown in Fig. 1 is composed of two fundamental parts: The mechanical part is composed of the mass m , the nonlinear spring and nonlinear damping, while the electrical subsystem is composed of fractional inductor L , a linear capacitor C and the linear resistor R . We particularly consider the dissipative force with nonlinear dis-

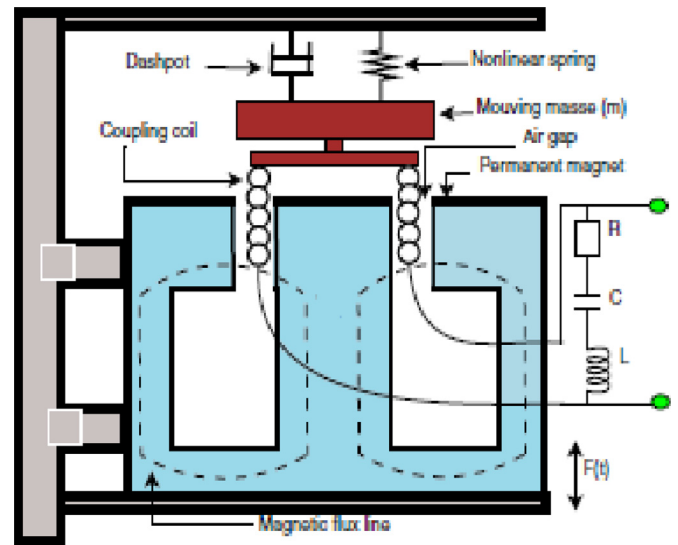


Fig. 1. Schematic model with the associated electric circuit.

sipation term proportional to the power of velocity $(y')^3$. The expressions defining damping force is as follows: [43]

$$f_d = c_1 y' + c_3 (y')^3. \quad (1)$$

Where y' is the velocity of the mass, c_1 and c_3 , the linear and nonlinear damping coefficients. The nonlinear damping introduced in this system is important insofar as it has been shown that it can improve efficiency in the context of EHS [42,43]. Moreover, it is close to the reality because experimental studies have been done recently or it appears that nonlinear dissipation is the one, that offers better performances in terms of optimization. The mathematical expression of the magnetic field is defined as in Ref. [40]

$$B = B_0 (1 + \gamma \cos(2\omega_1 t)), \quad (2)$$

where B_0 is the highest intensity that the field B reaches, γ is the amplitude of the parametric coupling. The motion equation of the system is given as follows[38]:

$$m y'' + g(y, y') - l B_0 (1 + \gamma \cos(2\omega_1 t)) q' = F(t) \\ l D_t^{\kappa+1} q + R q' + \frac{q}{c} + l B_0 (1 + \gamma \cos(2\omega_1 t)) y' = 0 \quad (3)$$

with

$$g(y, y') = c_1 y' + c_3 (y')^3 + k_0 y + k_1 y^3.$$

where $(\cdot)' = \frac{d}{dt}$, y and q are the displacement of the mass and charge respectively, k_0 and k_1 is the linear and nonlinear stiffness of the spring, while l is the length of the air gap. Using the following transformation of coordinates:

$\omega_0^2 = \frac{k_0}{m}$, $y = lx$, $q = Q_0 z$, $\alpha = \kappa + 1$ and by letting the time variable $t = \frac{\tau}{\omega_0}$, the dimensionless equation is given by:

$$\ddot{x} + f(x, \dot{x}) - \vartheta_m (1 + \gamma \cos(2\omega\tau)) \dot{z} = F(\tau), \quad (4)$$

$$\dot{z} + \beta D_{\tau}^{\alpha} z + \mu_e z + \vartheta_e (1 + \gamma \cos(2\omega\tau)) \dot{x} = 0$$

with

$$f(x, \dot{x}) = \mu_1 \dot{x} + \mu_3 \dot{x}^3 + \varrho x + \lambda x^3$$

and

$$\omega = \frac{\omega_1}{\omega_0}, \mu_1 = \frac{c_1 \omega_0}{k_0}, \mu_3 = \frac{l^2 c_3 \omega_0^3}{k_1}, \vartheta_e = \frac{l^2 B_0}{Q_0 R}$$

$$\lambda = \frac{l^2 k_1}{\omega_e^2 m}, \vartheta_m = \frac{B_0 \omega_0^3 Q_0}{k_0}, \mu_e = \frac{1}{\omega_0 R C}, \beta = \frac{\omega_0^{\kappa} L}{R}.$$

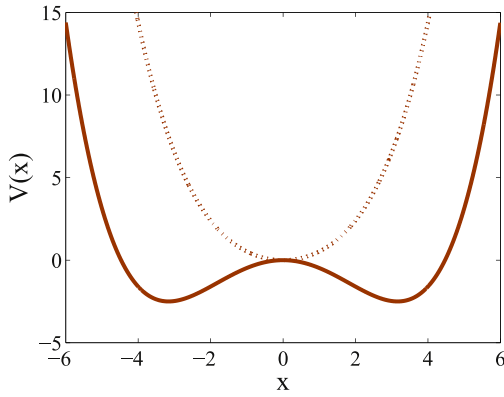


Fig. 2. Potential of the system (4) for $\lambda = 0.1$, the dot line obtained for $\rho = 1.0$ and solid line for $\rho = -1.0$.

x and z are the dimensionless displacement and current respectively. Contrary to the equations to the partial derivatives gotten in the case of the beams, the dot, as in x and z , will indicate differentiation with respect to time. ϑ_i are parameters of the coupling terms, λ is parameter due to nonlinear stiffness, μ_i and γ_e are damping coefficients, γ_e is the parametric coupling amplitude.

Throughout the paper, we consider an harmonic function with constant amplitude which can be expressed by mathematical presentation as:

$$F(\tau) = E_0 \cos(\omega\tau), \quad (5)$$

where E_0 and ω being respectively, the amplitude and frequency of the harmonic excitation.

Fig. 2 shows the potential of the mechanical part under two configuration: mono-stable and bistable for two values of linear coefficient of the stiffness. In the following, we discussed the system performance under these two configurations.

2.1. Harmonic balance method

In this section, we use the harmonic balance method [44] to provide the analytical solution of the model equation. To achieve our objective, we assume that the approximative solution of the system Eq. (4) is defined as follows:

$$x(\tau) = A \cos(\omega\tau + \varphi_1)(a) \quad (6)$$

$$z(\tau) = B \cos(\omega\tau + \varphi_2)(b)$$

where $A = \sqrt{A_1^2 + A_2^2}$ and $B = \sqrt{B_1^2 + B_2^2}$ are the amplitude of the mechanical and the electrical subsystem.

It is known in the literature that, there are many definitions of the fractional derivative. In this work, we used the Caputo's definition [45–47] given as:

$$\frac{d^\alpha z}{d\tau^\alpha} = D_\tau^\alpha[z(\tau)] = \frac{1}{\Gamma(1-\alpha)} \int_0^\tau (\tau-s)^{-\alpha} \dot{z}(s) ds. \quad (7)$$

where $0 < \alpha \leq 1$, while $\Gamma(\cdot)$ is the gamma function.

Substituting Eq. 6(b) into Eq. (7), we obtain:

$$D_\tau^\alpha[B \cos(\omega\tau + \varphi_2)] = D_\tau^\alpha[\zeta_1 \cos(\omega\tau) - \zeta_2 \sin(\omega\tau)] \quad (8)$$

with

$$\zeta_1 = B \cos \varphi_2; \quad \zeta_2 = B \sin \varphi_2,$$

By using the following approximation,

$$z(\tau - s) = B \cos(\omega(\tau - s) + \varphi_2) = B \cos(\theta_2 - \omega s),$$

with

$$\theta_2 = \omega\tau + \varphi_2.$$

Eq. (8) becomes:

$$D_\tau^\alpha[z(\tau)] = \frac{1}{\Gamma(1-\alpha)} \frac{d}{d\tau} \left[B \cos \theta_2 \int_0^\tau \frac{\cos \omega s}{s^\alpha} ds + B \sin \theta_2 \int_0^\tau \frac{\sin \omega s}{s^\alpha} ds \right] \quad (9)$$

By letting $u = \omega s$, we obtain the following expression:

$$D_\tau^\alpha[z(\tau)] = \frac{\omega^\alpha}{\Gamma(1-\alpha)} \left[-(\zeta_1 J_1 + \zeta_2 J_2) \sin \omega\tau + (\zeta_1 J_2 - \zeta_2 J_1) \cos \omega\tau \right] \quad (10)$$

with J_1 and J_2 are defined as [48]:

$$J_1 = \int_0^\tau \frac{\cos u}{u^\alpha} du = \Gamma(1-\alpha) \sin\left(\frac{\alpha\pi}{2}\right) + \frac{\sin u}{u^\alpha} + 0(u^{-\alpha-1}), \quad (11)$$

$$J_2 = \int_0^\tau \frac{\sin u}{u^\alpha} du = \Gamma(1-\alpha) \cos\left(\frac{\alpha\pi}{2}\right) - \frac{\cos u}{u^\alpha} + 0(u^{-\alpha-1}), \quad (12)$$

Taking into account Eqs. (11) and (12), Eq. (8) becomes:

$$D_\tau^\alpha[z(\tau)] = \omega^\alpha (B_1 \cos(\omega\tau) + B_2 \sin(\omega\tau)) \left(\cos\left(\frac{\alpha\pi}{2}\right) - \sin\left(\frac{\alpha\pi}{2}\right) \right). \quad (13)$$

Substituting Eqs. (13) and (6) into Eq. (4) and equating the coefficients of the terms containing only $\sin(\omega\tau)$ and $\cos(\omega\tau)$ separately to zero, we obtain the following equations:

$$\begin{aligned} (\rho - \omega^2 + \frac{3}{4}\lambda A^2)A_1 + (\mu_1\omega + \frac{3}{4}\mu_3\omega^3 A^2)A_2 + \zeta_2 B_2 - E_0 &= 0 \\ (-\mu_1\omega - \frac{3}{4}\mu_3\omega^3 A^2)A_1 + (\rho - \omega^2 + \frac{3}{4}\lambda A^2)A_2 - \zeta_1 B_1 &= 0 \\ \delta B_1 + \omega B_2 + \frac{\vartheta_e \zeta_2}{\vartheta_m} A_2 &= 0 \\ -\omega B_1 + \delta B_2 - \frac{\vartheta_e \zeta_1}{\vartheta_m} A_1 &= 0 \end{aligned} \quad (14)$$

where

$$\delta = \beta \omega^\alpha \left(\cos\left(\frac{\alpha\pi}{2}\right) - \sin\left(\frac{\alpha\pi}{2}\right) \right) + \mu_e,$$

$$\zeta_1 = \vartheta_m \omega \left(1 - \frac{\gamma}{2} \right), \quad \zeta_2 = \vartheta_m \omega \left(1 + \frac{\gamma}{2} \right).$$

Using some mathematics tools, the solution of Eq. (14), give rise to the amplitudes equation given as:

$$r_{10} A^{10} + r_8 A^8 + r_6 A^6 + r_4 A^4 + r_2 A^2 + r_1 = 0 \quad (15)$$

and

$$B^2 = b_4 A^4 + b_2 A^2 + b_0, \quad (16)$$

where all the coefficients of Eqs. (15) and (16) are defined in the appendix. The average output power is estimated using this formula:

$$P_{max} = \frac{1}{2T} \int_0^T \left(\frac{dz}{dt} \right)^2 dt. \quad (17)$$

2.2. Numerical simulation

With the goal to verify the efficiency of the analytical technique used, the numerical simulation of the system Eq. (4) is made. The physical parameters used in the simulation are given as follows: $c_1 = 0.55 \text{ kg/s}$, $c_3 = 2.5 \text{ kg/s}$, $k_0 = 25 \text{ N/m}$, $L = 1.34 \text{ H}$, $l = 0.17 \text{ m}$, $m = 1.082 \text{ kg}$, $R = 20.5 \Omega$, $k_1 = 90 \text{ N/m}$, $C = 0.01052$. The initial conditions used are $(x(0) = 0.0, \dot{x}(0) = 0.0, z(0) = 0.0)$.

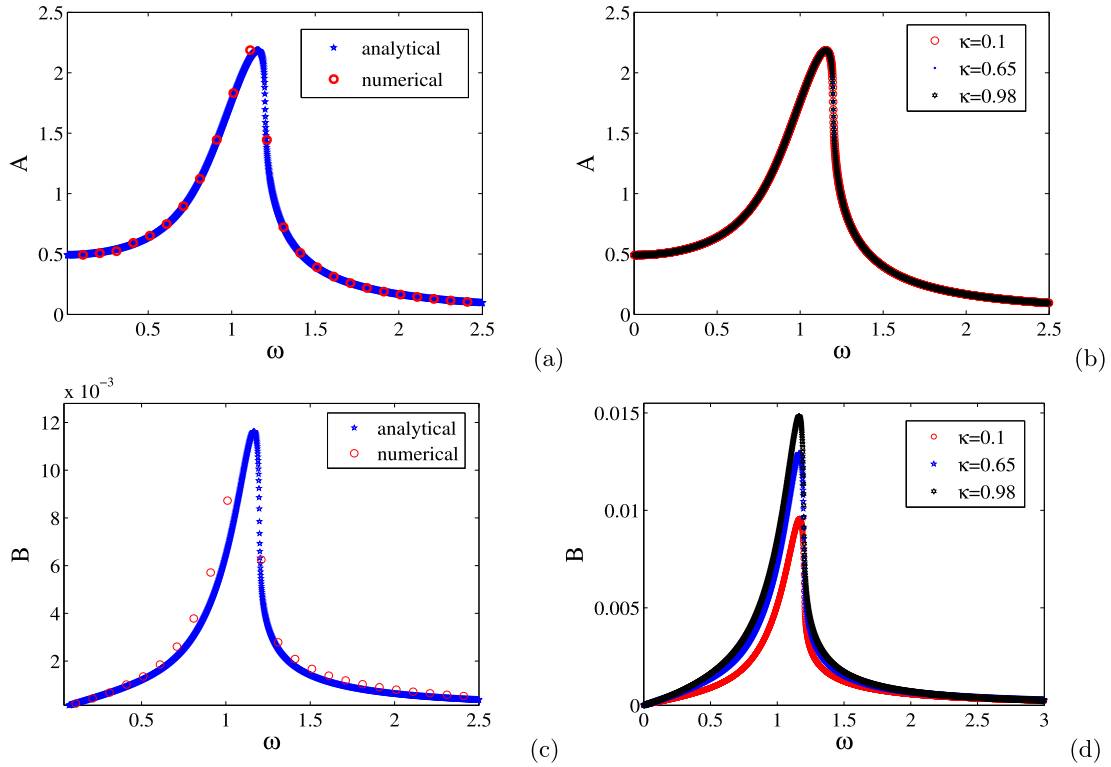


Fig. 3. Amplitudes response-curves of the driving frequency ω and $E_0 = 0.5$, $\kappa = 0.25$ with the parameters $\lambda = 0.1$, $\mu_1 = 0.1$, $\mu_3 = 0.018$, $\gamma = 0.5$, $\vartheta_m = 0.76$, $\vartheta_e = 0.0056$, $\mu_e = 0.96$ and $\varrho = 1.0$.

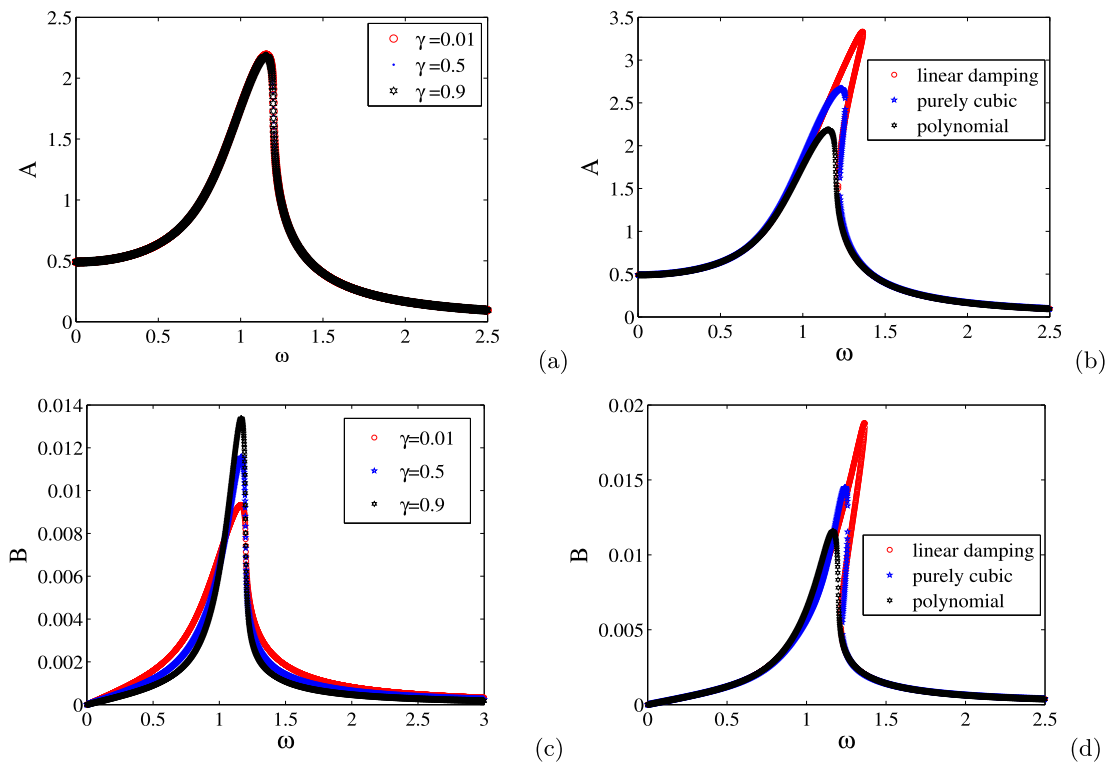


Fig. 4. Amplitudes response-curves of the driving frequency ω and $E_0 = 0.5$, $\kappa = 0.25$ with the parameters $\lambda = 0.1$, $\mu_1 = 0.1$, $\mu_3 = 0.018$, $\gamma = 0.5$, $\vartheta_m = 0.76$, $\vartheta_e = 0.0056$, $\mu_e = 0.96$ and $\varrho = 1.0$.

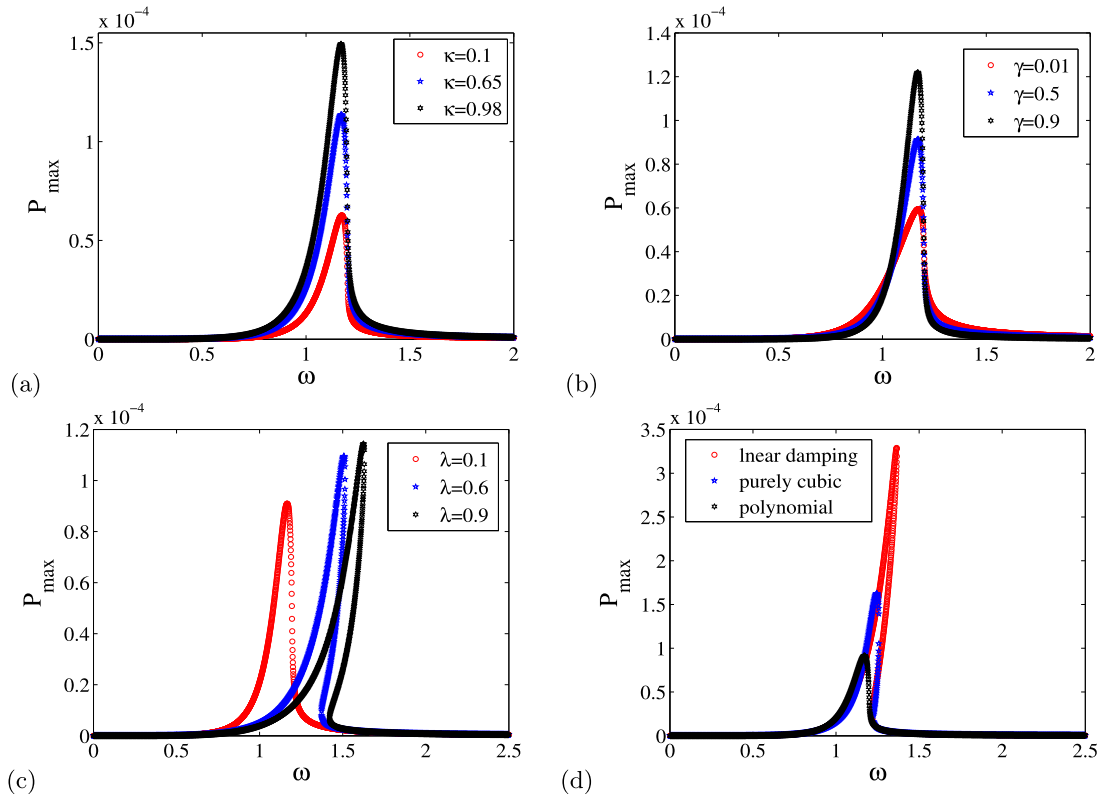


Fig. 5. Output electric power as function of the driving frequency with the parameters $\lambda = 0.1$, $\mu_1 = 0.1$, $\mu_3 = 0.018$, $\gamma = 0.5$, $\vartheta_m = 0.76$, $\vartheta_e = 0.0056$, $\mu_e = 0.96$, $Q = 1$, $E_0 = 0.5$ and $\kappa = 0.25$.

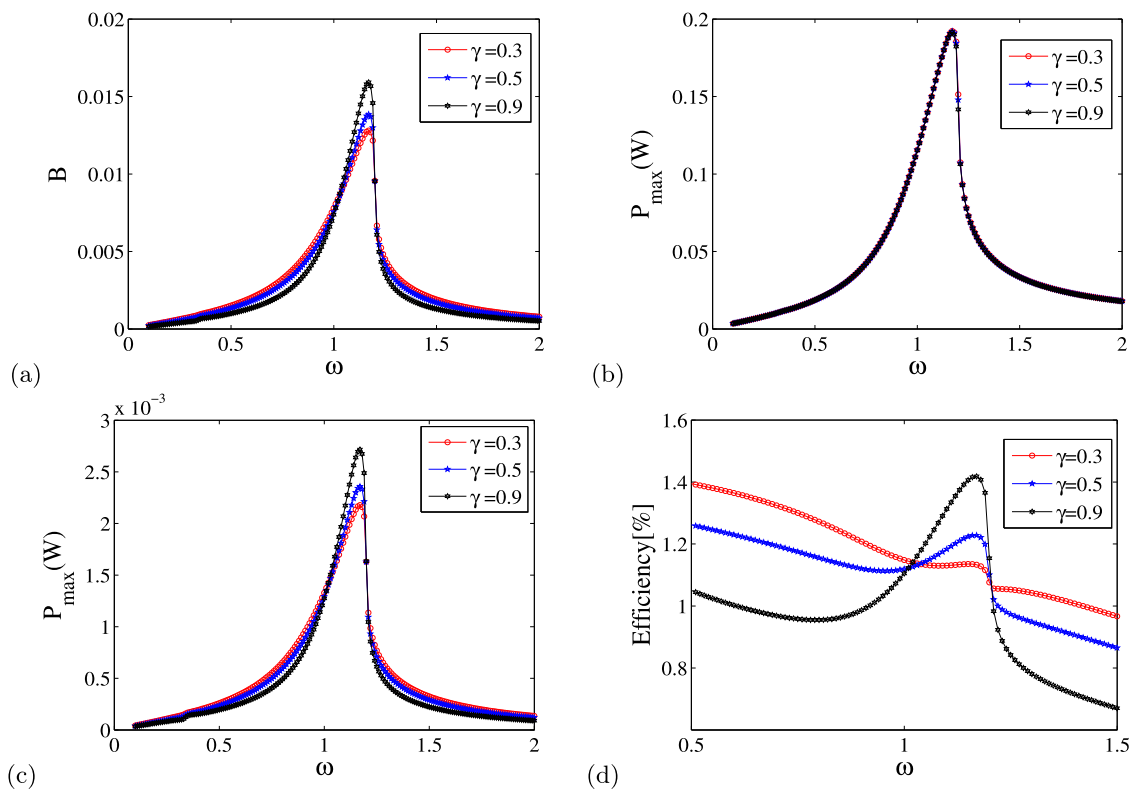


Fig. 6. Effects on the amplitude of parametric coupling γ on the amplitude response curve B and output power with the parameters $\lambda = 0.1$, $\mu_1 = 0.1$, $\mu_3 = 0.018$, $\vartheta_m = 0.76$, $\vartheta_e = 0.0056$, $\mu_e = 0.96$, $Q = 1$, $E_0 = 0.5$ and $\kappa = 1.0$. (a) amplitude response B , (b) mechanical input, (c) output electric power and (d) efficiency.

The numerical scheme used in this paper is based on the Newton–Leipnikov algorithm [50], Eq. (4) can be rewritten as:

$$x(k) = x(t_{k-1}) + u(t_{k-1})h \tag{18}$$

$$y(t_{k-1}) = \left[z(t_{k-1}) + \sum_{i=1}^{n-1} c_j^{(\alpha)} z(t_{k-1}) \right] h^{-\alpha} \tag{19}$$

$$u(t_k) = [-\mu_1 u(t_{k-1}) - \mu_p u(t_{k-1})^p - Qx(t_{k-1}) - \lambda x(t_{k-1})^3 + \vartheta_m(1 + \gamma \cos(2\omega(t_{k-1})))z(t_k) + E_0 \cos(\omega(t_{k-1}))]h + u(t_{k-1}) \tag{20}$$

$$z(t_k) = z(t_{k-1}) + (-\beta y(t_{k-1}) - \mu_e z(t_{k-1}) - \vartheta_e(1 + \gamma \cos(2\omega(t_{k-1}))))h \tag{21}$$

where h is the integration step and the coefficients $c_j^{(\alpha)}$ satisfy the following recursive relations:

$$c_0^{(\alpha)} = 1, c_j^{(\alpha)} = \left(1 - \frac{1 + \alpha}{j} \right) c_{j-1}^{(\alpha)}. \tag{22}$$

$$u(t_k) = [-\mu_1 u(t_{k-1}) - \mu_p u(t_{k-1})^p - Qx(t_{k-1}) - \lambda x(t_{k-1})^3 + \vartheta_m(1 + \gamma \cos(2\omega(t_{k-1})))z(t_k) + E_0 \cos(\omega(t_{k-1}))]h + u(t_{k-1}) \tag{23}$$

Fig. 3(a) and (c) show the comparison between the results obtained from analytical and numerical investigations. From these figures we notice the agreement between the two results. The effects of the fractional derivative κ on the amplitude are depicted in Fig. 3(b) and (d). We notice that, the amplitude of the mechanical vibration are almost unchanged when κ increases (see Fig. 3(b)). However, in Fig. 3(d), we observe that, the enhancing of the fractional order derivative leads to increase the output power change. We displayed on Fig. 4(a)–(d), the mechanical and electrical response versus frequency ω . In Fig. 4(a) and (c), the impact of the amplitude of the parametric coupling is presented. We notice in Fig. 4(a) that when γ increases, the response of mechanical part is not change. However, in Fig. 4(c), an increase of γ leads to enhance the output charge, and consequently, an enhancing of the output power. Fig. 4(c) and (d) show the impact of the linear ($\mu_1 \neq 0, \mu_3 = 0$), cubic ($\mu_3 \neq 0, \mu_1 = 0$) and polynomial damping ($\mu_1 \neq 0, \mu_3 \neq 0$) upon the electrical response. It emerges from these results that, the cubic and polynomial damping induced a reducing of harvested energy. Fig. 5 show the impact of κ, γ, λ and damping upon the output power. We notice in Fig. 5(a) and (b) that, when κ and γ increase, the output power increases. Similar result is observed in Fig. 5(c). When the coefficient of the cubic nonlinearly increases. However, in Fig. 5(d), an increase of the degree of the damping gives rise to the small output power.

We show in Fig. 6, the comparison between the mechanical and electrical power for three value of γ . We notice in Fig. 6(a)–(c) that for a fixed value of the γ , the resonance occurs for the same value of the frequency. For $\gamma = 0.9$, the real maximum electric power is obtained at $\omega = 1.17\text{Hz}$ and is about 2.7mW , for the corresponding input power(the mechanical power) equal to 0.19W . We show in Fig. 6(d) the efficiency conversion of the system. We notice that an increase of the γ leads to the increase of efficiency. We also notice in this figure that the efficiency is optimum when the resonance phenomenon occurs ($\omega = 1.17\text{Hz}$), this give rise to the maximum charge and output power (Fig. 6(a) and (c)).

Several works have been published in the field of energy harvesting using electromechanical system. However, several authors

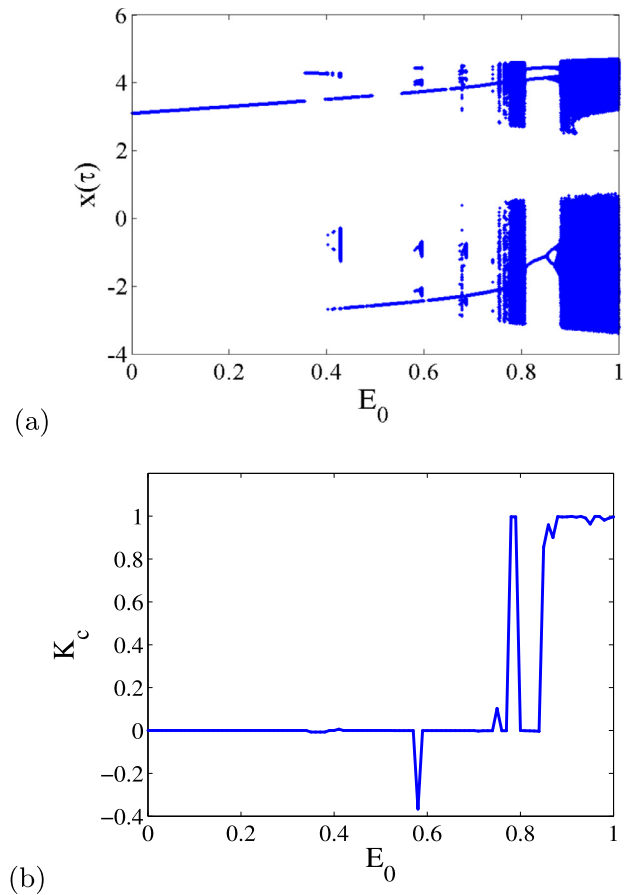


Fig. 7. Bifurcation diagram (a) and asymptotic growth rate k_c (b) curves for system (4) for E_0 varying with the parameters $\lambda = 0.1, \mu_1 = 0.1, \mu_3 = 0.018, \gamma = 0.5, \vartheta_m = 0.76, \vartheta_e = 0.0056, \mu_e = 0.96, \omega = 1.0, Q = -1.0$ and $\kappa = 1.0$.

have been used the standards materials [17,18] and other, the materials exhibiting the fractional properties. In contrarily in the previous works [35,37], a novelty of this present work is the introduction of the fractional inductor in the electrical subsystem. Kwimi et al. have been showed that for some value of amplitude of the excitation force, the voltage present the antagonistic phenomenon ie an increase of fractional order derivative leading to increase or decrease the output voltage. In addition, Oumbé et al. have been showed that, Energy harvesting system with fractional order viscoelastic properties has better performance at resonance. Indeed, small value of fractional derivative leads to large value of the maximum output voltage. On major observation in our study reveal that, the system performance is optimum for the high value of the fractional order derivative (see Fig. 5). However, for $\kappa \in]0, 1[$, while the output power increase when κ go up, the standards inductor ($\kappa = 1$) is better than the inductor exhibiting the fractional properties. It would be advantageous in this research field, to use a standard inductance. The performance of the system depends on the degree of nonlinear damping. In addition, the steady-state solution under the same conditions except $\mu_3 = 0$ (i.e., no nonlinear damping) is also plotted in Fig. 4. We notice that, the existence of non-negligible nonlinear damping has a strong impact on the frequency response of the system, specifically on the locations of the jump points. In particular, for the polynomial damping only the cubic term provides power harvested while the linear term is considered as a loss. When a polynomial damping is taken into account only, the cubic term is considered as power harvested. As shown in Fig. 5(d), the polynomial damping allows us to store less energy than the linear and the cubic damping. This is due to the fact

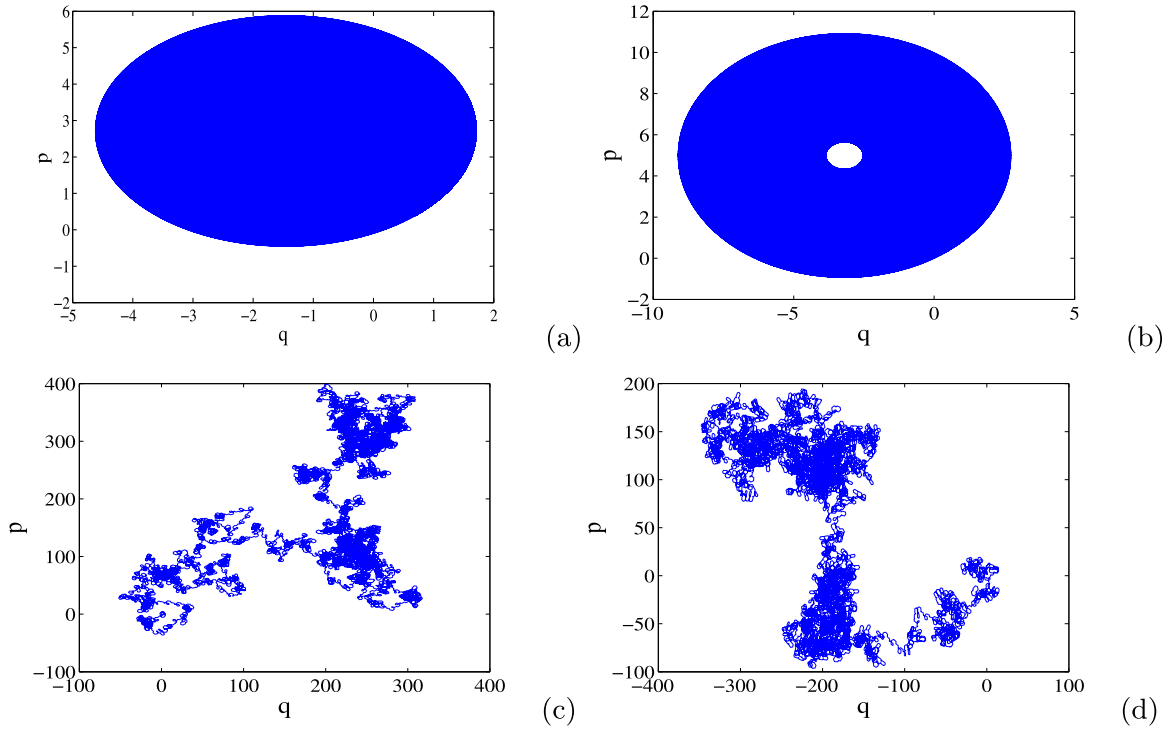


Fig. 8. Phase portraits of the mechanical part for crossing well dynamics as function of E_0 for $\kappa = 1$ and the value of Fig. 6.: (a) $E_0 = 0.09$, (b) $E_0 = 0.8$, (c) $E_0 = 0.9$, (d) $E_0 = 0.96$, with the parameters $\lambda = 0.1$, $\mu_1 = 0.1$, $\mu_3 = 0.018$, $\gamma = 0.5$, $\vartheta_m = 0.76$, $\vartheta_e = 0.0056$, $\mu_e = 0.96$, $\omega = 1.0$, $\varrho = -1.0$ and $\kappa = 1.0$.

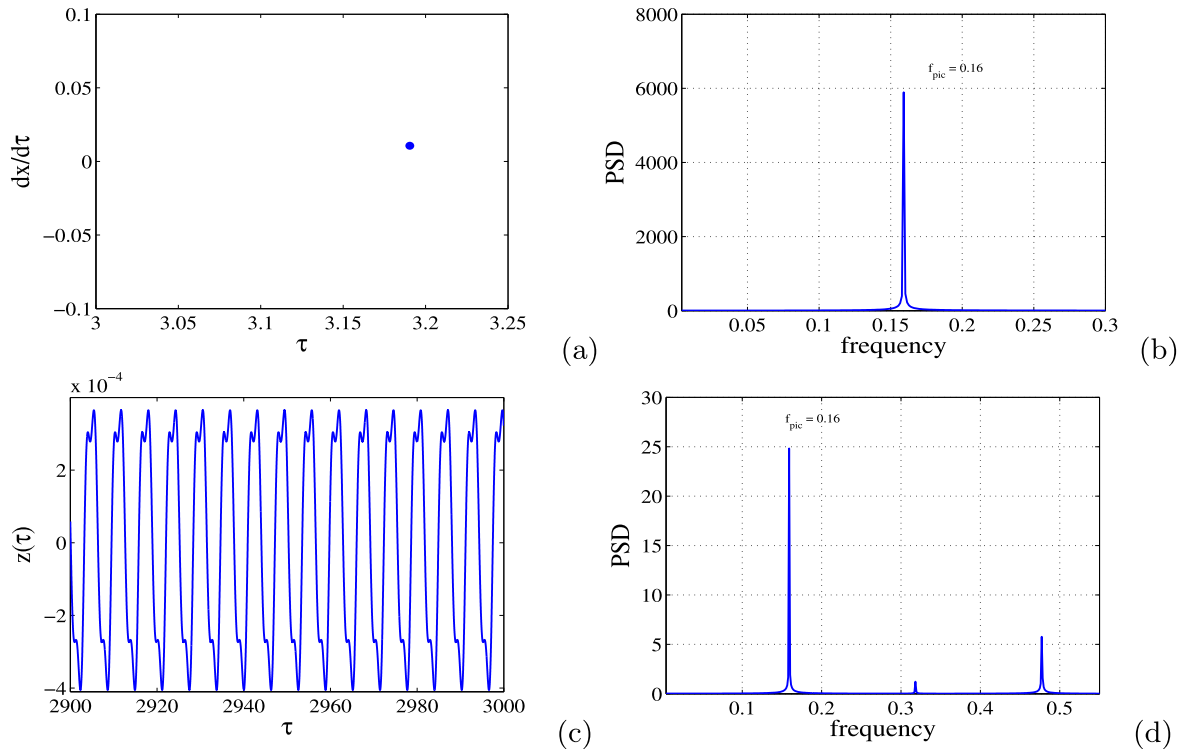


Fig. 9. Poincaré maps, time history and power spectral density from system (4) for $\kappa = 1$ and $E_0 = 0.0911$ with the parameters: $\lambda = 0.1$, $\mu_1 = 0.1$, $\mu_3 = 0.018$, $\gamma = 0.5$, $\vartheta_m = 0.76$, $\vartheta_e = 0.0056$, $\mu_e = 0.96$, $\varrho = -1.0$ and $\omega = 1.0$.

that the linear term is loss power. The effects of the amplitude of the parametric modulation are found in the response curves and output power. The amplitude of the parametric coupling can contribute to increase the harvested output voltage. The performance of the system depends also on the degree of nonlinearity of the potential and the electrical dissipation.

2.3. Description of 0-1 test and numerical study

With the aim to deeply characterize the long time dynamic of the system, we have used many standard indicators, namely bifurcation diagrams, phase portraits, power spectral density and computation of the 0-1 test.

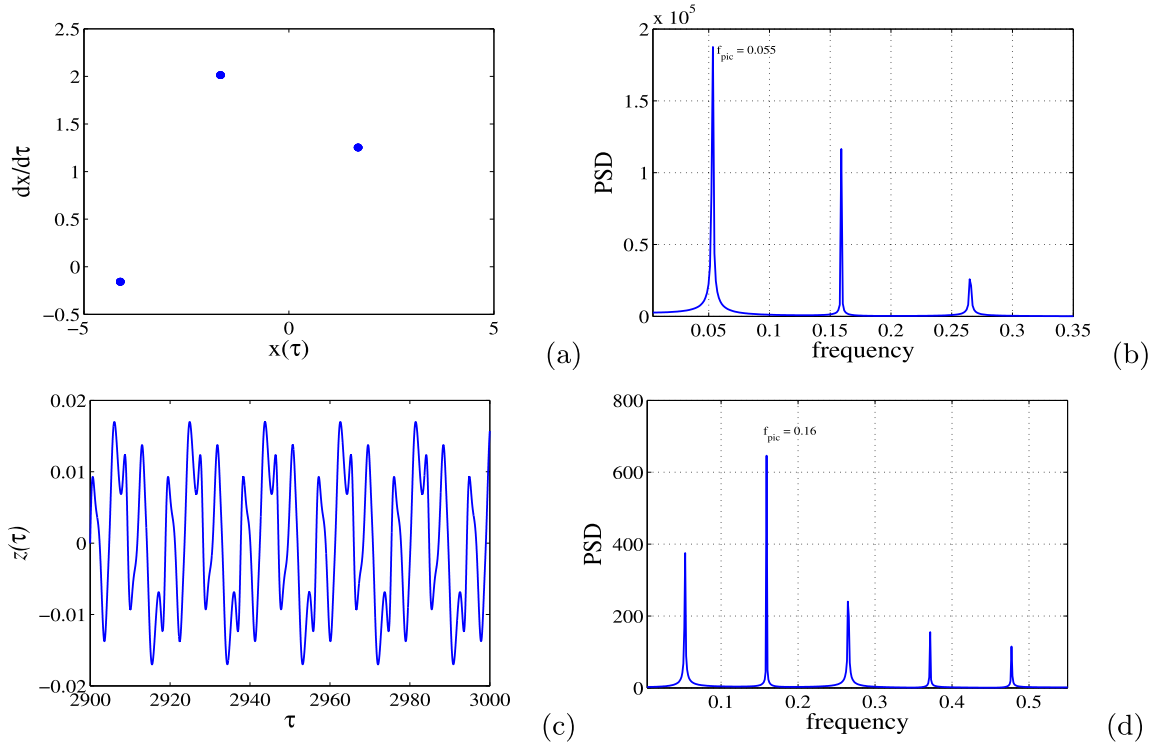


Fig. 10. Poincaré maps, time history and power spectral density from system (4) for $\kappa = 1$ and $E_0 = 0.8284$ with the parameters: $\lambda = 0.1$, $\mu_1 = 0.1$, $\mu_3 = 0.018$, $\gamma = 0.5$, $\vartheta_m = 0.76$, $\vartheta_e = 0.0056$, $\mu_e = 0.96$, $\varrho = -1.0$ and $\omega = 1.0$.

2.3.1. Description of the 0-1 test

To quantify the results obtained, we use the 0-1 test for chaos detection [51,52]. This test combines both spectral and statistical properties of the system and can distinguish different types of dynamics of the system by computing a number $K \in \{0, 1\}$. First of all, a change coordinates (x, \dot{x}) to a new set (p, q_1) is required

$$p(n) = \sum_{j=1}^n \tilde{x}_j \cos(jc), \quad q_1(n) = \sum_{j=1}^n \tilde{x}_j \sin(jc) \quad (24)$$

where $\tilde{x} = [\tilde{x}_1, \tilde{x}_2, \tilde{x}_3, \tilde{x}_4, \dots]$ is the discrete time series sampled from the originally simulated x using one-fourth of excitation period, while c is a constant ($c \in [0, \pi]$). The Mean Square Displacement (MSD) is defined as in Ref. [49,53]:

$$MSD(c, j) = \frac{1}{n-j} \sum_{i=1}^{n-j} \{ [p(i+j) - p(i)]^2 + [q_1(i+j) - q_1(i)]^2 \} \quad (25)$$

where j is the integer number varying as follows:

$$\frac{n}{100} \leq j \leq \frac{n}{10}.$$

Thus, the asymptotic growth rate of MSD is given as:

$$K(c) = \frac{Cov[j, MSD(c, j)]}{\sqrt{Cov[j, j] \cdot Cov[MSD(c, j), MSD(c, j)]}} \quad (26)$$

where $Cov(x, u)$ is the covariance of the serie x, u . In this paper, we let $(x = j$ and $u = MSD(c, j))$. The covariance of x, u is defined as:

$$cov[x, u] = \frac{1}{N} \sum_{n=1}^N (x(n) - \bar{x})(u(n) - \bar{u}) \quad (27)$$

where \bar{x} and \bar{u} are the average value of x and u , N is the element number of \bar{x} and \bar{u} are given by:

$$\bar{x} = \frac{1}{N} \sum_{n=1}^N x(n), \quad \bar{u} = \frac{1}{N} \sum_{n=1}^N u(n). \quad (28)$$

2.3.2. Numerical study

The main purpose of this section is to show the qualitative behavior of the solution of the extended electromechanical model. The system generates a complex behavior that directly depends on the amplitude and frequency of the modulated force. We now use the numerical simulations for examining the complicated behavior of Eq. (4). The initial conditions used in the numerical simulation are $(x(0) = 1.0, \dot{x}(0) = 0.0, z(0) = 0.0)$. The fourth-order RungeKutta algorithm is used to check the threshold of harmonic excitation amplitude for onset of possible chaos obtained for system (4). Fig. 7 shows a representative bifurcation diagram and the variation of the corresponding 0 – 1 test versus the amplitude E_0 of mechanical part. A bifurcation diagram is displayed in Fig. 7(a), showing the dependence of the system response when E_0 increases. We observe in this figure the regions corresponding to regular motion ($E_0 \in [0, 0.78]$), the region corresponding to period-3 orbit ($E_0 \in [0.8, 0.88]$) and regions corresponding to the chaotic states ($E_0 \in [0.78, 0.799] \cup [0.88, 1]$). In the goal to validate the result obtained in Fig. 7(a), the 0-1 test is provided (Fig. 7(b)). The result obtained ((Fig. 7(b))) confirms this obtained via the bifurcation diagram (Fig. 7(a)). The phase portrait provided in Fig. 8, allow us to know the different regimes in which the system involves. We observe a diffusive (Figs. 8(c)- 8(d)) and bounded dynamic (Fig. 8(a) and (b)) of the $p(n)$ and $q_1(n)$ in the phase space (p, q_1) . Let us notice that, a diffuse dynamic of $p(n)$ and $q_1(n)$ corresponds to the chaotic motion, which increases the bandwidth of oscillator there by allowing to enhance to output power. However, when the dynamic of $p(n)$ and $q_1(n)$ is bounded in the phase space, the motion is regular. In such condition, the energy storage by the mechanical oscillator is concentrated within its harmonic or superharmonic.

We provide in Figs. 9–11, the poincaré map, the time series and its corresponding power spectral density (PSD). We notice in Fig. 9(a) and (c) that the regular motion. These result are confirmed in Fig. 9(b) and (d) by plotting PSD. Only one peak located

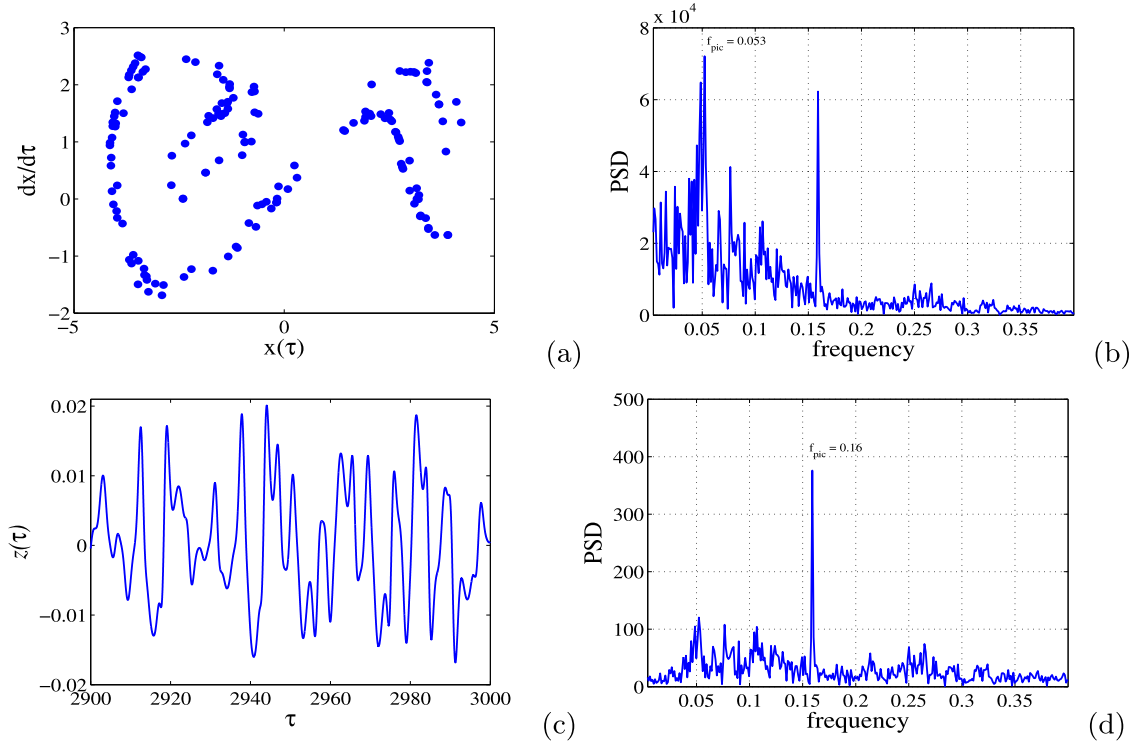


Fig. 11. Poincaré maps, time history and power spectral density from system (4) for $\kappa = 1$ and $E_0 = 0.9318$ with the parameters: $\lambda = 0.1$, $\mu_1 = 0.1$, $\mu_3 = 0.018$, $\gamma = 0.5$, $\vartheta_m = 0.76$, $\vartheta_e = 0.0056$, $\mu_e = 0.96$, $\varrho = -1.0$ and $\omega = 1.0$.

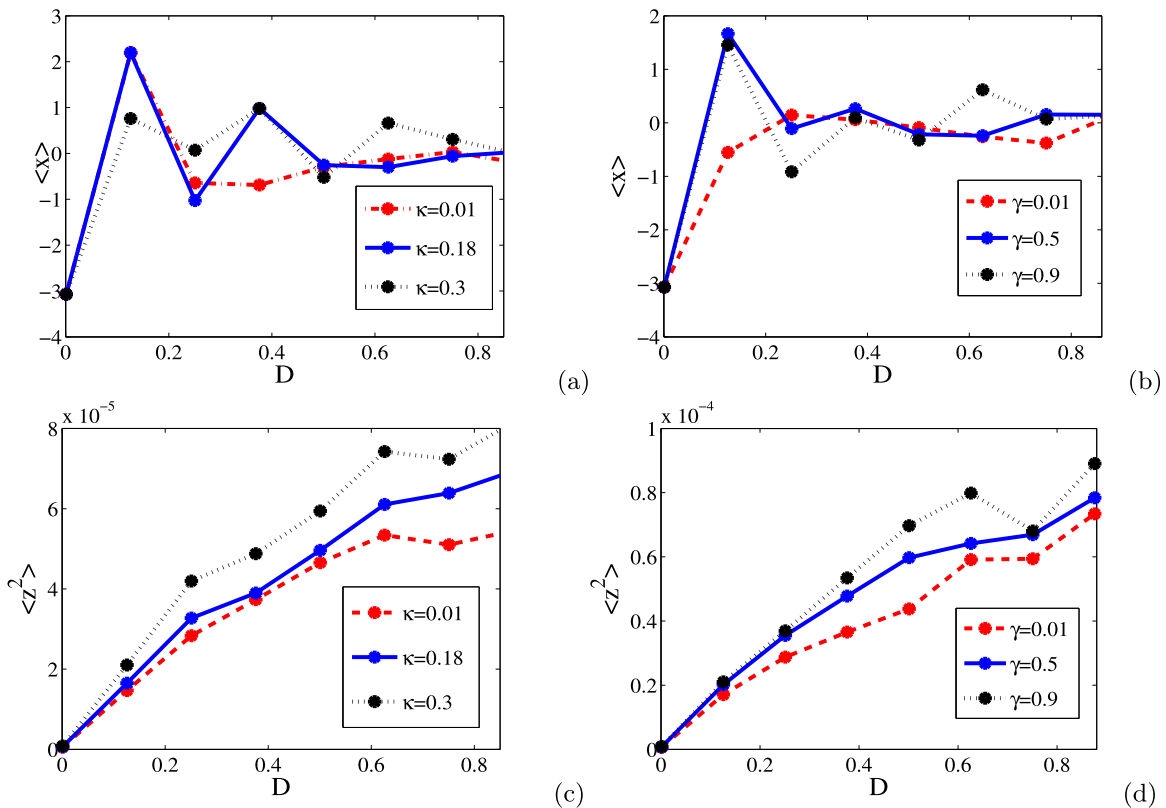


Fig. 12. Means square of the system with the parameters $\lambda = 0.1$, $\mu_1 = 0.1$, $\mu_3 = 0.018$, $\vartheta_m = 0.76$, $\vartheta_e = 0.0056$, $\mu_e = 0.96$, $\varrho = -1.0$ and $\omega = 1.0$.

to the dimensionless frequency ($f_{pic} = 0.16$) is observed for the mechanical subsystem. However, in Fig. 9(d) three peaks are observed. In Fig. 10(a) and (c), the motion of the system is quasi-period characterized by three harmonics. The agreement between these results and those obtained in Fig. 10(b) is observed. Fig. 10(d) shows five peaks. In this condition, the energy harvested by the system is high than obtained when the dynamic of the system is periodic. In Fig. 11(b) and (d), the system exhibits the chaotic motion giving rise to the large bandwidth of the frequency allowing to harvest more energy. These latter results are confirmed in Fig. 11(b) and (d) which present many harmonics.

3. Investigation of the system performance under the Gaussian white noise

The harmonic excitation is used in the previous section to investigate the system response. However, in the real environment, wave oscillations, atmospheric turbulence and seismic shocks, the vibration source are not harmonic but exists under a random form Ref. [54–56]. Thus we replace in the previous section, the harmonic excitation by a Gaussian white noise verifying the statistic properties:

$$\begin{aligned} \langle \xi(\tau)\xi(t + \tau') \rangle &= 2D\delta(\tau), \\ \langle \xi(\tau) \rangle &= 0, \end{aligned} \tag{29}$$

where $2D$ is the intensity of noise and $\delta(\tau)$, the Dirac function. The impact of fractional order derivative κ and γ upon the output power expressed in terms of mean square voltage (z^2) and mean displacement is presented in Fig. 12(a)–(d). Let us notice that in Fig. 12(a) and (b), when $\kappa \simeq 0$, the system oscillates by hopping symmetrically through the potential barrier. However, $\kappa \simeq 1$ indicates that the oscillating system is strapped in one of the potential wells. Fig. 12(c) and (d), the output power versus noise intensity for three values of fractional order derivative κ and amplitude of the parametric coupling γ . We notice in these figures that an enhancing of κ and γ leads to increase the output power.

4. Conclusion

In summary, the analytical investigation of the system response of the electromechanical energy harvesting system is presented. The harmonic balance method is used in this manuscript and gives rise to the amplitude equation. The results obtained by this analytical technique are checked numerically. The agreement between these two methods validates the analytical technique used. The impact of fractional order derivative and amplitude of the parametric coupling is investigated with detail. It emerges from these results that, the fractional order derivative κ and amplitude of the parametric coupling γ enhance the output power when these two parameters increase. The effect of linear cubic and polynomial damping is also investigated. We notice that a large value of the degree of the damping reduces the output power. In addition, replacing the harmonic excitation by the random force, the impact of noise intensity is investigated. It appears from these results that, the output power could be optimized for the best choice of the noise intensity D , the fractional order derivative κ and amplitude of the parametric coupling.

Appendix

$$r_{10} = (\omega^6 \mu_3^2 + \lambda^2)^2,$$

$$r_8 = -\frac{8}{3} \omega^3 \mu_3 (\omega^6 \mu_3^2 + \lambda^2) (\eta_1 - \eta_4 - \lambda(\eta_2 - \eta_3)),$$

$$\begin{aligned} r_6 &= \frac{16}{9} \omega^6 (\eta_1^2 - 4 \eta_1 \eta_4 + 2 \eta_2 \eta_3 + \eta_4^2) \mu_3^2 \\ &\quad - \frac{32}{9} \lambda \omega^3 (\eta_2 + \eta_3) (\eta_1 - \eta_4) \mu_3 \\ &\quad - \frac{16}{9} \lambda^2 (2 \eta_1 \eta_4 - \eta_2^2 - 4 \eta_2 \eta_3 - \eta_3^2), \end{aligned}$$

$$\begin{aligned} r_4 &= -\frac{16}{9} \omega^6 E_0^2 \mu_3^2 + \frac{128}{27} \omega^3 (\eta_1 - \eta_4) (\eta_1 \eta_4 - \eta_2 \eta_3) \mu_3 \\ &\quad - \frac{16}{27} \lambda (8 (\eta_2 + \eta_3) (\eta_1 \eta_4 - \eta_2 \eta_3) + 3 \lambda E_0^2), \end{aligned}$$

$$\begin{aligned} r_2 &= \frac{256}{81} \eta_1^2 \eta_4^2 + \left(\frac{128}{27} \omega^3 E_0^2 \mu_3 - \frac{512}{81} \eta_2 \eta_3 \eta_4 \right) \eta_1 \\ &\quad + \frac{256}{81} \eta_2^2 \eta_3^2 - \frac{128}{27} \eta_2 \lambda E_0^2, \end{aligned}$$

$$r_1 = -\frac{256}{81} E_0^2 (\eta_1^2 + \eta_2^2),$$

$$\begin{aligned} \xi &= 12 ((-\eta_1 + \eta_4) \mu_3 \omega^3 + \eta_2 \lambda + \eta_3 \lambda) A^2 \\ &\quad - 16 (\eta_1 \eta_4 - \eta_2 \eta_3) + 9 (\omega^6 \mu_3^2 + \lambda^2) A^4, \end{aligned}$$

$$b_0 = \frac{256 (\eta_1^2 \zeta_2^2 + \eta_2 \zeta_1^2) \vartheta_e^2 E_0^2}{(\delta^2 + \omega^2) \xi^2 \vartheta_m^2},$$

$$b_2 = \frac{384 (\eta_2 \lambda \zeta_1^2 - \eta_1 \omega^3 \zeta_2^2 \mu_3) \vartheta_e^2 E_0^2}{(\delta^2 + \omega^2) \xi^2 \vartheta_m^2},$$

$$b_4 = \frac{144 (\eta_2^2 \omega^6 \mu_3 + \lambda^2 \zeta_1^2) \vartheta_e^2 E_0^2}{(\delta^2 + \omega^2) \xi^2 \vartheta_m^2}$$

and

$$\eta_1 = -\omega \mu_1 - \frac{\zeta_1^2 \omega \vartheta_e}{\vartheta_m (\delta^2 + \omega^2)},$$

$$\eta_2 = -\omega^2 + \varrho - \frac{\zeta_1 \vartheta_e \delta \zeta_2}{\vartheta_m (\delta^2 + \omega^2)},$$

$$\eta_3 = -\omega^2 + \varrho - \frac{\zeta_1 \vartheta_e \delta \zeta_2}{\vartheta_m (\delta^2 + \omega^2)},$$

$$\eta_4 = -\omega \mu_1 - \frac{\zeta_2^2 \omega \vartheta_e}{\vartheta_m (\delta^2 + \omega^2)}.$$

References

- [1] Bagley RL, Torvik PJ. Fractional calculus in the transient analysis of viscoelastically damped structures. *AIAA J* 1985;23:918–25.
- [2] Rossikhin YA, Shitikova MV. Analysis of free nonlinear vibrations of a viscoelastic plate under the condition of different internal resonances. *Int J Non-Linear Mech* 2006;41:313–25.
- [3] Müller S, Kästner M, Brummund J, Ulbricht V. On the numerical handling of fractional viscoelastic material models in a FE analysis. *Com Mech* 2013;51:999–1012.
- [4] Debnath L. Recent applications of fractional calculus to science and engineering. *Int J Math Math Sci* 2003;2003:3413–42.
- [5] Agrawal O. Application of fractional derivatives in thermal analysis. *Nonlinear Dyn* 2004;38:191–206.
- [6] Silva MF, Machado JAT. Fractional order PDA joint control of legged robots. *J Vib Control* 2006;12:1483–501.
- [7] Stanton SC, Mann BP, Owens BA. Melnikov theoretic methods for characterizing the dynamics of the bistable piezoelectric inertial generator in complex spectral environments. *PhyD* 2012;241:711–20.
- [8] Atangana A, Alkahtani BST. Extension of the resistance, inductance, capacitance electrical circuit to fractional derivative without singular kernel. *Adv Mech Eng* 2013;7:16.
- [9] Lenzi EK, Netoa RM, Tateishi AA, Lenzi MK, Ribeiro HV. Fractional diffusion equations coupled by reaction terms. *Phy A* 2016;458:916.

- [10] Aguilar JFG, Martnez HY, Ramn CC, Ordua IC, Jimnez RFE, Peregrino VHO. Modeling of a mass-spring-damper system by fractional derivatives with and without a singular kernel. *Entr* 2015;17:6289–303.
- [11] Zhang B, Ducharne B, Guyomar D. Inverse model of the piezoelectric ceramic polarization under wide bandwidth mechanical excitations with fractional derivative consideration. *Opt Quant Electron* 2013;46:103110.
- [12] Atangana A, Baleanu D. New fractional derivatives with nonlocal and non-singular kernel: theory and application to heat transfer model. *Thermal Sci* 2016;20:763–9.
- [13] Prodanov D, Delbeke J. A model of space-fractional-order diffusion in the glial scar. *J Theor Biol* 2016;403:97–109.
- [14] Karami V, Inman DJ. Powering pacemakers from heart-beat vibrations using linear and nonlinear energy harvesters. *Appl Phys Lett* 2012;100:042901.
- [15] Harne RL, Wang KW. A review of the recent research on vibration energy harvesting via bistable systems. *Smart Mater Struct* 2013;22:023001.
- [16] Tang L, Yang Y. A nonlinear piezoelectric energy harvester with magnetic oscillator. *Appl Phys Lett* 2012;101:094102.
- [17] Tchuisseu EBT, Woaf P. Harvesting energy using a magnetic mass and a sliding behaviour. *Non Eng* 2014.
- [18] Tkam GTO, Tchuisseu EBT, Kwuimy CAK, Woaf P. Analysis of an electromechanical energy harvester system with geometric and ferroresonant nonlinearities. *Nonlinear Dyn* 2014. doi:10.1007/s11071-013-1228-6.
- [19] Buckjohn CND, Siewe MS, Fokou ISM, Tchawoua C, Kofane TC. Investigating bifurcations and chaos in magnetopiezoelectric vibrating energy harvesters using melnikov theory. *Phys Scripta* 2013;88:015006.
- [20] Owens BA, Mann BP. Linear and nonlinear electromagnetic coupling models in vibration-based energy harvesting. *J Sound Vib* 2012;331:922–37.
- [21] Borowiec M, Litak G, Friswell MI, Ali SF, Adhikari S, Lees AW, et al. Energy harvesting in piezoelectric systems driven by random excitations. *Int J Str Stab Dyn* 2013;13:1340006.
- [22] Coccolo M, Litak G, Seoane MJ, Miguel AFS. Energy harvesting enhancement by vibrational resonance. *Int J Bif Chaos* 2014;24:1430019.
- [23] Maimardi F. Fractional calculus and waves in linear viscoelasticity. London: Imperial College Press; 2010.
- [24] Alvelid M, Enelund M. Modeling of constrained thin rubber layer with emphasis on damping. *J Sound Vib* 2007;300:662–75.
- [25] Kwuimy CAK, Litak G. Enhance limit cycle oscillation in a wind flow energy harvester system with fractional order derivatives. *Theor Appl Mech Lett* 2014;4:053001.
- [26] Li D, Cao J, Zhou S, Chen Y. Fractional order model of broadband piezoelectric energy harvesters. *ASME/IEEE Int Conf on Mech and Embedded Sys Appl* 2015;9:2–5.
- [27] Zhang B. Model for coupled ferroelectric hysteresis using time fractional operators. Application to innovative energy harvesting. Other [cond-mat.other]. INSA de Lyon, 2014. English. < NNT: 2014ISAL0065 > . < tel – 01175848 > .
- [28] Zhang B, Ducharne B, Sebald G, Guyomar D. Characterization of fractional order for high-frequency bandwidth model of dielectric ferroelectrics. *J Int Mat Sys Struct* 2016;27:437–43.
- [29] Bagley RL, Torvik PJ. A theoretical basis for the application of fractional calculus to viscoelasticity. *J Rheol* 1983;27:201210.
- [30] Bagley RL, Torvik PJ. Fractional calculus a different approach to the analysis of viscoelastically damped structures. *AIAA J* 1983;21:741748.
- [31] Bagley RL, Torvik PJ. Fractional calculus in the transient analysis of viscoelastically damped structures. *AIAA J* 1985;23:918–25.
- [32] Koh CG, Kelly JM. Application of fractional derivatives to seismic analysis of base-isolated models. *Earthquake Eng Struct Dyn* 1990;19:229–41.
- [33] Makris N, Constantinou MC. Spring-viscous damper systems for combined seismic and vibration isolation. *Earthquake Eng Struct Dyn* 1992;21:649–64.
- [34] Cao J, Zhou S, Inman DJ, Chen Y. Chaos in the fractionally damped broadband piezoelectric energy generator. *Nonlinear Dyn* 2014;80:1705–19.
- [35] Kwuimy CAK, Litak G, Nataraj C. Nonlinear analysis of energy harvesting systems with fractional order physical properties. *Nonlinear Dyn* 2014.
- [36] Zhang B, Ducharne B, Guyomar D, Sebald G. Energy harvesting based on piezoelectric ericsson cycles in a piezoceramic material. *Eur Phys J Special Topics* 2013;222:1733–43.
- [37] Tkam GTO, Kwuimy CAK, Woaf P. Analysis of tristable energy harvesting system having fractional order viscoelastic material, chaos. *Interdiscip J Nonlinear Sci* 2015;25(013112).
- [38] Siewe MS, Buckjohn CND. Heteroclinic motion and energy transfer in coupled oscillator with nonlinear magnetic coupling. *Nonlinear Dyn* 2014;77:297–309.
- [39] Tripathy MC, Mondal D, Biswas K, Sen S. Experimental studies on realization of fractional inductors and fractional-order bandpass filters. *Int J Circ Theor Appl* 2014;43:1183–96.
- [40] Yamapi R, Bowong S. Dynamics and chaos control of the self-sustained electromechanical device with and without discontinuity. *Com Non Sci and Num Sim* 2006;11:355–75.
- [41] Yamapi R, Orou JBC, Woaf P. Harmonic dynamics and transition to chaos in a nonlinear electromechanical system with parametric coupling. *Phy Scripta* 2003;67:269–75.
- [42] Tehrani MG, Simeone L, Elliot SJ. Energy harvesting using nonlinear damping. *ENOC* 2013:6–11.
- [43] Tehrani MG, Elliot SJ. Extending the dynamic range of an energy harvester using nonlinear damping. *J Sound Vib* 2014;333:623–9.
- [44] Nayfeh AH, Mook DT. *Nonlinear Oscillations*. Wiley; 1979. New York
- [45] Miller KS, Ross B. *An introduction to the fractional calculus and fractional differential equations*. New York: Wiley; 1993.
- [46] Podlubny I. *Fractional differential equations*. San Diego: Academic Press; 1998.
- [47] Hristov J. Transient heat diffusion with a non-singular fading memory: from the cattaneo constitutive equation with jeffrey's kernel to the caputo-fabrizio time-fractional derivative. *Thermal Sci* 2016;20:765–70.
- [48] Bank B, Zambon S, Fontana F. A modal-based real-time piano synthesizer. *IEEE Trans Audio Speech Lang Process* 2010;18:809–21.
- [49] Petras L. *Fractional-order nonlinear systems modelling analysis and simulation*. note: Higher Education press; 2011.
- [50] Syta A, Litak G, Lenci S, Scheffler M. Chaotic vibrations of the duffing system with fractional damping. *Chaos* 2014;24(013107).
- [51] Gottwald GA, Melbourne I. Comment on reliability of the 0-1 test for chaos. *Proc R Soc A* 2004;460:603–11.
- [52] Litak G, Syta A, Budhraj M, Saha LM. Detection of the chaotic behaviour of a bouncing ball by the 0-1 test. *Chaos Sol Fractals* 2009;42:1511–17.
- [53] Litak G, Bernardini D, Syta A, Rysak A. Analysis of chaotic non-isothermal solutions of thermomechanical shape memory oscillators. *Proc IMechE, Part K* 2013;222:1637–47.
- [54] Rudiner F. Tuned mass damper with fractional derivative damping. *Eng Stru* 2006;28:1774–9.
- [55] Kumar P, Narayanan S, Adhikari S, Friswell MI. Fokker-planck equation analysis of randomly excited nonlinear energy harvester. *J Sound Vib* 2014;333:2040–53.
- [56] Jung P, Marcheloni F. Energetics of stochastic resonance. *Chaos* 2011;21(047516).



Hybrid electromagnetic and piezoelectric vibration energy harvester with Gaussian white noise excitation

O. Foupouapouognigni*, C. Nono Dueyou Buckjohn, M. Siewe Siewe, C. Tchawoua

University of Yaounde I, Faculty of science, Department of Physics, Laboratory of Mechanics, Materials and Structures, PO. Box: 812 Yaounde, Cameroon

HIGHLIGHTS

- The construction of the hybrid model is essential to increase the harvested energy by the harvester.
- The study of the stochastic p-bifurcation allows to know the value of the bifurcation parameter for which the system energy is improved.
- The occurring of the stochastic resonance enhances the system performance.

ARTICLE INFO

Article history:

Received 12 November 2017
Received in revised form 25 May 2018
Available online xxxx

Keywords:

Probability
Stochastic p-bifurcation
Stochastic resonance

ABSTRACT

In this work, we investigated the dynamical behavior of the hybrid energy harvester under Gaussian white noise using probabilistic approach. We find that under the influence of this kind of noise, the dynamics of the nonlinear electromechanical system exhibited the stochastic bifurcation which is characterized by a qualitative change of the stationary probability distribution. A stochastic averaging method is applied in this system in the aim to build the Itô Stochastic differential equations. From these equations, the Fokker–Planck Equations (FPE) of the electromechanical system is constructed whose the solution at the stationary state is a probability density. By combining the harmonic excitation to the random force, the harvested energy is improved. We also provided the optimization rate of the hybrid system with respect to the piezoelectric system. Besides, the comparison between the power obtained by the hybrid model, piezoelectric and electromagnetic energy harvester shows the interest to build the hybrid model. The analytical results agree very well with numerical simulation.

© 2018 Elsevier B.V. All rights reserved.

1. Introduction

The technological advance these last years in the electronics area and the growing need to render the electronics system autonomous drove to a renewal of the works of research on the renewable micro-energy harvesting. One of the challenge in this research field is the replacement of the batteries in the microelectronics system by a energy harvesting device, allowing to guarantee the energy needs in the embarked system without interruption. Several energy sources are available in the environment and can be used to power microelectronics systems. Among these energy sources, vibrations mechanics are the subject of the many investigation. As pointed by Williams et al. [1], three transduction mechanisms

* Corresponding author.

E-mail addresses: oumarfoupouagnigni@yahoo.fr (O. Foupouapouognigni), bucknono@yahoo.fr (C. Nono Dueyou Buckjohn), martinsiewesiewe@yahoo.fr (M. Siewe Siewe), ctchawa@yahoo.fr (C. Tchawoua).

are commonly used to convert vibrations mechanics to electricity, namely piezoelectric [2–5], electromagnetic [6,7] and electrostatic [8,9] transduction. However the most of the proposed harvesters are typically based on linear mechanical principles [1,10]. Such devices give appreciable response amplitude only if the dominant ambient vibration frequency is close to the resonance frequency of the harvester. In the goal to improve the efficiency of devices, nonlinear phenomena have been considered. Thus, Shahruz [11] shows that a bistable configuration of the potential energy of the system can be used to increase the output power. Coccolo et al. [12] have studied the electrical response of a bistable harvester driven by both a low and a high frequency forcing. The authors showed that the response amplitude at the low-frequency increases, reaches a maximum and then decreases to a certain range of the high frequency forcing. With a different perspective, Masana and Daqaq [13] proposed a comparative analysis of harvesters having bistable and mono-stable configuration of the potential energy, under harmonic excitation and demonstrated the effects of the potential shape on the performance of the system, for some ranges of frequencies. They concluded that mono-stable potential systems perform better than double-well systems for an excitation with a small amplitude. Considering the linear and nonlinear nature of the electromagnetic coupling, Owens and Mann [14] showed that depending on the system parameters, nonlinear coupling can be better than linear coupling. It is worth noting that, regardless of the type of transduction mechanism, any one exhibits advantage and disadvantage.

In order to overcome some disadvantage met in the transduction mechanism announced above, the construction of the hybrid model is essential. Wang et al. [15] developed a Piezoelectric and electromagnetic hybrid energy harvester for powering wireless sensor nodes in smart grid. The authors showed that from current-carrying conductor of 2.5 A at 50 Hz, the proposed harvester combining piezoelectric components and electromagnetic elements can generate up to 295.3 μ W. Zhenlong et al. [16] presented a novel tunable multi-frequency hybrid energy harvester. It comes from their study that the magnitude and direction of magnetic force have significant effect on the performance of the system. Friswell et al. [17] proposed a hybrid cantilever beam harvester with piezoelectric and electrostatic transducers for narrow band base excitation using an applied DC voltage as a control parameter to change the resonant frequency of the harvester to ensure resonance as the excitation frequency varies. Wacharasindhu et al. [18] proposed a micro machined energy harvester from a keyboard typing motions, using combined electromagnetic and piezoelectric conversion. Bin et al. [19] built a hybrid energy harvester combined piezoelectric with electromagnetic mechanism to scavenge energy from external vibration. They explored the effect of the relative position of the coils and magnets on the PZT cantilever end and the poling direction of magnets on the output voltage of the harvested energy. Karami et al. [20] proposed a hybrid model using piezoelectric and electromagnetic induction effect. They showed that electromechanical coupling has a strong impact upon the system performance. This manuscript gets an interest on the model of Wen et al. [15], where the full study of the piezoelectric energy harvester subjected to the harmonic excitation is consider. However, in the real environment, the vibration mechanics is not harmonic but is presented in the most of the time under the random signal. Thus, this manuscript considers that the mechanical subsystem is subjected to the stochastic excitation. Besides, from the model built in Ref. [15], we construct the hybrid energy harvester combining piezoelectric and electromagnetic mechanisms subjected to the stochastic excitation. In the order to enhance the harvested energy by the harvester, many research groups combined a coherent and random signal, which gives rise to the stochastic resonance phenomenon [21,22]. Mokem et al. [23] investigated the dynamics of sandwiched buckled beam with axial compressive force under Gaussian white noise energy harvesting system. The authors showed the optimization of the harvested energy when the stochastic resonance phenomenon occurs. Borowiec et al. [24] investigated the effect of noise on the performance of an energy harvester. They showed that noise component of the excitation impact on the system stability.

We extend our study in this paper by considering the dynamics of the hybrid energy harvester combining piezoelectric and electromagnetic mechanisms under harmonic and stochastic excitation. We explore the effects the Gaussian white noise and harmonic excitation on the system performance. The remain of paper is organized as follows: Section 2 is devoted to the description of the system with model equation. In Section 3.1, the stochastic averaging method is theoretically carried out to build the Fokker–Planck equation whose the solution in the stationary state is a probability density. The stochastic bifurcations are discussed in Section 3.2. Section 4 is devoted to the numerical simulation. Finally in Section 5 we conclude.

2. The model and governing equations

As pointed by Wen et al. [15], the electromechanical device shown in Fig. 1 is composed of three fundamental parts: The mechanical part is composed of the mass m , the nonlinear spring and nonlinear damping, while the electrical subsystem is composed of linear inductance L , a linear capacitor C and the linear resistor R . The nonlinear damping introduced in this system is important insofar as it has been shown that it can improve efficiency in the context of EHS [25,26]. We consider the dissipative force with nonlinear dissipation term proportional to the power of velocity \dot{x}^3 [25]. The expressions defining the damping force is given as follow [25]:

$$f_d = c_1\dot{x} + c_3\dot{x}^3 \quad (1)$$

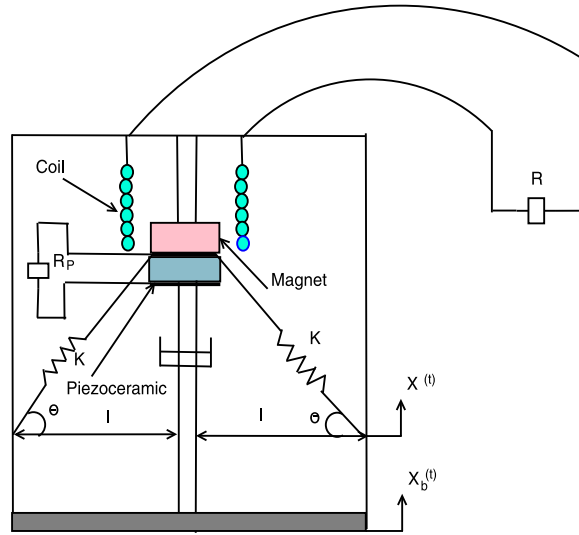


Fig. 1. Schematic of the hybrid energy harvester.

where \dot{x} is the velocity of the mass, c_1 and c_3 , the linear and nonlinear damping coefficients. The governing equations can be derived for Newton's law and Kirchoff's law [15]:

$$m\ddot{x} + \psi_1(x, \dot{x}) + \eta v + \theta_m i = -m\ddot{x}_b$$

$$C_p \dot{v} + \frac{1}{R_p} v - \eta \dot{x} = 0 \tag{2}$$

$$L \dot{i} + R i - \theta_m \dot{x} = 0$$

with

$$\psi_1(x, \dot{x}) = c_1 \dot{x} + c_3 \dot{x}^3 + 2k \left(1 - \frac{l_0}{\sqrt{x^2 + l^2}} \right) x$$

where m is the mass, x is the displacement of the mass, k is the spring stiffness, l_0 is the original length of the spring, l is the distance between the center and the edge of the frame, θ_m and η are the electromechanical coupling, v is the voltage across the load resistance, C_p is the capacitance of the piezoceramic, R_p is the resistance, θ is the inclination of the spring with respect to the horizontal, and \ddot{x}_b is the base displacement. Using the following transformation of coordinate $X = \frac{x}{l_0}$ and

$\gamma = \frac{l}{l_0}$, Eq. (2) can be rewritten as:

$$\ddot{X} + \psi_2(X, \dot{X}) + \frac{\eta}{l_0 m} v + \frac{\theta_m}{l_0 m} i = -\frac{\ddot{x}_b}{l_0}$$

$$\dot{v} + \frac{1}{C_p R_p} v - \frac{\eta l_0}{C_p} \dot{X} = 0 \tag{3}$$

$$\dot{i} + \frac{R}{L} i - \frac{\theta_m l_0}{L} \dot{X} = 0$$

with

$$\psi_2(X, \dot{X}) = \frac{c_1}{m} \dot{X} + \frac{c_3 l_0^2}{m} \dot{X}^3 + \frac{2k}{m} \left(1 - \frac{1}{\sqrt{X^2 + \gamma^2}} \right) X.$$

In this work, we consider the weak amplitude of vibration. In this case, the nonlinear term in Eq. (3) can be expanded into the Taylor series at equilibrium $(X_0, 0)$. By omitting higher order terms in the resulting expanding expression and shifting the origin of the coordinate by introducing the new variable $X = z - X_0$, with X_0 is the positive stable static equilibrium position obtained by solving the non-dimensional potential $U(X) = \frac{2k}{m} (\sqrt{X^2 + \gamma^2} - 1)^2$. Using the following transformation

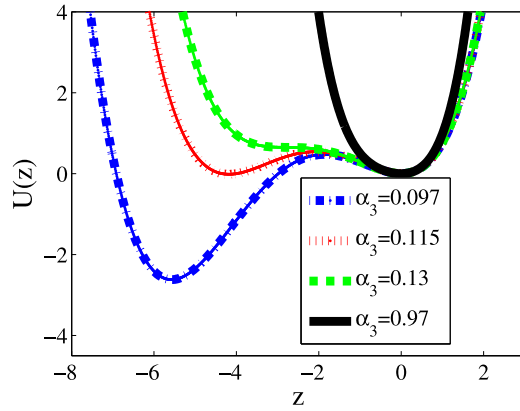


Fig. 2. One-dimensional bistable potential governed by Eq. (4)(a) with parameters $\omega_1 = 1, \alpha_2 = 0.72$ and Metastable potentials $\alpha_3 = 0.13$, symmetric bistable potentials $\alpha_3 = 0.115$ and asymmetric bistable potentials $\alpha_3 = 0.097$.

of coordinates $\omega_1^2 = \frac{2|k|(1-\gamma^2)}{m}, z = z_0z, i = i_0\rho, v = v_0y$ and by letting the time variable $t = \frac{\tau}{\omega_1}$, the dimensionless equation is given by:

$$\ddot{z} + \psi_3(z, \dot{z}) + \zeta_m \dot{z} + \zeta_e v = \xi(\tau) \quad (a),$$

$$\dot{y} + \lambda y - \vartheta_p \dot{z} = 0 \quad (b), \tag{4}$$

$$\dot{\rho} + \beta \rho - \vartheta_e \dot{z} = 0 \quad (c),$$

where the potential $U(z)$ is defined as

$$U(z) = \frac{\omega_1^2}{2}z^2 + \frac{1}{3}\alpha_2 z^3 + \frac{1}{4}\alpha_3 z^4,$$

$\psi_3(z, \dot{z})$ is Eq. (4) is given by

$$\psi_3(z, \dot{z}) = \zeta_1 \dot{z} + \zeta_3 \dot{z}^3 + \omega_1^2 z + \alpha_2 z^2 + \alpha_3 z^3$$

where

$$\zeta_1 = \frac{c_1 \omega_1}{2|k|(1-\gamma^2)}, \zeta_3 = \frac{(z_0 l_0)^2 c_3 \omega_1^3}{2|k|(1-\gamma^2)}, \vartheta_e = \frac{\theta_m l_0 z_0}{i_0 L}$$

$$\lambda = \frac{1}{\omega_1 C_p R_p}, \zeta_m = -\frac{\theta_m i_0}{2z_0 l_0 |k|(1-\gamma^2)}, \zeta_e = -\frac{\eta v_0}{2z_0 l_0 |k|(1-\gamma^2)},$$

$$\beta = \frac{R}{\omega_1 L}, \vartheta_p = \frac{\eta l_0 z_0}{v_0 C_p}, \alpha_3 = \frac{z_0^2 \gamma^2 (5\gamma^2 - 4)}{\gamma^2 - 1}, \alpha_2 = \frac{3z_0 \gamma^2}{2\sqrt{1-\gamma^2}}.$$

$\xi(\tau) = -\frac{\ddot{x}_b}{2|k|l_0(1-\gamma^2)}$ is the Gaussian white noise verifying the statistic properties:

$$\langle \xi(\tau)\xi(t + \tau') \rangle = 2D\delta(\tau),$$

$$\langle \xi(\tau) \rangle = 0,$$

(5)

where $2D$ is the intensity of noise and $\delta(\tau)$, the Dirac function. The variables z, y and ρ are the dimensionless displacement, voltage and current respectively. The dot in z, y and ρ indicates differentiation with respect to the time. $\vartheta_p, \vartheta_e, \zeta_e$ and ζ_m are parameters of the coupling terms, α_2 is the coefficient of quadratic nonlinearity, α_3 is the coefficient of cubic nonlinearity, ζ_1 and ζ_3 are damping coefficients, λ is the ratio of the resistance and inductance and $\omega_1 = 1$.

The potential $U(z)$ depends on the values of the parameters α_3, α_2 and ω_1 . We can have a mono-stable or a bistable configuration according to the system parameters. Several patterns of potential are shown in Fig. 2. One can clearly observe that the height of the right potential well goes up when α_3 decreases.

3. Stochastic averaging method and stochastic P-bifurcation

3.1. Stochastic averaging method

In this section, the objective is to study the stochastic bifurcation. To reach this objective, it is necessary to construct the Fokker–Planck equation. Eq. (4) can be rewritten in the following form:

$$\begin{aligned}\dot{z} &= u \\ \dot{u} &= -\varphi_3(z, u) - \zeta_m \rho - \zeta_e y + \xi(\tau), \\ \dot{y} &= -\lambda y + \vartheta_p u, \\ \dot{\rho} &= -\beta \rho + \vartheta_e u\end{aligned}\quad (6)$$

with

$$\varphi_3(z, u) = \zeta_1 u + \zeta_3 u^3 + \omega_1^2 z + \alpha_2 z^2 + \alpha_3 z^3.$$

According to the principle of the stochastic averaging method, the amplitude of the oscillations vary slowly in the period scale. For this reason, the derivative of the amplitude with respect to the time is neglected. In the quasi-harmonic regime, we assume that noise intensity is small, we introduce a change of variables

$$z(\tau) = a(\tau) \cos(\varphi), \quad (7)$$

$$\dot{z}(\tau) = -a(\tau) \omega_0 \sin(\varphi),$$

where $\varphi = \omega_0 \tau + \theta(\tau)$, $a(\tau)$ is amplitude of mechanical subsystem. Substituting Eq. (7) into Eq. (4)(b) and (c), we have:

$$y(\tau) = C_1(\tau) e^{(-\lambda \tau)} + \frac{a \vartheta_p \omega_0}{\lambda^2 + \omega_0^2} (\omega_0 \cos \varphi - \lambda \sin \varphi), \quad (8)$$

$$\rho(\tau) = C_2(\tau) e^{(-\beta \tau)} + \frac{a \vartheta_e \omega_0}{\beta^2 + \omega_0^2} (\omega_0 \cos \varphi - \beta \sin \varphi). \quad (9)$$

The first term and the second term in the right hand are the general solution of the associated homogeneous equation and the special solution, respectively. For the stationary responses concerned here, the terms $C_1(\tau) \exp^{(-\lambda \tau)}$ and $C_2(\tau) \exp^{(-\beta \tau)}$ in Eqs. (8)–(9) tends to zero when the time (τ) is large. Thus, Eqs. (8) and (9) can be rewritten as:

$$y(\tau) = \frac{a \vartheta_p \omega_0}{\lambda^2 + \omega_0^2} (\omega_0 \cos \varphi - \lambda \sin \varphi) \quad (10)$$

and

$$\rho(\tau) = \frac{a \vartheta_e \omega_0}{\beta^2 + \omega_0^2} (\omega_0 \cos \varphi - \beta \sin \varphi). \quad (11)$$

The term $(\omega_0 \cos \varphi - \lambda \sin \varphi)$ in Eq. (10) can be rewritten as follows:

$$\begin{aligned}\omega_0 \cos \varphi - \lambda \sin \varphi &= \\ \sqrt{\lambda^2 + \omega_0^2} \left(\frac{\omega_0}{\sqrt{\lambda^2 + \omega_0^2}} \cos \varphi - \frac{\lambda}{\sqrt{\lambda^2 + \omega_0^2}} \sin \varphi \right) \\ &= \sqrt{\lambda^2 + \omega_0^2} (\cos \Theta \cos \varphi - \sin \Theta \sin \varphi)\end{aligned}\quad (12)$$

with

$$\cos \Theta = \frac{\omega_0}{\sqrt{\lambda^2 + \omega_0^2}} \quad \text{and} \quad \sin \Theta = \frac{\lambda}{\sqrt{\lambda^2 + \omega_0^2}}.$$

Finally,

$$\omega_0 \cos \varphi - \lambda \sin \varphi = \sqrt{\lambda^2 + \omega_0^2} \cos(\Theta + \varphi). \quad (13)$$

Thus

$$y(\tau) = \frac{a \vartheta_p \omega_0}{\lambda^2 + \omega_0^2} \sqrt{\lambda^2 + \omega_0^2} \cos\left(\varphi + \tan^{-1}\left(\frac{\lambda}{\omega_0}\right)\right). \quad (14)$$

In the steady state, the amplitude of the voltage is expressed as follow:

$$V_0 = \frac{a\vartheta_p\omega_0}{\lambda^2 + \omega_0^2} \times \sqrt{\lambda^2 + \omega_0^2} = \frac{a\vartheta_p\omega_0}{\sqrt{\lambda^2 + \omega_0^2}}. \tag{15}$$

Similarly, the amplitude of the steady state current (Eq. (11)) is given as:

$$I_0 = \frac{a\vartheta_e\omega_0}{\beta^2 + \omega_0^2} \times \sqrt{\beta^2 + \omega_0^2} = \frac{a\vartheta_e\omega_0}{\sqrt{\beta^2 + \omega_0^2}}. \tag{16}$$

Substituting Eqs. (10), (11) and (7) into Eq. (4) by letting $\omega_1 = \omega_0$ we obtain:

$$\begin{aligned} \dot{a} = & -\zeta_1 a \sin^2 \varphi - \zeta_3 \omega_0^2 a^3 \sin^4 \varphi + \frac{\alpha_2 a^2 \sin \varphi \cos^2 \varphi}{\omega_0} \\ & + \frac{\alpha_3 a^3 \sin \varphi \cos^3 \varphi}{\omega_0} + \frac{\zeta_e \omega_0 \vartheta_p a \sin \varphi \cos \varphi}{\lambda^2 + \omega_0^2} - \frac{\zeta_e \vartheta_p \lambda a \sin^2 \varphi}{\lambda^2 + \omega_0^2} \\ & + \frac{\zeta_m \omega_0 \vartheta_e a \sin \varphi \cos \varphi}{\beta^2 + \omega_0^2} - \frac{\zeta_m \vartheta_e \beta a \sin^2 \varphi}{\beta^2 + \omega_0^2} - \frac{\sin \varphi \xi(\tau)}{\omega_0} \end{aligned} \tag{17}$$

$$\begin{aligned} \dot{\theta} = & -\zeta_1 \cos \varphi \sin \varphi - \zeta_3 \omega_0^2 a^2 \cos \varphi \sin^3 \varphi + \frac{\alpha_2 a \cos^3 \varphi}{\omega_0} \\ & + \frac{\alpha_3 a^2 \cos^4 \varphi}{\omega_0} + \frac{\zeta_e \omega_0 \vartheta_p \cos^2 \varphi}{\lambda^2 + \omega_0^2} - \frac{\zeta_e \vartheta_p \lambda \cos \varphi \sin \varphi}{\lambda^2 + \omega_0^2} \\ & + \frac{\zeta_m \omega_0 \vartheta_e \cos^2 \varphi}{\beta^2 + \omega_0^2} - \frac{\zeta_m \vartheta_e \beta \cos \varphi \sin \varphi}{\beta^2 + \omega_0^2} - \frac{\cos \varphi \xi(\tau)}{\omega_0 a} \end{aligned} \tag{18}$$

Thus, after applying the deterministic averaging method to Eqs. (17)–(18), we obtained the following approximated system:

$$\begin{aligned} \dot{a} = & \chi_1 - \frac{\sin \varphi \xi(\tau)}{\omega_0}, \\ \dot{\theta} = & \chi_2 - \frac{\cos \varphi \xi(\tau)}{a\omega_0} \end{aligned} \tag{19}$$

where

$$\begin{aligned} \chi_1 = & -\frac{3}{8} \zeta_3 \omega_0^2 a^3 - \frac{1}{2} \left(\frac{\lambda^2 \zeta_1 + \lambda \zeta_2 + \zeta_3}{(\lambda^2 + \omega_0^2)(\beta^2 + \omega_0^2)} \right) a, \\ \chi_2 = & \frac{3}{8} \frac{\alpha_3 a^2}{\omega_0} + \frac{1}{2} \frac{\omega_0 (\vartheta_p \zeta_e (\beta^2 + \omega_0^2) + \vartheta_m \zeta_m (\lambda^2 + \omega_0^2))}{(\lambda^2 + \omega_0^2)(\beta^2 + \omega_0^2)} \end{aligned} \tag{20}$$

and

$$\zeta_1 = \zeta_m \beta \vartheta_e + (\beta^2 + \omega_0^2) \zeta_1,$$

$$\zeta_2 = (\beta^2 + \omega_0^2) \zeta_e \vartheta_p,$$

$$\zeta_3 = \zeta_m \beta \vartheta_e \omega_0^2 + (\beta^2 \omega_0^2 + \omega_0^4) \zeta_1.$$

By applying the stochastic averaging method [27,28], we can obtain the following stochastic equations for a and θ :

$$da = \left(\chi_1 + \frac{D}{2\omega_0^2 a} \right) d\tau + \sqrt{\frac{D}{\omega_0^2}} d\eta_1(\tau) \tag{a}$$

$$d\theta = \chi_2 d\tau + \sqrt{\frac{D}{\omega_0^2 a^2}} d\eta_2(\tau) \tag{b}$$

(21)

where $\eta_1(\tau)$ and $\eta_2(\tau)$ are two independent normalized Wiener processes. It is worth pointing out that a and θ are independent, allowing us further to develop a probability density for amplitude a , rather than a joint density for θ . The probability density $p(a, \tau)$ of the instantaneous amplitude a satisfied the Fokker–Planck–Kolmogorov equations [29,30]:

$$\begin{aligned} \frac{\partial}{\partial t} p(a, \tau) = & -\frac{\partial}{\partial a} \left[\left(\chi_1 + \frac{D}{2\omega_0^2 a} \right) p(a, \tau) \right] \\ & + \frac{1}{2} \frac{\partial^2}{\partial a^2} \left[p(a, \tau) \left(\frac{D}{\omega_0^2} \right) \right] \end{aligned} \quad (22)$$

In the context of energy harvesting systems, we are primarily interested in the long-term system behavior. Thus, the stationary solutions of Eq. (22) of electrical and mechanical part respectively are obtained as:

$$p(a) = N_1 a \exp \left[-\frac{1}{16D} (3\zeta_3 \omega_0^4 a^4 + K_0 a^2) \right], \quad (23)$$

where N_1 is the normalization constant expressed by

$$N_1 = \left| \frac{3\sqrt{D}\zeta_3\omega_0^4}{N_0} \right|, \quad (24)$$

with

$$N_0 = \sqrt{\pi D} \exp \left(\frac{1}{192} \frac{K_0^2}{D\zeta_3\omega_0^4} \right) \left(1 - \operatorname{erf} \left(\frac{K_0}{8\sqrt{3}\omega_0^2\sqrt{D}\zeta_3} \right) \right), \quad (25)$$

$$K_0 = K_1 + K_2 + K_3$$

and

$$K_1 = \frac{8\omega_0^2\lambda^2(\zeta_m\beta\vartheta_e + (\beta^2 + \omega_0^2)\zeta_1)}{(\beta^2 + \omega_0^2)(\lambda^2 + \omega_0^2)},$$

$$K_2 = \frac{8\omega_0^2\lambda(\beta^2 + \omega_0^2)\zeta_e\vartheta_p}{(\beta^2 + \omega_0^2)(\lambda^2 + \omega_0^2)},$$

$$K_3 = \frac{8\omega_0^2(\zeta_m\beta\vartheta_e\omega_0^2 + (\beta^2\omega_0^2 + \omega_0^4)\zeta_1)}{(\beta^2 + \omega_0^2)(\lambda^2 + \omega_0^2)}.$$

Through a transformation from variables (a, θ) to the original variables (z, \dot{z}) , an expression for the stationary density function of (z, \dot{z}) can be derived from Eq. (23) as

$$p(z, \dot{z}) = \frac{1}{2\pi\omega_0 a} p(a), \quad (26)$$

by letting $a = z^2 + \frac{\dot{z}^2}{\omega_0^2}$, Eq. (26) becomes

$$p(z, \dot{z}) = \frac{N_1}{2\pi\omega_0} \exp \left(-\frac{1}{16D} (3\zeta_3\omega_0^4(z^2 + \frac{\dot{z}^2}{\omega_0^2})^4 + K_0(z^2 + \frac{\dot{z}^2}{\omega_0^2})^2) \right). \quad (27)$$

Thus, the expected value of the mean square voltage of the piezoelectric circuit and electric current of the magnetic circuit can be calculated following this formula:

$$\langle y^2 \rangle = \langle V_0^2 \rangle = \frac{\vartheta_p^2\omega_0^2}{\lambda^2 + \omega_0^2} \langle a^2 \rangle \quad (28)$$

with

$$\langle a^2 \rangle = \int_0^{+\infty} a^2 p(a) da. \quad (29)$$

Substituting Eq. (29) into Eq. (28), we obtain:

$$\langle y^2 \rangle = \frac{\vartheta_p^2\omega_0^2}{\lambda^2 + \omega_0^2} \int_0^{+\infty} a^2 p(a) da = \frac{\vartheta_p^2\sqrt{D}N_1\Lambda}{2\sqrt{\pi}(\lambda^2 + \omega_0^2)K_4^2}. \quad (30)$$

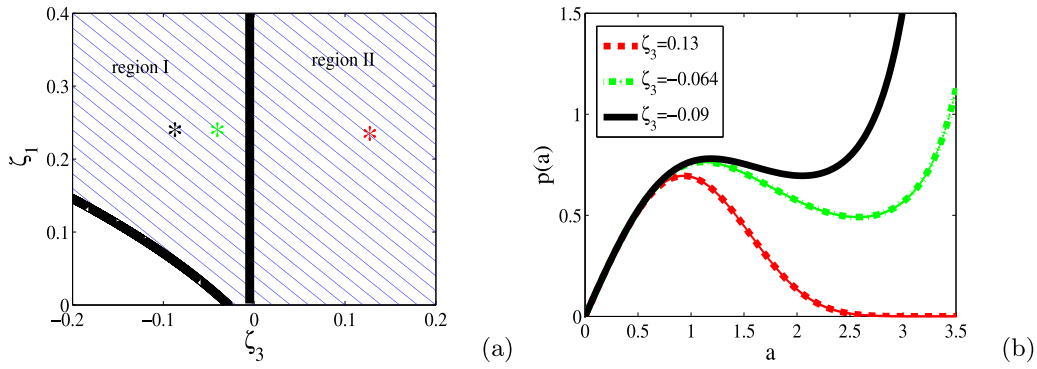


Fig. 3. (a) Bifurcation diagram of Eq. (35) in the parameter plane (μ_3, μ_1) , (b) Stationary probability density of amplitude for three value of ζ_3 . The other parameters used are given as: $\zeta_1 = 0.25, \alpha_1 = 0.72, \alpha_3 = 0.97, \zeta_e = 0.84, \lambda = 2.0, \zeta_m = 0.057, \vartheta_p = 0.38, \beta = 2.05, \omega_0 = 1.0, \vartheta_e = 0.05$ and $D = 0.4$.

Similarly

$$\langle \rho^2 \rangle = \frac{\vartheta_e^2 \omega_0^2}{\beta^2 + \omega_0^2} \int_0^{+\infty} a^2 p(a) da = \frac{\vartheta_e^2 \sqrt{DN_1} \Lambda}{2\sqrt{\pi}(\beta^2 + \omega_0^2)K_4^2} \tag{31}$$

with

$$\Lambda = \pi K_0 \sqrt{K_4} \exp\left(\frac{1}{64} \frac{K_0^2}{DK_4}\right) \left(\operatorname{erf}\left(\frac{1}{8} \frac{K_0}{\sqrt{K_4 D}}\right) - 1\right) + 8\sqrt{\pi DK_4} \tag{32}$$

and

$$K_4 = 3\zeta_3 \omega_0^4.$$

The average output power harvested by the hybrid system is estimated using this formula:

$$P_{\text{hybrid}} = \frac{\beta}{2T} \int_0^T y^2 d\tau + \frac{\lambda}{2T} \int_0^T \rho^2 d\tau. \tag{33}$$

Using the expressions of the mean square voltage of the piezoelectric circuit and electric current of the magnetic circuit, Eq. (33) become

$$P_{\text{hybrid}} = \beta \langle \rho^2 \rangle + \lambda \langle y^2 \rangle. \tag{34}$$

3.2. Stochastic bifurcations

This subsection is devoted to discuss the stochastic bifurcation through qualitative changes of the stationary probability density function (SPDF). The SPDF of prototype dynamical system Eq. (4) for amplitude a would be either unimodal or bimodal, which implies the transitions between unimodal and bimodal distribution with the variation of certain parameters. Moreover, by letting $\frac{\partial p(a)}{\partial a} = 0$, the extrema of the distribution Eq. (23) are the roots of equations:

$$1 - \frac{3}{4} \frac{\zeta_3 \omega_0^4 a_m^4}{D} - \frac{1}{8} \frac{K_0 a_m^2}{D} = 0 \tag{35}$$

a_m is the amplitude corresponding to the extremum of distribution Eq. (35) and m is the index number of the extremum. For a suitable choice of system parameters, the probability density function of the harvester can present one or two positive

extrema (one minimum and one maximum). By taking $\zeta_3 > 0$, the positive root of Eq. (35) is $\sqrt{\frac{1}{12} \frac{-K_0 + \sqrt{192D\zeta_3\omega_0^4 + K_0^2}}{\zeta_3\omega_0^4}}$, and then the probability density function in Eq. (26) has a maximum (Fig. 3(b)). However, by taking $\zeta_3 < 0$, there are two real positive

roots of Eq. (35) for a convenient choice of system parameters: $\sqrt{\frac{1}{12} \frac{-K_0 + \sqrt{192D\zeta_3\omega_0^4 + K_0^2}}{\zeta_3\omega_0^4}}$ and $\sqrt{-\frac{1}{12} \frac{K_0 + \sqrt{192D\zeta_3\omega_0^4 + K_0^2}}{\zeta_3\omega_0^4}}$ whose the shape is similar to a crater, and then the probability density function $P(a)$ presented in Fig. 3(b) has one maximum and one minimum respectively. Thus, a transition from a craterlike distribution to the unimodal distribution observed in Fig. 3(b) can be defined as a type of P-bifurcation.

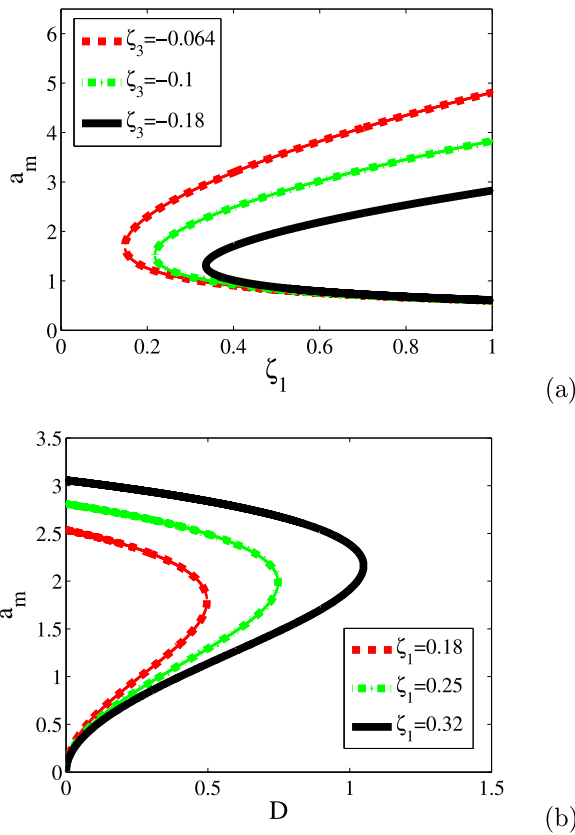


Fig. 4. (a) Amplitude response of mechanical subsystem versus ζ_1 for $D = 0.4$, (b) Amplitude response of mechanical subsystem versus D for $\zeta_3 = -0.064$. The parameters are the same as those in Fig. 3.

We plotted in (Fig. 3(a)), the bifurcation diagram of Eq. (35), for a fixed value of the noise intensity D . However, in region I, two positive roots are observed and give rise to the craterlike distribution. In region II, we have only one positive root, the distribution is unimodal.

Fig. 4(a)–(b) show the amplitudes of the mechanical subsystem, when varying the noise intensity and for three fixed values of ζ_1 and ζ_3 . In Fig. 4(a), we observe that, an increase of ζ_3 lead to decrease the maximum amplitude. However, an opposite phenomenon is observed in Fig. 4(b) when ζ_1 increase: an increase of ζ_1 leads to increase the maximum amplitude.

4. Numerical simulations

4.1. Algorithm of numerical simulations

The numerical simulations are made by integrating Eq. (4). By introducing the new variable $\dot{z} = u$, Eq. (4) can be rewritten in the form

$$\begin{aligned}
 \dot{z} &= u \\
 \dot{u} &= -\zeta_1 u - \zeta_3 u^3 - \omega_1^2 z - \alpha_2 z^2 - \alpha_3 z^3 - \zeta_e y - \zeta_m \rho + \xi(\tau) \\
 \dot{y} &= -\lambda y + \vartheta_p u \\
 \dot{\rho} &= -\beta \rho + \vartheta_e u.
 \end{aligned}
 \tag{36}$$

The discrete equations can be written as:

$$\begin{aligned}
 z_{n+1} &= z_n + u_n \Delta\tau \\
 u_{n+1} &= u_n - (\zeta_1 u_n + \zeta_3 u_n^3 + \omega_1^2 z_n + \alpha_2 z_n^2 + \alpha_3 z_n^3 \\
 &\quad + \zeta_e y_n + \zeta_m \rho_n) \Delta\tau + \xi_n(\tau), \\
 y_{n+1} &= y_n + (-\lambda y_n + \vartheta_p u_n) \Delta\tau, \\
 \rho_{n+1} &= \rho_n + (-\beta \rho_n + \vartheta_e u_n) \Delta\tau,
 \end{aligned}
 \tag{37}$$

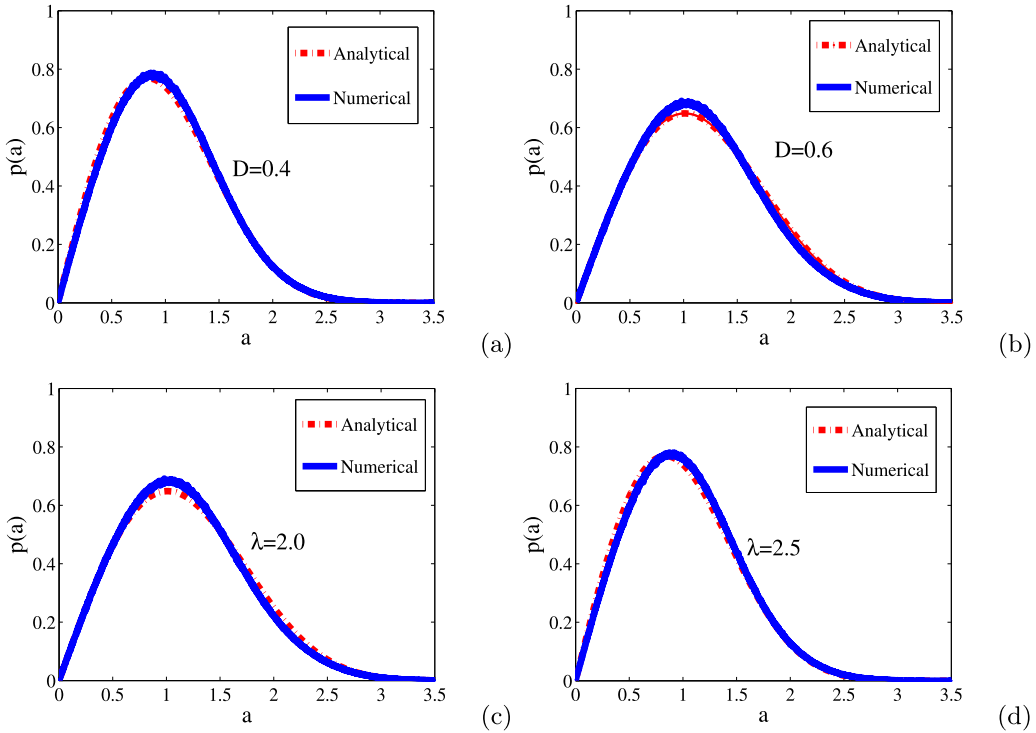


Fig. 5. Stationary probability density of mechanical subsystem for different values of electrical impedance λ . The other parameters used are given as : $\zeta_1 = 0.25, \zeta_3 = 0.064, \alpha_1 = 0.72, \alpha_3 = 0.97, \zeta_e = 0.84, \zeta_m = 0.057, \vartheta_p = 0.38, \beta = 2.05, \omega_0 = 1.0, \vartheta_e = 0.05$. The initial conditions: $(z(0), \frac{dz(0)}{dt}, y(0), \rho(0)) = (0, 0, 0, 0)$.

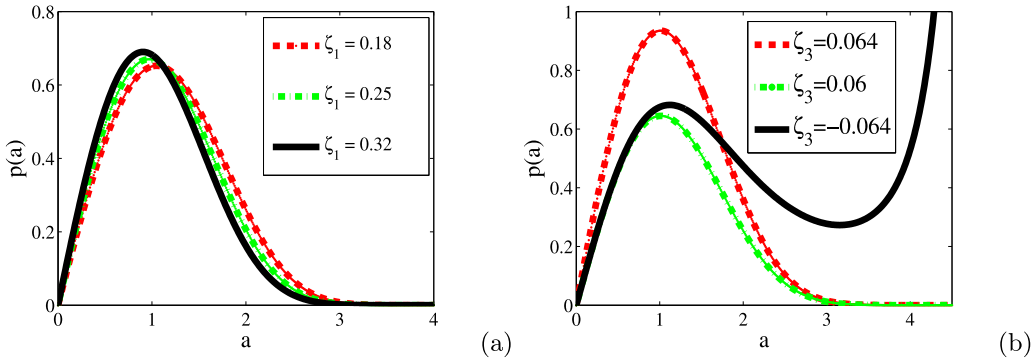


Fig. 6. Stationary probability density function of mechanical system: (a) for different values of linear damping with $\zeta_3 = 0.064$, (b) for different values of nonlinear damping with $\zeta_1 = 0.25$. The other parameters used are given as : $\alpha_1 = 0.72, \alpha_3 = 0.97, \zeta_e = 0.84, \lambda = 2.0, \zeta_m = 0.057, \vartheta_p = 0.38, \beta = 2.05, \omega_0 = 1.0, \vartheta_e = 0.05$ and $D = 0.4$.

where ξ_n is a sequence of random numbers distributed normally by the Box–Mueller algorithm. The Box–Mueller algorithm [31,32] is used to generate the Gaussian white noise from two random numbers a_1 and b_1 which are uniformly distributed on the unit interval [0, 1]. Thus, for each step Δt , it is worth nothing that ξ_n is defined as:

$$\xi_n = \sqrt{-4D\Delta t \log(a_1)} \cos(2\pi b_1) \tag{38}$$

with a time step for numerical simulations equal to $\Delta t = 0.01$.

4.2. Numerical simulation of probability density

With the goal to verify the efficiency of the analytical technique used, the numerical simulation of the system Eq. (4) is made. The physical parameters used in the simulation are given as follows: $c_1 = 0.001 \text{ N s/m}, c_3 = 4.5 \text{ N s}^3/\text{m}^3$,

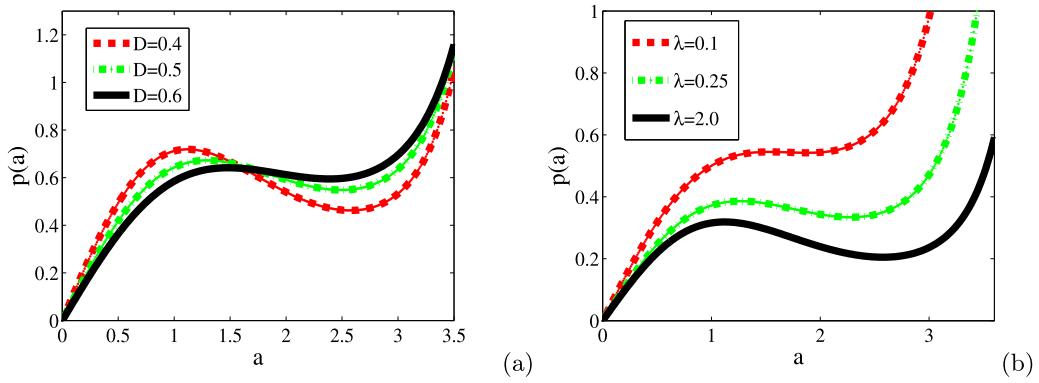


Fig. 7. Stationary probability density function of mechanical system: (a) for different values of noise intensity D with $\lambda = 2.0$, (b) for different values of impedance λ with $D = 0.4$. The other parameters used are given as : $\zeta_1 = 0.25, \zeta_3 = -0.064, \alpha_1 = 0.72, \alpha_3 = 0.97, \zeta_e = 0.84, \zeta_m = 0.057, \vartheta_p = 0.38, \beta = 2.05, \omega_0 = 1.0, \vartheta_e = 0.05$.

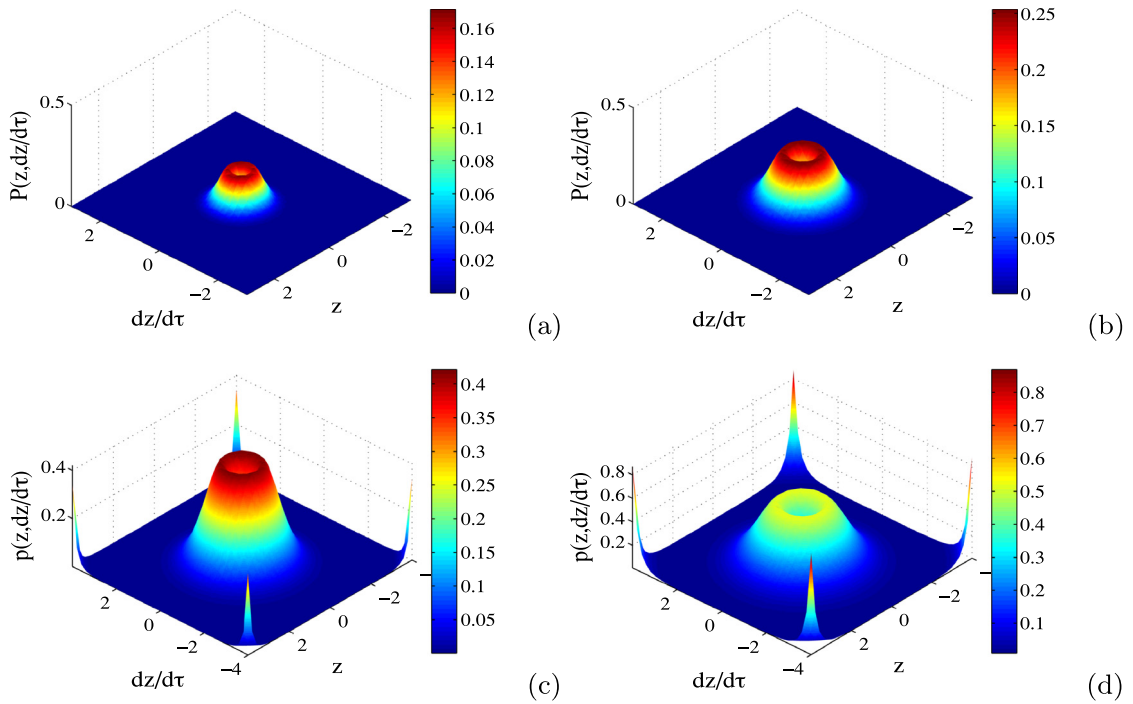


Fig. 8. Stationary probability density of the system in 3D representation for: (a) $D = 0.09$; (b) $D = 0.2$; (c) $D = 0.4$; (d) $D = 0.6$. The other parameters used are given as : $\zeta_1 = 0.25, \zeta_3 = -0.064, \alpha_1 = 0.72, \alpha_3 = 0.97, \zeta_e = 0.84, \zeta_m = 0.057, \vartheta_p = 0.38, \beta = 2.05, \omega_0 = 1.0, \vartheta_e = 0.05$ and $\lambda = 2.0$.

$k = 0.05 \text{ N/m}, L = 10 \text{ H}, l_0 = 0.075 \text{ m}, R = 20.5 \text{ } \Omega, m = 0.004 \text{ kg}, c_p = 0.00005 \text{ F}, R_p = 10\,000 \text{ } \Omega, \eta = 0.00025 \text{ N/V}, l = 0.0735 \text{ m}, z_0 = 0.017 \text{ m}$ and $v_0 = 0.1 \text{ V}$.

In this heading, we numerically and analytically plotted in Fig. 5, the probability density of mechanical subsystem for two values of noise intensity D and electrical impedance λ . We notice in Figs. 5(a) and (b) that, when D increase, the peak of the probability density function decreases. However, when the electrical impedance λ increases, the peak of probability density increases by shifting towards the weak amplitude values of (Figs. 5(c–d)). Within this framework, when the probability density reaches his maximum for a fixed value of electrical impedance coefficient, the amplitude a and the accumulated energies of the ambient energy collector are higher than those received in any oscillation. The agreement between the numerical and analytical simulation justifies the efficiency of the analytical technique used. In Figs. 6(a) and (b), we studied the impact of a linear and nonlinear damping coefficient ζ_1 and ζ_3 on probability density function $P(a)$. One can observe in Fig. 6(a) that, the probability distribution has only one maximum situated in the vicinity of zero for the high value of ζ_1 . In Fig. 6(b), one interesting phenomenon is observed when we enhance ζ_3 . A transition from a craterlike distribution to an unimodal distribution occurs. We also observe in these figure (Fig. 6(b)) that, the increasing of ζ_3 leads to the enhancement

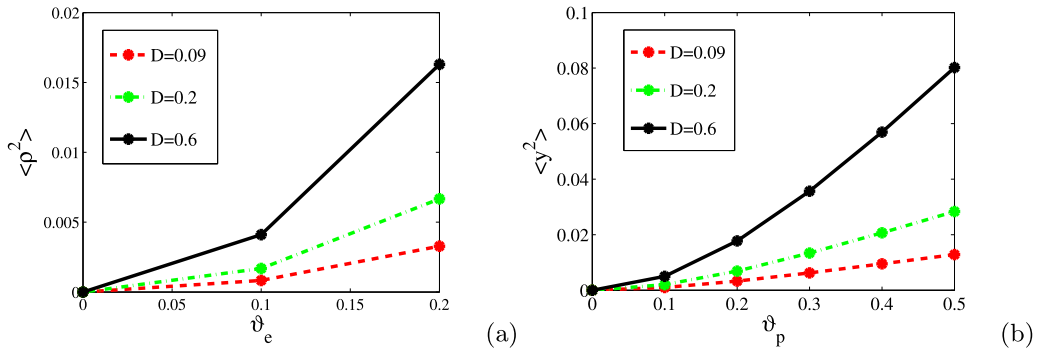


Fig. 9. (a) Evolution of mean square voltage of magnetic circuit versus ϑ_e for $\vartheta_p = 0.38$; (b) Evolution of mean square current of piezoelectric circuit versus ϑ_p for $\vartheta_e = 0.05$. The other parameters are given as: $\zeta_1 = 0.25, \zeta_3 = 0.064, \alpha_1 = 0.72, \alpha_3 = 0.115, \zeta_e = 0.84, \zeta_m = 0.057, \beta = 2.05, \omega_0 = 1.0$ and $\lambda = 2.0$.

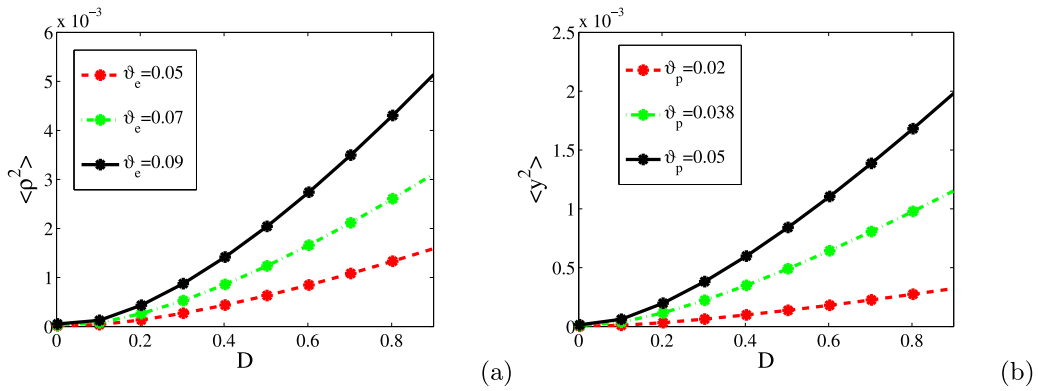


Fig. 10. (a) Evolution of mean square voltage of magnetic circuit noise intensity D for $\vartheta_p = 0.38$; (b) Evolution of mean square current of piezoelectric circuit versus noise intensity D for $\vartheta_e = 0.05$. The other parameters used are given as: $\zeta_1 = 0.25, \zeta_3 = 0.064, \alpha_1 = 0.72, \alpha_3 = 0.115, \zeta_e = 0.84, \zeta_m = 0.057, \beta = 2.05, \omega_0 = 1.0$ and $\lambda = 2.0$.

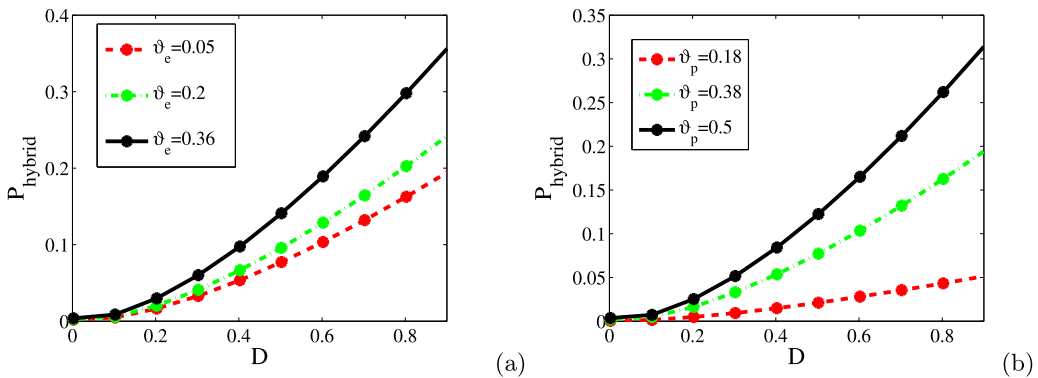


Fig. 11. Output power harvested by the hybrid system as function of the driving noise intensity with the parameters $\zeta_1 = 0.25, \zeta_3 = 0.064, \alpha_1 = 0.72, \alpha_3 = 0.115, \zeta_e = 0.84, \zeta_m = 0.057, \beta = 2.05, \omega_0 = 1.0$ and $\lambda = 2.0$.

of the probability density function by shifting its maximum towards small amplitude values. This means that the system energy could be optimized for the small values of linear and nonlinear damping coefficient. In Figs. 7(a) and (b), we studied the impact of a noise intensity D and impedance λ on probability density function $P(a)$ for $\zeta_3 < 0$. One can observed in Fig. 7(a) that, the amplitude distribution has only one minimum situated in the vicinity of zero for the high value of D . However, beyond the peak, the probability density function decreases when D increases. In Fig. 7(b), an enhancement of impedance λ leads to decrease, the maximum value of peak and increases its maximum.

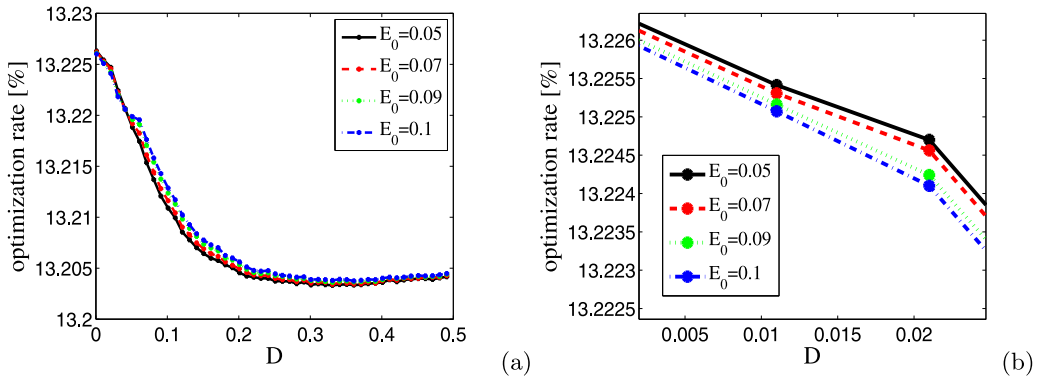


Fig. 12. Increase rate op_{max} versus noise intensity, (a) overall view; (b) detailed view for $\zeta_1 = 0.25$, $\zeta_3 = 0.064$, $\alpha_1 = 0.72$, $\alpha_3 = 0.115$, $\zeta_e = 0.84$, $\zeta_m = 0.057$, $\vartheta_p = 0.38$, $\beta = 2.05$, $\vartheta_e = 0.05$ and $\lambda = 2.0$ and $\omega = 0.35$.

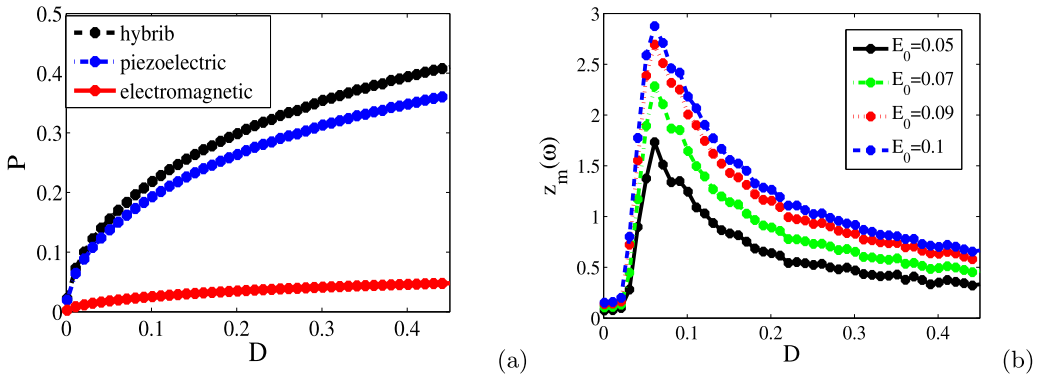


Fig. 13. (a) Comparison of the output power with $E_0 = 0.05$; (b) Mean response amplitude versus noise intensity D ; with the parameters $\zeta_1 = 0.25$, $\zeta_3 = 0.064$, $\alpha_1 = 0.72$, $\alpha_3 = 0.115$, $\zeta_e = 0.84$, $\zeta_m = 0.057$, $\vartheta_p = 0.38$, $\beta = 2.05$, $\vartheta_e = 0.05$ and $\lambda = 2.0$ and $\omega = 0.35$.

Figs. 8(a)–(d) show the probability density in 3D representation for four values of noise intensity. In Figs. 8(a)–(b), the unimodal distribution is observed. However, in Figs. 8(c)–(d), the craterlike distribution characterized by one maximum and one minimum is observed. A similar result was observed in Ref. [23].

4.3. Mean square electrical charge

In this section, we use equations Eqs. (28)–(31) giving respectively the expressions of the mean square values of the voltage for the piezoelectric circuit ($\langle y^2 \rangle$) and mean square values of the instantaneous electrical current for the magnetic circuit ($\langle \rho^2 \rangle$). We provided in Figs. 9(a)–(b), the mean square values of the instantaneous electrical charge ($\langle z^2 \rangle$) and mean square voltage versus coupling coefficient of the piezoelectric circuit ϑ_p and the magnetic circuit ϑ_e for three values of the noise intensity. In Fig. 9(a), we observed that, the output power in terms of mean square voltage increases when the noise intensity increases. Similar result is observed in Fig. 9(b) when the noise intensity increase.

We plotted in Figs. 10(a)–(b), the output power versus D for three values of the ϑ_e and ϑ_p . We notice in these figures that, an increase of ϑ_e and ϑ_p leads to increase of the output power.

We also provided in Figs. 11(a)–(b), the total output harvested by the hybrid system versus the noise intensity D for three values of the coupling coefficient ϑ_e and ϑ_p . It emerges from these figures that, when ϑ_e and ϑ_p increase, the amount of harvested energy by the system is improved. This result obtained in previous figure (Figs. 11(a)–(b)) shows the interest to build the hybrid model.

4.4. Stochastic resonance

In this subsection we discuss the impact of the combination of the deterministic and random signal on the system performance. The determinist excitation is expressed as $(E_0 \cos(\omega\tau))$. It is well known in the literature that the adding of the coherent signal to the random excitation can give rise to the stochastic resonance phenomenon which can increase the bandwidth of the harvester and consequently, improves the system performance [33,34]. In this manuscript, the response

amplitude $z_m(\omega)$ at the frequency ω is calculated using Fourier coefficients as follow [23]:

$$z_m(\omega) = \sqrt{A_s^2 + A_c^2} \quad (39)$$

where A_s and A_c are the sine and cosine components of the Fourier coefficients defined by:

$$A_c = \frac{2}{nT} \int_0^{nT} x(\tau) \cos(\omega\tau) d\tau \quad (40)$$

$$A_s = \frac{2}{nT} \int_0^{nT} x(\tau) \sin(\omega\tau) d\tau \quad (41)$$

where n is the integer number. In this work, $n = 300$, while $T = \frac{2\pi}{\omega}$ is the period of the harmonic excitation. In the purpose to know the degree of optimization of the hybrid model with respect to the piezoelectric circuit, we compute the increase rate using this formula:

$$op_{max} = \frac{p_{hybrid} - p_{piezoelectric}}{p_{piezoelectric}} \times 100 [\%] \quad (42)$$

where p_{hybrid} and $p_{piezoelectric}$ are the output power harvested by the hybrid system and piezoelectric circuit. In the simulation, we took 100 realizations.

We depicted in Fig. 12, the increase rate op_{max} versus D , for four values of amplitudes of the harmonic excitation E_0 . This figure reveals that, an increase of E_0 leads to decrease the op_{max} . In addition, we also observed in this figure that, regardless of the value of the harmonic excitation, when the noise intensity is large, op_{max} decreases and tends towards the constant value.

We provided in Figs. 13(a)–(b), the comparison between the output power harvested respectively in the piezoelectric circuit, the electromagnetic circuit and the overall system and the mean amplitude response versus noise intensity D . We notice in Fig. 13(a) that, the energy harvested by the hybrid model is higher than that harvested by the piezoelectric or electromagnetic circuit (Fig. 13(a)). Fig. 13(b) show the mean amplitude response versus noise intensity, for four values of the noise intensity D . One observes that, for some values of amplitude of the noise excitation, the mean amplitude response presents a maximum. This maximum is a signature of the stochastic resonance, which gives the largest oscillation amplitude for a given excitation level, and reflects the transition in the system response from single well to double well oscillations. In addition, we can note in this figure (Fig. 13(b)) that, the maximum amplitude response is obtained for the highest amplitude of the harmonic excitation.

5. Conclusion

In this manuscript, the dynamic behavior of the hybrid energy harvester under Gaussian white noise using probabilistic approach is investigated. By applying a stochastic averaging method on this system, the stochastic response is obtained. The results obtained show that, the shape of the statistic response strongly depends on the coefficient of the nonlinear damping. The impact of the system parameters is investigated with detail. The obtained results show that, when the coupling coefficients and noise intensity increase, the harvested energy is improved. In addition, the stochastic bifurcation phenomenon characterized by the qualitative change of the stationary probability density is observed and allows to obtain the best value of the bifurcation parameter for which the harvester presents a high limit cycle. Besides, combining the harmonic force to the random signal, the stochastic resonance phenomenon occurs and improves the system performance. The comparison between the harvested energy by the hybrid model to that harvested by the piezoelectric model is investigated. The impact of the amplitude of the harmonic excitation is investigated on the system performance. It emerges from this result that, the harvested energy is very significative for the high value of the E_0 . The results obtained in this manuscript show the interest to build the hybrid harvester.

References

- [1] C. Williams, R. Yates, *Sensors Actuators A* 52 (1996) 8.
- [2] A. Erturk, D.J. Inman, *J. Vib. Acoust.* 130 (2008) 041002-1.
- [3] H.A. Sodano, D.J. Inman, G. Park, *Shock Vib. Digest* 36 (2004) 197.
- [4] G. Sebald, H. Kuwano, D. Guyomar, B. Ducharne, *Smart Mater. Struct.* 20 (2011) 102001.
- [5] M.A. Ahmad, H.N. Alshareef, *J. Electron. Mater.* 40 (2011) 1477.
- [6] C.R. Saha, T. O'Donnell, Heiko Loder, S. Beeby, J. Tudor, *IEEE Trans. Magn.* 42 (2006) 3509.
- [7] C.R. Saha, T. O'Donnell, H. Loder, S. Beeby, J. Tudor, *IEEE Trans. Magn.* 42 (2006) 3509.
- [8] P.D. Mitcheson, P. Miao, B.H. Stark, E.M. Yeatman, A.S. Holmes, T.C. Green, *Sensors Actuators A* 115 (2006) 523.
- [9] S. Meninger, J.O. Mur-Miranda, R. Amirtharajah, A.P. Chandrakasan, J.H. Lang, *IEEE Trans. Very Large Scale Integr. (VLSI) Syst.* 9 (2001) 64.
- [10] S. Roundy, P. Wright, J. Rabaey, *Springer Science Business Media*, 2009.
- [11] S.M. Shahrz, *J. Sound Vib.* 292 (2006) 987.
- [12] M. Coccolo, G. Litak, M.J. Seoane, A.F.S. Miguel, *Internat. J. Bifur. Chaos Appl. Sci. Engrg.* 24 (2004) 1430019.

- [13] R. Masana, M.F. Daqaq, *J. Sound Vib.* 330 (2011) 6036.
- [14] B.A. Owens, B.P. Mann, *J. Sound Vib.* 331 (2012) 922.
- [15] J. Wen-An, Li-Qun Chen, *J. Sound Vib.* 333 (2014) 4314.
- [16] X. Zhenlong, S. Xiaobiao, C. Danpeng, X. Tao, *Appl. Sci.* 6 (2016) 10.
- [17] B. Madinei, H.K.H. Haddad, S. Adhikari, M.I. Friswell, *Shock, Vibration, Aircraft/Aerospace, Energy Harvesting Acoustics Optics*, Vol. 9, Springer, 2016.
- [18] T. Wacharasindhu, J.W. Kwon, *J. Micromech. Microeng.* 18 (2008) 104016.
- [19] B. Lee, L. Wei, *J. Micro/Nanolith. MEMS MOEMS* 9 (2010) 023002.
- [20] M.A. Karami, D. Inman, *J. Sound Vib.* 330 (2011) 5583.
- [21] C.R. McInnes, D.G. Gorman, M.P. Cartmell, *J. Sound Vib.* 318 (2008) 655.
- [22] L. HaiTao, W. Qin, D. Wangzheng, T. Ruilan, *Eur. Phys. J. Plus* 131 (2016) 60.
- [23] I.S. Mokem Fokou, C. Nono Dueyou Buckjohn, M. Siewe Siewe, C. Tchawoua, *Chaos Solitons Fractals* 92 (2016) 101.
- [24] M. Borowiec, G. Litak, S. Lenci, *Int. J. Struct. Stab. Dyn.* 14 (2014) 1440020.
- [25] M.G. Tehrani, L. Simeone, S.J. Elliot, *ENOC*. (2013) 6.
- [26] M.G. Tehrani, S.J. Elliot, *J. Sound Vib.* 333 (2014) 623–629.
- [27] V.S. Anishchenko, V. Astakhov, A. Neiman, T. Vadivasova, L. Schimansky-Geier, *Tutorial and Modern Developments*, Springer, Berlin, 2007.
- [28] R.L. Stratonovich, *Gordon and Breach*, New York, 1967.
- [29] H. Risken, T. Frank, *The Fokker–Planck Equation: Methods of Solution and Applications*, in: *Springer Series in Synergetics*, 1996.
- [30] M.I. Freidlin, A.D. Wenzel, *Random Perturbations in Dynamical Systems*, Springer, New York, 1984.
- [31] W.S. Cho, 2012.
- [32] L. Arnold, Springer, Berlin, 2003.
- [33] J.H. Yang, M.A.F. Sanjuan, H.G. Liu, G. Litak, X. Li, *Commun. Nonlinear Sci. Numer. Simul.* 41 (2016) 104.
- [34] R.N. Mantegna, B. Spagnolo, L. Testa, M. Trapanese, *J. Appl. Phys.* 97 (2005) 223.